Dissertation
submitted to the
Combined Faculties for the Natural Sciences and for Mathematics
of the Ruperto-Carola University of Heidelberg, Germany
for the degree of
Doctor of Natural Sciences

presented by

Dipl. Physicist Sergey Yurevich

born in St. Petersburg, Russia

Oral Examination: 10.05.2006

Electron-Pair Production

in 158 AGeV/c Pb-Au Collisions

from CERES

Referees: **Prof. Dr. Johanna Stachel**

Prof. Dr. Ulrich Uwer

Das CERES Experiment beschäftigt sich mit der Messung von Elektronenpaaren im niederen Massenbereich in protonen- und ioneninduzierten Kollisionen am Super Proton Synchrotron. Im Mittelpunkt steht dabei die Untersuchung von Veränderungen hadronischer Eigenschaften unter dem Einfluß heißer und dichter Kernmaterie. Eine signifikant erhöte Produktionsrate von Dileptonenpaaren, bezogen auf Erwartungen aus hadronischen Zerfällen, wurde im Massenbereich $0.25 < m_{ee} < 0.7$ GeV/c^2 beobachtet. Dieses faszinierende Ergebnis kann nur durch Modelle erklärt werden, die Veränderungen des ρ-Mesons innerhalb des Mediums zulassen. Um eine bessere Massenauflösung im Bereich der Vektormesonen zu erreichen und somit zwischen den verschiedenen theoretischen Erklärungsmöglichkeiten unterscheiden zu können, wurde das Experiment im Jahr 1998 durch eine TPC mit radialer Drift ergänzt. Die in dieser Doktorarbeit vorgestellte Analyse beruht auf dem Datensatz von 158 A GeV/c Pb-Au Kollisionen, der im Jahr 2000 mit dem erweiterten experimentellen Aubau aufgenommenen wurde. Die beobachtete erhöhte Produktionsrate der e^+e^--Paare bestätigt frühere CERES Ergebnisse. Ein Vergleich der Daten mit theoretischen Vorhersagen favorisiert Rechnungen, die auf der Veränderung der Spektralfunktion des ρ-Mesons im Medium beruhen, gegenüber solchen, die auf einer reduzierten ρ-Mesonen Masse beruhen.

The CERES experiment is devoted to the measurement of low-mass electron pairs in proton and ion-induced collisions at the Super Proton Synchrotron accelerator. The main goal of the CERES experiment is to investigate modifications of hadron properties in hot and dense nuclear matter. A significant enhancement of dilepton pair yield with respect to expectations based on hadron decays was observed in the mass range $0.25 < \mathrm{m}_{ee} < 0.7$ GeV/c^2. This fascinating result can only be described by models invoking in-medium modifications of the ρ meson. To distinguish between different theoretical explanations of the enhancement the experiment was upgraded in 1998 by the addition of a radial TPC to improve the mass resolution in the vector meson region. In this thesis, the analysis of the data sample taken in 2000 in 158 A GeV/c Pb-Au collisions with the upgraded experimental setup is presented. The observed enhancement of the e^+e^- pairs confirms previous results of CERES. The data, compared to the theoretical calculations based on dropping ρ mass approach and in-medium ρ spectral function modifications, favor the latter.

Contents

List of Figures

List of Tables

1

Introduction

1.1 Relativistic Heavy Ion Physics

The primary motivation for studying the relativistic heavy ion collisions is to gain an understanding of properties of strongly interacting hadronic and partonic matter at high energy densities. The hadronic and partonic matter is commonly referred to as nuclear matter. The examination of nuclear matter is of cross-disciplinary interest to nuclear physics as well as to astrophysics, cosmology and particle physics. Fig. 1.1 displays a schematic phase diagram of nuclear matter [2, 10, 11]. The behavior of nuclear matter as a function of temperature and density is governed by its equation of state. The lower left part of the diagram at low temperatures and near normal nuclear matter density concerns conventional nuclear physics. Here the normal nuclei exist. At higher temperatures nucleons are excited into baryonic resonance states, along with accompanying particle production and hadronic resonance formation. In heavy ion collisions, such excitations are expected to create hadronic resonance matter. The two accelerator facilities, the Alternating Gradient Synchrotron (AGS) at Brookhaven National Laboratory and the Super Proton Synchrotron (SPS) at CERN, accessed this region with heavy ion beams. These collisions may traverse the transition region into the new state of matter: the Quark-Gluon Plasma (QGP) [12]. Formation of the quark-gluon plasma, a deconfined state of quarks and gluons, is the major focus of relativistic heavy ion experiments at higher energies. The Relativistic Heavy Ion Collider (RHIC) at Brookhaven is presently the operating accelerator facility delivering the highest energy in the heavy ion field. The operation with heavy ions is also planned for the Large Hadron Collider (LHC) at CERN in 2007. As shown in the phase diagram, the temperature and density trajectories at RHIC (and LHC) lie close to that of the early universe, while those at the AGS and SPS occur at higher baryon densities.

The universe temperature at around ten micro-seconds after the Big Bang was approximately 150-200 MeV. At this temperature a quark-hadron phase transition is predicted, which is the same transition as that from hadronic matter to a quark-gluon plasma, but in the reverse direction by cooling from a higher temperature. Also of interest in cosmology is general nucleosynthesis, various aspects of stellar evolution, neutron star collapse and supernova expansion dynamics which occur at high baryon densities and very low

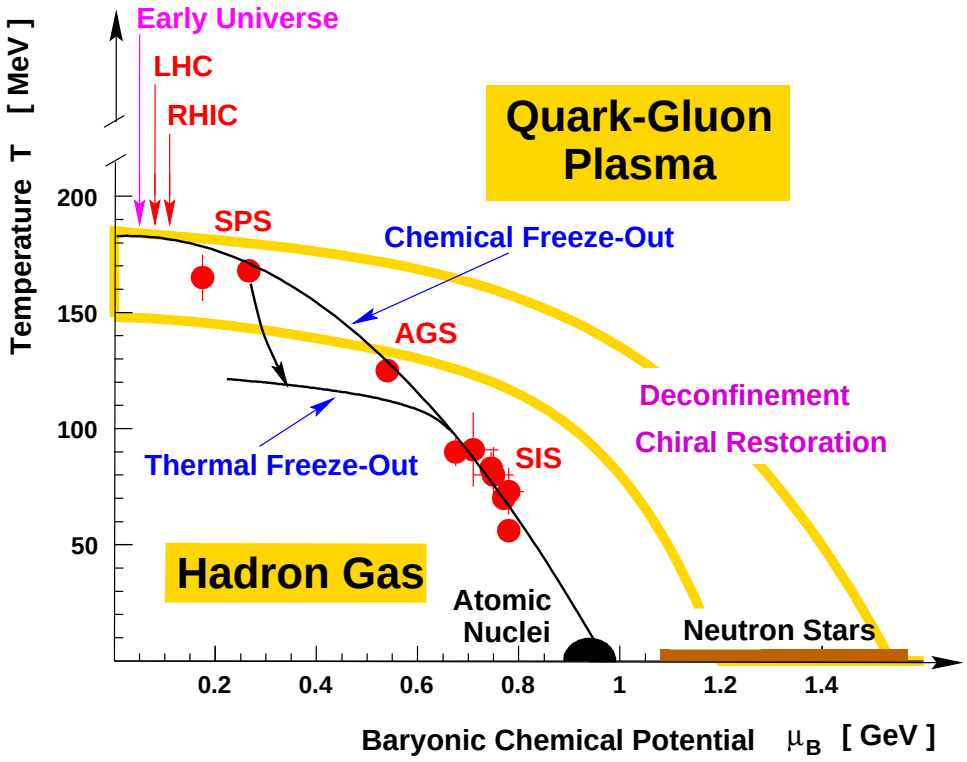

Figure 1.1: Phase diagram of hadronic matter and hadrochemical freeze-out points for heavy ion collisions at SIS, AGS and SPS. The region between two yellow lines indicates the expectation [10] for the phase boundary based on lattice QCD calculations at $\mu_b = 0$. The arrow from chemical to thermal freeze-out curve for the SPS is calculated for expansion with constant entropy per baryon [13].

temperatures. Thus the study of extreme states of matter created in high-energy nuclear collisions provides scientists with an opportunity of gaining insight into many important aspects in different fields of physics.

The symmetry breaking mechanisms and the origin of particle masses are the key questions. An investigation of the perturbative vacuum of the Quantum Chromo-Dynamics (QCD) using collisions of relativistic heavy ions may allow to find the answers. The complex internal structure of the QCD vacuum consists of a quark-gluon condensate sea. This sea fluctuates about its zero point. At low energy densities, quarks and gluons are confined into hadrons (baryons and mesons). Thus, the vacuum acts as color dielectric. At the high temperatures in high energy collisions of heavy ions, the quark-antiquark condensate vacuum melts. The quarks and gluons confined in hadrons become free and the vacuum transforms from a color dielectric to a color conductor. This is the quark-gluon plasma phase. Another phase transition, namely the restoration of chiral symmetry, is also predicted at high temperatures.

1.2 Concepts of Quantum Chromo-Dynamics

The Quantum Chromo-Dynamics has two remarkable features. The strong coupling constant is large at large distances or small momentum transfer (Q^2) and quarks are confined into colorless particles, so-called color-singlets. At short distances or large momentum transfer, the coupling constant is small, approaching zero for $Q^2 \rightarrow \infty$. This is the regime of asymptotic freedom.

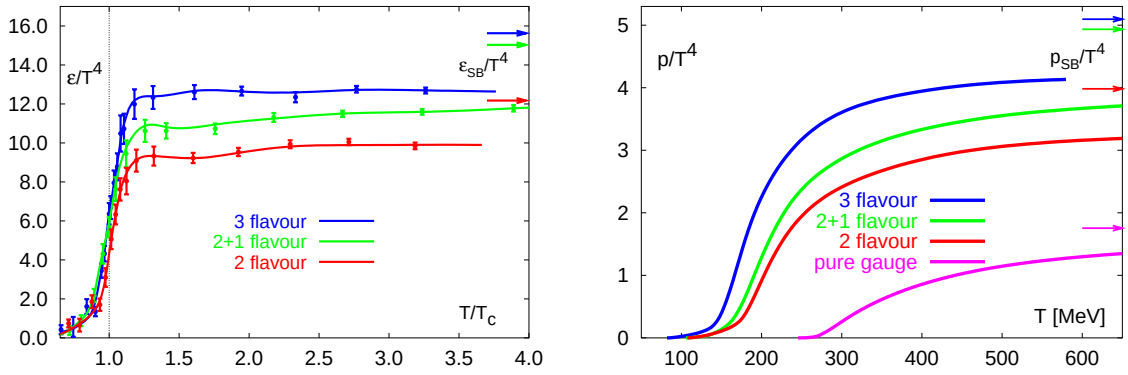

Figure 1.2: Results of a lattice QCD calculation using 0, 2, 3 light quarks and 2 light quarks plus strange quark [14]. Plotted are the energy density ϵ/T^4 (left panel) and the pressure P/T^4 (right panel). The energy density and the pressure values for the ideal gas are shown with arrows.

The more quantitative understanding of the QCD thermodynamics can be obtained by carrying out non-perturbative numerical calculations of thermodynamic variables on a lattice [14–16]. The results of the calculations based on 2 or 3 quark flavors are displayed in Fig. 1.2. The critical conditions for a phase transition from a confined phase (hadronic matter) to a deconfined phase (quark-gluon plasma) are predicted to occur at a temperature of $T_c \approx 170$ MeV corresponding to the energy density $\epsilon \approx 1$ GeV/fm^3. For the energy density a smooth and rapid transition is observed as a function of temperature. A more gradual transition is found for the pressure p. Due to the finite lattice size it is hard to say whether the phase transition is a weak first order one or a second order transition.

The chiral symmetry restoration at high temperatures is also of great interest. The mass of quark depends on the distance over which it is probed by another quark. Since the nucleon is made up from three quarks, the quark mass should be approximately one third the mass of the nucleon, or about 300 MeV/c^2. These are so-called constituent quarks, which are dressed in a virtual cloud of quark-antiquark pairs and gluons. Due to the fact that interaction becomes weaker at short distances, the shorter the distance between quarks, the smaller the mass. Therefore the mass of the current quark in the regime of asymptotic freedom is near zero. The estimate for the up-quark mass is approximately 5 MeV and that for the down-quark is approximately 7 MeV. For massless quarks the QCD Lagrangian factorizes into a left-handed term and right-handed term, and is therefore chirally symmetric. For the case of nucleon, which has non-zero mass, the

chiral symmetry is spontaneously broken. In this case the QCD Lagrangian has an additional term which is proportional to the light quark mass times the vacuum expectation value of the quark-antiquark condensate $\langle\bar{\psi}\psi\rangle$. Since this expectation value is finite, the Lagrangian can not be chirally symmetric.

In summary, at low energy densities quarks and gluons are bound into colorless objects, called hadrons, and are confined. The quarks obtain large effective masses ($m_u \sim m_d \sim$ 300 MeV/c^2, $m_s \sim$ 500 MeV/c^2) by interactions among themselves and with the surrounding vacuum. This is called broken chiral symmetry. At high energy densities, which are reached in relativistic heavy ion collisions, a phase transition is expected to occur. The partons become deconfined and their masses decreases ($m_u \sim m_d \sim 0$, $m_s \sim$ 150 MeV/c^2) and the chiral symmetry is partially restored.

1.3 Space-Time Evolution of Relativistic Heavy Ion Collisions

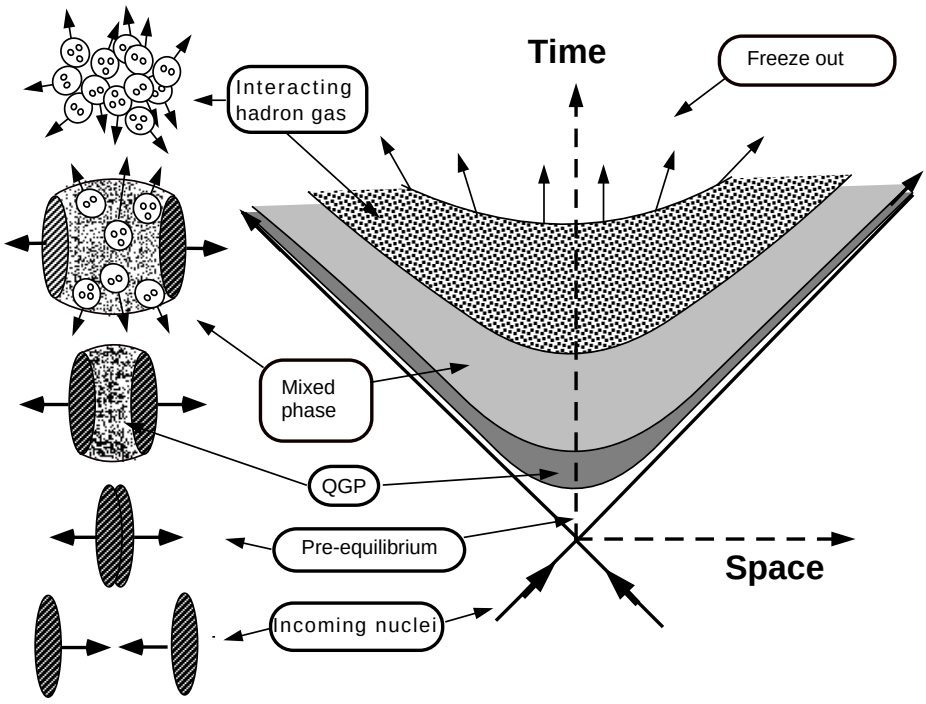

Figure 1.3: Space-time evolution of heavy ion collisions.

A transition from a quark-gluon plasma to a hadronic matter must have existed about 10 microseconds after the Big Bang. As predicted by lattice QCD a reverse transition to a quark-gluon plasma should occur at sufficiently high energy densities. To reproduce a deconfinement transition in the laboratory is the task of the relativistic heavy ion physics.

The computer simulations of space-time evolution of the collisions predict that a life time of the fireball should be 5 - 10 fm/c. The strength of potential QGP signals relative to the background created by the hot hadronic phase and final state modifications depends on the overall time evolution: the collision process at the parton level, formation of a quark-gluon plasma, expansion, cooling, and hadronization.

The space-time evolution of a heavy ion collision can be classified by thermodynamic variables. This involves determination of the energy density ϵ, pressure P, and entropy s of the interacting system as a function of temperature and the baryochemical potential μ. The dynamics of the collision process can be also addressed by the nuclear stopping power. The nuclear stopping power determines the amount of energy accessible in the interaction region, the volume of the interaction region and therefore the energy density. Various measurements made using different nuclear systems at the AGS and SPS indicate that the amount of nuclear stopping power is large. This means that the amount of energy in the interaction region is sufficient to produce energy densities well above the critical energy density predicted by lattice QCD calculations ($\approx$ 1 GeV/fm^3).

The space-time evolution of heavy ion collisions is schematically displayed in Fig. 1.3. Two incoming nuclei moving almost with speed of light are Lorentz contracted. Within 1 fm/c after the collision, the energy of relative motion of the incoming nuclei is transformed into other degrees of freedom. After the pre-equilibrium stage the QGP is expected to be formed via the parton-parton interactions. The interacting system then expands due to the huge pressure inside the hot and dense medium. At the same time, temperature and density of the medium are decreasing. A mixed phase follows the quark-gluon plasma. First hadrons are created in the expanding QGP. Once temperature and density of the fireball become sufficiently low, the remaining islands of plasma hadronize. The interacting gas of hadrons further expands and cools to the point referred to as chemical freeze-out, where all inelastic interactions between particles cease and the abundances of hadrons are fixed. With further decrease of the temperature and density also the elastic interactions vanish (thermal freeze-out) and particles stream towards the detectors.

1.4 Electromagnetic Probes

There are many experimental observables providing information on the evolution of the nuclear collisions. The observation of electromagnetic radiation seems ideally suited because photons and leptons have no strong coupling and therefore information from the time of their emission can be detected undistorted by final state interactions. Since electromagnetic radiation is emitted throughout the evolution of the interaction it supplies information on the full dynamics of the collision system. Electromagnetic radiation can be detected via virtual photons (dileptons) or via real photons. It can be emitted in QGP phase as $q\bar{q}$ annihilation [17] and also in the hadron gas phase, essentially as $\pi^+\pi^-$ annihilation. The thermal radiation emitted via quark-antiquark annihilation process produces an exponential spectrum with a slope parameter reflecting the temperature of the system and might be observed only in the mass region above 1 GeV/c^2. On the other hand, the $\pi^+\pi^-$ annihilation rising from threshold at $m = 2m_\pi$ is expected to contribute in the region around and below ρ^0-meson mass.

Photons and leptons may provide a measure of the thermal radiation from a quark-gluon plasma, if a region of photon energy, or equivalently lepton pair invariant mass, can be isolated for emission from the QGP relative to other processes. However, the yields for electromagnetic probes are small with respect to background processes, which are primarily electromagnetic decays of hadrons and resonances after freeze-out of the collision system. Fig. 1.4 illustrates a schematic dilepton mass spectrum. Lepton pairs from a quark-gluon plasma are expected to be identified in the 1 - 1.2 GeV/c^2 invariant mass range. The low mass region, where most of the cross section lies, includes the Dalitz decays of the π^0, η, η', ω, and the resonance decays of the ρ, ω and ϕ. At somewhat higher masses the semileptonic decay of the charmed mesons $D\bar{D}$ and the Drell-Yan process dominate. The high mass region above 3 GeV/c^2 includes the J/ψ and the ψ' resonances and the underlying continuum dominated by Drell-Yan mechanism.

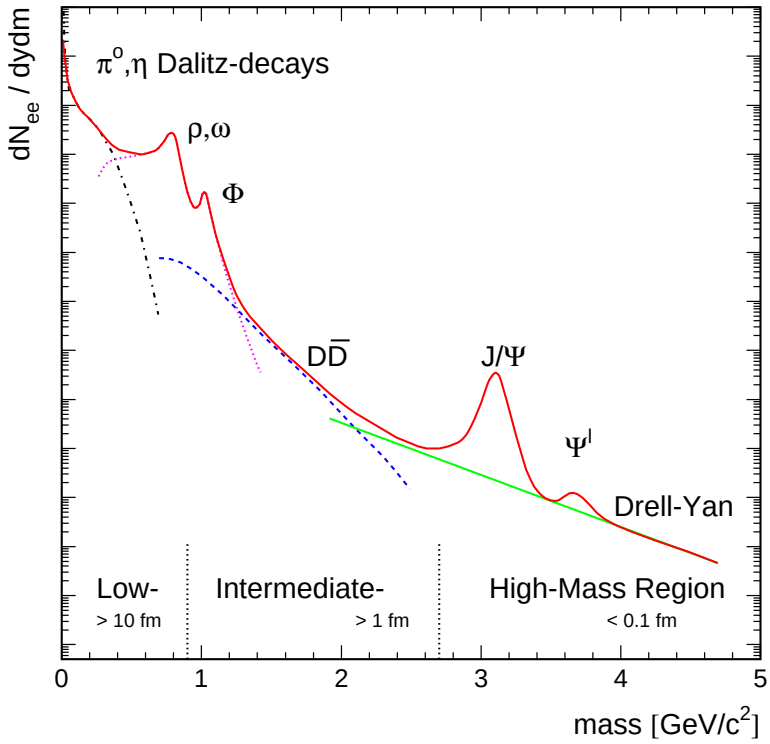

Figure 1.4: Schematic view of the e^+e^- invariant spectrum.

At lower invariant masses between 0.5 and 1 GeV/c^2, lepton pairs from hadronic sources are expected to dominate and provide information on possible medium modifications of hadrons at high density. The widths and positions of the ρ, ω, and ϕ peaks in the lepton pair invariant mass spectrum are expected to be sensitive to medium-induced modifications of the hadronic mass spectrum, such as drop and/or broadening of the vector meson masses preceding chiral symmetry restoration. Among all vector mesons the ρ-meson is of special interest. In fact, the thermal fireball is expected to live significantly longer than the 1.3 fm/c lifetime of the ρ-meson. Due to its very short life time compared to the fireball lifetime, most of the ρ-mesons produced in the collision will decay

inside the interaction region. If the temperature and/or the baryon density are high enough for partial chiral symmetry restoration to take place, the properties of the ρ-meson will change leading to a detectable signal in the low-mass dilepton spectrum. The ω and ϕ mesons live much longer. Their live times are about 23 and 44 fm/c respectively. Since the strength of the ρ-meson is expected to increase relative to the longer-lived ω, the ρ/ω ration may serve as a "clock" for the lifetime of the thermal fireball.

1.5 Previous CERES Results

The CERES experiment is dedicated to the measurement of low-mass electron-positron pairs in ultra-relativistic heavy ion collisions. The kinematic region close to mid-rapidity accessible by CERES is displayed in Fig. 1.5. The other two muon pair spectrometers at CERN SPS, NA38/NA50 [18–20] and NA34/HELIOS-3 [21, 22] cover more forward rapidities, as shown in Fig. 1.5.

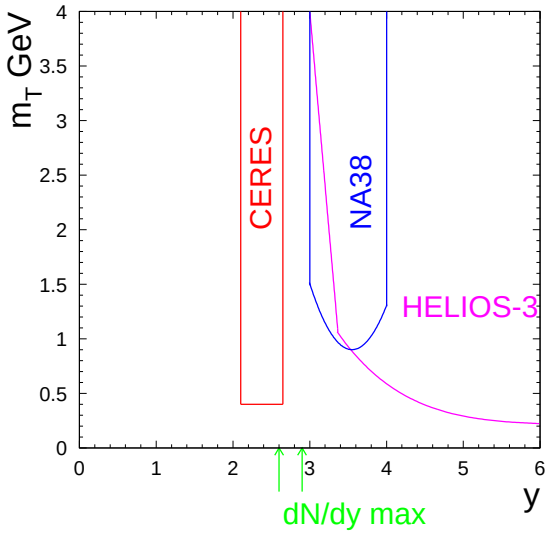

Figure 1.5: Dilepton kinematical acceptance in the m_t-y plane. The rapidities with the largest particle production in central collisions of sulfur ions at 200 A GeV (left arrow) and lead ions at 158 A GeV (right arrow) are indicated in the plot.

CERES has completed a systematic physics program including the measurement of electron pairs in p-Be and p-Au collisions at 450 GeV/c [23–25], S-Au collisions at - 200 A GeV [26, 27] and Pb-Au collisions at 158 A GeV [28–36], Pb-Au collisions at 40 A GeV [37–40]. A very interesting results has been found in this systematic study. A strong enhancement of low-mass electron pairs in S-Au and Pb-Au collisions was observed, indicating the onset of a new source, beyond the mere superposition of p-p collisions. However, no enhancement was observed in p-Be and p-Au collisions as shown in Fig. 1.6. The discovered enhancement of e^+e^- pairs is also confirmed by the latest

results obtained with the upgraded experimental set-up in Pb-Au collisions, which will be discussed in this thesis.

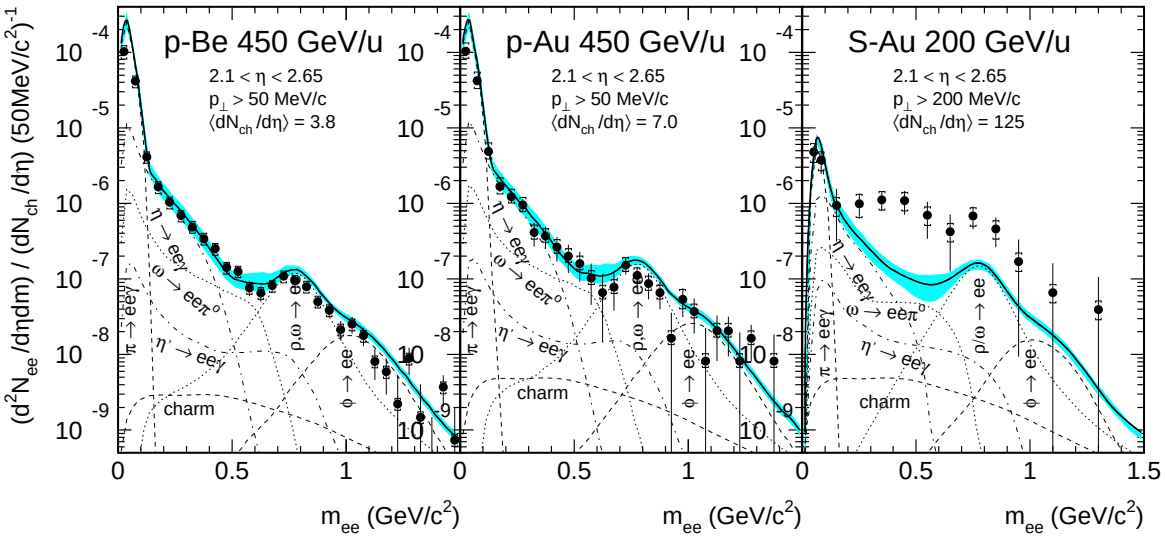

Figure 1.6: e^+e^- mass spectra for p-Be collisions at 450 GeV (left), p-Au at 450 GeV (middle) and S-Au at 200 A GeV (right) [30]. The solid line depicts the contribution from hadronic decays. Strong enhancement of the electron pair yield over the hadronic sources is observed for S-induced reactions while in p-Be and p-Au collisions the e^+e^- mass spectra are perfectly described by the hadronic cocktail.

Inclusive e^+e^- mass spectrum for S-Au data collected in 1992 is illustrated in Fig. 1.6. The data are normalized to represent the pair density per charged particle density within the CERES rapidity acceptance. This normalization allows to scale the dilepton yield from proton-proton to nucleus-nucleus collisions with the event multiplicity, since the particle production ratios remain unchanged in the different collision systems. In the absence of new physics, electron pairs are expected to originate from the known hadronic sources: Dalitz decays π^0, η, $\eta\prime \rightarrow e^+e^-\gamma$, $\omega \rightarrow e^+e^-\pi^0$, and resonance decays, ρ, ω and $\phi \rightarrow e^+e^-$. All the contributions from conventional hadron decays calculated with a generator (see chapter 5) are also shown in Fig. 1.6. The solid line represents the superposition of all these sources extrapolated from hadron multiplicities, as measured in p-p collisions. The measured spectrum has a different shape than a sum of the generated decays and shows a strong enhancement over the hadronic contributions at masses above 200 MeV/c^2, reaching one order of magnitude around m $\approx$ 400 MeV/c^2. To provide a quantitative measure of the observed excess the enhancement factor is defined as the integral of the data over the integral of the predicted sources in the given invariant mass range. For the mass range $0.2 < m_{ee} < 1.5$ GeV/c^2 an enhancement factor of 5.0 ± 0.7(stat.)±5.0(syst.) was found. An enhancement of low-mass muon pairs was also observed by HELIOS-3 in S-W collisions (although less developed but still significant) and by NA38 in S-U collisions, both at 200 A GeV.

In 1993 CERES collected a large sample of electron pairs from 450 GeV p-Be and

p-Au collisions to gain an accurate understanding of the physics background and to provide a basis for comparison with nuclear collisions. A very good agreement between the invariant mass spectrum measured in p-Be and the predictions based on the known hadron decay sources was observed, as illustrated in Fig. 1.6. The same observation was found in case of p-Au collisions. Thus, within the systematic errors, there is no need to invoke any unconventional source to explain the results for proton-induced reactions. The CERES assessment of the cocktail in proton-induced reactions has been confirmed by microscopic transport calculations [41, 42]. The latter give equivalent results for the dimuon data of HELIOS-3 [21,22] taken in p-W collisions. Therefore the measured e^+e^- and $\mu^+\mu^-$ spectra in proton-induced reactions at CERN SPS energies are well understood by the final state hadron decays in a consistent way.

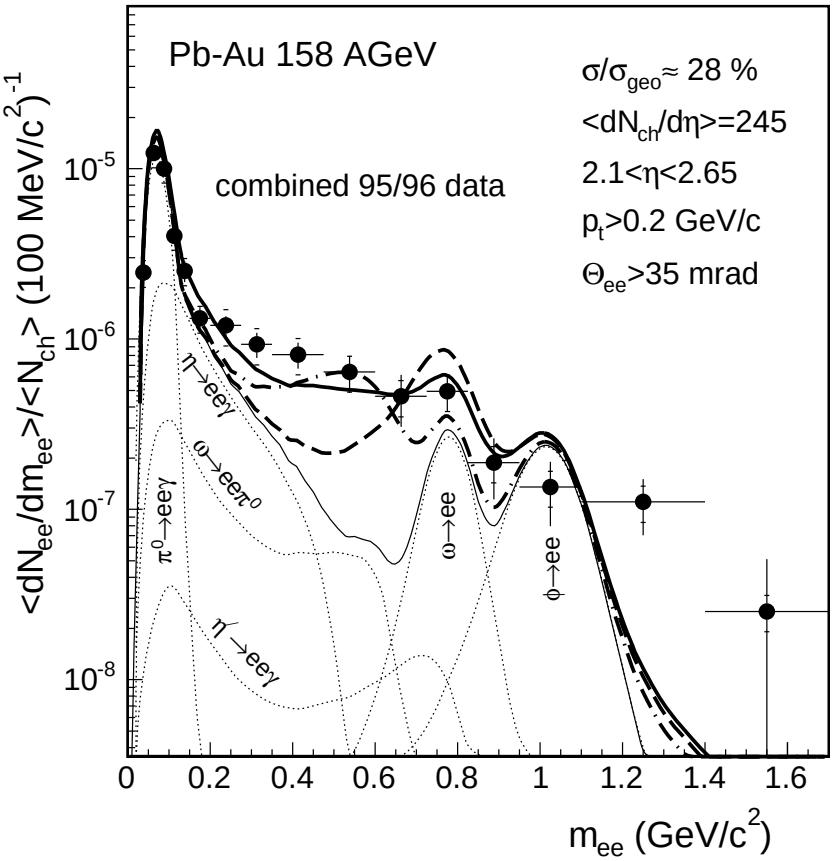

Figure 1.7: Comparison of the inclusive mass spectrum from '95 and '96 data analyses [30] to three calculations: with a vacuum ρ spectral function (thick dashed line), with dropping in-medium ρ mass (thick dashed-dotted line) and with a medium-modified ρ spectral function (thick solid line). The hadronic cocktail is plotted without ρ decay.

The resulting invariant mass spectrum for the combined data set from 158 A GeV Pb-Au collisions collected during 1995 and 1996 runs is shown in Fig. 1.7. Integrating over the mass region 0.2 to 1.5 GeV/c^2 CERES found that the inclusive dilepton yield is

enhanced by a factor of 2.8±0.3(stat.)±1.0(syst.) compared to the expected hadron decay contribution. Similarly to S-Au data, the enhancement is mostly localized in the mass range $0.2 < m_{ee} < 0.7$ GeV/c^2.

The inclusive e^+e^- pair transverse momentum spectra in 158 A GeV Pb-Au collisions normalized to the observed charged particle density are shown in Fig. 1.8 for three mass regions.

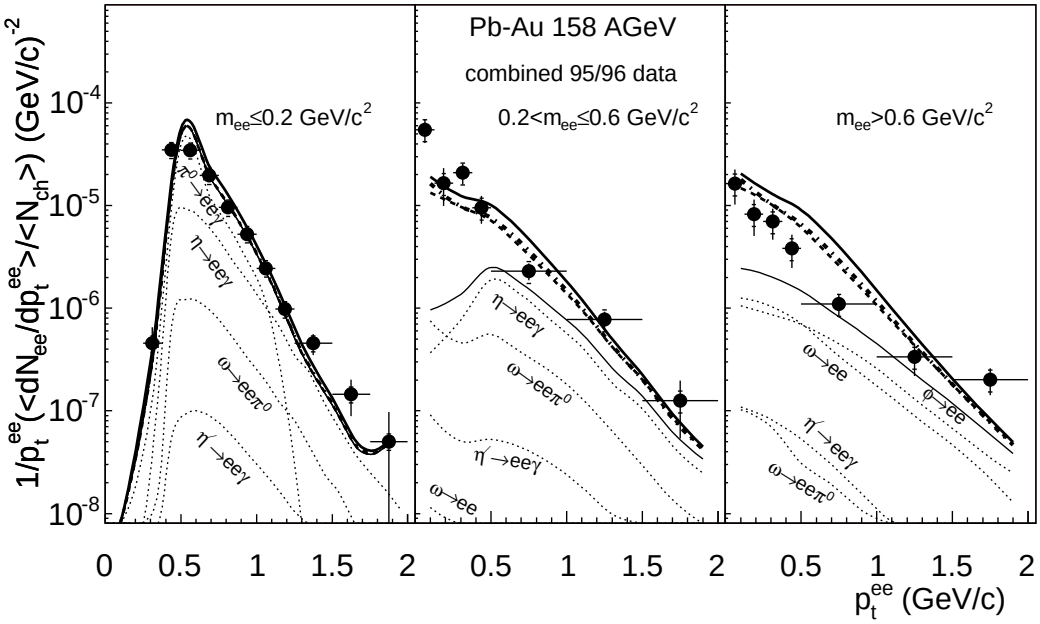

Figure 1.8: The p_t^{ee} spectra [30] compared to three models: calculation with vacuum ρ spectral function (thick dashed line), dropping im-medium ρ mass (thick dashed-dotted line) and a medium-modified ρ spectral function (thick solid line). Hadronic cocktail does not include the ρ decay.

For masses below 200 MeV/c^2 the pair p_t^{ee} distribution agrees with the predictions for π^0-Dalitz decays. For higher masses, the enhancement is observed over the entire p_t^{ee} range, but it increases significantly towards very low pair transverse momentum.

Another result is based on data taken for Pb-Au collisions at 40 A GeV during the running period 1999. In the high mass region above 200 MeV/c^2 the enhancement factor of 5.1±1.3(stat.)±1.0(syst.,data)±1.5(syst.,cockt.) was found [37]. Compared to 158 A GeV, the larger enhancement at 40 A GeV, where multiplicity and temperature are low, is interpreted as a consequence of the rising baryon density.

These results have stimulated considerable activity among theorists in an attempt to explain the observed enhancement. Presently, the thermal dilepton production via $\pi\pi$-annihilation is believed to account for the effect. Many calculations have addressed these data utilizing $\pi\pi$-annihilation, however they all have difficulty fitting the enhancement in the electron pair data at pair masses $0.2 < m_{ee} < 0.5$ GeV/c^2. A model has been proposed which incorporates a decrease in the ρ-meson mass due to chiral restoration in the dense medium [43]. Another approach incorporates a spectral function for the ρ, pion

modification in-medium and ρ scattering leading to a significant broadening in the ρ resonance [44, 45] fits the data equally well. Both model calculations provide a reasonable description of the observed low mass enhancement in the various data sets collected by CERES in ion-induced reactions. However the mass resolution of the spectrometer did not allow for a more accurate measurement of the vector meson region where the results of the calculations based on the two mentioned theoretical approaches differ. A substantial improvement of the data in terms of statistics and resolution was required. This motivated an upgrade of the CERES spectrometer by the addition of a new downstream Time Projection Chamber in 1998. A mentioned analysis of e^+e^- pair production at 40 A GeV/c recorded in 1999 was the first analysis of the data taken with the upgraded experimental setup. However the limited performance of the TPC read-out system caused large statistical errors. In this thesis, measurements of the dilepton production in Pb-Au collisions at 158 A GeV/c with fully operational TPC and complete calibration from the year 2000 data set are presented.

In the framework of this thesis I have developed, optimized and tested the code for the step2 production described in section 3.2.1. I have also prepared the corrections for the calculated magnetic field map based on the measurements of the B-field (see section 3.4). In terms of the data reconstruction software I have developed and optimized the ring reconstruction algorithm based on the Hough transform for the combined RICH detector system (see section 4.4.2). As a result the ring reconstruction efficiency was significantly improved. I have also further developed and optimized the TPC tracking algorithm which led to an increased number of hits per track and improved track reconstruction efficiency, especially for the soft tracks (see section 4.5.2). In the second part of my work within the CERES collaboration I was mainly concentrated in the analysis of the data taken in the year 2000, different rejection strategies (chapter 4) and MC issues (chapter 6). The results of the analysis are presented in this thesis.

2

The CERES Experiment

2.1 Experimental Setup Overview

The CERES (**Ch**e**r**enkov **R**ing **E**lectron **S**pectrometer) experiment has a fixed target geometry optimized to measure electron pairs in the mass region from $\sim$50 MeV/c^2 up to $\sim$1.5 GeV/c^2 at mid-rapidity $2.1 < \eta < 2.65$ with 2π azimuthal coverage. The CERES spectrometer scheme is shown in Fig 2.1.

Any experiment dedicated to a measurement of low mass electrons faces several challenges. The number of produced e^+e^- pairs compared to the number of produced charged hadrons is only of the order of 10^{-5}. Another problem is the large amount of photons produced in the collision converting into e^+e^- pairs. The CERES group developed a novel spectrometer with two Ring Imaging CHerenkov (RICH) [46] detectors which are almost "blind" to hadrons. The amount of material within the acceptance is kept below 1 % of a radiation length [1]. This minimizes the amount of conversions which would otherwise contribute to the combinatorial background. The UV detectors are placed upstream of the target, and thus they are not traversed by the intense flux of forward-going charged particles produced in the interaction.

The original spectrometer started to take data in 1992. It consisted only of two RICH detectors placed before, the other after a short superconducting double solenoid, which was reasonable for the low multiplicities with proton and sulfur beams. The first upgrade of the experiment setup took place from 1994 to 1995 with a doublet of Silicon Drift Detectors (SDD) and a multiwire proportional chamber with pad readout (the pad chamber) allowing operation in the high multiplicity environment of lead on gold collisions [47–49]. A second time the spectrometer was upgraded in 1998 with a radial-drift Time Projection Chamber (TPC), while the pad chamber was removed. This improved the invariant mass resolution and provided additional particle identification tool via specific energy loss to the already existing electron identification with RICH detectors.

The present CERES setup consists of the target area, RICH detector system and TPC. The target region includes a segmented Au target itself and two silicon drift detectors, located downstream of the target. Two RICH detectors with methane gas radiator ($\gamma \sim$

[1] Mirror of RICH2 is not included.

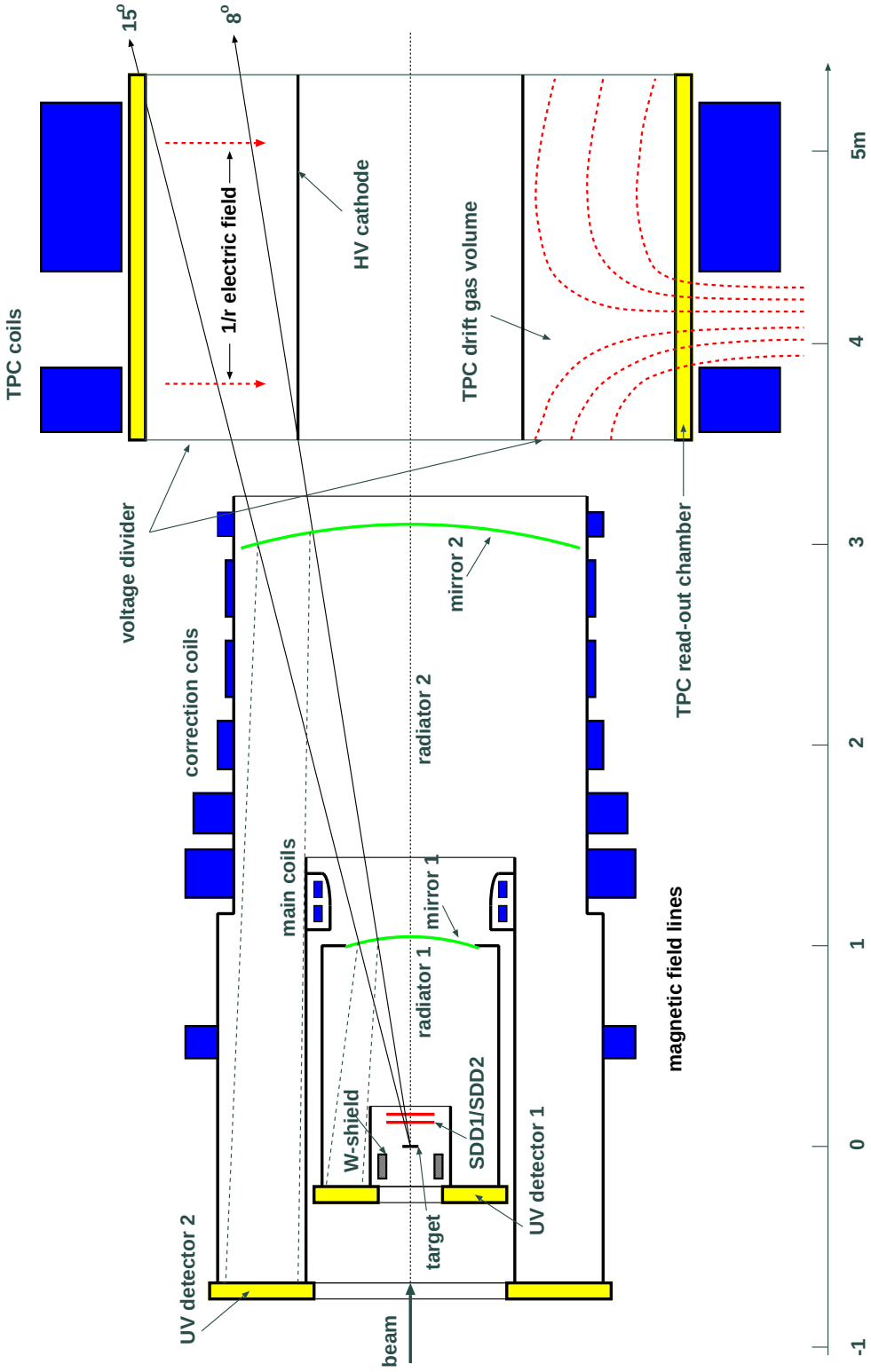

Figure 2.1: Cross section through the CERES experimental setup in 2000.

32, which makes it blind to most of the hadrons) are used to identify electrons. The original magnetic field between them was switched off allowing to use a doublet of RICH detectors in a combined mode. This results in improved reconstruction efficiency. The TPC used for the momentum measurement is located behind the mirror of the second RICH detector.

The achievements of the present setup are listed below.

- Improved mass resolution: $\delta m/m = 3.8$ % at $m \approx 1$ GeV/c^2 (for details see section 4.5.4).
- Additional PID via dE/dx in TPC (see section 4.6.5) together with efficient charged particle tracking provides new capabilities for the hadron physics studies.
- Improved RICH efficiency (section 4.4.2).

2.2 The Target Region with Two SDD Detectors

Fig. 2.2 shows the target region of the CERES spectrometer with two radial silicon drift detectors (SDD1, SDD2) placed approximately 10 cm behind the target.

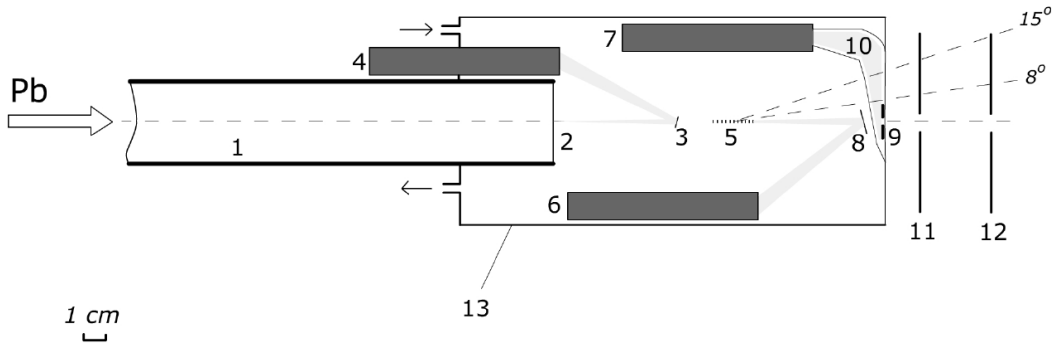

Figure 2.2: Scheme of the target area: 1 - the carbon vacuum pipe, 2 - aluminium entrance window, 3 - the mirror of BC2, 4 - PMT of BC2, 5 - segmented gold target, 6 - PMT of BC3, 7 - PMT of MC, 8 - mirror of BC3, 9 - scintillator of MC, 10 - Al-mylar light guide, 11 - SDD1, 11 - SDD2, 13 - gas volume of Cherenkov detectors BC2 and BC3.

The target area consists of the segmented target and various Cherenkov and scintillation counters used in the trigger system. The beam enters the target area via an evacuated Al tube that reaches until a few millimeters short of the segmented target and is sealed by a thin mylar window. A segmented Au target used during the beam-time 2000 consists of 13 disks spaced uniformly by 1.98 mm along the beam. Each disk has a diameter of 600 μm and a thickness of 25 μm. Due to the design of the target the particle produced in the collision reach the sensitive detection volume of the spectrometer without traversing the target disks located downstream of the interaction point. This minimizes the amount

of electron pairs originating from γ-conversions. The Au disks were measured to contain 95% of the beam over the full length of the target once collimators and settings of the beam line have been optimized.

The two radial Silicon Drift Detectors (SDD) play an important role in the electron analysis. These detectors provide:

- A very precise reconstruction of the interaction vertex within the segmented target.
- A measurement of energy loss by charged particles used for identification and rejection of close electron pairs.
- A track segment construction used in the formation of global tracks by matching to other detectors.
- Determination of charged particle density.

The SDD telescope made up of two closely spaced cylindrical silicon drift detectors is located approximately 10 cm behind the target. The active area of both detectors is almost the full area of silicon wafer with 4 inch diameter and a thickness of 280 μm which has a central hole for the passage of the beam. The sensitive area covers the region between the radii 4.5 mm and 42 mm with full azimuthal acceptance. The principle of operation of the silicon drift detector [50, 51] is shown in Fig. 2.3.

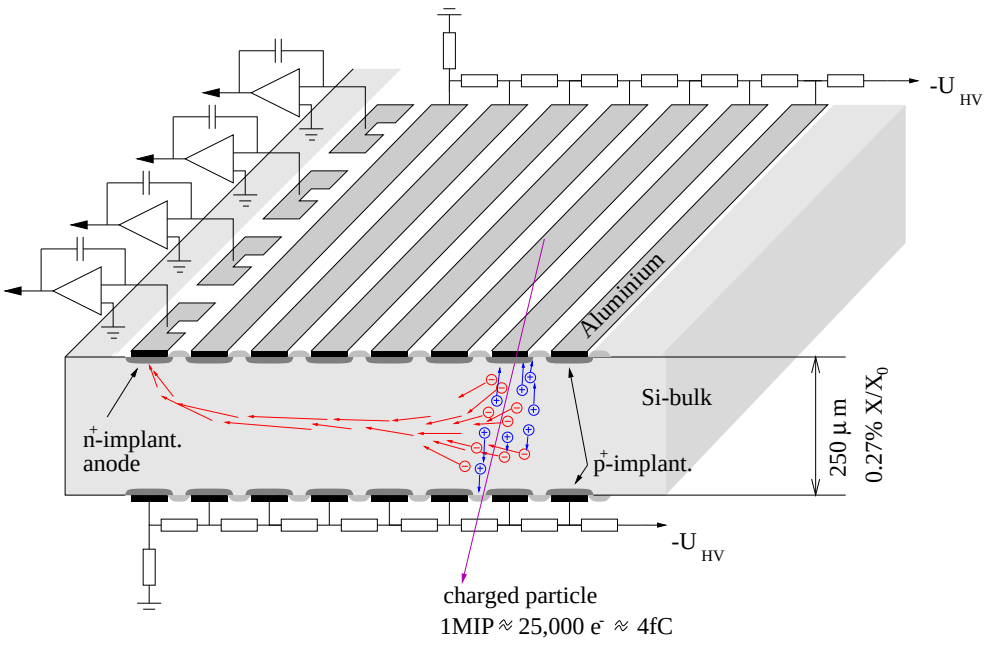

Figure 2.3: Principle of the Silicon Drift Detectors. Electrons move from the ionization region in the direction of anodes [1].

A charged particle traversing the depleted silicon wafer creates electron-hole pairs along its trajectory. To create one electron pair ionization energy of 3.6 eV is required

Thus around 25000 electron-hole pairs are created by a minimum ionizing particle penetrating the detector. Then the electrons are transported along the superimposed radially symmetric linear electric field towards the outer part of the SDD detector, where they are collected on the n^+ anodes, while holes are attracted to the p^+ electrodes on the detector surface.

Due to the fact, that the drift time of electrons depends on the drift distance, the SDD detector is position sensitive. The practical disadvantage of the drift detectors is a strong dependence of the electron mobility μ on temperature T

$$\mu \approx T^{-2.4} \tag{2.1}$$

and consequently a temperature dependent drift velocity $\vec{v}_{drift}$

$$\vec{v}_{drift} = \mu \cdot \vec{E}, \tag{2.2}$$

where $\vec{E}$ is an applied electric field. The typical drift time is approximately 3.8 μs. The signal induced by ionized electrons in the 360 anodes located at the periphery of the detector is read out with charge sensitive amplifiers. The radial coordinate r of the point where a charged particle crossed the detector plane is measured by the drift time t of the electron cloud. The azimuth angle ϕ is determined by the centroid of the charge shared by adjacent anodes. To measure the centroid of the charge cloud with a high precision, an interlaced structure was developed where each anode is subdivided into 5 pieces. The pair of coordinates (r, ϕ) is provided for each crossing charged particle.

2.3 The RICH Detectors

A schematic view of the CERES RICH detector is shown in Fig. 2.4. An electron emits Cherenkov photons while traversing the radiator volume, with refractive index n, filled with CH_4. A spherical mirror reflects the Cherenkov light backward onto 2-dimensionally position-sensitive gas detectors, located at the mirror focal plane and separated from the radiator volume by a UV-transparent window. The detecting plane will see a ring of photon impacts whose radius can be measured once the center is known from the tracking algorithm. The resulting pattern is a circle of radius

$$R = f \cdot \tan\theta_c \tag{2.3}$$

which approaches for $\theta_c \to \theta_\infty$ its maximal value

$$R_\infty = f \cdot \tan\theta_\infty. \tag{2.4}$$

Both, the ring radius and the number of Cherenkov photons N, depend on particle momentum and mass as

$$\frac{R}{R_\infty} = \sqrt{1 - \left(\frac{m\gamma_{\text{th}}}{p}\right)^2} \tag{2.5}$$

and

$$\frac{N}{N_\infty} = 1 - \left(\frac{m\gamma_{\text{th}}}{p}\right)^2. \tag{2.6}$$

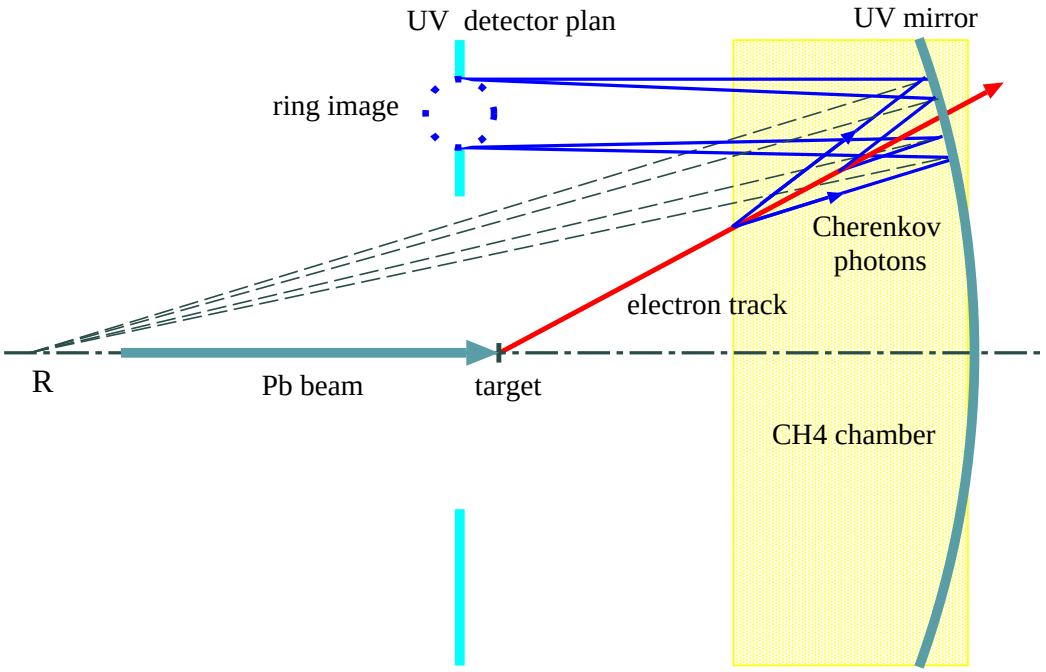

Figure 2.4: Schematic view of the CERES RICH detector [34, 46].

The CERES spectrometer includes two RICH detectors (RICH1 and RICH2). The RICH detectors are ”hadron-blind”, i.e. most of the charged hadrons do not produce photons, while essentially all electrons and positrons create Cherencov rings of asymptotic radius. This is achieved by using CH_4 at atmospheric pressure as the radiator gas, which results in a Cherenkov threshold of $\gamma_{th} \simeq 32$.

The acceptance of the doublet of RICH detectors is given by RICH2 which covers the pseudo rapidity range $2.03 < \eta < 2.65$. The magnetic field between two RICH detectors used for the momentum determination in the pre-TPC era was switched off. Thus, the RICH detectors were used in a combined mode, which improved ring reconstruction efficiency (for details see section 4.4.2).

In order to minimize the number of e^+e^- pairs from γ conversions and to reduce the loss of momentum resolution due to multiple scattering and bremsstrahlung, the mirror of RICH1 is made of only 1.1 mm (0.41% X/X_0) thick carbon fiber. The reflection quality of the mirror is excellent and the influence on the resolution is minimal ($\sigma < 0.10$ mrad). The second mirror is built from standard glass, 6 mm thick (4.5% of radiation length), and consequently is the main source of multiple scattering.

The UV-detectors consist of a conversion space followed by two parallel-plate avalanche stages and a multi-wire proportional chamber. By their position upstream of the target, the UV-detectors are not exposed to the huge forward flux of charged particles. The price to pay for this geometry is a limited acceptance in polar angle θ. The main properties of the UV detectors are a high detection efficiency for UV-Cherenkov photons and

a good spatial resolution. The gas counters are filled with 94 % He + 6 % CH_4 at atmospheric pressure. The gas mixture containing TMAE (Tetrakis-di-Methyl-AminoEthylen) vapor is heated upto 50^{o}C to reach the partial TMAE pressure necessary for high photoionization and to avoid TMAE condensation. The ion clouds produced in the last wire amplification stage induce signals on the pads. The latter form a grid of pitch 2.74 mm and 7.62 mm, and the resulting total number of pads 53800 and 48400 in RICH1 and RICH2, respectively [52]. This corresponds to 2 mrad per pad in both detectors.

To summarize, 95% of all charged particles do not lead to detectable signals in the RICH detectors while the electrons are detected starting from a momentum $p = 120$ MeV/c at which they reach asymptotic ring radius.

2.4 The TPC

The CERES spectrometer was upgraded during 1998 by the addition of a Time Projection Chamber (TPC) with a radial electric drift field. This improved the di-electron mass resolution which is dominated by the momentum resolution and provided an additional pion rejection tool via specific energy loss (dE/dx).

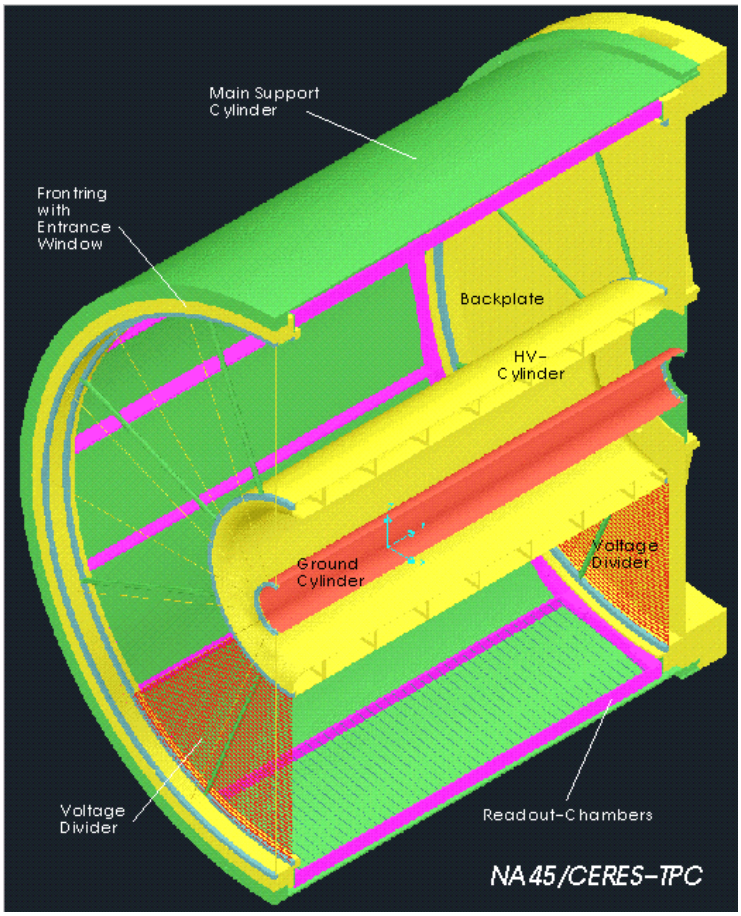

Figure 2.5: The CERES Time Projection Chamber with a radial drift [53].

The design of the TPC was constrained by the need to preserve the azimuthal symmetry of the existing spectrometer. The TPC is located downstream of the rest of the experimental setup immediately after RICH-2 and covers in beam direction z = 3.80 - 5.80 m. It is placed inside the two large coils of a warm magnet with a currents (up to 4000 A) running in opposite direction. The measurement of the track curving through the magnetic field in the TPC provides the momentum information. The TPC has a cylindrical geometry as all the other detectors in the experiment and covers similar acceptance in the pseudorapidity range $2.1 \leq \eta \leq 2.6$. The TPC has an active length of 2 m, an inner radius of 48.6 cm and an outer radius of 132 cm (see Fig 2.5). A charged particle traversing the gas volume of the TPC produces electron-ion-pairs along its trajectory. The electrons liberated along the path of the charged track drift towards the anode wire and finally reach one of the sixteen readout-chambers that are mounted in a cage-like aluminium structure and define the outer surface of the TPC. The drift takes place in a radial electric field with field strength proportional to 1/r. The electric drift field is provided by a cylindrical aluminium electrode with a diameter of 97.2 cm at a potential of typically -30 kV, and by the cathode wire planes of the readout chambers at ground potential. Each of the 16 readout chambers has three wire planes with wires running in azimuthal directions: gating grid, cathode wire, and anode wire plane. The arriving charge cloud passes the gating and cathode wire planes and finally produces an avalanche close to the anode wires which induces a signal in the chevron-type cathode pads. The chevron pad shape was chosen due to its efficient charge sharing in azimuthal direction and minimization of differential non-linearities [54–56]. The TPC comprises a total of $48 \times 16 \times 20$ = 15360 readout channels and provides a measurement of up to 20 space points per particle. Each channel is equipped with low noise electronics [57] which samples the analog signals with 8-bit ADC in 256 time bins per channel. An overview of the TPC readout is given in [58].

The TPC operates with Ne(80%)CO_2(20%) gas mixture which is optimal in terms of diffusion, multiple scattering, Lorenz angle, primary ionization and drift velocity.

2.5 The Magnetic Field

The magnet system of the TPC consists of two closely spaced short solenoids with opposite sense currents. The two coils are located at z = 3.8 and 4.5 m. The resulting magnetic field lines in the r-z plane are displayed in Fig. 2.6. Fig. 2.6 shows also the radial and longitudinal components of the magnetic field both at the inner and outer end of the acceptance in θ as a function of the z-coordinate. Also shown is the trajectory of a single positively charged particle with momentum 1 GeV/c on the surface of a cone with angle θ again for the minimum and maximum θ accepted (Fig. 2.6, bottom). The plot shows the distance, on the surface of a cone, from the location of a track without magnetic field, and, in addition, the quantity that determines the extent of the primary ionization trail in direction parallel to the wires of the read-out chambers, r·dϕ/dz. This quantity needs to be multiplied with the length δz covered by each read-out pad. The kinks at z $\approx$ 1.2 m are due to the two two super-conducting magnet coils located between the two RICH counters, which were switched off during the beam time. The strong bend at z $\approx$ 4.2 m, *i.e.* approximately in the middle of the TPC, represents the region of maximal radial field

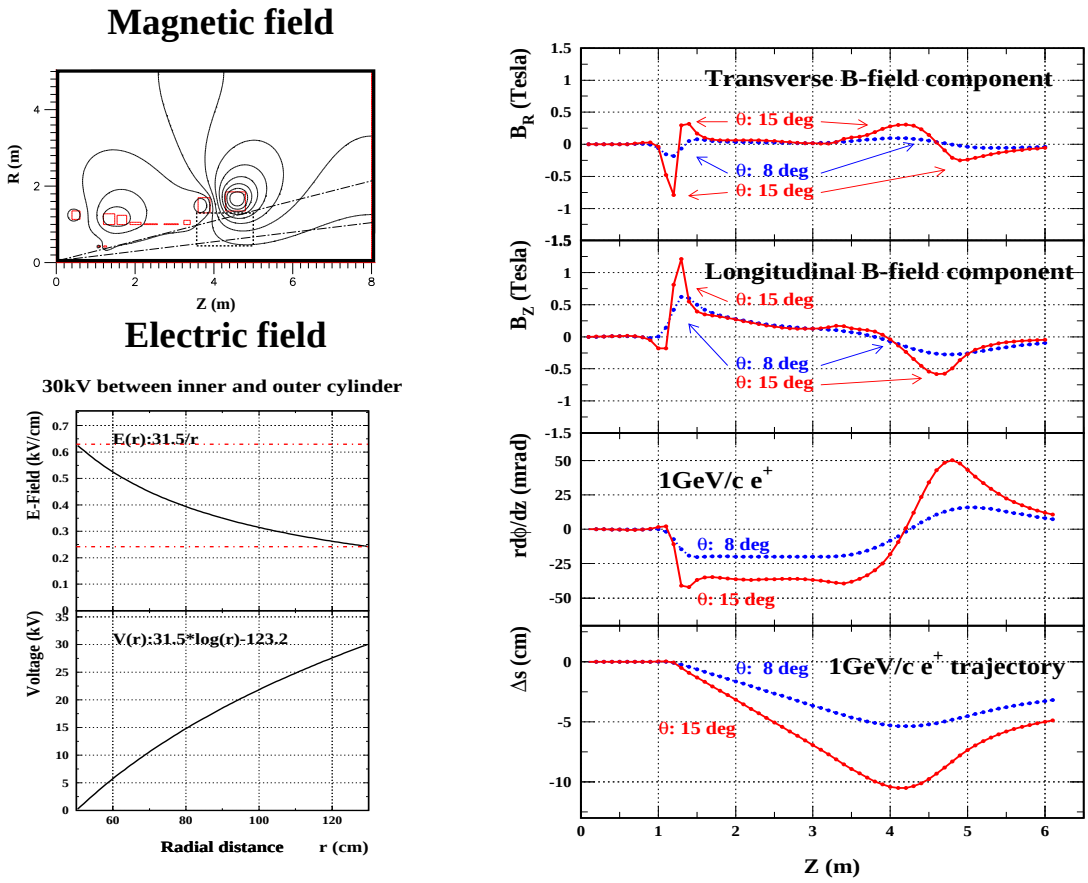

Figure 2.6: Magnetic field of the TPC [59,60]: calculated magnetic field lines for the combination of the existing CERES spectrometer and the additional analyzing coils in the TPC region where the active volume of the TPC is indicated by the dashed rectangle (top left). Magnetic field components transverse to and in beam direction are shown in the right top and next to top plots as well as a displacement from an undeflected track on the surface of a cone with angle θ of a 1 GeV/c singly charged particle (right bottom). The length of the arc projected into the r-ϕ plane per unit length in z, r·dϕ/dz, is displayed in the next to bottom plot.

strength.

2.6 The Trigger

The idea behind the trigger design is a fast selection of the events produced in the interactions in the gold target. To meet the requirements of minimal mass exposure in the beam and target region and sufficient radiation hardness a system of beam counters (BC) was developed [61].

The trigger consists of micro gas Cherenkov and scintillation detectors located in the

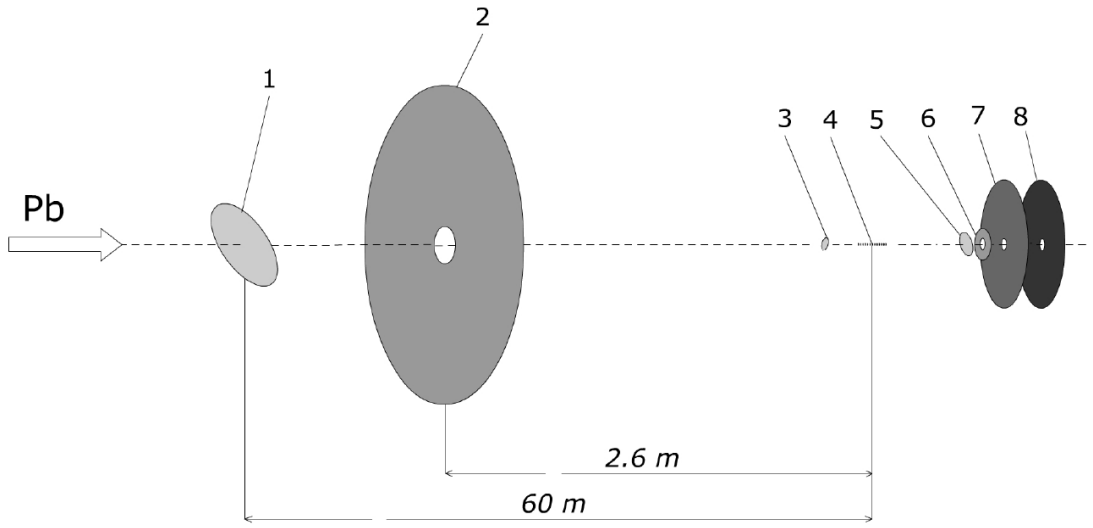

Figure 2.7: Trigger detectors on the beam line: 1 - BC1 mirror, 2 - VC scintillator, 3 - BC2 mirror, 4 - segmented gold target, 5 - BC3 mirror, 6 - MC scintillator, 7 - SDD1, 8 - SDD2.

target area upstream and downstream of the target. Incident beam particles were monitored by the gas Cherenkov detectors BC2 and BC3 with a pulse height proportional to a projectile charge squared. The Cherenkov light was reflected by thin Al-mylar mirrors to PMT photocathodes. A selection of central Pb-Au collisions on charged particle multiplicity was performed by a scintillation multiplicity counter (MC) in the forward pseudo-rapidity range covered by the detector. The scintillation light was reflected to photomultiplier photocathode by an Al-mylar light guide. The layout of the trigger detectors together with the two silicon drift detectors is shown in Fig. 2.7.

BC1 detects first a signal produced by the projectile traversing the gas radiator of the detector about 60 m upstream of the target. The veto counter (VC) is a plastic scintillator with a hole of 15 mm in diameter and outer diameter of 145 mm placed inside the vacuum beam pipe. The VC was used to reject the events with high upstream background. The main trigger detectors, BC2, BC3, and MC, are located in the target area, followed by the doublet of silicon drift detectors. The active transport of beam ions to the target was controlled by the system of BC1, BC2 and MC. Approximately 99% of the projectiles seen by BC1 reached the target.

The CERES trigger in 2000 was based on 10 ns analysis of pulses from the BC and the MC detectors selecting Pb-Au collisions with various centrality. Fig. 2.8, obtained with a trigger on incident lead ions, shows the minimum bias trigger (MBT) with a low threshold on the BC3 pulse height and the central trigger (CT) with high threshold on the MC pulse height. In fact, any mixture of different triggers can be realized with the help of the BC and the MC detector system. The physics triggers are provided by the following combinations: Valid Beam (VB) = BC1 $\cap$ $\overline{\text{VC}}$, Beam Trigger (BT) = VB $\cap$ BC2, Min Bias Trigger (MBT) = BT $\cap$ $\overline{\text{BC3}}$, Centrality Trigger (CT) = MBT $\cap$ MC(>bias).

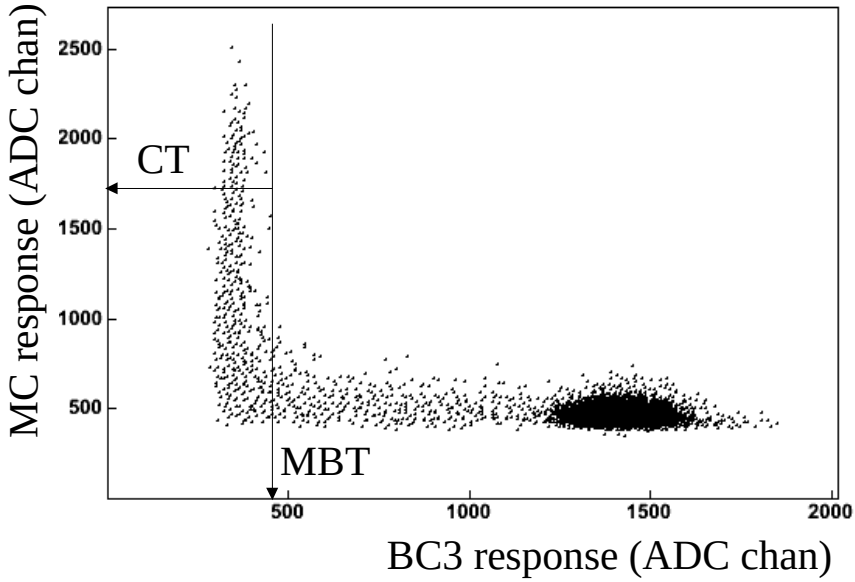

Figure 2.8: Correlation between MC and BC3 responses obtained with trigger on incident Pb ion. Central trigger (CT) and minimum bias trigger (MBT) are indicated by lines. The black spot corresponds to Pb ion responses.

3

Data Production and Detector Calibration

3.1 Data Production Overview

During the production run in the year 2000 CERES collected in total $31 \cdot 10^6$ events with the a centrality corresponding to the most central 7% of the geometrical cross section and $3.5 \cdot 10^6$ events at 20% centrality at the maximum SPS momentum which is for Pb ions 158 A GeV/c. In addition, runs without magnetic field, with minimum bias trigger, and with lower beam intensity as well as runs without target and laser runs were taken for the calibration purposes. The quality of the data analysis crucially depends on the accuracy of the reconstructed information such as coordinates of the hits/tracks, pulse heights of signals induced in the detectors by traversing particles, measured momentum, etc. On the other hand all these quantities depend on the detector parameters. Many of those parameters such as drift velocity in SDD, gain variations in RICH detectors,variations in temperature and pressure in TPC gas and so on change with time. Therefore, before starting the physics analysis, all the parameters must be calibrated for the whole data set. In order to take into account the time dependence of the different detector quantities, a calibration was performed for every piece of data of a given size separately.

The data analysis was divided into several stages explained below in more detail.

(i) **step0** - trigger calibration.

(ii) **step1** - analysis of the raw data, first pass.

(iii) calibration of the experimental setup based on the output of step1.

(iv) **step2** - analysis of the raw data, second pass. This step includes a monitoring procedure controlling the quality of the processed data.

(v) **step3** - analysis of the output of step2 including fine tuning and final calibration of

the various experimental quantities. During this step a significant reduction of the data size was achieved by keeping only information necessary for the electron analysis.

(vi) **step4 -** final analysis of the output of step3.

Stages from (i) to (iv) were combined into a large scale production of the raw data called **step2** production (charged particle production common for every analysis of the CERES 2000 data).

3.2 Production Steps

3.2.1 Step2

The requirements for CPU power for the off-line analysis in a HEP (High Energy Physics) experiment are high. Production of the raw data took 2 months during summer 2003. The main computing resource was a Batch Farm running RedHat7 at the CERN Computing Center. All jobs processing the physics and the calibration run on this farm. The prod400 queue was dedicated to running the production which allowed to obtain up to 400 running jobs simultaneously. Table 3.1 shows the CPU frequency distribution of the Batch Farm.

CPU frequency (GHz)	2.8	1	0.75	0.55
%	55	28	14	3

Table 3.1: Relative CPU frequency distribution during step2 production.

The main storage facility was the CASTOR [62] hierarchical mass storage system. This system provided the necessary disk space (pool with a size of 2.47 TB) for both the input buffer and the output buffer. A process running in batch transfered the raw data files from the CASTOR tapes to the pool. Then these files were accessed via RFIO (Remote File I/O). The output ROOT [63] files were migrated to CASTOR tapes. Unless the processes reading and analyzing the data are stalled for a very long time or the CPU capacity of the batch farm is degraded, all files should be used before being purged from the pool and recall from tape should not be necessary.

Since, as already mentioned, the complete CERES data set taken in 2000 had to be calibrated, it was decided to perform a calibration of the data piece by piece. The raw data were split into 415 units. Every unit consists of about 200 bursts which was proven to be a minimal amount of the data needed for the calibration with enough precision. Figure 3.1 shows a diagram of the **step2** production organization.

All production components were implemented using Perl and Unix text processing programming language [64]. The production scripts submit 30 executables per unit to the batch farm. All jobs belonging to a given step run in parallel. However, as the next step depends on the output of the previous one, all available nodes can not be constantly loaded by processing only one unit. To avoid a decrease of the overall production efficiency three

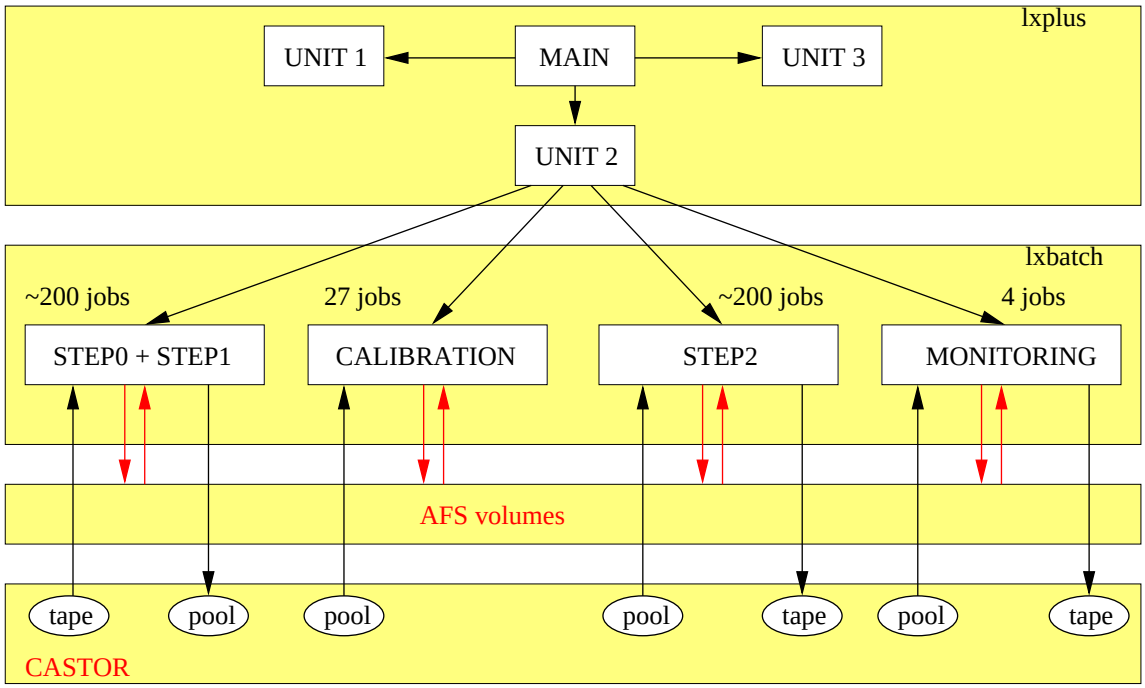

Figure 3.1: Step2 production scheme. The complete processing of one unit is illustrated including interactions with AFS volumes and CASTOR.

step	total time per event (sec)	CPU time per event (sec)	data access time (min)	max memory (MB)	max swap (MB)
step1	6	4	5	270	320
step2	7	5	< 1	250	320

Table 3.2: Step2 production performance.

units were analyzed simultaneously. Thus, an equilibrium stage was reached keeping all provided processing resources busy and analyzing events at the rate at which they arrived from CASTOR and also taking into account the CASTOR writing bandwidth.

The main script executes locally three scripts with the unit numbers as parameters. Let us call them manager scripts. The manager script submits jobs to the batch farm and controls the flow of the analysis of the unit. Each batch job interacts with CASTOR and AFS [65] (a network-distributed file system). The two parts of the analysis consuming most of the CPU are step1 and step2. The job array structure provided by the LSF Batch [66] system allowed hundreds of identical jobs to be created with a single job submition and the same job ID. This essentially simplified tracking and controlling submitted jobs. In order to decrease the memory used by the executables and to avoid swapping of the code, a significant amount of work was invested to optimize various algorithms in the CERES software. Table 3.2 shows the performance of the production.

Production-wise the analysis is based on four distinct activities.

- The first two phases of the analysis, namely step0 and step1 consist of the trigger calibration and the complete analysis of the raw data ending with track and ring reconstruction. The goal of step1 is to generate ntuples and histograms for the following calibration of SDD, RICH and TPC[1].
- The calibration procedure of all detectors is the third phase (described later in chapter).
- The fourth phase (step2) again processes the raw data taking into account newly calibrated parameters and produces the final ROOT trees where all hits, tracks, rings and other necessary information are stored.
- Finally the monitoring runs on the output of step2 to check the status of the calibrated detectors and to follow the time evolution of their performance.

3.2.2 Step3

The analysis of step2 took place at the CERN Computing Center. The first attempt done in Autumn 2003 was still with incomplete calibration of some quantities. The possible improvements of the rejection strategy and electron selection required additional experimental information. A final run was taken in Autumn 2004 after intensive study of the behavior of the detectors and rejection procedures.

The following features were implemented in the step3 analysis of electron pairs.

- Vertex refitting.
- Momentum refitting.
  Remaining residuals of the TPC hits distorted the momentum. Hence the strategy was to correct for the residuals and to refit the TPC tracks. High momentum pion tracks were selected as a good approximation of straight lines. For every unit $\Delta\phi$ and $\Delta\theta$ between a hit on track and crosspoint of the fitted track trajectory and a mirror of the second RICH were obtained for every plane. Limited statistics within one unit did not allow to get the correction factors for different bins in ϕ and θ. Therefore, in addition, another map of residuals versus ϕ and θ was calculated for all 30×10^6 events selecting tracks with momentum larger than 1 GeV/c.
- Single use of rings and tracks in a smarter matching procedure which was developed to decrease a number of fake matches [67]. The sophisticated algorithm can be illustrated with the following example. Trying to find the best match between two SDD tracks and two TPC tracks one firstly searches for the closest possible pair and then creates a second pair. For the large track multiplicities all pairs are

[1] In fact, a calibration of the TPC already starts with a set of 'best guess values' obtained from the slow control. Thus, purpose of the calibration procedure is to tune the parameters in order to achieve even better accuracy.

sorted according to increasing matching distance. The pair with smallest distance is always selected.

- 3σ matching windows are momentum dependent. Additionally SDD1-SDD2 matching was carefully studied for different topologies of the hits on tracks and fixed as follows. The difference between θ-coordinates was fixed for all hit topologies (see also section 4.3), while $\Delta\phi$ was split up into three groups: $\Delta\phi < 9$ mrad in case of two single-anode hits, $\Delta\phi < 3$ mrad for single- and multi-anode hits and $\Delta\phi < 8$ mrad in case when both hits are multi-anode hits.

- Select rings with high threshold on double hough amplitude to avoid fakes eating real good tracks (see section 4.4.2). Dependence of the double hough amplitude on the ring θ-coordinate was introduced to improve the efficiency of the rings which are partially outside of the RICH acceptance.

- Select electron TPC tracks with $\mathrm{d}E/\mathrm{d}x$ above 250 ADC channels. These tracks participate in the matching of SDD, RICH and TPC segments in addition to SDD-TPC tracks selected without any cut on energy loss in the TPC within 15 mrad around global tracks. A hadron fraction of SDD-TPC tracks with low $\mathrm{d}E/\mathrm{d}x$ is used to identify and to eliminate SDD hits produced by pions. This improves electron track efficiency for the resummation $\mathrm{d}E/\mathrm{d}x$ cut in silicon drift detectors.

- Create and keep global tracks (SDD-RICH-TPC). The tracks from SDD and TPC, and rings from RICH were matched within $3{\cdot}\sigma$ momentum- and θ-dependent windows.

- Create and keep SDD-RICH tracks within 100 mrad around global track. SDD-RICH tracks were meant to be used for the rejection of partially reconstructed Dalitz pairs.

- Keep TPC tracks which did not match to SDD within 30 mrad around global track. This is required to reject close pairs identified in the TPC.

- Keep all SDD hits within 10 mrad around SDD track. This is needed for further rejection of close pairs. Similarly to a single use of track segments in the matching procedure the hits can not be shared. That means a hit can belong to only one (closest) SDD track.

- Keep all events which did not pass trigger selection (event must include at least one electron track) as empty ones. It allows proper event counting.

3.2.3 Step4

The final fine tuning of the momentum calibration is performed in the last phase of the analysis. The main physics analysis and the rejection cuts are done in this part (see chapter 4.6.2).

3.3 Detector Calibration

This section is devoted to the description of the calibration procedure performed for each detector individually.

3.3.1 SDD Calibration

The calibration of the silicon drift detectors [68] consists of the following steps:

- Gain calibration.
- Calibration of t_{min} and t_{max}.
- Skewness correction of time distribution of signal.
- Stop pulse correction.
- Ballistic deficit correction.

After unpacking, the pedestals are subtracted from the pulse amplitudes, changing the mean pulse sum amplitude and pulse shape for the low amplitude pulses. The mean pedestal of 13 ADC counts is flat as a function of anode number for both silicon drift detectors. All pulses with amplitude above a threshold of 3 ADC counts are further processed.

Gain calibration of pulses is performed for each anode. A proper calibration of the gain is of importance, since incorrect gain calibration may lead to a shift of the hit position in the anode direction. Without any selection of pulses according to a number of anodes per hit and time-bins, the pulse amplitude distributions are broad. Consequently, the fit of these distributions with Gamma, Landau and Gauss functions is unstable. Therefore, for the gain calibration, only the pulses belonging to a track are selected. The pulse with maximum amplitude within a hit is chosen. In order to reduce the effect of multiplicity and diffusion the outer half of the radial acceptance is selected by conditions on time-bin values of $<$ 160 TDC counts for SDD1 and $<$ 115 TDC counts for SDD2. The full acceptance is between 80 and 240 TDC counts for SDD1 and between 10 and 220 TDC counts for SDD2. The single-anode hit selection is biased since single-anode hits include mostly pulses with low amplitudes and with a large probability close to the dead anodes. Therefore by excluding single-anode hits the low amplitude component is much suppressed and the amplitude distribution becomes very close to the Landau functional shape, which was never achieved with single-anode selection. Each amplitude distribution is fitted by a Landau function with a limited range around the peak (typically from $\sim$ -0.7$\cdot\sigma$ to $\sim$ +1.2$\cdot\sigma$ with respect to the peak position). The fitted gain parameters are stored and applied to the data.

At_{min} **and** t_{max} **calibration** is required in order to achieve the best performance of the silicon detectors. To first order, the relation between the drift distance and the time is linear. The drift velocity can be calculated as

$$\langle v_{drift} \rangle = \frac{\Delta d}{\Delta t}, \tag{3.1}$$

where Δd is the radial extension of the detector active area and Δt is the total drift time. The length of the drift is given by the inner edge of the detector r_{min}, which corresponds to the inner most voltage ring located at 4.5 mm, and the anode position r_{max} at 42 mm:

$$\Delta d = r_{max} - r_{min}. \tag{3.2}$$

The total drift time can be derived from the time t_{min} corresponding to the particles which do not drift and fall directly on the anodes, and the drift time t_{max} of particles coming from r_{max}:

$$\Delta t = t_{max} - t_{min}. \tag{3.3}$$

Then the radial position is given by

$$r = r_{max} - v_{drift}(t - t_{min}). \tag{3.4}$$

In order to determine the values of t_{min} and t_{max}, the leading and trailing edges of the hit distribution in the drift time are fitted by Fermi functions. The determination of t_{min} is performed by the fit with

$$f(t) = \frac{C}{1 + \exp(-(t - t_{min})/d)}, \tag{3.5}$$

while t_{max} is derived from the fit with

$$f(t) = \frac{C}{1 + \exp((t - t_{max})/d)}, \tag{3.6}$$

where C, t_{min}, t_{max} and d are the fit parameters. t_{min} and t_{max} represent the leading and trailing edges of the distribution. The pulses are selected according to their amplitude after pedestal subtraction. For SDD1 detector the pulse amplitude must be between 100 and 2000 FADC counts while for SDD2 detector the amplitude must lie between 200 and 2000 FADC counts. Correction based only on t_{min} assumes a drift velocity common to all anodes: $t' = t - t_{min}$. However variations in the θ-matching distribution as a function of ϕ between SDD detectors remain after calibration. This is avoided by taking into account both t_{min} and t_{max}:

$$t' = \frac{t - t_{min}}{(t_{max} - t_{min})/(t_{r1} - t_{r0})}. \tag{3.7}$$

Skewness correction is an additional step to correct the hit positions for every anode. The skewness is the third moment of the pulse profile. The hit position derived by the center-of-gravity method can be distorted due to skewness. The linear correction for each pulse is performed as a function of the skewness:

$$t' = t_{CoG} + (skew - s_0) \cdot s_1, \tag{3.8}$$

where $skew$ is the skewness, s_0 and s_1 are the parameters extracted form the dependence of the θ-matching between two SDD detectors on skewness. This correction improves θ-matching by approximately 10%.

Stop pulse correction is required due to an observed jitter of the TDC stop pulse. There is a discontinuous structure which reflects the phase difference between the synchronized NIM signal generated by the scanner and the First Level Trigger (FLT) which determines the last time-bin (= 255). The correction is based on t_{min} and t_{max} determined for every slice of stop pulse offset.

Ballistic deficit correction is required to suppress the dependence of the hit amplitudes on drift time. Ballistics has to do with the nature of the motion of charge carriers in the SDD detectors. Traversing the detector particles can interact with material anywhere within the active volume of the detector. If the interactions take place close to outer and inner acceptances of the SDD, the two sets of charge carriers will have very different in path lengths. Since the charge collection is not finished until the last of the carriers completed its travel this will yield a preamp pulse rise-time. Therefore each pulse will have different rise-time depending where within the detector the associated interaction took place. Due to relatively short shaping time constant the pulse processing is stopped before it has risen to its maximum amplitude. This means that the amplitude of the amplifier's output will be too low, which mean loss of the resolution in the data. Fig. 3.2 shows the hit amplitude distributions in SDD1 and SDD2 as a function θ-coordinate after correction of pulse height distortions (ballistic deficit [69]).

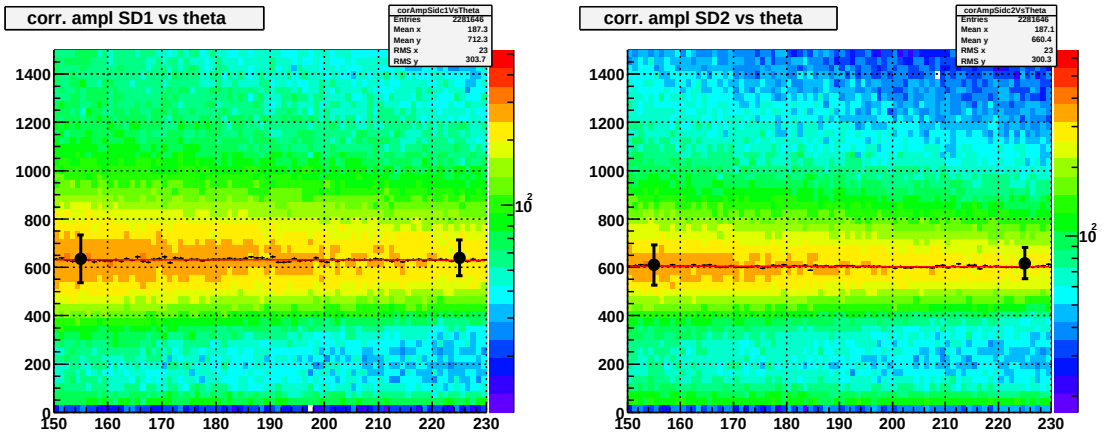

Figure 3.2: Distributions of hit amplitudes as a function of θ after ballistic deficit correction in SDD1 (left panel) and SDD2 (right panel).

3.3.2 RICH Calibration

The event treatment of the RICH data proceeds through the pedestal subtraction and gain equilibration. A pad is active if its amplitude exceeds the value of the pedestal by three

standard deviations of the pedestal width. The value of the pedestal is typically about 19-20 ADC counts with a standard deviation of 1 ADC count. After unpacking the pedestal is subtracted and the pad amplitude is stored.

The aim of the gain equilibration is to adjust the mean amplitude of all pads in the RICH detectors to the same value [70]. The gain equilibration is down in two steps.

- Firstly, the gain equilibration is performed in every High Voltage (HV) sector. In order to determine the average amplitude of each pad, "good" pads are selected. The selection is done according to the frequency response. In a typical frequency distribution of the active pads in one HV sector in RICH1, the pads with very low frequency, below the minimum, lie under the spokes of the mirror. These pads are not used in the determination of the global pad amplitude average and not corrected themselves. Then the "good" pad frequency distributions are fitted with a Gaussian in the different θ regions. The pads falling within ± 3 standard deviations are selected for further processing. The pads exceeding 3 standard deviations (high frequency) are noisy pads, and the ones below 3 standard deviations (low frequency) are placed very close to the spokes or to the acceptance limits. The latter have usually a lower gain and are referred to as "weak" pads. The "weak" pads do not participate in the determination of the global average amplitude but they are corrected as normal pads. About 80% of all pads are selected as "good" in RICH1 detector.

  The average amplitude $\langle g_i \rangle$ of each pad determined with a large enough sample of the events is given by

  $$\langle g_i \rangle = \frac{\sum_{i=0}^{N} g_i}{N_{ev}}, \tag{3.9}$$

  where g_i is an amplitude of pad i in a given event, N_{ev} is a total number of analyzed events in sample. Along with the average amplitude of a separate pad the global average amplitude of all "good" pads is determined by

  $$\langle g \rangle = (\sum_{i=0}^{N} \langle g_i \rangle)/N, \tag{3.10}$$

  where N is the number of all "good" pads and $\langle g_i \rangle$ is a mean amplitude of pad i defined for a calibrated event sample. Then the raw amplitude of each pas is multiplied by the correction factor $\langle g \rangle / \langle g_i \rangle$. The pad correction factor is determined from the data of one calibration unit which corresponds to approximately 200 bursts, as was already mentioned. Although the pad correction factors provide stable results for the following 5-7 hours of the data taking, it is convenient to use the same fixed data samples (units) for the calibration of all five detectors.

- Secondly, to perform the gain equilibration between sectors, the mean amplitude of all sectors is fixed to 12 ADC counts in RICH1 and 15 ADC counts in RICH2.

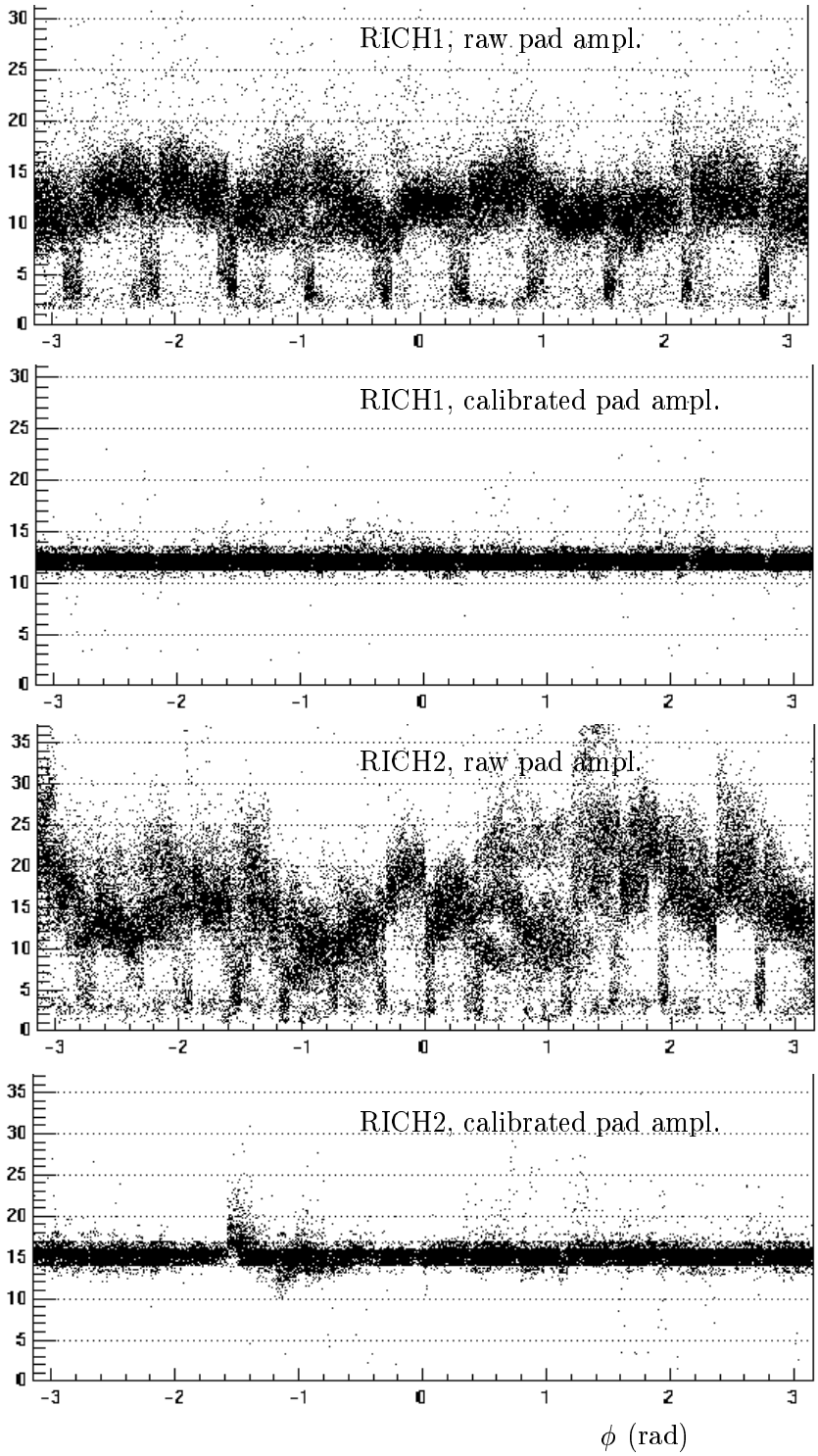

Figure 3.3: The amplitudes of the pads before (top) and after (second from top) gain equilibration for RICH1 and the amplitudes of the pads before (third from top) and after (bottom) gain calibration for RICH2 as a function of ϕ-coordinate. Values for both the "good" pads with healthy behavior and the "weak" pads placed close to the spokes and the acceptance limits are represented.

The gain equilibration in the RICH2 detector is performed in a similar way. The pad correction factors are derived for each of the 16 “hardware” sectors instead of the 8 HV sectors. Additionally, RICH2 has four regions with ill behavior due to electronics. Thus special treatment of these four areas is required.

(i) The first region is a horizontal subchain situated close to the top of the UV detector. The pads in this area have a mean amplitude almost a factor of two greater, a pad frequency 4-5 times lower, and a mean hit size smaller with respect to neighboring pads.
(ii) The second region is a vertical subchain in the third HV sector. Although the pads have normal mean amplitude, the frequency is higher by a factor of two. These pads are also not used in the determination of the global average pad amplitude.
(iii) The third and fourth regions have always low gain but show a reasonable behavior. Otherwise the treatment of these areas is similar to the calibration of the first region.

Fig. 3.3 shows the amplitudes of “good” and “weak” pads in RICH1 and RICH2 before and after gain equilibration. Variations of the pad amplitudes up to 100% in RICH1 and even higher in RICH2 are observed before the gain equilibration. Once equilibration is done, almost no deviations are seen for both RICH detectors.

3.3.3 TPC Calibration

In order to improve the mass resolution the CERES spectrometer was upgraded with the Time Projection Chamber. Thus the calibration of the TPC is the main challenge of the analysis in order to get to the design limits. A major progress has been made in all areas of the TPC calibration. The following problems were taken into account [71, 72]:

- The complicated electric field which is dominantly radial with $E_r \sim 1/r$, but the 16 read-out chambers with flat surface at the outside generate a polygonal symmetry.
- The inhomogeneous magnetic field generated by two large coils with current in opposite direction leading to strong local variations of the Lorentz angle and therefore to the need to know very precisely the location and orientation of the TPC relative to the magnet.
- Strong variations of the drift velocity due to the choice of the drift gas (Ne/CO_2 80/20) and potential on the HV cathode (30 kV) together with the approximate radial geometry.
- Changes in temperature and atmospheric pressure, leading to drift velocity variations. The temperature was measured at the outer surface of the TPC and not in the gas volume.
- Small inaccuracies in the knowledge of the gas composition.
- Gain variations for the 15 k cathode read-out pads, depending on the capacitance.
- Time offsets due to different capacitances in the printed circuit boards (FEE boards).

Thus the calibration of the TPC is a clearly very complicated and time-consuming process. The main task is to obtain an accurate knowledge on the E- and B-fields, mobility, and geometry of the detector. The problem was attacked by the use of laser tracks with and without magnetic field. The TPC is equipped with a laser system generating 2 laser rays per chamber (7 laser rays in one special chamber) at different radii. The positions of the laser rays were measured absolutely by a calibrated diode system. It was found that tracks reconstructed with the nominal electric field exhibited a z-dependent distortion. The measurements on the actual CERES TPC field cage which were later verified with individual resistors of the same type, showed that about half of the resistors used change resistance with the applied voltage. A custom program based on the relaxation method was developed for calculating the 3D electric field with the modified resistivity with sufficient accuracy in a reasonable computing time. Another 2D-calculation with a very fine grid in the transverse (x,y) plane was performed to account for the field distortions caused by displaced chambers and the leakage of the amplification field the cathode wire plane. The two obtained potential maps were then added. The boundary conditions (voltages) used in both calculations were chosen such that their sum was equal to the voltages actually applied. This new field reduced distortions of the reconstructed tracks from about 10 to less that 1 mm.

The magnetic field in the TPC is also subject to correction. Due to the equipment in the experimental area the magnetic field is not completely ϕ-symmetric with deviations of up to a few % that are included as a corrections on top of a calculated Poisson map. The drift of the electron clouds and the momentum determination utilize the r, z, and ϕ dependences of both the electric and the magnetic fields.

The electron mobility can be calculated as function of the electric field strength using the Magboltz package [73] with the drift gas parameters: composition, temperature, and pressure which were monitored by the slow control system of the experiment. However contamination of other gases and temperature gradients in r could not be measured leading to variations of the mobility. Since the laser measurement is more accurate, the data from the seven laser rays were used. The gas mobility was determined by comparing the laser track positions measured in the TPC and in the laser diode system. The results obtained in this fashion were scaled during the production automatically in calibration units suitable in terms of changes in temperature, pressure, and gas composition according to the variation calculated with Garfield/Magboltz.

The transformation from pad, time, and z-plane to the coordinates in the laboratory system (x, y, and z) is done using a Runge Kutta method that calculates the drift trajectory using in each point the drift velocity vector, starting at the cathode wire plane. The drift between the cathode wire plane and the anode wire pad plane is absorbed in a time offset that is ϕ dependent because each Front End Electronic (FEE) channel had a slightly different capacitance. The difference between the Magboltz Monte Carlo and the drift velocity vector is accounted for with a z and r(E)-dependent correction for the drift velocity component parallel to the electric field and the one parallel to $\vec{E} \times \vec{B}$. A residual correction of the Lorentz angle is done assuming that identified pions with infinite momentum are straight.

The gain correction was performed for every cathode readout pad. It was obtained from the total hit amplitude in the pad of maximum amplitude. A correction of the un-

dershoot after each pulse was based on non-zero suppressed data [74]. After these corrections the radial dependence of the pulse height was explained for the bulk of the TPC by electron attachment and an oxygen content of 8 ppm which is in agreement with a value measured by the slow control system. An electron attachment correction [75] was determined by analyzing the dependence of the hit amplitude on the drift path length and taking into account the population of different particles in the polar angle θ. Due to this correction the $\mathrm{d}E/\mathrm{d}x$ resolution was improved which is of great importance for the electron identification.

3.4 Magnetic Field Map Correction

Charged particle momenta are measured by the ϕ-deflection in the magnetic field in the TPC. Technically the momentum information is provided by the fitting the reconstructed hits with a reference track. In order to generate the realistic reference tracks the precise knowledge of the magnetic field is required.

A calculated magnetic field map does not completely reproduce the magnetic field inhomogeneities. There are two known significant distortions of the magnetic field. A first distortion is produced by the iron equipment of the experimental setup located under TPC at ϕ = 90 deg. (in the coordinate system used for the B-field measurements where ϕ = 0 rad. is horizontal and to the left looking to the beam direction and $\phi = \pi/2$ rad. corresponds to a bottom of the TPC). The second distortion is due to the cables connected to the coils which are placed at about 60 deg. While the first distortion induces an additional strength of the B-field and is supposed to be independent of a current running in the coils, the second distortion somewhat weakens the magnetic field and is proportional to a current.

In order to correct the calculated magnetic field map three measurements of the magnetic field were performed at current values of 1550 A, 2325 A and 3100 A with a reasonably small grid. Since a measurement of the B-field at full current of 4160 A was not possible, an extrapolation procedure was developed and applied on top of the calculated map. An observed very accurate scaling of the B_z and B_r with current confirmed the applicability of the linear extrapolation using only two B-field measurements with highest current of 2325 A and 3100 A. The extrapolation is then given by

$$\begin{pmatrix} I_2 & 1 \\ I_3 & 1 \end{pmatrix} \cdot \begin{pmatrix} X_2 \\ X_3 \end{pmatrix} = \begin{pmatrix} B_2 \\ B_3 \end{pmatrix}, \tag{3.11}$$

where I_2, I_3 are the currents 2325 A, 3100 A and B_2, B_3 are the measured B-field components B_z (or B_r) corresponding to these two currents. Thus the extrapolated value of the magnetic field can be derived as

$$B_4 = B_3 + (B_3 - B_2) \cdot \frac{I_4 - I_3}{I_3 - I_2}, \tag{3.12}$$

where I_4, I_3, I_2 are the currents 2325 A, 3100 A, 4160 A and B_4, B_3, B_2 are the corresponding B-field components. However, in order to make a use of all three measurements a more accurate extrapolation was performed:

$$\begin{pmatrix} I_1 & 1 & 1/I_1 \\ I_2 & 1 & 1/I_2 \\ I_3 & 1 & 1/I_3 \end{pmatrix} \cdot \begin{pmatrix} X_1 \\ X_2 \\ X_3 \end{pmatrix} = \begin{pmatrix} B_1 \\ B_2 \\ B_3 \end{pmatrix}, \tag{3.13}$$

where B_1 is the measured B-field component at the current value of 1550 A. Then the extrapolation of the magnetic field components reads

$$B(I) = I \cdot X_1 + X_2 + X_3/I. \tag{3.14}$$

After computing the coefficients X_1, X_2 and X_3 the results obtained using Eq. 3.14 agree very well with the calculations based on only two measurements at highest currents. An agreement of the extrapolated B-field projections B_z and B_r derived with two methods proves the accuracy of the linear extrapolation. The correction value B_4^{corr} is equal to the difference between calculated B_4^{calc} and extrapolated B_4^{extr} components of the B-field. Since the grid sizes of calculated and extrapolated maps do not match exactly, a bilinear interpolation is used on a square grid for the extrapolated maps. The difference between the calculated magnetic field and the correction gives the final corrected magnetic field map for the current value of 4160 A:

$$B_4 = B_4^{calc} - (B_4^{calc} - B_4^{extr}). \tag{3.15}$$

It is important to note that the measured maps start at z = 3.4 m. Since, upstream of the TPC the magnetic field strength still deviates from zero, an extrapolation procedure ending at z of 3.4 m will introduce a step function in a B-field correction maps. Therefore a smooth transition to zero at z = 2 m was required for the extrapolated maps. Fig. 3.4 shows B_z and B_r maps extrapolated to the current value of 4160 A.

3.5 Matching between Detectors

Once the calibration of the SDD, the RICH and the TPC is finished and all corrections are applied, the track segments from SDD and TPC and the RICH rings are combined into global tracks. The width of the matching distributions depends on the accuracy of the calibration. The matching quality for the tracks with high enough momentum is limited by the resolution of detectors while for the low momentum tracks the quality of the matching deteriorates due to multiple scattering in the material, and it is no longer determined by the detector resolution alone.

A study of the matching quality for various detector combinations showed a dependence of width of the matching distributions both in ϕ and in θ on the θ-coordinate, given by the point resolution. Following this observation the matching distributions between SDD and TPC were plotted for seven different θ-bins. In case of RICH-TPC matching, six θ-bins were selected. Another observation indicated a dependence of the matching on a topology of hits belonging to tracks in silicon drift detectors. Therefore the matching distributions were divided into three different classes corresponding to three hit topologies: both SDD hits are single-anode hits, one hit is single-anode and another one is multi-anode, both hits are multi-anode hits.

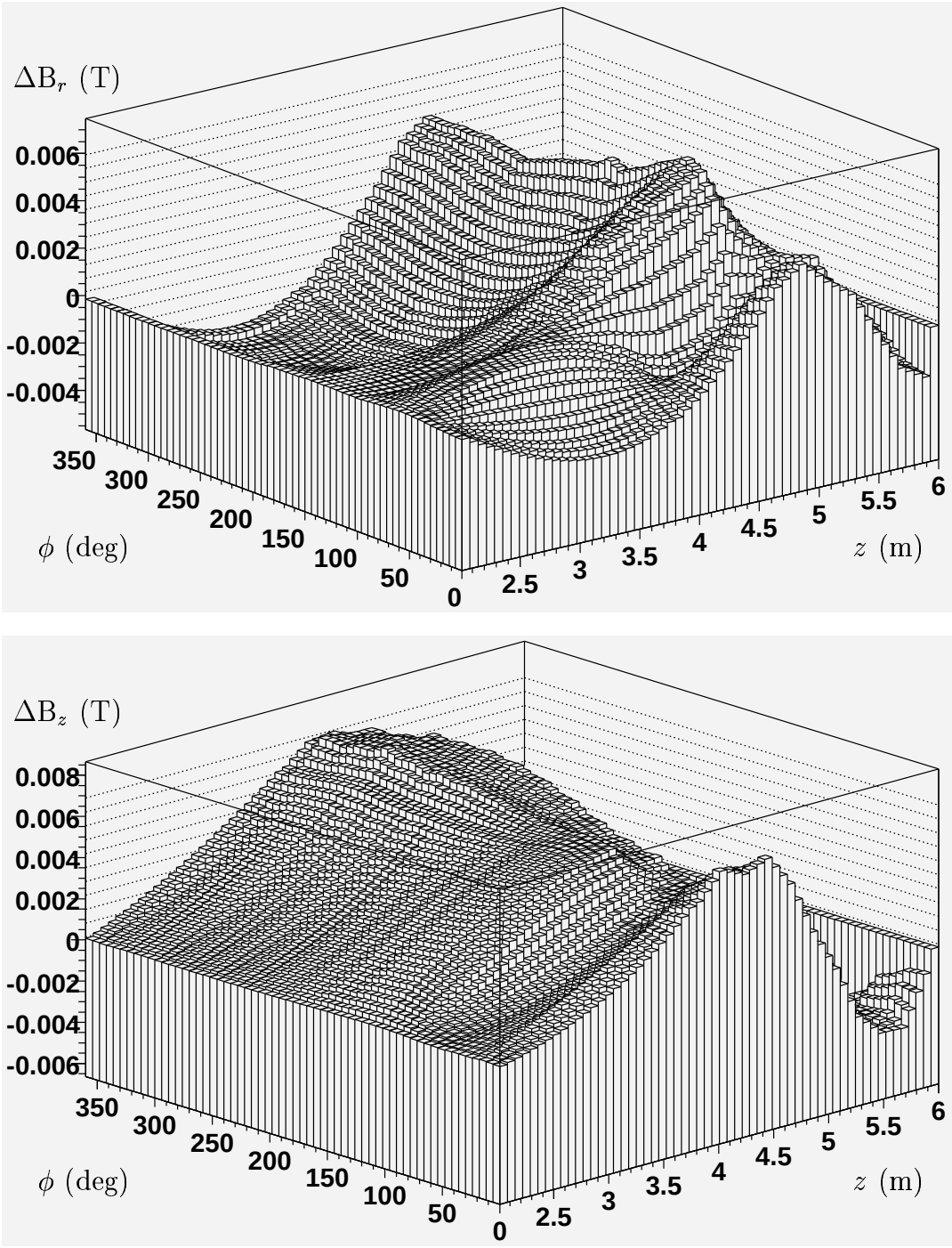

Figure 3.4: Correction maps for B_r (top panel) and B_z (bottom panel) projections as a function of ϕ and z at a radius of 0.965 m and 0.97 m, respectively. The corrections are derived from the difference between the calculated B-field map and the extrapolated map. To avoid a step function in the correction map the extrapolation was forced to match zero smoothly at z = 2 m.

A dependence of the width of matching distributions on track momentum extracted from a fit of slices of the corresponding two-dimensional distribution is displayed in Fig. 3.5[2] for RICH-TPC matching for the θ-bin 190 $<$ θ $<$ 210 mrad.

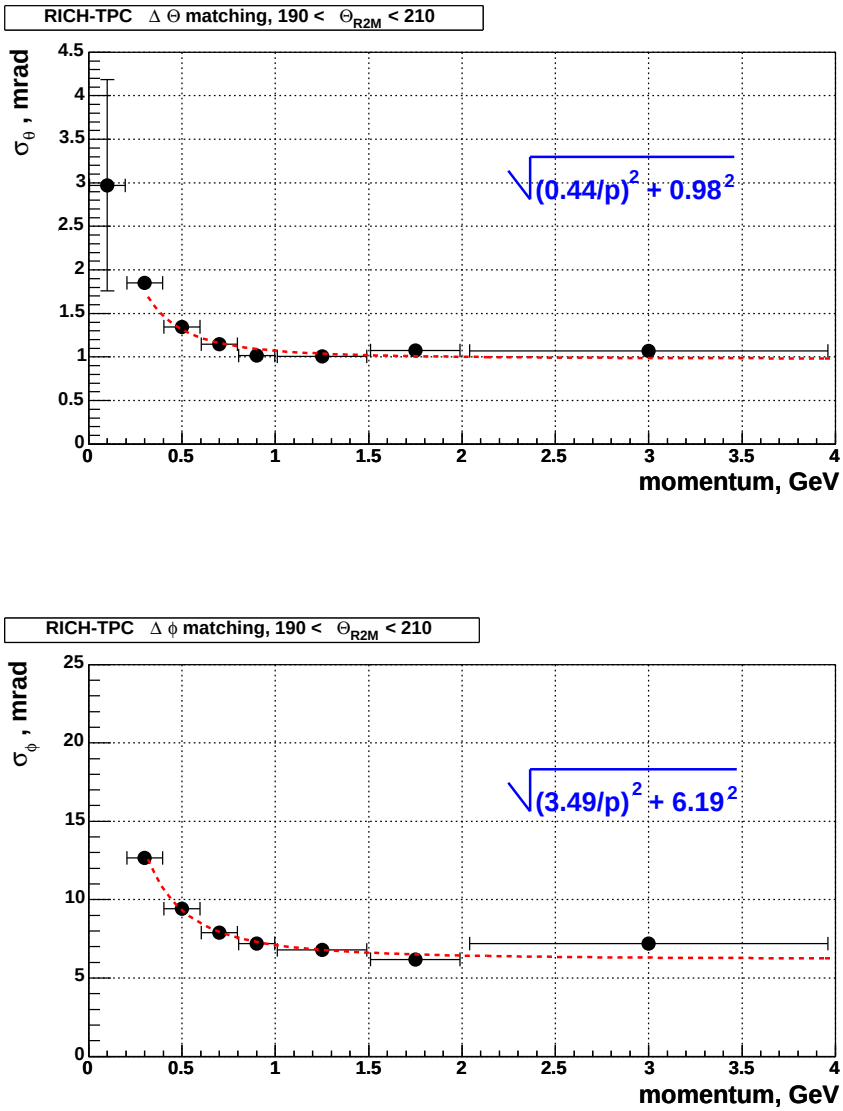

Figure 3.5: Width of the matching distributions between RICH and TPC in θ (top) and ϕ (bottom) as a function of momentum for θ-bin 190 $<$ θ $<$ 210 mrad. The parameterization of the momentum dependence is shown by red dashed line.

Fig. 3.6 shows the matching width for the θ-range 200 $<$ θ $<$ 220 mrad as a function of track momentum for SDD-TPC matching in case of two multi-anode hits on SDD segments.

[2] A unit of momentum for the matching distributions is exceptionally given in notation of c=1.

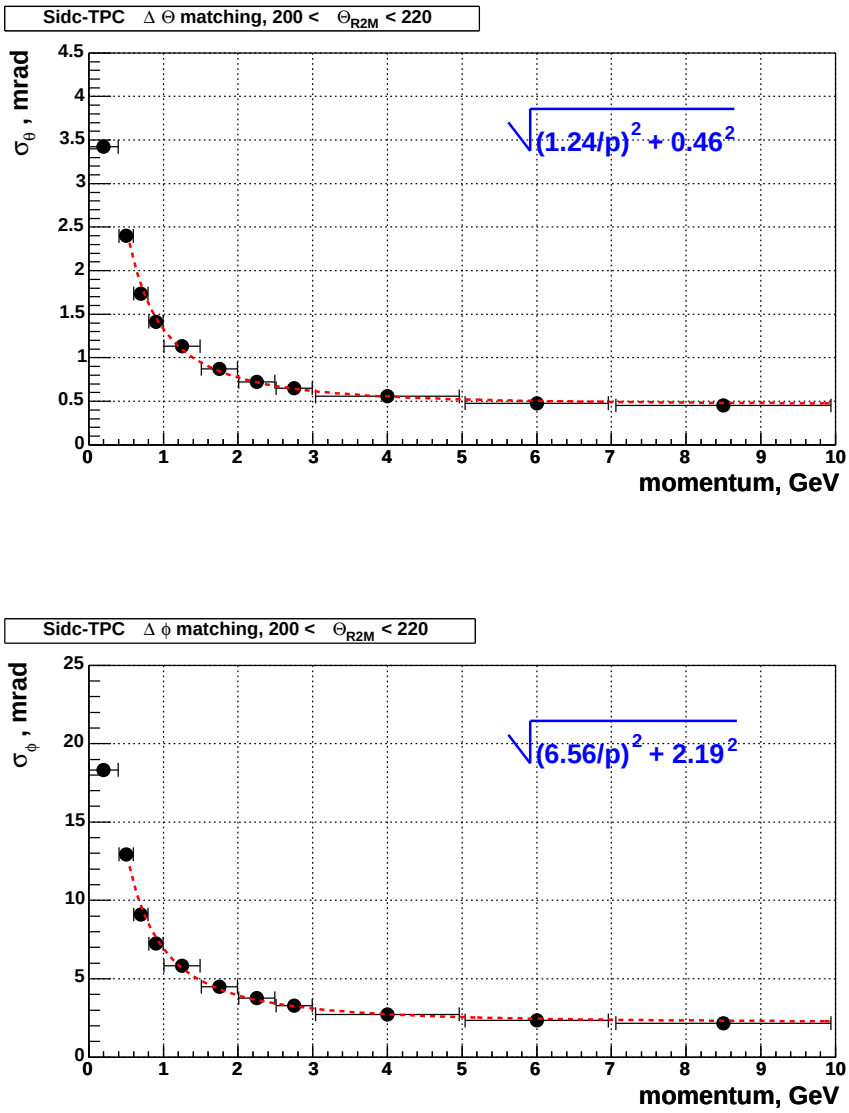

Figure 3.6: Width of the matching distributions between SDD and TPC in θ (top) and ϕ (bottom) as a function of momentum for θ-bin 200 $<$ θ $<$ 220 mrad. Both hits on SDD segments are multi-anode ones. The parameterization of the momentum dependence is shown by red dashed line.

The width of matching distributions between SDD and RICH detectors plotted for θ-bin 190 $<$ θ $<$ 210 mrad for a case of two multi-anode hits on SDD segment is shown in Fig. 3.7. All matching distributions are shown after background subtraction. The background was evaluated by rotation of one of the detectors by random angle. The width scales with 1/p which exhibits an effect of multiple scattering dominating over the detector resolution at low momenta. The width was parameterized as a function of momentum by

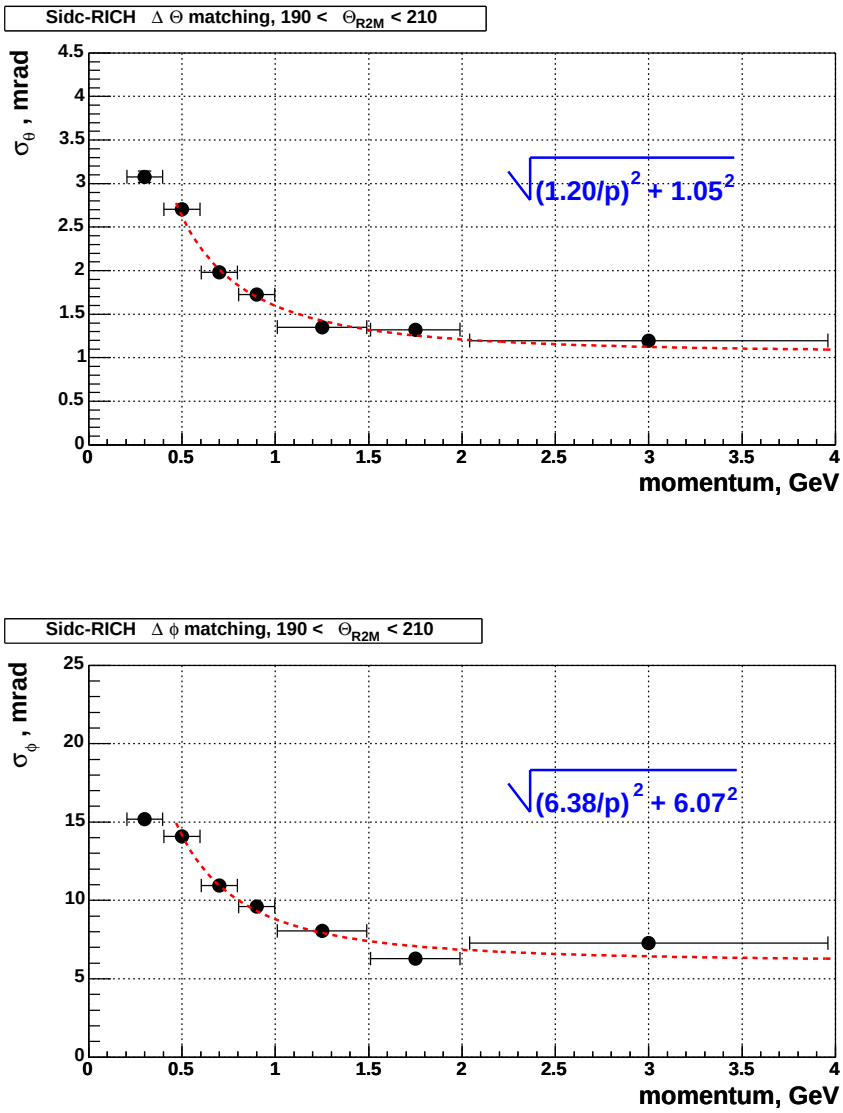

Figure 3.7: Width of the matching distributions between SDD and RICH in θ (top) and ϕ (bottom) as a function of momentum for θ-bin 190 $<$ θ $<$210 mrad. Both hits on SDD segments are multi-anode ones. The parameterization of the momentum dependence is shown by red dashed line.

$$\sigma = \sqrt{(\sigma_m/p)^2 + \sigma_\alpha^2}, \tag{3.16}$$

where σ_m is a momentum dependent multiple scattering term and σ_α is a detector resolution term ($\alpha = \theta, \phi$).

In the dilepton analysis tracks are selected according to momentum dependent cuts on the width of matching distributions in θ and ϕ.

4

Data Analysis

The results presented in this thesis were obtained from the analysis of the data taken during the SPS Pb beam period in the fall of 2000. The data were collected with an interaction trigger corresponding to the top 7% of geometrical cross section with an average multiplicity of $\langle dN_{ch}/dy \rangle$ = 321 in η = 2.1-2.65. A total of 18.2 million events were analyzed due to discharges in RICH detectors which affected significant part of events.

4.1 Data Analysis Sequence

The CERES data analysis is carried out in three stages. The first stage includes the charged track reconstruction procedure and calibration refinement described in Chapter 3. The second stage invokes vertex refitting, TPC track refitting and the output data compression. In the third stage, the global electron tracks are constructed and output ROOT trees are further compressed. In the final fourth stage, the rejection cuts are applied, all survived tracks are combined into pairs in each event and the mass spectra are filled.

The main steps of the analysis are as follows:

(i) Charged track reconstruction

- SDD track reconstruction
  - Event clean-up
  - Hit finding
  - Vertex reconstruction
  - Track reconstruction
- RICH ring reconstruction
  - Event clean-up
  - Hit finding
  - Ring finding

  - Ring fitting

- TPC track reconstruction
  - Hit finding
  - Track finding
  - Track fitting
- Global track construction (matching of SDD, RICH and TPC tracks)

(ii) Final refinement of experimental information

- Vertex refitting
- TPC track refitting

(iii) Physics analysis

- Background rejection cuts
- Pairing: global tracks are combined into like-sign (++,- -) and unlike-sign (+-) pairs
- The mixed event background is subtracted: S = N_{+-} - F·N_{+-}^{mix}
- Final mass spectra and pair-p_t^{ee} spectra are obtained

4.2 CERES Event Display

To visualize the CERES data the 3D Event Display Liana [76] was developed. Liana is coded using C++ language and based on SGI's OpenGL library [77, 78] and Open Inventor toolkit [79], which significantly extends 3D programming capabilities. The goal of the new event display is a representation of tracks and hits as well as main detector systems of the CERES experimental setup on 3D scene. Rich and flexible functionality was provided by introducing interactive operation with the objects and the scene. Higher performance, relative to many other 3D event displays, in rendering complex 3D scenes and massive sets of objects in interactive regime was achieved by utilizing unique architecture and efficient algorithms. To operate with thousand of interactive objects the STL based containers as well as scene optimization and caching routines are used. Liana is a multithreaded application, which runs ROOT for the experimental data representation and core 3D graphics engine in two separate threads including various event loops and thread synchronizations. To summarize, Liana offers a comprehensive solution to interactive graphics, efficient analysis of 3D scenes, and interactive representation of physics data.

4.3 SDD Tracks Reconstruction

The two radial Silicon Drift Detectors (SDD) play an important role in the electron analysis. The tasks are the following:

- Vertex determination: the vertex location is determined with high precision by two closely-spaced large silicon drift detectors.
- Tracking of electrons: good single-hit resolutions in r and ϕ provide a high accuracy for the tracking of the electron candidates from the vertex point into the spectrometer.
- Identification/rejection of close pairs: the doublet of silicon detectors provides a powerful tool for rejection of physical background via energy loss. Double energy loss in both SDD's is a pattern of close pairs (γ-conversion or close π^0-Dalitz decay).
- Charged particle density determination: good double-hit resolution decreases amount of pile-ups and, thus, limits the degree of miscounting N_{ch}.

4.3.1 Hit Reconstruction

A typical event in the silicon drift detector is shown in the SDD event display in Fig. 4.1.

The charged particle passing the silicon drift detector deposits a certain amount of energy. A minimum ionizing particle produces a signal which is typically spread over 8-12 time bins in the radial direction and 2-3 anodes in the azimuthal direction. Thus, one hit usually consists of 20-40 cells.

The cells assigned to one hit are combined into a cluster. A recursive algorithm joins all adjacent cells to a currently being created cluster. All cells within a cluster of a fixed anode form a pulse. The known dead anodes are included into the clusters. Each cluster is scanned for a local maxima in the amplitude profile in the time direction as well as local minima if more than one maximum was found. If the amplitude of the minimum is less than 10% of that of maximum, the two pulses are separated and treated as if they were two single ones, otherwise they are further considered as two close pulses.

The time positions of the pulses are combined in the anode direction into hits within a certain time window. Since the hit splitting crucially depends on the time window, a size of the window was optimized to minimize artificial hit splitting. In case of three or more aligned pulses connected to a hit candidate, a minimum in the amplitude profile along the anode direction is searched for. Once the minimum is found, the hit candidate is split into two hits using the center of gravity to calculate its position along the anode direction.

A double-hit resolution is of importance for both the determination of the number of charged particles and for the rejection of the physical background. Fig. 4.2 represents the distance between hits on SDD tracks and next closest hits in SDD1 and SDD2 for the experimental data.

In order to estimate the ideal double-hit resolution the distance between a point with random θ- and ϕ-coordinates and the closest SDD hit was calculated. The difference

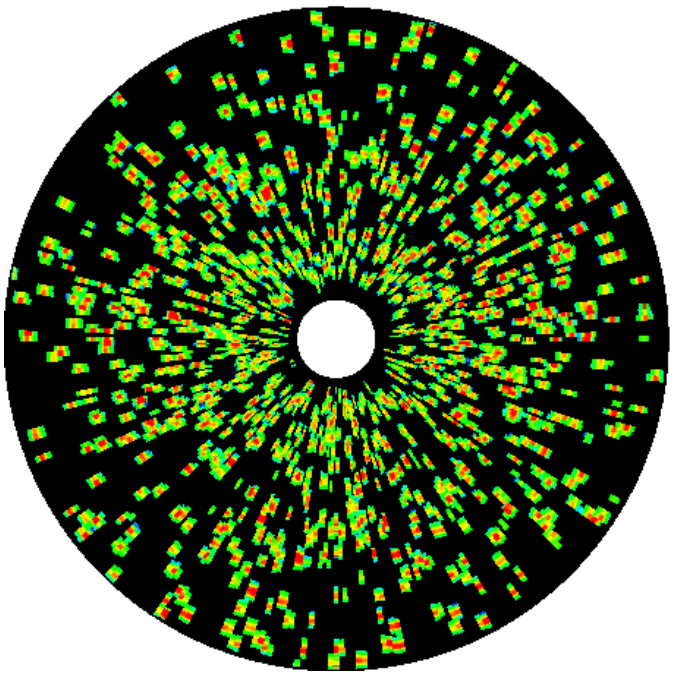

Figure 4.1: SDD1 event display. Each hit represent a charged particle produced at central Pb-Au collision.

between the distribution based on random pointing and real distribution is observed for low values of distance, where the two-hit resolution problem occurs. The right parts of distributions coincide in both silicon detectors. Thus the double-hit resolution is 8 mrad in SDD1 and 6 mrad in SDD2.

Fig. 4.3 shows the status of the hit splitting algorithm in SDD1 and SDD2 detectors. The distance to the next closest hit is plotted for all SDD hits on tracks.

If the software with not optimized time window is used for the hit reconstruction, artificially split hits appear as a narrow peaks at 4 mrad distance in both silicon drift detectors. The improved hit reconstruction algorithm allows to minimize the problem of artificial hit splitting which results in the absence of the mentioned peak in SDD1 and significant reduction of the peak in SDD2.

Since two-hit resolution is different in two SDD detectors and is not a step function, but rather a smooth transition between poor and complete separation of the hits, the rejection based on $\mathrm{d}E/\mathrm{d}x$ information can not work with full power. To improve the rejection tool a resummation procedure is performed. The amplitudes of the hit on SDD track and the next closest hit are summed within a certain window. It's worth to note that resum-

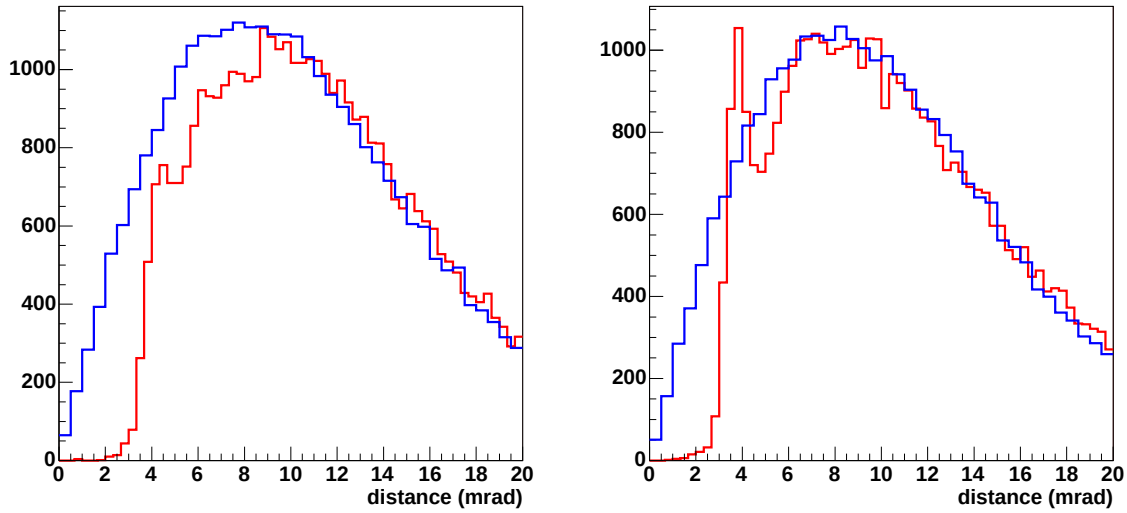

Figure 4.2: Distribution of the distance between hits on SDD tracks and neighboring hits (red line) and the distance between a random point and closest SDD hit (blue line) illustrating the ideal reconstruction algorithm with perfect double-hit resolution. The histograms are shown for SDD1 (left panel) and SDD2 (right panel).

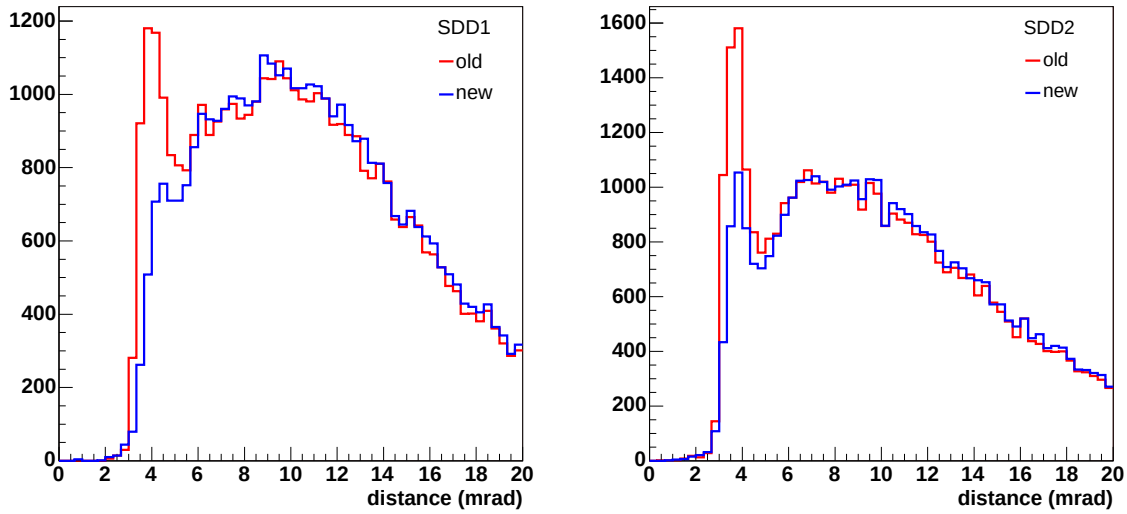

Figure 4.3: Experimental data distribution on the distance between hits on SDD tracks and neighboring hits in SDD1 (left panel) and SDD2 (right panel). The two histograms shown for both silicon drift detectors represent the results of the different hit reconstruction algorithms. The peak at 4 mrad illustrates the artificial hit splitting for the old reconstruction software. The new algorithm with optimized time window solves the hit splitting problem in SDD1 and significantly decreases the amount of split hits in SDD2.

mation is not done for all hits in the window but only one closest hit contributes with its amplitude. Moreover, the two-hit resolution derived from the distance distributions is a resultant sum of different contributions from one-anode hits and multi-anode hits. Since,

the two-hit resolution in SDD detectors significantly affects the rejection of γ-conversions and close π^0-Dalitz decays, it is of importance to separately consider different types of hits. See table 4.1 for a detailed information.

4.3.2 Vertex and Track Reconstruction

Once hits are reconstructed, the information of hit positions in the laboratory coordinate system is used to combine hits to tracks and find the vertex position to which almost all tracks of a given event point to. The procedure of minimizing the quadratic sum of hit mismatches between the two detectors and its iteration is extremely time consuming. Therefore a robust vertex fitting algorithm is used [80]. In contrast to approaches using standard minimization packages the robust iterative procedure is about an order of magnitude faster. All hits in SDD1 and SDD2 are combined to straight track segments and a weighted sum of their projected distances to the assumed vertex position is calculated. Once the z-coordinate of the vertex is determined, it is refined to the exact position of the closest target disc. Fig. 4.4 shows the resolved 13 Au target disks of 26 μm thickness each with average Gaussian width of about 205 μm. The sum of residual distances of the

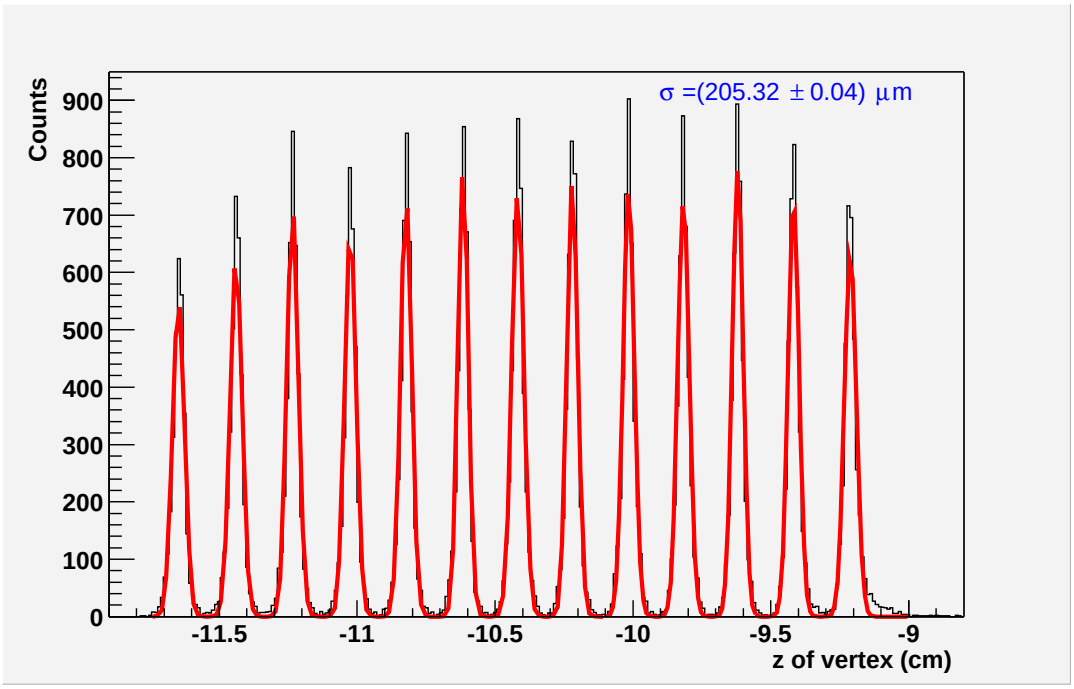

Figure 4.4: Distribution of reconstructed vertex position along the beam axis with the doublet of silicon drift detectors showing the resolved 13 Au target disks.

tracks pointing to the target is minimized in order to define the precise x-y vertex position. After refinement of the vertex position an optimized set of the vertex track segments is obtained. Each hit in SDD2 is connected to the vertex point and the closest hit in SDD1 is searched for. The searching windows used at the stage of step2 production were wide in order to include non-vertex tracks for the hadron analysis. In the final electron analysis

much tighter windows based on a resolution of individual SDD hit types are applied. Two tracks are allowed to share the same hit in SDD1 (called V-tracks). Such a signature can be an indication of γ-conversions or close π^0-Dalitz decay. Finally, all remaining tracks with one hit missing due to detector defects are constructed by connecting the vertex point and unused hits of other healthy silicon drift chamber. The average of the θ- and the ϕ-coordinates of the hits gives the coordinates of the constructed track. However, in case of the single anode hit in one of the detectors, the ϕ-coordinate of the multiple anode hit in the other silicon drift detector is preferred, rather than an average of both ϕ-coordinates.

4.3.3 The Energy Loss

The detection of charged particles depends on the fact that they transfer energy to the medium they are traversing. The Bethe-Bloch equation gives the average value of the energy loss dE in a layer dx, but there are fluctuations about the mean, dominated by the relatively small number of primary collisions with large energy of electrons knocked in the process of primary ionization. The resultant so-called Landau distribution about the mean value is therefore asymmetric, with a tail extending to values much greater than the average (Fig. 4.5). Only for a thick layer with dE/dx/δx much larger than the maximum energy transfered to an electron is the distribution nearly Gaussian.

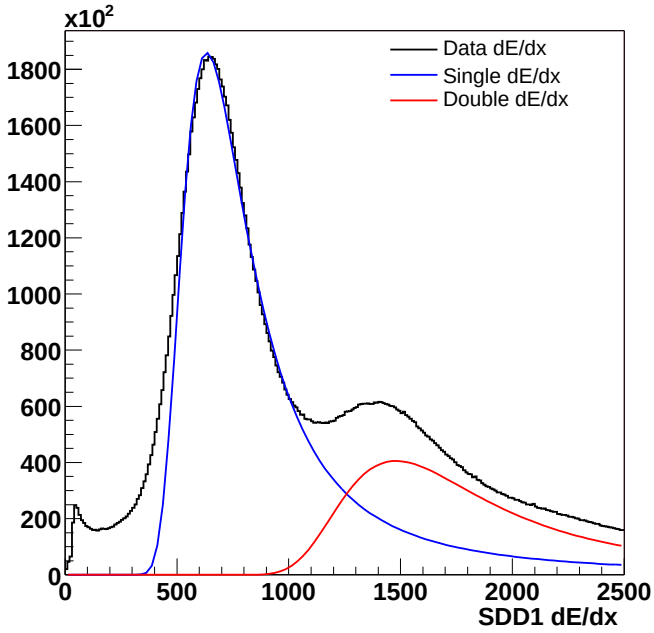

Figure 4.5: Energy loss distribution in SDD1. The left peak shows the energy loss by single particles, the right peak corresponds to dE/dx of close unresolved tracks. The blue and red lines represent two separate contributions to the dE/dx distribution extracted from the double Landau fit. The distribution is skewed toward big values due to fluctuations. The enhanced low dE/dx tail is due to γ-conversions in SDD, dead anodes and partially due to hit splitting.

The two Landau functions obtained from the double Landau fit of the dE/dx distribution represent separate contributions of the resolved single tracks and unresolved close pairs. However, the artificial hit splitting, hits placed close to dead anodes and γ-conversions in silicon drift detectors distort the energy loss distribution and produce a structure at low dE/dx.

4.3.4 Charged Particle Multiplicity

The determination of the charged particle multiplicity in the event was based on the analysis of minimum bias data. To improve the accuracy of the N_{ch} determination, random coincidences between hits in the two silicon detectors, finite two-hit resolution and SDD tracks originated from δ electrons were taken care of [81, 82].

- The distribution of "z"-coordinate of SDD tracks in the event coordinate system exhibits two contributions: one arising from real tracks, which appear as peaks in the target region -12 $< z <$ -9 cm, and another one corresponding to random matches of SDD hits. The fake track contribution was estimated by calculating the z-position of the vertex via combination of the two hits in SDD1 and SDD2 belonging to different intervals in ϕ (flat in both silicon drift detectors). Then the true number of tracks coming from the target was obtained by subtracting the found background and $dN_{ch}/d\eta$ was computed by repeating the whole procedure for every pseudorapidity bin (Fig. 4.6).

- Due to a limited two-hit resolution, the close tracks are reconstructed with smaller efficiency. This effect was suppressed by requiring a certain distance to neighboring hits. The dependence of the SDD track multiplicity on the distance value was extrapolated to zero. The extrapolated charged particle densities were checked to be very similar for different values of the distance cut.

- The multiplicity of the δ-electrons was estimated by applying the described procedure to beam trigger data. The obtained contribution from δ-electrons displayed in Fig. 4.6 was then subtracted from the minimum bias run.

The maximal pseudorapidity density of charged particles per participant (at η = 3.1) is estimated to be dN_{ch}/deta(3.1)/N_{part} = 1.18 $\pm$ 0.15(syst), independent of centrality within 0-50%. The nuclear overlap model [83] was used to calculate the number of participants for a given centrality. The central collision dN_{ch}/dy(2.9), evaluated via 1.02 times dN_{ch}/dη(3.1), fits the available beam energy systematics displayed in Fig. 4.6 [84]. A charged particle multiplicity value of N_{ch} = 321 $\pm$ 39 was obtained for our centrality in the pseudorapidity range 2.1 $< \eta <$ 2.65.

The collision centrality estimated using the charged particle multiplicity around midrapidity y_{beam}/2 = 2.91, was also verified with the measurements of amplitude of the Multiplicity Counter covering 2.3 $< \eta <$ 3.5 (Fig. anacentral top) and the track multiplicity in the TPC covering 2.1 $< \eta <$ 2.8 (Fig. anacentral bottom). Taking into account the data acquisition dead time factor and the target thickness, the event counts can be translated to the cross section for collisions with a given multiplicity assuming that all beam particles

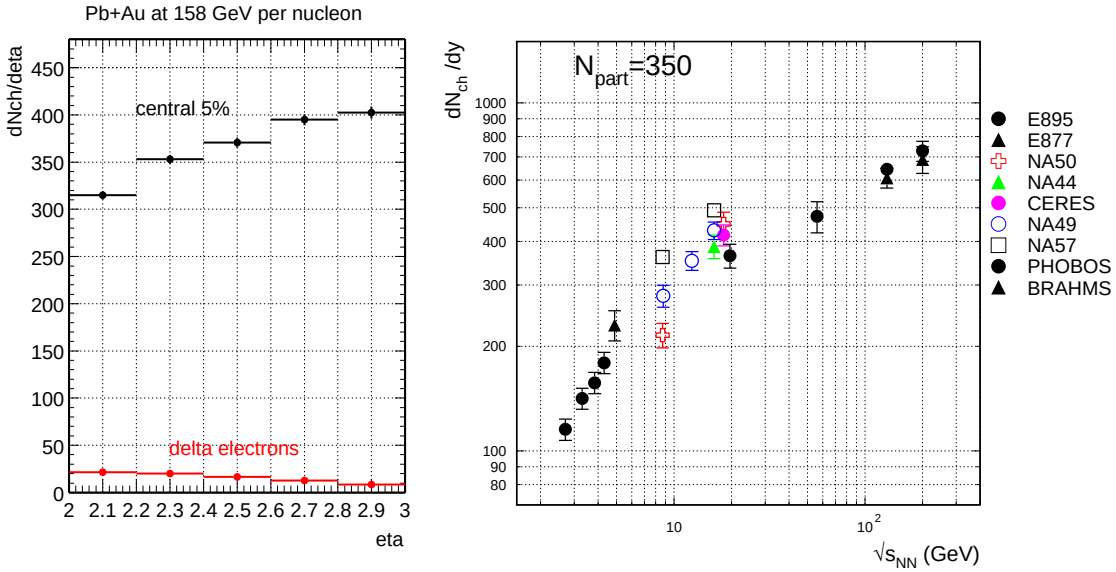

Figure 4.6: $\mathrm{d}N_{ch}/d\eta$ for 5% centrality class (black points) and contribution to the charged particle density from δ-electrons (left panel), and $\mathrm{d}N_{ch}/\mathrm{d}y(2.9)$ compared to the available beam energy systematics.

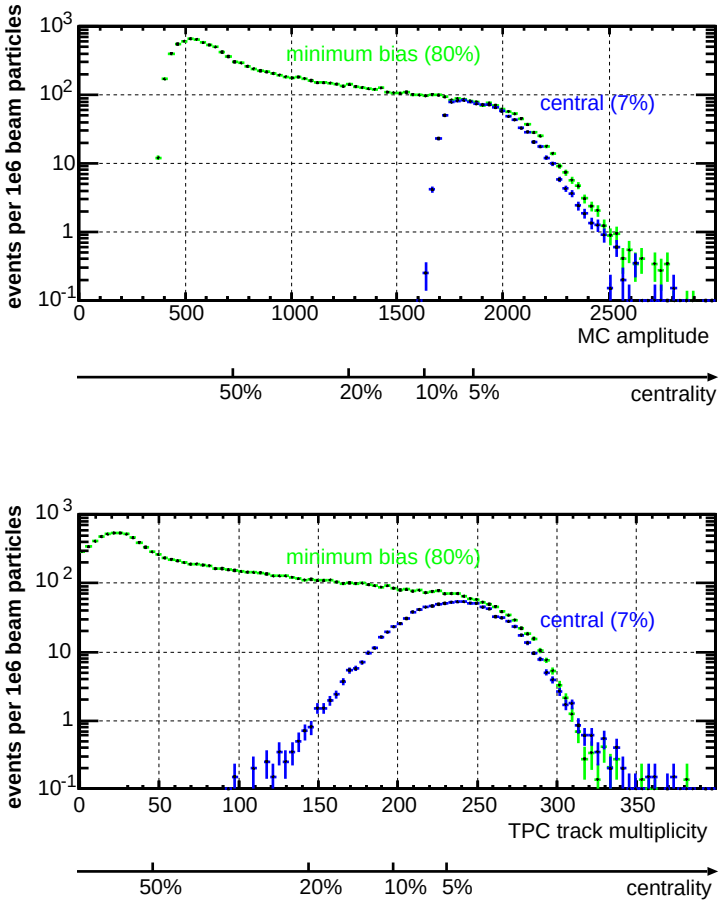

Figure 4.7: Response of the MC detector (top) and the TPC track multiplicity (bottom) used for centrality determination.

were hitting the target. The ratio of the integrated cross section to the geometrical cross section (σ_G = 6.94 barn) is shown as the additional axis in Fig. 4.7.

4.4 RICH Ring Reconstruction

4.4.1 Event Clean-up and Hit Finding

Signals of the RICH detectors are read out from the checkerboard-like arrangement of pads which receive the charge amplified in multi-wire proportional chambers. The RICH event display is shown on Fig 4.8.

Adjacent pads with amplitude above a readout threshold are grouped to clusters. Some clusters are caused by background. The RICH reconstruction algorithms aim to reach a high efficiency and at the same time to produce a low amount of fakes. However both the efficiency and the fakes are very sensitive to a level of background. To suppress the electronic noise and other background sources a clean-up procedure is applied. The cleaning algorithms mostly remove the typical background clusters, like long and thin stripes from ionizing particles on oblique trajectories, clusters with many pads in saturation, or permanently illuminating noisy pads. Remaining clusters are split into regions containing one local maximum and are identified as UV-photon hits in the RICHes. Hit centers are calculated as the centers of gravity of the pads connected to the hit.

4.4.2 Pattern Recognition Algorithm

A number of various methods of processing the RICH detector data for particle identification are well known. Some of these methods are based on the maximum likelihood approach [85], or on comparing probability distributions [86] of Cherenkov photons for different hypotheses. Reconstruction of RICH rings in CERES is performed by a standalone method based on pattern recognition called Hough transform [87]. The choice of Hough transform is motivated by the following considerations:

(i) A substantial speeding up of processing of RICH measurement.
(ii) Eliminating an external information such as the knowledge of Cherenkov ring centers.
(iii) Possibility to use RICH counter as a rejection tool of partially reconstructed Dalitz decays. The soft leg of the Dalitz decay might miss the TPC and, thus, only SDD-RICH segment might be reconstructed. Therefore the strategy to reject partially reconstructed Dalitz decays can be based on a distance between global track and SDD-RICH segment.
(iv) Ability to process the bulky array of many thousand pads.

The Hough transform is a standard tool in image analysis that allows recognition of global patterns in an image space by recognition of local patterns in a transformed parameter space. Around each photon hit (or illuminated pad) a circle is drawn with a radius which forms a Hough (transformed parameter) space. Hits that belong to the same ring will have circles intersecting in the same point. The sharp peak at the ring center in the Hough space will only appear if the radius corresponds to the asymptotic radius of the electron

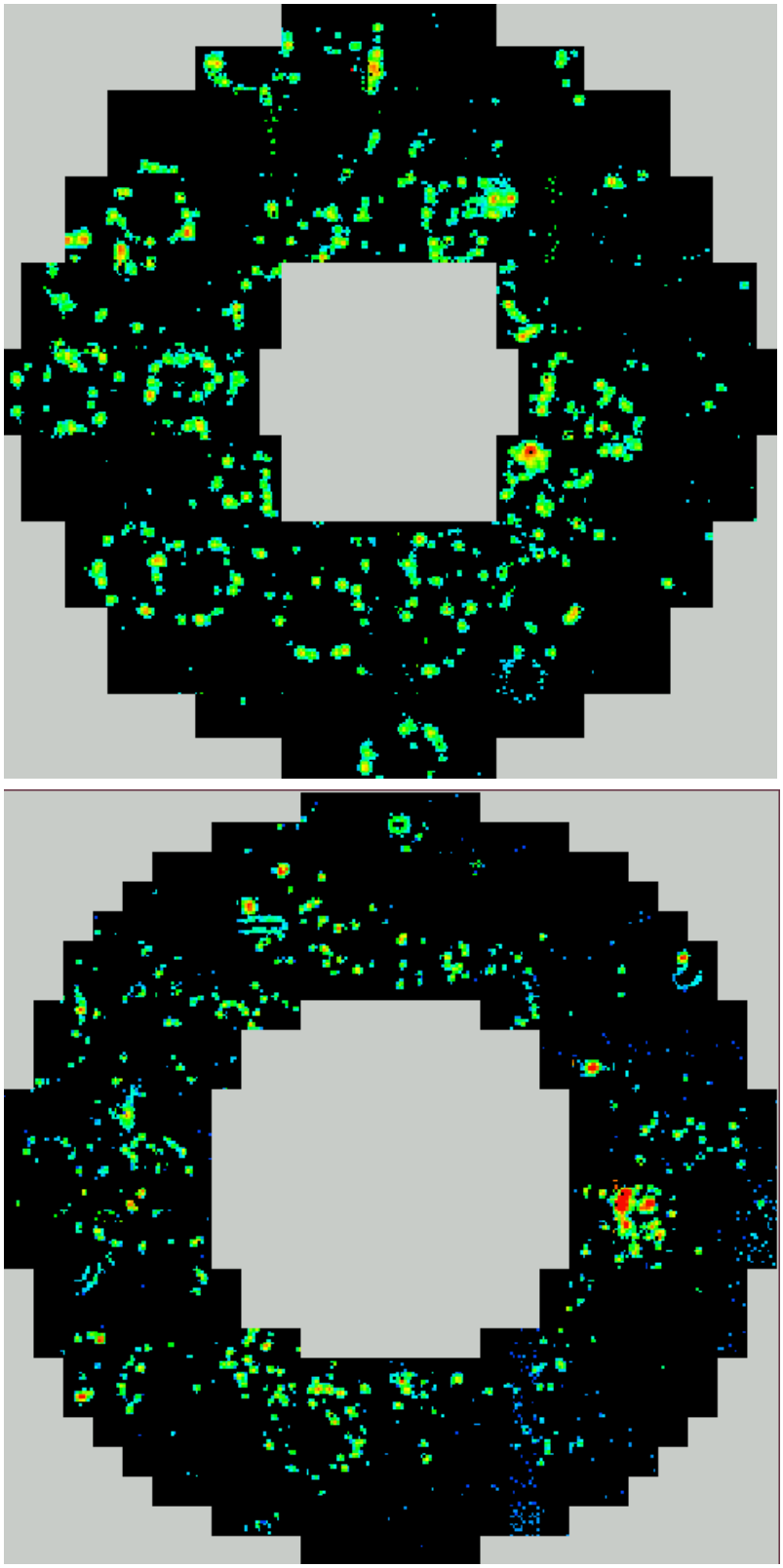

Figure 4.8: RICH1 (upper panel) and RICH2 (lower panel) event display for run 1303 burst 332.

ring, otherwise the intersections will form a wide cluster and will not stand out from the background. Therefore the method distinguishes between electron rings and pion rings that approach the asymptotic radius only at high momenta. Fig. 4.9 shows the Hough space corresponding to the original ring as well as the resulting peak on the Hough space.

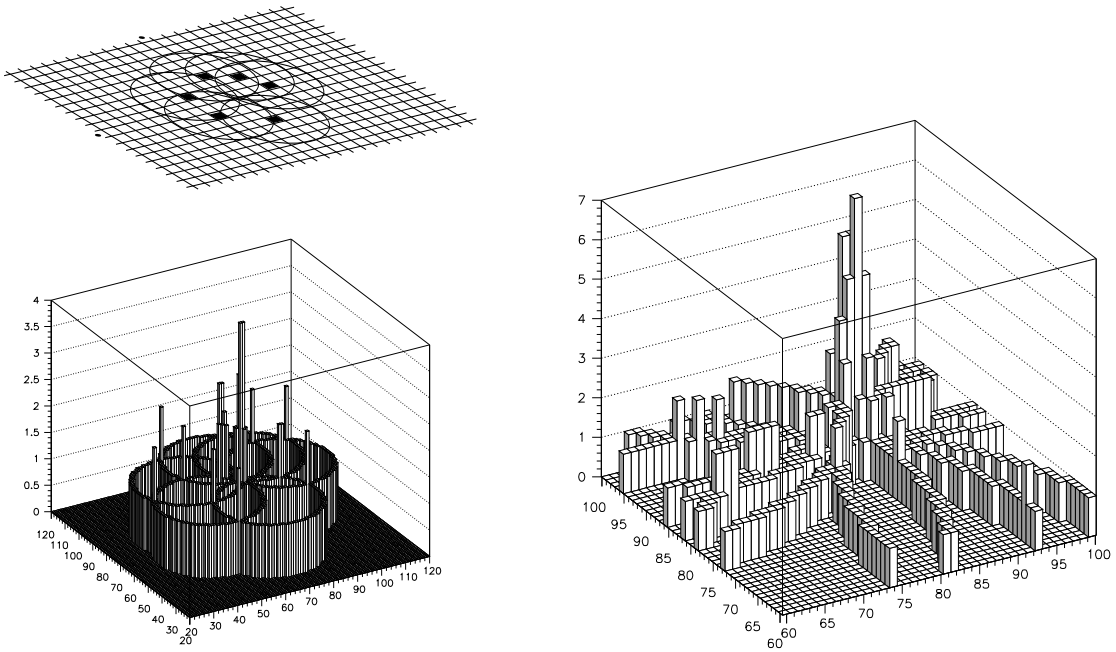

Figure 4.9: Left panel: application of the Hough transform in the ring search on a granular detector; the original pattern above and the histogram on the Hough space. Right panel: the resulting peak on the Hough space corresponding to the ring center.

The algorithm as implemented consists of three stages:

- The fist step is a linear Hough transform. For each pad with a signal above a given threshold, a point-to-ring transformation is made with a ring radius equal to the asymptotic ring radius of electron rings (14.5 mrad). The absence of magnetic field between the two RICH detectors allows to use them in a combined mode resulting in an increased Hough signal connected to the correlated electron rings in contrast to uncorrelated background. The pads from both RICH's are transformed onto the Hough plane of the first RICH counter which has wider acceptance. The mask used in the algorithm is shown in Fig. 4.10.

  In the Hough space, an electron ring in the pad plane leads to a peak. The resulting Hough space after the first step usually consists of many local peaks corresponding to the fake ring centers besides the real maximum.

- To suppress the fake peaks a smoothing procedure is applied. Every illuminated cell in the Hough space is given a weight equal to a sum of weights of the neighboring cells in a box of 3×3. As result the fluctuations in the Hough space significantly decrease.

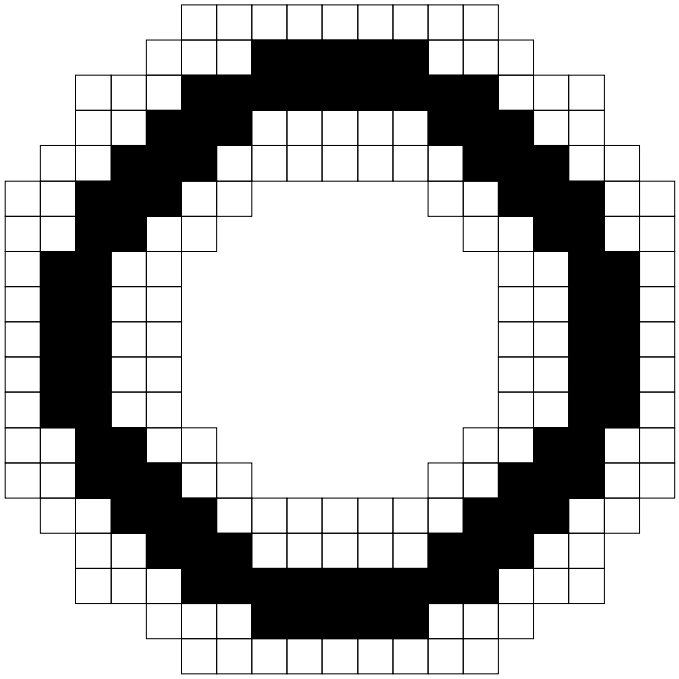

Figure 4.10: RICH hough mask.

- To further develop the Hough peak connected to a real ring center a second, non-linear Hough transform is performed. The new relative weight normalized to the average sum of weights in the Hough ring mask is calculated for every cell in the Hough space with a smoothed amplitude bigger than the average amplitude for the given ring mask. Finally a threshold is applied and, in case of two close local Hough peaks with a distance between peaks below 6 mrad, the one with lower amplitude is removed. All surviving maxima are the candidates to ring centers.

The ring reconstruction efficiency was studied using the pure Monte Carlo and overlay Monte Carlo techniques. The ring reconstruction efficiency obtained in the pure MC with one electron track per event is above 95% which is, of course, not realistic. The overlay Monte Carlo technique, allowing to reproduce the occupancy in the data by overlaying the MC track on top of the real event, gives 80% reconstruction efficiency. This seams to be also not realistic due to the fact that the ϕ-distribution of RICH rings in the data is not reproduced in Monte Carlo because of gain variations and ill behavior of several regions in RICH detectors. The experimental method for the RICH efficiency determination described in section 4.6.4 gives 68% for the Hough amplitude cut of 180. Additional studies of the double Hough and single Hough [1] approaches showed that the double Hough transform provides almost twice better efficiency compared to the single Hough transform for the 2000 data.

[1] In single Hough approach the Hough transform is applied separately in RICH1 and RICH2. Therefore the resulting RICH ring reconstruction efficiency is a product of RICH1 and RICH2 efficiencies.

4.4.3 RICH Ring Fitting

The final accurate determination of the x-y coordinates of the ring candidate centers is performed by a robust ring fit [88]. The least-squares fit with asymptotic ring radius is applied for a set of hits from the area around the ring candidate. The hits from RICH2 are transformed into RICH1 coordinate system. Therefore the combined set of hits from both RICH detectors is used exploiting the advantage of switched magnetic field. The weights assigned to the hits are recalculated after every iteration. The analog amplitude of the ring consists of summed amplitudes of all hits belonging to the ring within ± 6 mrad window. Additional information about ring quality is given by χ^2 of the fit.

Thus the set of fitted rings is the final result of the RICH reconstruction software. The most important information used in the electron analysis consists of refined position of the rings, number of fitted hits on ring, the sum analog amplitude and the non-linear Hough amplitude of the ring obtained by the Hough transform procedure.

4.5 TPC Track Reconstruction

The radial-drift TPC is the most important detector in the CERES experimental setup. The improved momentum resolution allows to measure ω and ϕ mesons. Additionally the energy loss information provides a possibility for particle identification. A typical event reconstructed in the TPC is illustrated in Fig. 4.11.

4.5.1 TPC Hit Finding

Before the hit finding algorithm starts [89] the unpacking of the zero suppressed data from a binary file is performed. The restored information on amplitudes, pad and time-bin coordinates of the pixels is written into dedicated lists.

The task of the hit reconstruction is to locate connected pixels and finally to define the coordinates of the hits. The first step is to localize the pads with local maxima in the pad and the time directions in all 20 planes with a criteria allowing to suppress fake peaks originating from noise fluctuations. Next step is to calculate the center of gravity in pad and time directions and to define the exact coordinates of the hits. The calculation is performed in an area of 3 pads $\times$ 5 time-bins around the local maximum. The center of gravity in ϕ and time directions is given by:

$$t = \frac{\sum_i A_i A_{max0}/f_i t_i}{\sum_i A_i A_{max0}/f_i}$$

$$\phi = \frac{\sum_i A_i A_{max0}/f_i \phi_i}{\sum_i A_i A_{max0}/f_i}$$

where i is the index of the pixels in the 3 pads $\times$ 5 time-bins area around a hit, A_i is the amplitude of pixel i, t_i is ϕ_i are the nominal positions in time- and ϕ-direction of the pixels, f_i is a counter variable assigned to each pixel in the hit-area and used to weight the individual pixels. f_i is a sum of the maximum amplitudes of all hits connected to the hit-area. This variable is introduced in order to cope with the overlapping hits which have

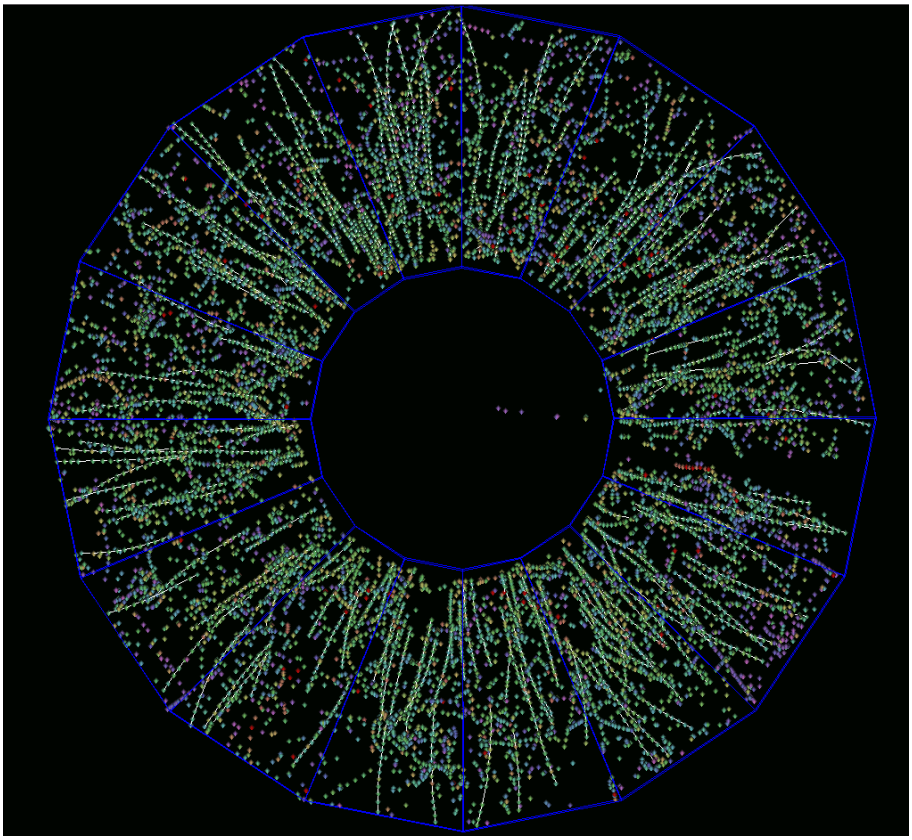

Figure 4.11: TPC event display corresponding to a central Pb on Au collision at 158 A GeV/c.

a common part of their hit-areas. Since the track consists maximally of 20 points, it is of extreme importance to achieve high efficiency of the hit finding algorithm.

4.5.2 TPC Track Finding

The track reconstruction algorithm aims the following goals:

- **To maximize efficiency** in the low momentum region as well as the overall efficiency. The challenge is therefore extremely high, since the softer the track the greater the deflection in the magnetic field. Both π^0-Dalitz decays and γ-conversions have soft momentum spectra. Thus the rejection power of the TPC depends on the capability to reconstruct soft tracks.

- **To maximize number of hits on the track**. This task is of major importance, since both the $\mathrm{d}E/\mathrm{d}x$ resolution and momentum resolution crucially depend on the number of hits on track. Therefore not only the rejection based on the specific energy loss in the TPC but also the mass resolution of the spectrometer can be significantly affected.

- **To minimize number of ghost tracks**. Ghost track problem comes from the fact that the number of hits in the TPC exceeds the number of hits on tracks by a factor of

two. This observation was confirmed by detailed Monte-Carlo simulations including beam particles which do not make interactions in target and δ-electrons. The danger is that fake tracks may eat hits from the real tracks. In case of large number of ghost tracks they may decrease the rejection power of the TPC and contribute to the combinatorial background.

In order to cope with all the tasks mentioned above, the TPC tracking was divided into several stages. Every stage was carefully optimized using Monte-Carlo and the data to maximally improve the performance of the tracking algorithm. Newly developed CERES event display LIANA was actively used in a process of tracking optimization as well.

Track reconstruction is based on the track following algorithm. The track finding starts at the middle planes of the TPC where the hit density is at its lowest and then proceeds in the upstream and downstream directions using the predicted position of the next hit as a guide. The track finding process contains the following steps:

- Track root formation: The first step aims to find first 5 point-to-point connected hits.

  Track finding starts from candidate hit with a z-position in the middle of the TPC between 5th and 10th planes. The tracking then proceeds searching for the hits from the two downward and two upward planes. Five found hits are used to determine the sign of the track curvature in ϕ-direction. Since the analysis time is very crucial, a "corridor" in the three dimensional space is defined to limit the number of candidate hits. Due to the new feature of the tracking, namely the possibility of adding the neighboring arrays of hits in case the track leaves its initial "corridor", the dimensions of "corridor" are chosen to be rather small ($\Delta\phi = 20$ deg. and $\Delta\theta = 0.7$ deg.). Such narrow "corridor" significantly safes analysis time, since the majority of the tracks are straight enough and never cross the borders of the "corridor".

- Track formation: This step makes an attempt to associate more hits with the track root using simple algorithm.

  The search of further hits in the narrow windows in the ϕ direction is based on simple formula which predicts the deflection:

$$\phi_{i+1}^{guess} = \phi_i + \Delta_i \cdot (\phi_i - \phi_{i-1}), \tag{4.1}$$

  where ϕ_i is a coordinate of the hit at plane number i and Δ_i is a factor which defines a relative deflection of the track in ϕ direction for a given plane i. For a given plane the ϕ deflection factor is a constant for all momenta and is given by

$$\Delta_i = \frac{\phi_{i-1} - \phi_i}{\phi_i - \phi_{i+1}}. \tag{4.2}$$

  The deflection factors were obtained using Monte-Carlo simulations for all 20 planes including all 15 chambers except chamber 0. Chamber 0 includes several planes located in the middle of TPC which are placed at different z-positions. Therefore additional deflection factors were specially calculated for chamber 0.

A prediction of the hit coordinate in the θ direction is performed by linear extrapolation of the two previously found hits. It is given by

$$\theta_{i+1}^{guess} = \frac{\theta_{i-1}Z_i - \theta_i Z_{i-1}}{Z_i - Z_{i-1}} + \frac{\theta_i - \theta_{i-1}}{Z_i - Z_{i-1}} \cdot Z_{i+1}, \tag{4.3}$$

where Z_i and is θ_i are z- and θ-coordinates of previously found hit at plane i. Chamber 0 is, of course, treated separately according to its different z-positions of planes. A change of θ-coordinate is due to a second order field effect which is weak. Therefore the prediction based on the linear extrapolation is good enough. Then the tracking proceeds in upward and downward directions until it does not find the hit. If, at least one hit is not found in upward as well as in downward directions a hole appears in the continuous set of hits. Thus the prediction of the next hit using Eq. (4.3) can not be precise enough. The present tracking stage stops at this point and the tracking proceeds to the next phase. It is worth to note that windows for the next hit search were kept narrow at this stage of the tracking. Due to the fact that in the CERES TPC there are twice as many hits as can be matched with actual tracks, lose windows can lead to a fake track formation by picking background hits.

- Track extension: This step uses a second order polynomial fit to accumulate all hits possibly belonging to the track.

  To maximize the efficiency, all hits found so far are used as input for the polynomial fit with Tukey's weights. The fit gives more exact prediction of the ϕ position for the next hit and automatically removes hits which stay too far from the current trajectory of the track. The fit is performed again on the new bigger set of hits when the next hit is found.

- Track edge correction: This step provides fine tuning of the predictions for the edges of the tracks.

  To maximize the number of hits on tracks, the strong inhomogeneity of the B field and therefore the complicated track trajectory was taken into account. The second order polynomial fit does not give precise enough prediction of the ϕ position for the soft tracks in the last five planes in the TPC. Thus, the corrections are applied to improve the precision as a function of track curvature and z-position of the predicted point. The corrections reach its maximum for hits on soft tracks in the last plane. On the other hand, the hits belonging to high momentum tracks located in the 17th and 18th planes are almost not corrected. The corrections are based on the equation of plane

  $$a \cdot x + b \cdot y + c \cdot z = h \tag{4.4}$$

  in (x = ϕ^{corr}, y = $\Delta\phi$, z = Z) coordinate space, where $\Delta\phi$ is overall deflection of track in ϕ direction, Z is a z-coordinate of hit and ϕ^{corr} is a searched correction. The equation of plane is based on three experimentally defined points:

$$\begin{vmatrix} x & y & z & 1 \\ x_1 & y_1 & z_1 & 1 \\ x_2 & y_2 & z_2 & 1 \\ x_3 & y_3 & z_3 & 1 \end{vmatrix} = 0. \tag{4.5}$$

The a, b, c and h coefficients then are calculated as follows

$$\begin{aligned} a &= y_1 \cdot (z_2 - z_3) - y_2 \cdot (z_1 - z_3) + y_3 \cdot (z_1 - z_2); \\ b &= -(x_1 \cdot (z_2 - z_3) - x_2 \cdot (z_1 - z_3) + x_3 \cdot (z_1 - z_2)); \\ c &= x_1 \cdot (y_2 - y_3) - x_2 \cdot (y_1 - y_3) + x_3 \cdot (y_1 - y_2); \\ h &= x_1 \cdot (y_2 z_3 - y_3 z_2) - x_2 \cdot (y_1 z_3 - y_3 z_1) + x_3 \cdot (y_1 z_2 - y_2 z_1). \end{aligned} \tag{4.6}$$

Then the correction value ϕ^{corr} is given by

$$\phi^{corr} = \frac{1}{a}(h - b \cdot |\Delta\phi| - c \cdot Z) \cdot \frac{\Delta\phi}{|\Delta\phi|}, \tag{4.7}$$

where $\Delta\phi/|\Delta\phi|$ determines a sign of inclination of the track. Finally the prediction of the hit ϕ-coordinate ϕ_{i+1}^{guess} reads

$$\phi_{i+1}^{guess} = \phi_{i+1}^{fit} - \phi_{i+1}^{corr}. \tag{4.8}$$

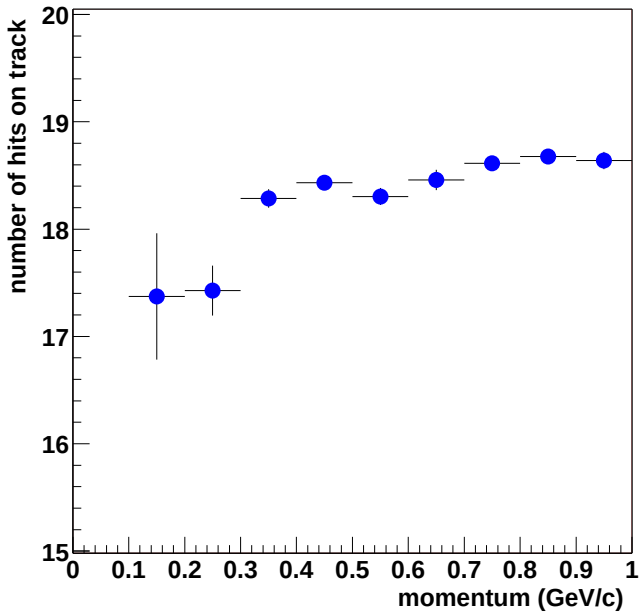

Figure 4.12: Most probable values for hits per track as a function of momentum for the experimental data. The points are the result of fitting slices of the two-dimensional distribution. For p $>$ 0.3 GeV/c the number of hits exceeds 18.

Fig. 4.12 shows most probable values for the number of hits on tracks as a function of momentum for the experimental data. The momentum scale is limited by 1 GeV/c to

illustrate the power of the tracking in the soft momentum region. The points are obtained from the fits of slices of the corresponding two-dimensional distribution. The tracks have more than 18 hits down to momentum of 300 MeV/c as illustrated in Fig. 4.12.

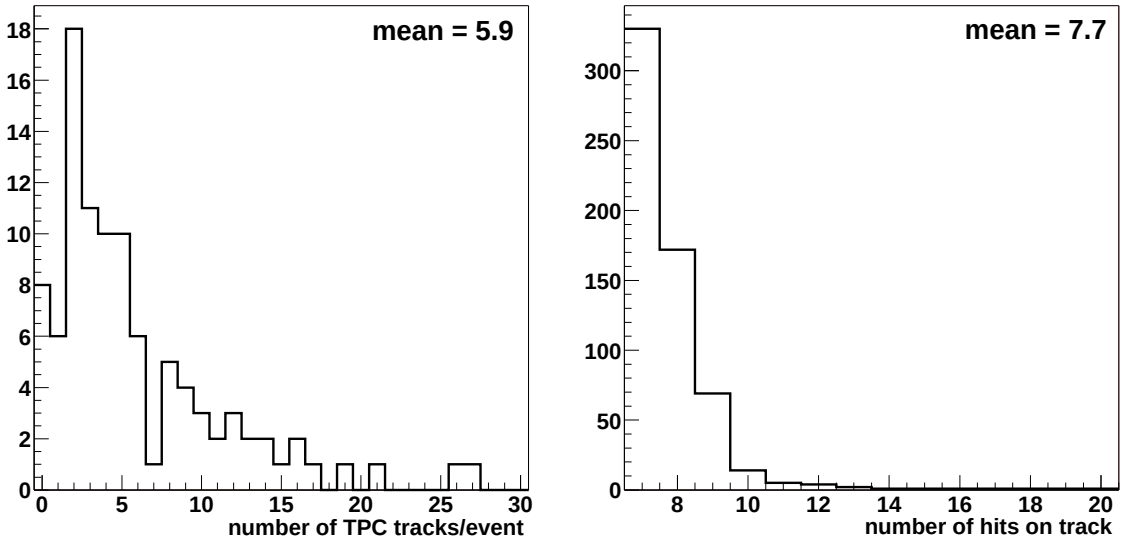

Figure 4.13: Number of ghost tracks per event (left panel) and number of hits per ghost track (right panel). To estimate the amount of fake tracks all 20 TPC planes were independently rotated in order to destroy the correlations between hits.

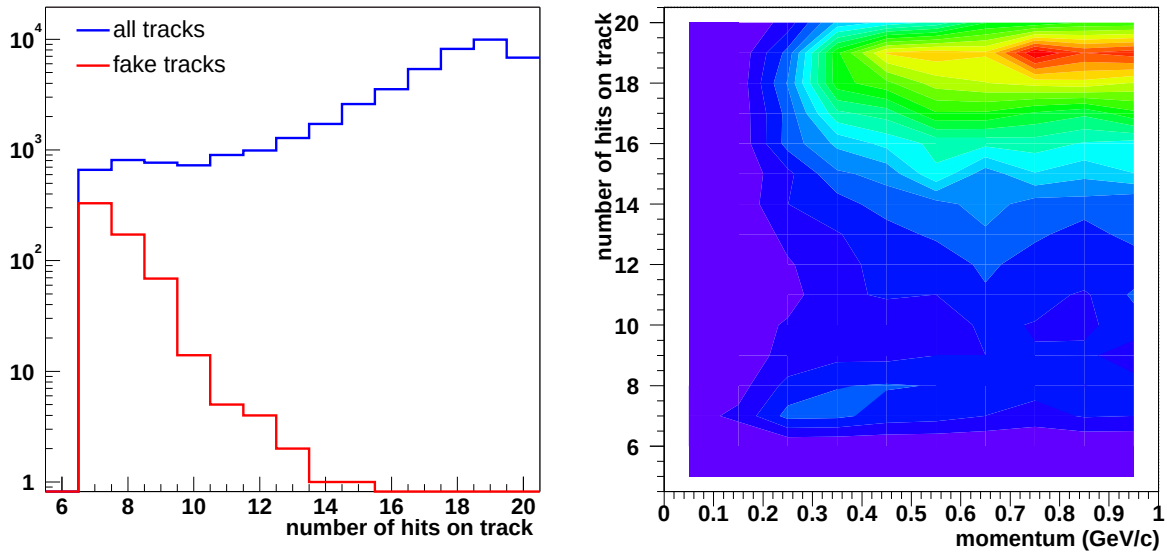

Figure 4.14: Comparison between two distributions on number of hits per track for real tracks and ghost tracks (left panel), and number of hits on track as a function of momentum (right panel). The ghost tracks with low number of hits populate the momentum region about 0.3 GeV/c

The ghost track issue was addressed by breaking all correlations between the hits. Each of 20 planes in the TPC was randomly rotated in the ϕ-direction. The obtained set

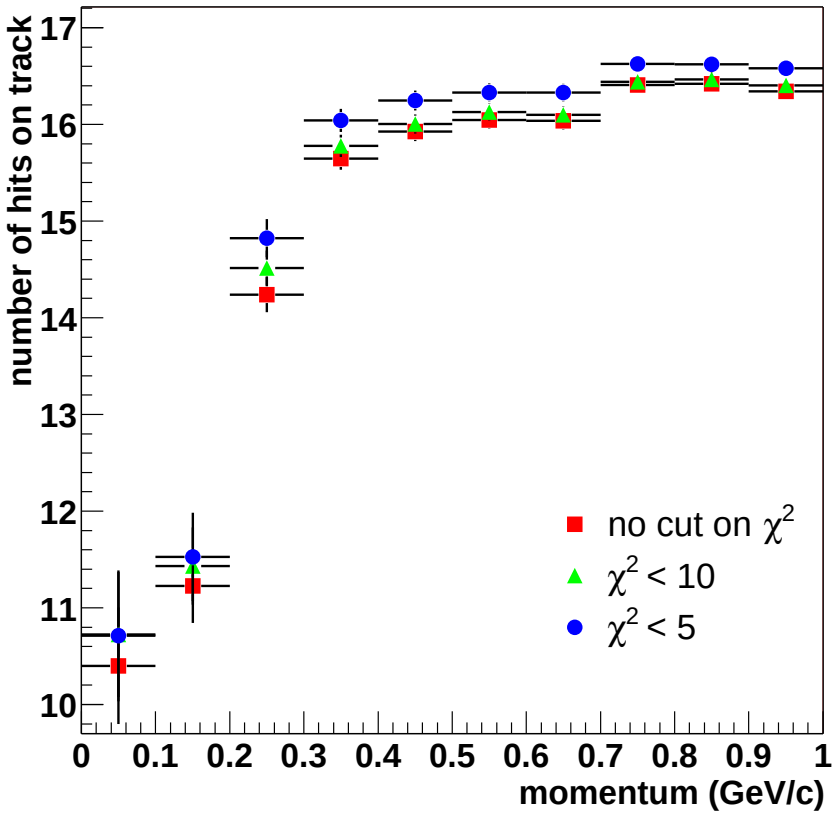

Figure 4.15: Average number of hits on track as a function of momentum for different χ^2 cuts. Stronger cut removes larger amount of fake tracks which leads to the increase of a number of hits.

of uncorrelated hits was further analyzed by the track reconstruction software. In total 100 events were analyzed. Fig. 4.13 represents the amount of fake tracks produced by the tracking per event and the number of hits on the ghost tracks. In average 6 fake tracks with a low number of hits per event correspond to ≈1.5% of total amount of tracks in a normal event. The distribution of the number of hits on track in real events is compared in Fig. 4.14 to the hits on ghost tracks obtained as described above.

The fake tracks contribute to the low tail of the distribution artificially decreasing the average number of hits on tracks. The number of hits per track plotted as a function of momentum is also shown in Fig. 4.14. The tracks with low amount of hits occupy the soft momentum region proving their ghost nature, since kinky fake tracks produced by the tracking are automatically getting soft momenta during the track fitting procedure. The short fake tracks are built from a random combination of hits and therefore must have a bad χ^2 of the fit. Thus the average number of hits on tracks should increase once the cut on χ^2 of the fit is applied. The difference in the hit distributions can reach a value of 1 hit for $\chi^2 < 10$ with respect to no cut applied as shown in Fig. 4.15.

In summary, the ghost tracks are mostly very short and of poor quality. Thus, the track quality cuts as well as the matching to other detectors will reduce the amount of fake track to a negligible number.

The efficiency of the TPC tracking algorithm was studied using overlay MC technique allowing to reproduce high occupancy in the data by overlaying the simulated MC track on top of the real event. MC input consists of one electron track per event generated within θ-acceptance of the TPC. Fig. 4.16 shows a dependence of the single track reconstruction efficiency in the TPC on ϕ and θ coordinates. The track efficiency dependence on ϕ exhibits a hole at approximately -3 rad., which corresponds to a known dead region. The dependence of the efficiency on θ is rather flat within θ acceptance cut $0.141 < \theta < 0.244$ with exception of the outer edge where the tracks approach the full track acceptance limit of the TPC. In average the single track efficiency within the full track acceptance is about 90%.

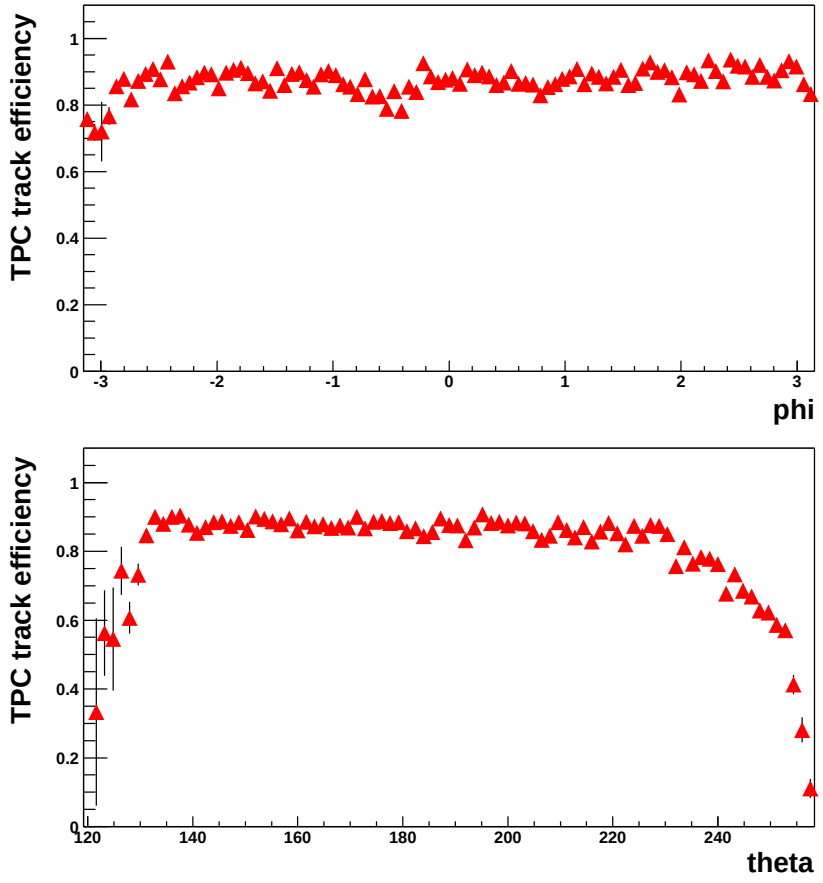

Figure 4.16: TPC track reconstruction efficiency as a function of ϕ (top panel) and θ (bottom panel).

4.5.3 TPC Track Fitting

The prime task of the track fitting is the precise estimation of the kinematical parameters of a particle from the measured trajectory. The inhomogeneous magnetic field makes it impossible to analytically describe the trajectory of a track in the TPC. Thus, a collection of reference tracks generated with the magnetic field map are used for the momentum calculation. Several reference tables for different values of inverse momentum containing the hit coordinates of reference particles for different θ angles have been produced using the GEANT simulation package.

The track fitting algorithm consists of two steps: a straight line radial fit in r-z plane, since to zero order there is no deflection in the polar angle θ of a track, and a fit of the momentum dependent azimuthal deflection. The quality of the fit is iteratively improved by applying the inverse momentum and the theta dependent second order corrections.

The next step is the refitting procedure which assigns a weight to each hit on track. The weights are inversely proportional to the accuracy of the hit reconstruction, measured by the average residuals determined in previous fits. The fitting procedure invokes the robust fit with Tukey's weights which is much faster than the MINUIT fitting routines. The algorithm deals with two different functions with 2 and 3 parameters. The two parameter fit provides the radial offset and the inverse momentum. Additional third parameter in the three parameter fit absorbs effects of the multiple scattering.

Most of soft particles scatter in the massive mirror of the RICH2 detector with a thickness of 4.7% of a radiation length. Thus, the resulting momentum measurement is a combination of the two and three parameter azimuthal fits. The two parameter fit alone assumes that the particle comes straight from the primary vertex without changing trajectory due to multiple scattering. Therefore the two parameter fit provides better results at high momenta, while the three parameter fit is better at low momenta.

For the same reason of multiple scattering the extrapolation of the fit results to the RICH2 mirror is performed, taking into account the curvature of the spherical mirror. The calculated intersection point between RICH2 mirror and the fitted track trajectory gives the undistorted θ- and ϕ-coordinates of the TPC track.

The resultant parameters of the TPC track provided by track fitting are θ- and ϕ-coordinates, and absolute value of the momentum.

4.5.4 Momentum Resolution

The di-electron mass resolution is dominated by momentum resolution. The goal of the addition of a radial TPC with magnetic field is to achieve a momentum resolution which allows the experiment to be sensitive to the vector meson resonances.

The momentum resolution is determined by the detector position resolution at high momenta, multiple scattering in the detector material at low momenta and the number of hits on the track. To estimate the momentum resolution a full tracking simulation is performed. In the GEANT simulation package the points on the deflected particle are smeared according to the multiple scattering inside the gas volume. The original width of the ionized trail and the transverse diffusion σ_t contribute to the width σ of the electron cloud at the read-out chamber. A number of primary electrons, determined by the gas

mixture, together with the electron cloud width define, in first approximation, the position resolution. Additional effect on the position resolution is given by occupancy.

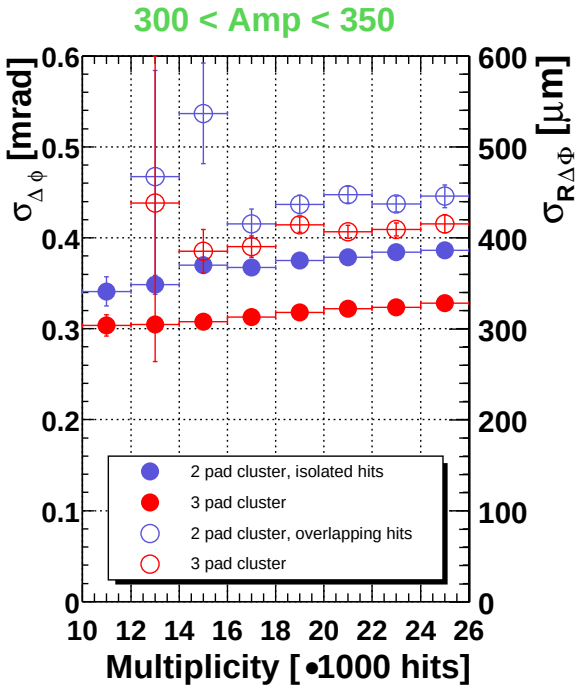

Figure 4.17: The hit resolution in azimuthal direction as a function of multiplicity for different cluster topologies.

New hit-finding and track-finding algorithms are able to efficiently reconstruct tracks down to a momentum of 300 MeV/c. Tracks with momentum greater than 1 GeV/c have in average 18 hits with the most probable value of 19 hits per track. Below 1 GeV/c the number of hits on track decreases down to 17.

The single-hit position resolution is obtained comparing the reconstructed hit position with the ideal hit positions given by the fitted trajectory of the track. The width of the residual distribution gives the spatial resolution. The resolution in azimuthal direction scaled with the radius r of the hit ($\sigma_{r\delta\phi}$) is shown in Fig. 4.17.

In order to cope with the non-perfect knowledge of the drift properties inside the TPC which causes systematic distortions of the reconstructed hit positions, additional smearing of the points on track according to the measured hit residual distributions (Fig. 4.17) is applied in the Monte-Carlo. The result for the momentum resolution evaluated using a microscopic drift Monte Carlo simulation with single point resolution as observed in the data, is shown in Fig. 4.18. The momentum resolution is defined as the standard deviation of the distribution of differences between the original momentum and the reconstructed momentum.

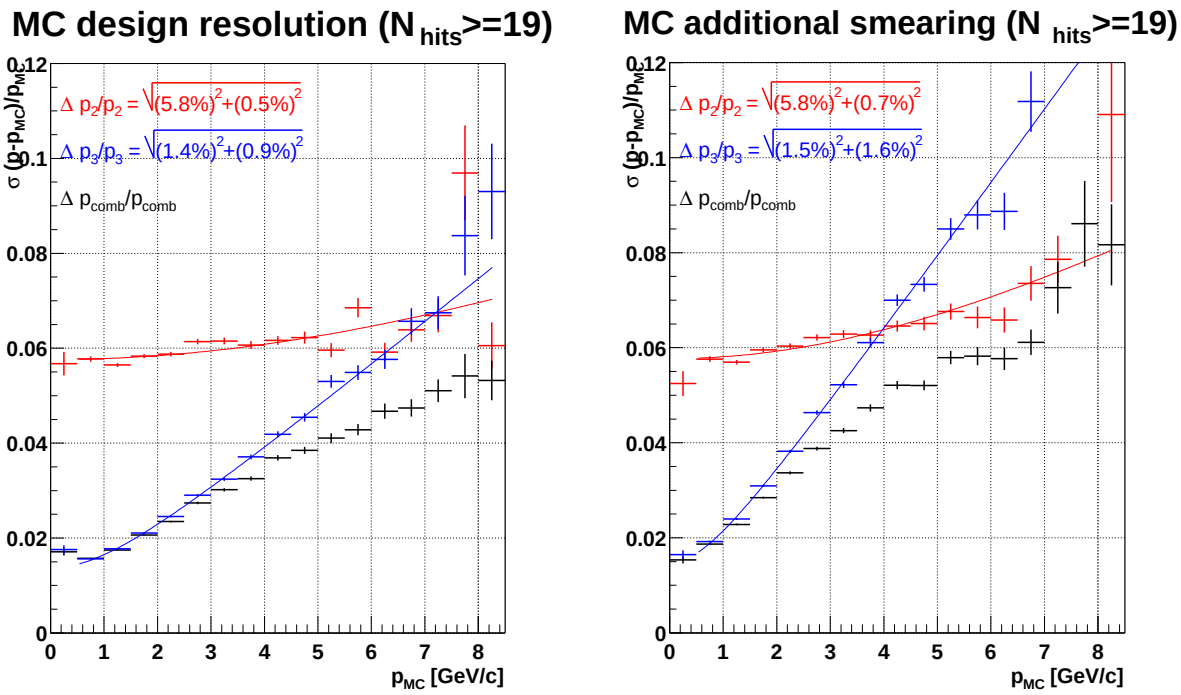

Figure 4.18: Momentum resolution as a function of momentum without smearing (left panel) and with smearing of hit positions (right panel). The two parameter fit (red line) provides better results at high momenta, while the three parameter fit (blue line) improves momentum resolution at low momenta. The combination of the two fits leads to a better momentum resolution over the whole momentum range.

The relative momentum resolution for the combination of the two parameter and three parameter fits plotted as a function of momentum in units of GeV/c can be parameterized as

$$\frac{\sigma_p}{p} = \sqrt{(2\%)^2 + (1\% \cdot p(GeV/c))^2} \tag{4.9}$$

The observed momentum resolution is worse than the designed resolution. All the remaining inconsistencies in the magnetic and electric fields, gas properties, geometry of the TPC, occupancy, and the Lorentz-angle sum up and produce such a discrepancy in the resolution.

The mass resolution derived from the momentum resolution including effects of the bremsstrahlung is about 3.8% at the ϕ meson mass reconstructed in the e^+e^- channel.

The radial TPC provides a possibility to look into hadron decay channels and, thus, to crosscheck the results of the TPC Monte Carlo simulation by comparing the reconstructed invariant masses of the particle in the data and in the simulation. The neutral Λ-hyperon in the pπ decay mode with a branching ratio of about 64% as well as K^0_s meson in the $\pi^+\pi^-$ decay mode were investigated. The reconstructed invariant mass spectra of both the Λ-hyperon and K^0_s meson [89] are shown in Fig. 4.19.

The detailed calibration improves the mass resolution by approximately a factor of 2 compared to the old calibration [90]. The K^0_s has been carefully studied to crosscheck the

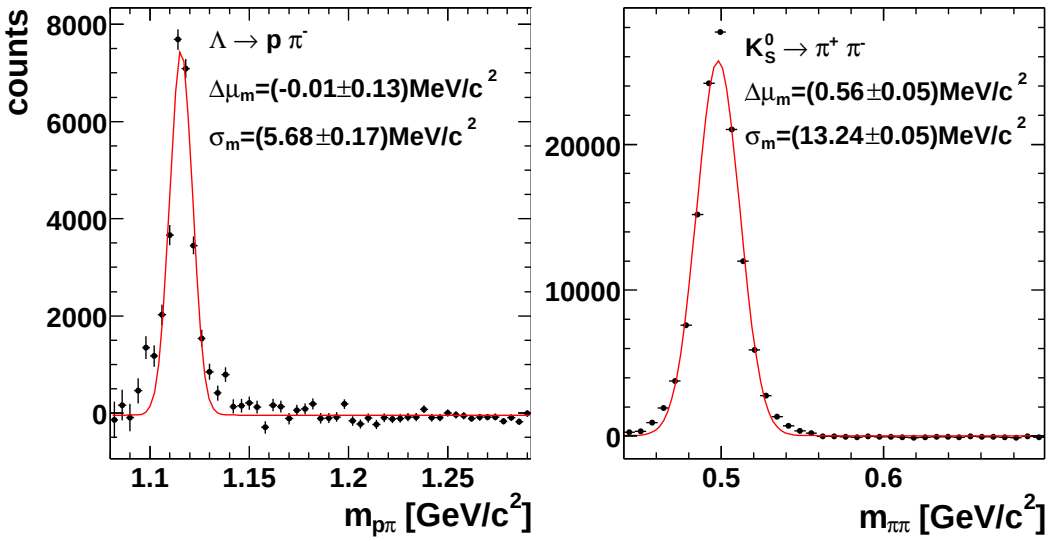

Figure 4.19: Invariant mass spectra of $p\pi^-$ (left panel) and $\pi^+\pi^-$ (right panel) pairs after background subtraction. The peaks of Λ and K^0_s are fitted with a Gaussian function.

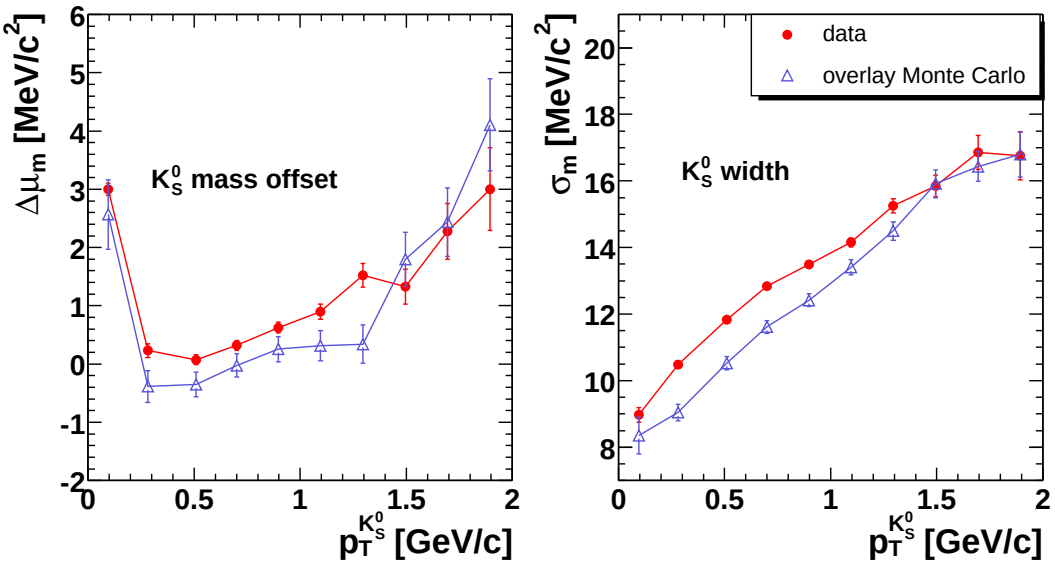

Figure 4.20: K^0_s mass shift (left panel) and width (right panel) as a function of transverse momentum for data (red) and MC (blue).

improvements of the calibration and to confirm the understanding of the Monte-Carlo. Fig. 4.20 shows the K^0_s width and a shift of the K^0_s mass as a function of transverse momentum for both the data and the MC simulations [89]. A reasonable agreement was observed between the data and the MC for the K^0_s mass shift and width for the whole range of transverse momentum.

4.5.5 Specific Energy Loss

The energy loss of charged particles traversing a medium is given by Bethe-Bloch equation. The truncated mean energy loss, measured in the CERES TPC, for different species of particles is shown in Figure 4.21. The number of samples is 20 with each sample corresponding to a path-length of $\sim$ 2.4 cm. The energy loss measured in each sample has a considerable fluctuation according to Landau distribution. There is a long tail to the distribution and 35% highest charge samples is rejected when determining the mean energy loss per track. The difference in the energy loss at a given momentum by various particles can be used to distinguish between them. Since

$$p = m\beta\gamma \text{ and } \frac{dE}{dx} \sim \frac{1}{\beta^2} ln(\beta^2\gamma^2) \tag{4.10}$$

a simultaneous measurement of p and dE/dx will yield the mass of the particle. The average energy loss for an electron, pion, kaon, proton and deuteron in 80%/20% Ne/CO_2 gas mixture is shown in Figure 4.21. Fig. 4.22 shows projections of the correlated plot [2]

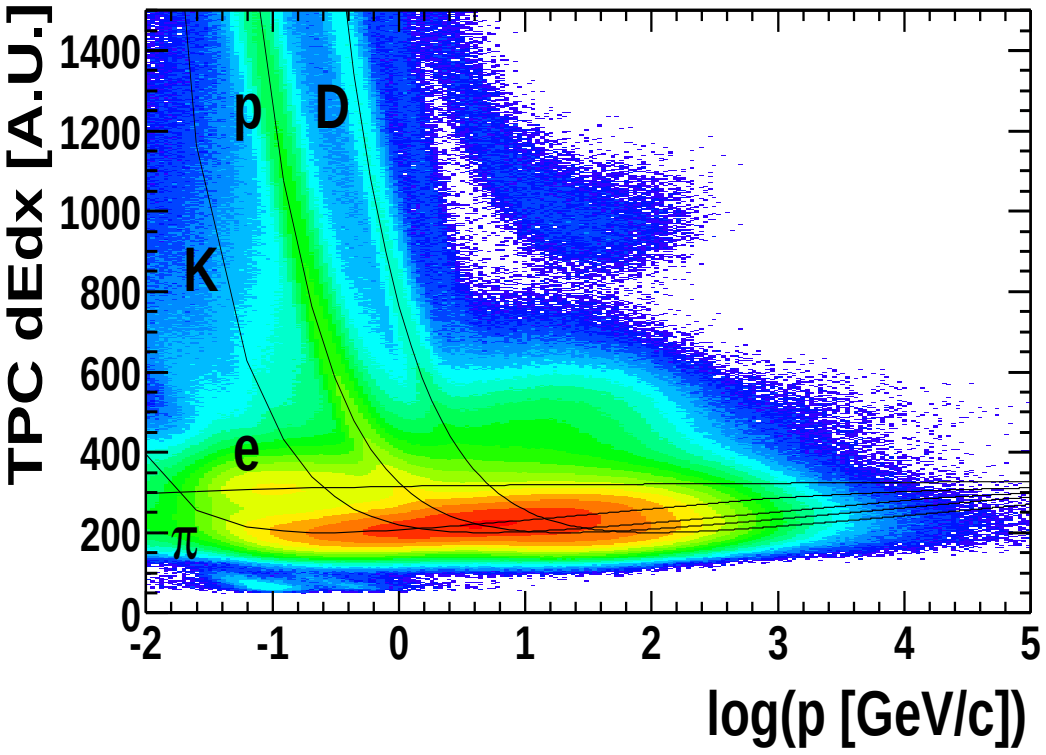

Figure 4.21: The truncated mean energy loss as a function of momentum for different species of particles.

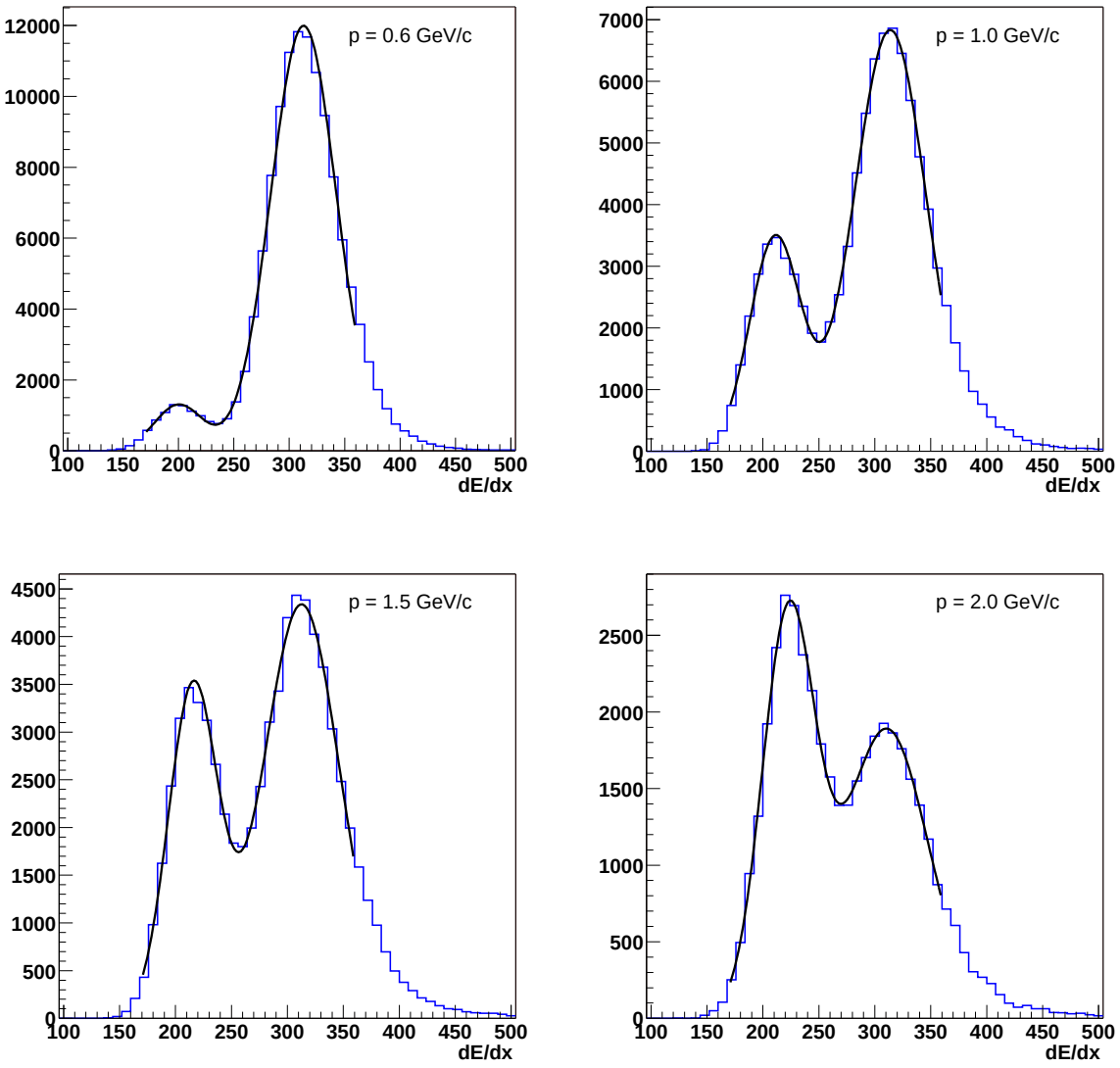

Figure 4.22: Projections of two-dimensional plot for four momentum intervals with mean values of 0.6 GeV/c, 1.0 GeV/c, 1.5 GeV/c, 2.0 GeV/c. The pion and electron peaks are well described by the double Gaussian fit.

for four different momentum slices. The left peak corresponds to a pion contribution and right peak represents an energy loss by electrons. A double Gaussian fit shows a good description of the $\mathrm{d}E/\mathrm{d}x$ distributions. While the mean $\mathrm{d}E/\mathrm{d}x$ of the electrons almost does not change, the energy loss of pions increases logarithmically at relativistic velocities. The electrons mostly populate a region around 1 GeV/c momentum (because majority of electrons in the sample originates from γ-conversions and π^0-Dalitz decays), whereas a relative amount of pions grows with momentum. Thus already at 1.5 GeV/c momentum there is a significant overlap of pion and electron peaks giving a pion admixture to the

[2]Note, that additional pre-selection based on RICH was applied to enhance a fraction of electrons in a sample. Therefore the electron peak is well pronounced.

electrons. The non-Gaussian tails are understood with Monte-Carlo simulations.

The particle-identification capability and the rejection power depend on the dE/dx resolution. Truncated mean dE/dx resolution depends on the number and size of samples, and gas pressure:

$$\sigma_{dE/dx} \propto N^{-0.46} \times (Pl)^{-0.32} \tag{4.11}$$

After pad-to-pad calibration based on total amplitude in the pad of maximum amplitude, correction of undershoot after each pulse [74] and attachment correction taking into account different particle composition at different θ the dE/dx resolution was significantly improved. A comparison between the calibrated truncated mean dE/dx resolution and the Allison/Cobb parameterization as a function of number of hits on track for electrons is shown in Figure 4.23.

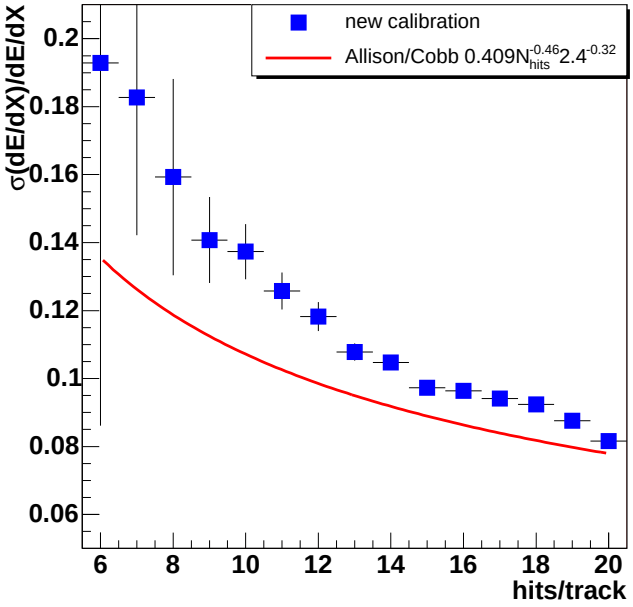

Figure 4.23: Truncated mean dE/dx resolution as a function of number of hits on track is compared with the parameterization by Allison and Cobb. For the number of hits above 15 dE/dx resolution is better than 10%.

For the maximum number of hits the dE/dx resolution approaches the parameterization by Allison and Cobb [91]. As the number of hits on track is peaked at 18, most of the electrons in this analysis are measured with dE/dx resolution of better than 10%.

4.6 Reduction of Combinatorial Background

Disentangling the signal of interest from the more conventional sources is one of the major experimental challenges. Only one event out of about 7600 recorded central Pb-Au events contains an interesting e^+e^- pair.

4.6.1 Sources of Combinatorial Background

In the absence of new physics the dielectron yield in nuclear collision is expected to originate from the decays of the known hadronic sources. In the invariant mass region covered by the CERES experiment the main contributions to the e^+e^- yield are given by leptonic and semi-leptonic decays of the π^0, η, η, ρ, ω and ϕ neutral mesons. The Dalitz decays mostly populate the low mass region (m $<$ 0.2 GeV/c^2) of the invariant mass spectrum while the vector meson resonances occupy the high masses.

Di-leptons radiated during the hot and dense phase of the collision are expected to occur in the high mass region. Thus of interest are the e^+e^- pairs with masses above 200 MeV/c^2. However in the presence of many hadrons an extremely weak source of dielectrons should be detected. The ratio of the e^+e^- pairs to the number of charged particles N$_{ee}$/N$_{ch}$ is of the order of 10^{-5}. In the low mass dilepton experiments the π^0 meson decays significantly contribute to the combinatorial background in different ways. The three body Dalitz decay is an asymmetric decay with soft momentum spectrum. When a track with softest momentum is lost due to the low reconstruction efficiency, the remaining partner is randomly combined with another electron track of opposite charge in the current event. The π^0 Dalitz decay is the main source of the combinatorial background due to its highest yield among all Dalitz decays as well as softest momentum spectrum and closest opening angle distribution. These all make it extremely difficult to reconstruct π^0 Dalitz decays.

The π^0 meson decaying in the $\gamma\gamma$ channel is also the main source of photons. Although the amount of material in the experimental set-up was minimized decreasing the radiation length within spectrometer acceptance down to 1% (5.5% including RICH2 mirror), the γ-conversions still exceed high mass pairs by three orders of magnitude. The photons convert into electron-positron pairs mostly in target, silicon drift chambers and RICH2 mirror. In a similar way to the π^0 Dalitz decay the unreconstructed e^+e- pair originating from the γ-conversion contributes to the combinatorial background with one found track. However the signature of photon conversions is very specific due its extremely small opening angle which makes them easier to detect with respect to other background sources.

Another experimental problem lies in the limited particle identification capabilities and reconstruction algorithms. The particle identification provided by the specific energy loss distribution in the TPC crucially depends on the dE/dx resolution. As shown in section 4.5.5, electron and pion clouds overlap leading to misidentification of some pions as electrons. The RICH detectors identify electrons and suppress hadrons with exception of the high momentum pions. In the presence of huge occupancy the RICH reconstruction software produces few rings originating from pions or pure fakes. Although an effect of these experimental problems seems to be small, on a scale of dielectron signal it can make significant impact on the combinatorial background.

4.6.2 Rejection Strategy

Once the reconstruction of hits, rings and tracks in all detectors is complete and all separate segments are matched into global electron tracks, the final electron analysis is per-

formed. For details on matching see section 3.5.

Due to very central interaction trigger and therefore large multiplicities and occupancies leading to a huge level of the background the rejection steps were carefully selected and tuned.

The main quality criteria and rejection steps on a single track level are listed below. The cuts are numbered in accordance with Fig. 4.24 illustrating the Dalitz and open pair yields after background subtraction as well as the background yields as a function of cut number.

1.
   - All global tracks which include a SDD segment with one hit missing either in SDD1 or SDD2 are removed. This requirement is necessary, since SDD dE/dx cut works efficiently only in a correlated mode when applied on the energy loss information in both silicon drift chambers simultaneously.
   - Rejection of target photon conversions by applying simultaneous cut on double dE/dx signal in the two silicon drift chambers. The hits on the SDD track are additionally required to be multi-anode hits. This cut copes with a clean close conversion signature not affected by artificial hit splitting.

2.
   - Theta dependent cut on Hough amplitude of the ring of > 180 suppresses fakes. In addition the number of hits on ring is required to be greater than 4 in every RICH detector.
   - Number of hits on rings in both RICH detectors must be above 4.
   - Energy loss in the TPC should be higher than the average dE/dx of the electrons minus twice dE/dx resolution.

3. Single track momentum cut of < 9 GeV/c removes remaining high momentum pions.

4. Correlated cut on TPC dE/dx and RICH Hough amplitude. TPC dE/dx cut is applied as a function of momentum which prevents a loss of electrons at low momenta.

5. Two-dimensional cuts on the double dE/dx signal in silicon drift detectors as a function of the hit topology in the SDD detectors.

6. Cut on a distance to a closest electron TPC segment rejects conversions in RICH2 mirror, in SDD detectors as well as survived SDD dE/dx cuts target conversions.

7.
   - Two-dimensional cuts on the recalculated dE/dx signal by summing the amplitude of the hits in a certain window in silicon drift detectors for different SDD hit topologies.
   - Reject low tail in SDD1 dE/dx distribution corresponding to the photon conversions in the first silicon drift detector.

8. Theta dependent cut of the number of hits on the TPC track.

9. Apply TPC dE/dx cut as a function of momentum to suppress pion tracks (dE/dx > 260+10·log(p)). This cut is applied in combination with a 2D-cut on dE/dx versus Hough amplitude to keep high efficiency for high-mass electron pairs.

10. Cut on the opening angle between global tracks of > 35 mrad. The purpose of this isolation cut is to remove close well identified oppositely charged electron tracks which most likely originate from π^0-Dalitz decays.

11. Cut on the TPC dE/dx versus number of hits on RICH rings rejects remaining pions.

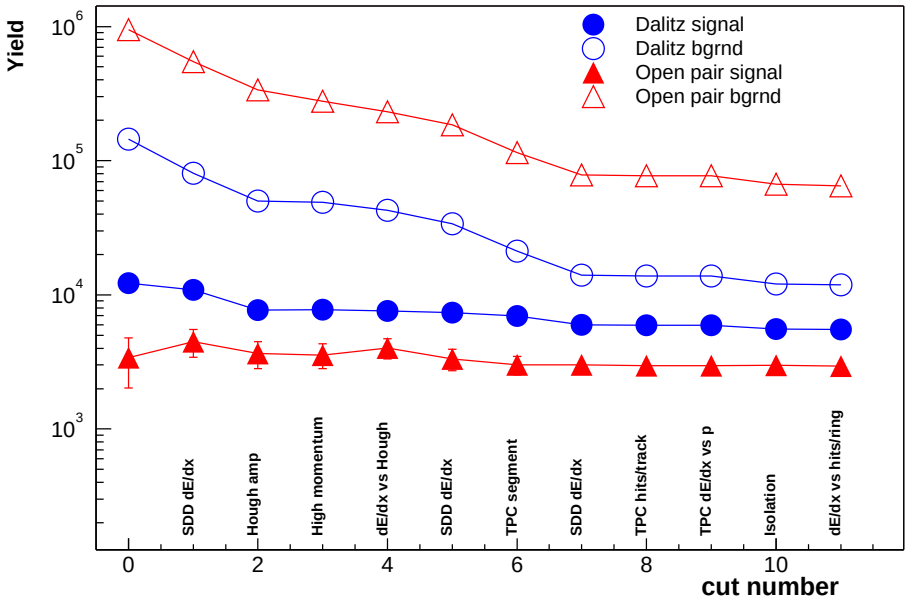

Figure 4.24: Yields of signal and background for Dalitz decays and open pairs versus cuts.

The pairing procedure is performed after all single track cuts are applied. All electrons and positrons are combined into unlike-sign pairs (N_{+-}^{tot}). Although the background is significantly suppressed (approximately 13 times for Dalitz decays and 15 times for open pairs) there are still many random combinations of electron and positron tracks originating from unreconstructed Dalitz decays and survived photon conversions. In order to extract a signal of interest the statistical approach is used. Like-sign pairs (N_{++}^{comb}, N_{--}^{comb}) are constructed from positron-positron and electron-electron combinations. The weak four body decay of $\pi^0 \rightarrow e^+e^+e^-e^-$ can be neglected which allows to use the uncorrelated unlike-sign pairs coming from different decays for the combinatorial background. Thus the total number of the unlike-sign pairs is a sum of the correlated signal (S_{+-}) and uncorrelated random combinations (N_{+-}^{comb}), which can be described by a twice the geometrical mean of the like-sign pairs of positive and negative signs:

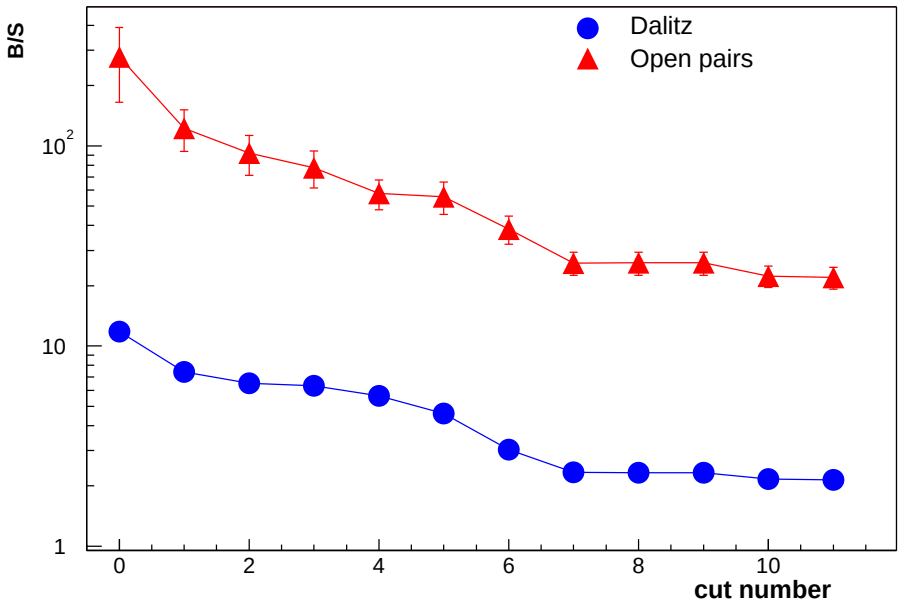

Figure 4.25: Background-to-signal ratio for Dalitz decays and open pairs as a function of cut number.

$$N_{+-}^{tot} = S_{+-} + N_{+-}^{comb} = S_{+-} + 2\sqrt{N_{++}^{comb}, N_{--}^{comb}}. \tag{4.12}$$

Another method which allows to improve statistical errors is the event mixing technique. It will be discussed in in section 4.7.2.

Before the mass spectra are filled there is a number of cuts applied on a pair level. Any pair with opening angle below 50 mrad and mass < 200 MeV/c^2 is recognized as Dalitz decay and excluded from further pairing. All survived pairs then should pass through the single track transverse momentum cut of $p_t > 200$ MeV/c applied for both pair legs. Finally the pairs must fulfill the standard cut on opening angle of > 35 mrad and lie within CERES theta acceptance $0.141 < \theta < 0.244$ rad.

The invariant mass of the pair is given as the sum of the electron 4-momenta:

$$m_{ee} = \sqrt{\mathbf{p}_{\mathbf{e}^+} + \mathbf{p}_{\mathbf{e}^-}}. \tag{4.13}$$

All plotted in Fig. 4.24 numbers are obtained for the electron pairs fulfilling the single track p_t cut of > 200 MeV/c, opening angle cut of > 35 mrad and spectrometer acceptance cut. The real challenge is to reject the background as much as possible and at the same time to keep high pair reconstruction efficiency. Although several rejection steps, namely Hough amplitude cut of > 150, were applied at pre-analysis stage, the level of the open Dalitz as well as open pair backgrounds is huge (cut 0). The first major improvement on the background rejection (Fig. 4.25) is achieved by cutting the correlated double dE/dx signal in the SDD detectors and the ring Hough amplitude. The high momentum cut of

$<$ 9 GeV/c suppressing pions gives further improvement of the signal to background ratio. The two groups of the hit topology dependent cuts on SDD dE/dx with and without resummation of the pulse heights with a help of the TPC close partner cut bring additional gain in rejection by a factor of 3 for both open pairs and Dalitz decays. Although the power of the cut on distance to the closest partner in the TPC is masked by the previous rejection steps it still contributes to the background suppression by correlating the information of the momentum, the specific energy loss and the opening angle to prevent a loss of the efficiency. Once the signal to background ratio reaches the reasonable level the isolation cut on the opening angle between electron and positron is applied. This cut is in fact a pair cut which removes close pairs originating mostly from Dalitz decays. Another cut applied on pair level is the so-called Dalitz removal. It identifies Dalitz pairs by close opening angle of $<$ 50 mrad, opposite charge and invariant mass of $<$ 200 MeV/c^2. However the Dalitz removal has almost no effect because of the previously applied isolation cut which does the job.

4.6.3 Rejection with dE/dx in SDD

The doublet of SDD detectors besides the vertex reconstruction provides a powerful tool to identify and reject γ-conversions and close π^0-Dalitz decays. Any close pair with opening angle smaller than two-hit resolution of silicon drift detectors and not affected by the hit splitting algorithm leaves the double dE/dx signal. Fig. 4.26 shows the correlation of the energy loss in two silicon drift detectors in case both SDD hits are multi-anode. The dE/dx cut is represented as a product of two Landau functions.

The projections of the similar plot with enhanced amount of electrons (coming mostly from γ-conversions and close π^0-Dalitz decays) by requiring additional PID cut on dE/dx in the TPC show two peaks exhibiting the dE/dx information in SDD1 and SDD2 separately (Fig. 4.27).

The left peak corresponds to the energy loss by single particle while the right peak represents the double dE/dx of close unresolved tracks. However the rejection based on one-dimensional dE/dx distribution would cut the long Landau tail and thus destroy efficiency. The correlated cut on dE/dx shown by a red line is a product of the two Landau distributions. The cut almost does not cost efficiency but significantly rejects background.

The two-hit resolution for silicon drift detectors is of the order of 10 mrad for SDD1 and 6 mrad for SDD2 which prevents the rejection of close pairs with single dE/dx signal by applying a cut on an opening angle. The limited by the pattern recognition algorithm two-ring resolution in the RICH detectors is above 10 mrad. Thus the hole in the rejection occurs for the semi-close pairs with opening angles between 4 and 10 mrad. Unfortunately the TPC with much better two-track resolution (especially for soft tracks) can not cover the gap because of limited reconstruction efficiency for low momenta. Therefore the summing of the amplitudes of the hit on SDD track and next closest hit for the two silicon drift detectors separately is performed. However the occupancy for the central Pb-Au events of the 2000 data is higher than in previous runs. Thus the resummation procedure is of danger due to the possible pick up of hits belonging to hadron tracks. The probability to find a SDD hit was studied by calculating the distance between random point and the closest hit in both silicon drift detectors (Fig. 4.28).

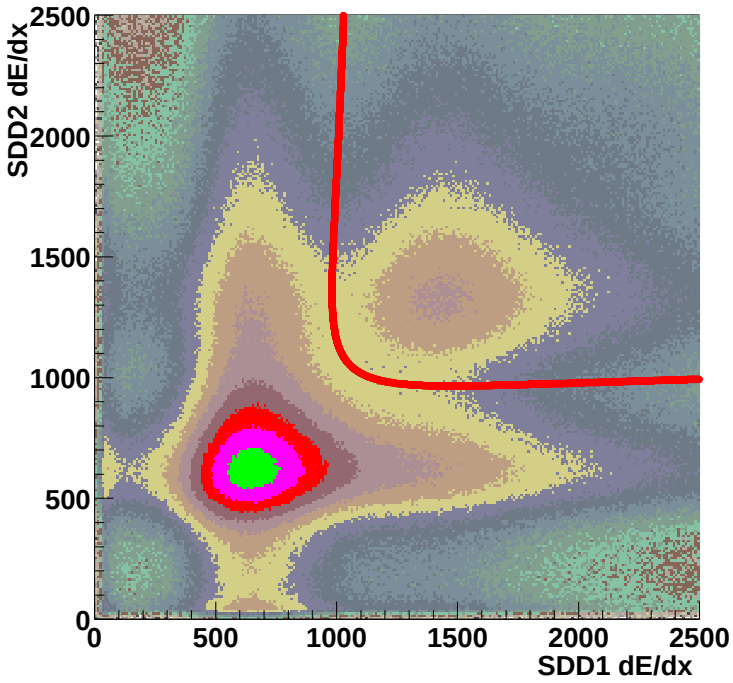

Figure 4.26: Correlated energy loss distribution in SDD1 and SDD2. The red line based on the product of two Landau functions represents the cut. Both hits in SDD1 and SDD2 are multi-anode; no resummation is applied.

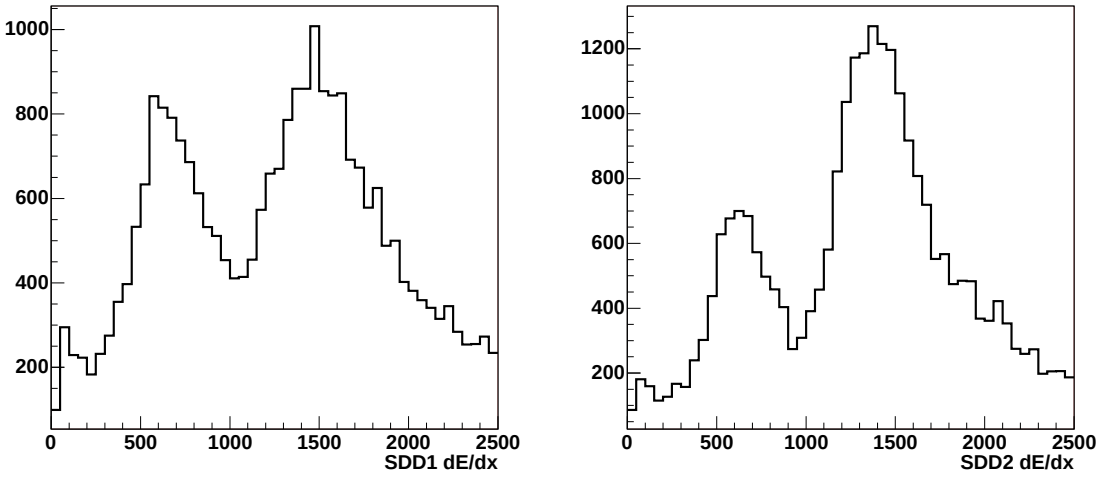

Figure 4.27: The projection of the two-dimensional distribution in SDD1 (left panel) and SDD2 (right panel). To enhance the amount of γ-conversions the matching between two electron TPC tracks with opposite charge and SDD track is required.

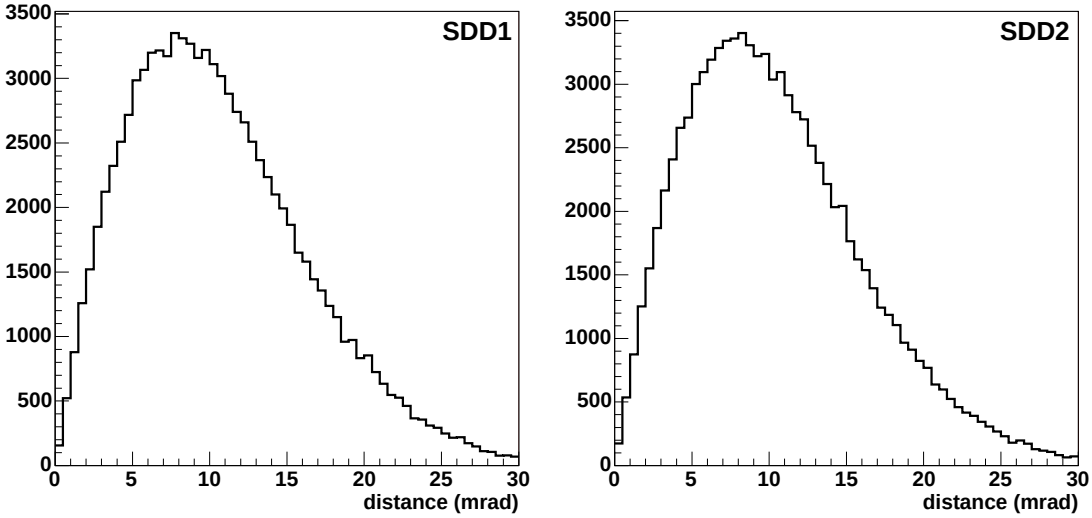

Figure 4.28: Distance from random point to closest hit in SDD1 (left panel) and SDD2 (right panel).

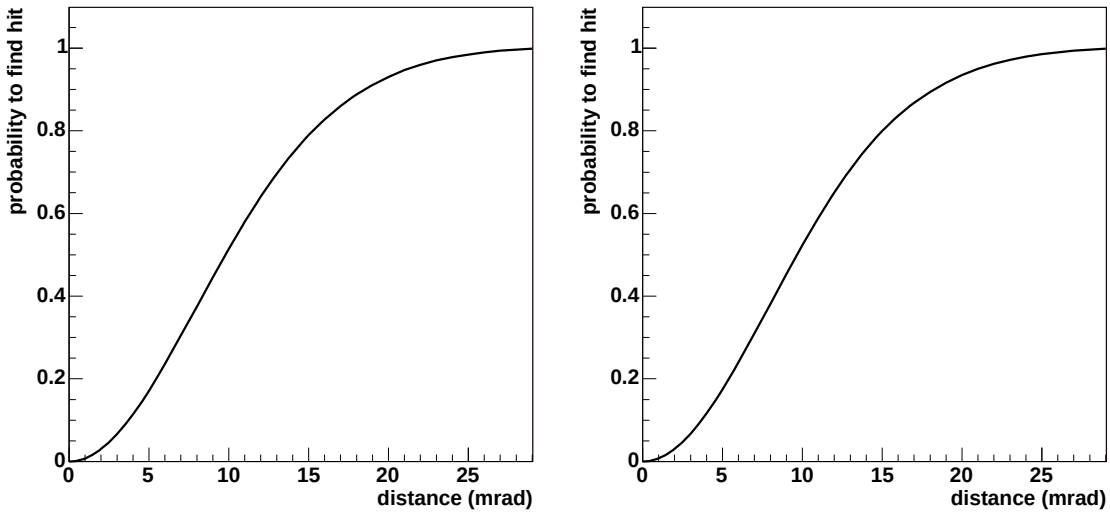

Figure 4.29: Probability to pick up hit in SDD1 (left panel) and SDD2 (right panel).

The probability functions obtained from the distance distributions are shown in - Fig. 4.29. The probability to pick up a hadron hit exceeds 20% at a distance of 6 mrad. As a consequence, the straight forward cut on the resummed dE/dx in 10 mrad window used in 1999 analysis can not be applied for the 2000 data. In order to achieve most efficient rejection the resummation procedure was studied for different hit topologies. The results are shown in Table 4.1.

The deviation of the experimental energy loss distribution from the Landau fit at small dE/dx is an indication of the photon conversions in silicon drift detectors. Thus all tracks with a signature of low dE/dx tail in SDD1 and double dE/dx in SDD2 are recognized as conversions in a material of the first silicon drift detector and get rejected. This cut is

Cut #	1	2	3	4	5
SDD1 hit topology	single	single	single	single	multi
SDD2 hit topology	multi	multi	multi	multi	single
SDD1 next closest hit	single	single	multi	multi	single
SDD2 next closest hit	single	multi	single	multi	single
SDD1 resum window (mard)	9	6	9	6	7
SDD2 resum window (mrad)	9	9	8	8	5
Cut #	6	7	8	9	10
SDD1 hit topology	multi	multi	multi	single	all
SDD2 hit topology	single	single	single	single	all
SDD1 next closest hit	single	multi	multi	all	all
SDD2 next closest hit	multi	single	multi	all	all
SDD1 resum window (mard)	7	-	-	6	5
SDD2 resum window (mrad)	7	5	7	6	5

Table 4.1: Dependence of the resummation window on a topology of the closest and next closest hits to the silicon segment in SDD1 and SDD2.

placed at the end of the rejection based on SDD dE/dx information. Therefore it is not affected by the artificial hit splitting which is taken care of by previous cuts.

4.6.4 Rejection with RICH

During the pre-TPC era the two RICH detectors were used as a main rejection tool in addition to the dE/dx information in silicon drift detectors. The ring properties such as Hough amplitude, number of hits on the ring and sum analog amplitude determine a quality of the ring. Additionally an enhanced sum analog amplitude or other ring quantity can be a signature of the unresolved close e^+e^- pair which is subject to rejection.

To study the rejection power of the RICH on the 2000 data, the three samples were selected: isolated tracks, target conversions and π^0-Dalitz decays. All tracks in the three samples are identified as electrons in the TPC with energy loss cut dE/d$x > 260+25log(p)$ with a number of hits on TPC tracks above 12. The full ring acceptance of the RICH-system is also required. In the target conversion sample every ring must match with two TPC tracks and with SDD track with dE/d$x > 1000$ in the two silicon drift detectors. Both TPC tracks must have opposite charges. The isolated rings necessary for the efficiency control of the single tracks were selected as follows. The ring matches with only one TPC track. The distance to the next closest electron track in the TPC is required to be above 70 mrad independently of a charge. This ensures an isolation of the ring since the complete two-ring separation occurs at the opening angle of > 60 mrad. Additionally the cut on dE/d$x < 1000$ is applied for the matched SDD track in both SDD detectors. The analysis cuts operating on the experimental distributions remove a part of the searched signal together with the background. Thus the quantities of the isolated rings should illustrate the effect of the rejection cuts on single tracks. However it is rather hard to select a clean sample of single rings, since the open e^+e^- pairs are highly suppressed with re-

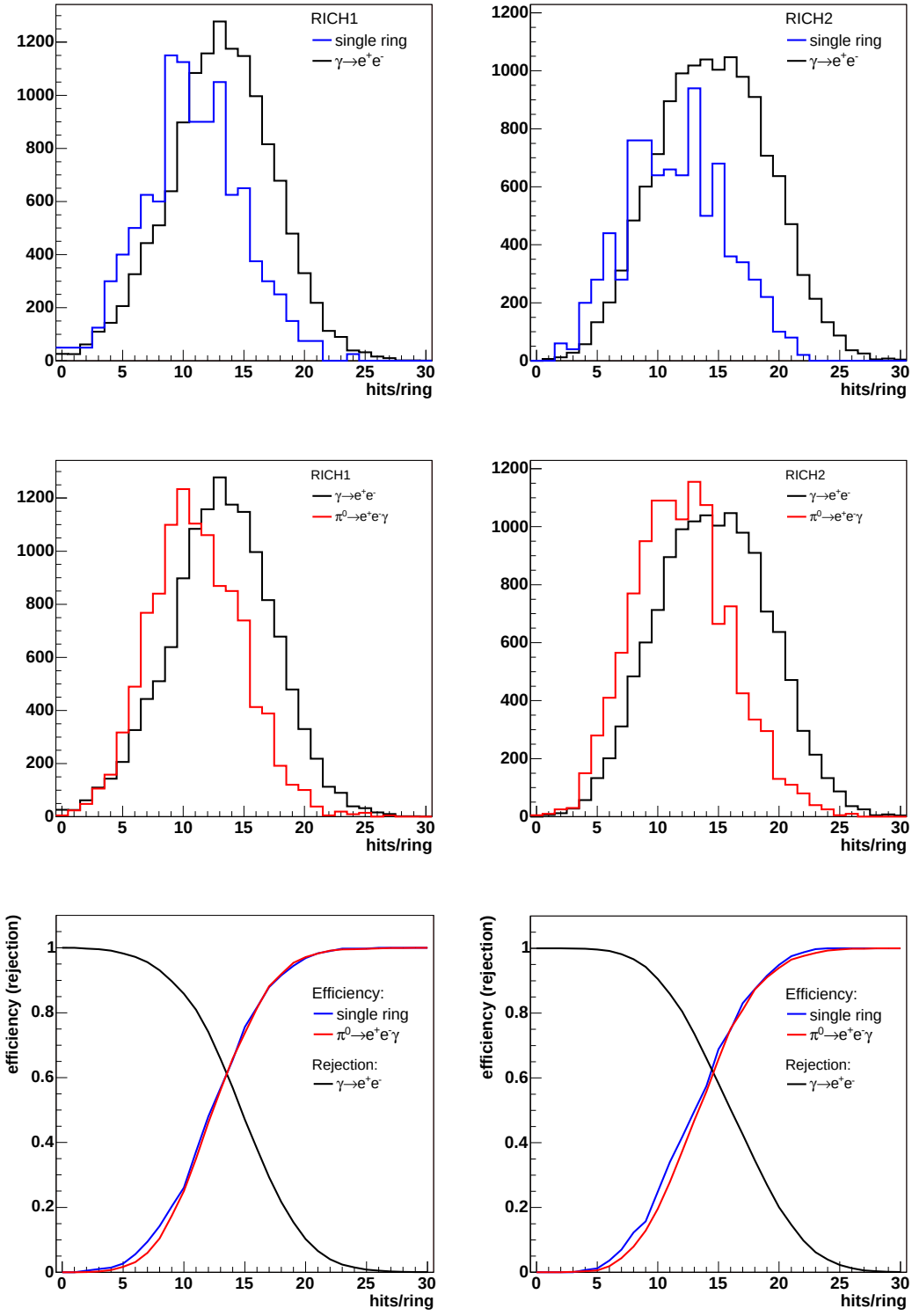

Figure 4.30: Distributions of hits on rings for target conversions, π^0 Dalitz decays and isolated rings in RICH1 (left side) and RICH2 (right side). The efficiency and rejection curves (bottom) are shown for single rings (π^0 Dalitz decays) and conversions.

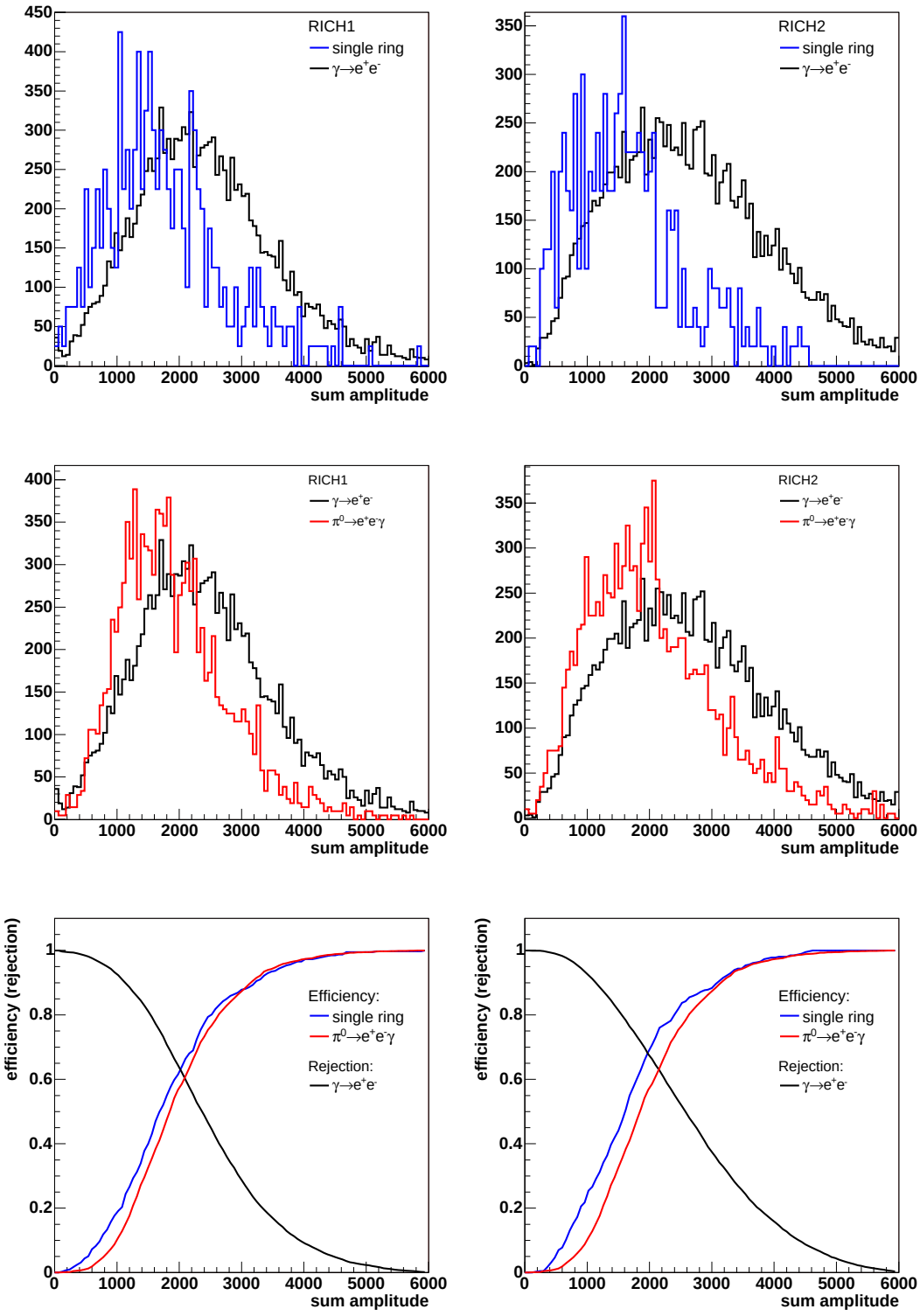

Figure 4.31: Distributions of sum analog amplitudes for target conversions, π^0 Dalitz decays and isolated rings in RICH1 (left side) and RICH2 (right side). The efficiency and rejection curves (bottom) are shown for single rings (π^0 Dalitz decays) and conversions.

spect to photon conversions and close π^0-Dalitz decays. Therefore a well defined sample of open π^0-Dalitz decays with opening angle between 10 and 50 mrad was collected. Two oppositely charged TPC tracks are matched with two RICH rings and two SDD tracks. Both SDD tracks must have single $\mathrm{d}E/\mathrm{d}x < 1000$ in SDD1 and SDD2.

Fig. 4.30 shows the comparison between the distributions of hits on rings for the isolated ring sample, the target conversion sample and the π^0-Dalitz sample. To avoid a loss of the information the ring parameters in the combined RICH-system provided by the reconstruction algorithms are available also for RICH1 and RICH2 separately. Thus all the distributions are plotted for both RICH detectors. The ratio of the integral of the remaining part of the isolated ring distribution after the cut to the full integral of the distribution represents the single track efficiency:

$$\epsilon = \left(1 - \int\limits_{cut}^{30} \frac{dN}{dn_{hit}^{single}}\, dn_{hit}^{single}\right) \Bigg/ \int\limits_{0}^{30} \frac{dN}{dn_{hit}^{single}}\, dn_{hit}^{single}. \tag{4.14}$$

The rejection power is given by the ratio of the integral of the cut part of the target conversion distribution to the full integral of the distribution:

$$\epsilon_{rej} = \int\limits_{cut}^{30} \frac{dN}{dn_{hit}^{conv}}\, dn_{hit}^{conv} \Bigg/ \int\limits_{0}^{30} \frac{dN}{dn_{hit}^{conv}}\, dn_{hit}^{conv}. \tag{4.15}$$

Usually the cross point of the rejection and efficiency lines represents the performance of the cut on the given quantity. The higher the cross point, the more powerful the cut. The dynamical range between the distributions of hits per ring for single tracks and conversions is too small due to the high pileup probability for the double rings. This results in the low rejection of the cut based on the hits on ring. At 95% single electron track efficiency the rejection reaches only 15%. It is worth to note that the hit distributions for isolated rings and π^0-Dalitzes are very similar with a mean of $\approx$11. Thus, e^+e^- pairs with opening angle between 10 and 50 mrad are a good approximation of the single rings which is also indicated by the identical efficiency curves (Fig. 4.30).

A cut on sum analog amplitude was studied in a similar way. Fig. 4.31 shows the distributions of sum amplitudes corresponding to the three samples described above. The dynamical range between the distributions is again rather small. However the pileup should not affect the ring analog amplitudes. What may enter here is the remaining fluctuations of pad amplitudes after the gain equilibration, dead areas and defects of electronics. There are four known areas in the RICH2 detector where the electronics behavior was very unstable which results in a greater spread of the sum analog distributions with respect to RICH1. The cross point of the rejection and efficiency curves in case of isolated rings and photon conversions is at a level of 65% in RICH1 and 70% in RICH2 which is slightly higher than for hits per ring distributions. However at 95% single electron track efficiency the rejection exceeds only 20%.

In order to improve the rejection capability of the spectrometer additional tool on the basis of SDD and RICH detectors has been developed. In contrast to the RICH system, where the two-ring resolution is above 10 mrad, the two-track reconstruction efficiency in the doublet of SDD detectors is already significantly high at 4 mrad separation. Thus

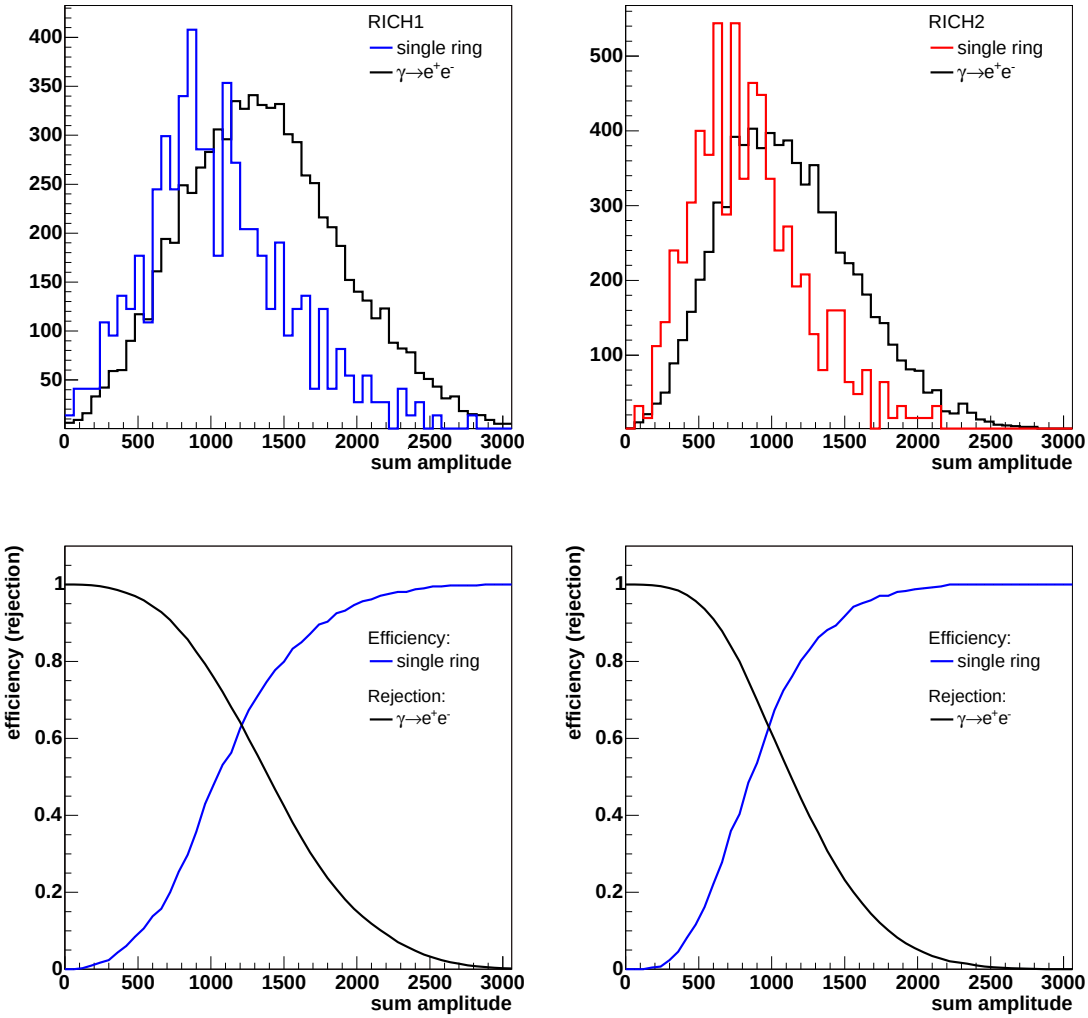

Figure 4.32: Distributions of sum analog amplitudes from SDD predictors for target conversions and isolated rings in RICH1 (left side) and RICH2 (right side). The efficiency and rejection curves (bottom) are shown for single rings and conversions.

the SDD tracks can be used as predictors for the ring centers in the RICH detectors in the opening angle region between 4 mrad and 10 mrad. Technically the method works in the following way. Every RICH ring is matched to the SDD track and another closest track in the silicon drift detectors is searched for. Once the track is found within the distance of 10 mrad it is defined as a second predictor, whereas the initial matched SDD track is a first predictor. These two SDD tracks determine the possible centers of the two rings in RICH1 and RICH2. Since the maximal distance between two predictors is much smaller than 60 mrad (the distance at which two rings are completely separate) the two ring areas significantly overlap. Thus the amplitudes of the hits in the intersecting parts of the rings are summed with half weights. The recalculated sum analog amplitudes are shown in Fig. 4.32 for single rings and γ-conversions. Unfortunately, the difference between the distributions is not sufficient to achieve a powerful rejection which is confirmed by efficiency/rejection plot.

To summarize, the ring quantities such as hits on ring and sum analog amplitude of the ring provide very poor rejection and might cost large systematic uncertainties. Therefore the cuts on those variables were mostly discarded.

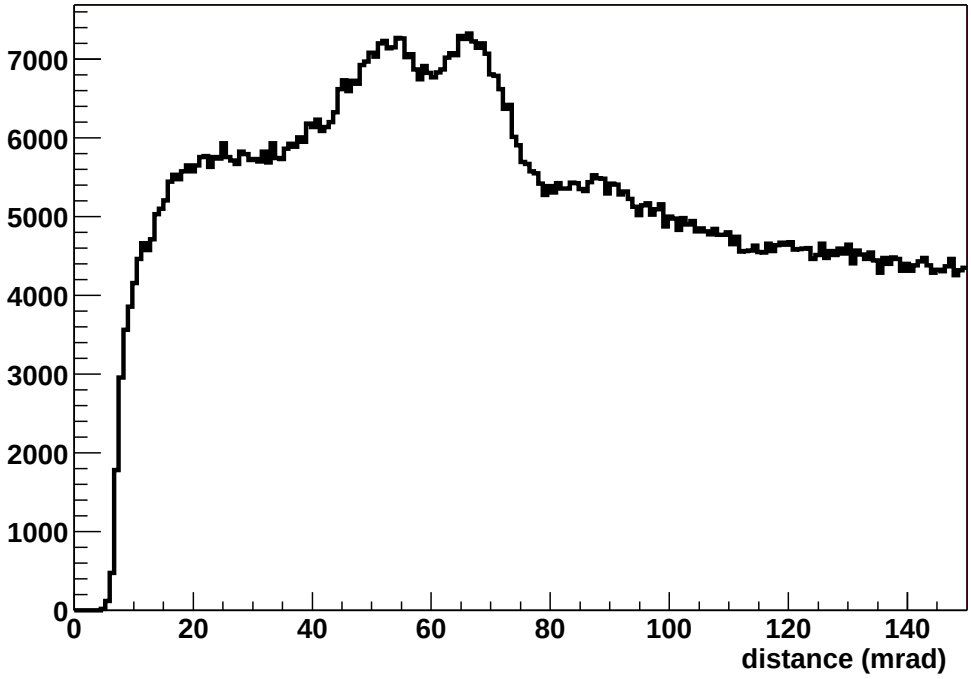

Figure 4.33: Opening angle distribution between global tracks and SDD-RICH segments. The structure at 60 mard distance is due to touching rings.

Some of the so-called partially reconstructed π^0-Dalitz decays may loose the soft leg in the TPC due to limited reconstruction efficiency for the low momentum tracks, but may still have a SDD track and a ring in the RICH. In the previous electron analysis the rejection of those decays was based on the distance between the global track and the SDD-RICH segment. Similar attempt was done in the present analysis. The corresponding distribution is shown in Fig. 4.33. The quality of the SDD-RICH tracks is ensured by the θ-dependent cuts on the Hough amplitude of > 150, the number of hits per ring > 4 in the two RICH detectors and $\mathrm{d}E/\mathrm{d}x < 1000$ resummed within 7 mrad window in both SDD detectors. The expected rise of the distribution towards the small distances is absent. The structure around 60 mrad is an indication of the fake rings. The ring radius is 30 mrad, thus the distance between touching rings is 60 mrad. In the high background environment the hits of the ring help to form a fake ring at the distance of two radii. Since there is no indication of the contribution from π^0-Dalitz decays the cut on closest SDD-RICH segment was no used.

Rejection power of the Hough transform was estimated using the method described in detail in [92]. The electron and pion samples were selected based on TPC particle identification capabilities. The TPC tracks in the momentum range $0.7 < \mathrm{p} < 0.85$ GeV/c

were required to lie within fiducial acceptance of the RICH system. The electrons were selected by the dE/dx cut above the mean energy loss for electron tracks 310 $<$ dE/dx $<$ 360. The dE/dx window for non-radiating pions around the mean pion energy loss 180 $<$ dE/dx $<$ 220 at mentioned above momentum range was chosen. Good dE/dx resolution is insured by requiring high number of hits on the track. The γ-conversions are excluded with isolation cut on oppositely charged tracks. Thus, both electron efficiency and pion rejection were experimentally estimated by matching selected TPC tracks with RICH rings within matching window of 1.5$\cdot\sigma$. Ghost rings created by the RICH reconstruction software in the high occupancy environment may lead to the fake matches with non-radiating pion tracks. The stronger the cut on the Hough amplitude of the ring, the less amount of ghost rings and, consequently, the higher pion rejection. In fact, electron efficiency and pion rejection are the correlated quantities: the higher electron efficiency, the lower pion rejection and vice versa. Fig. 4.34 illustrates the dependence of electron efficiency on pion rejection varying the Hough amplitude cut between 90 and 230 with a step of 20. For the electron electron efficiency of 68% the pion rejection is 0.9997.

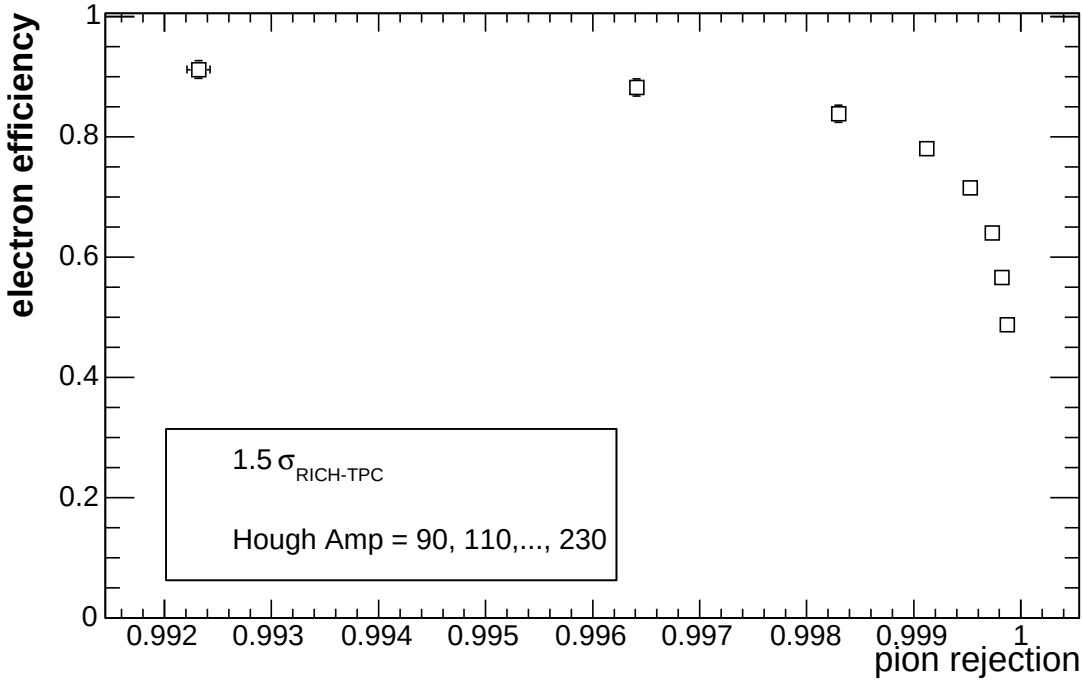

Figure 4.34: Electron efficiency as a function of pion rejection for different cuts on Hough amplitude.

4.6.5 Rejection Power of dE/dx in TPC

The addition of the TPC significantly increased the rejection capabilities of the CERES spectrometer. In order to study the rejection power of the TPC based on the energy loss

by charged particles traversing the detector the measured dE/dx distributions should be well understood.

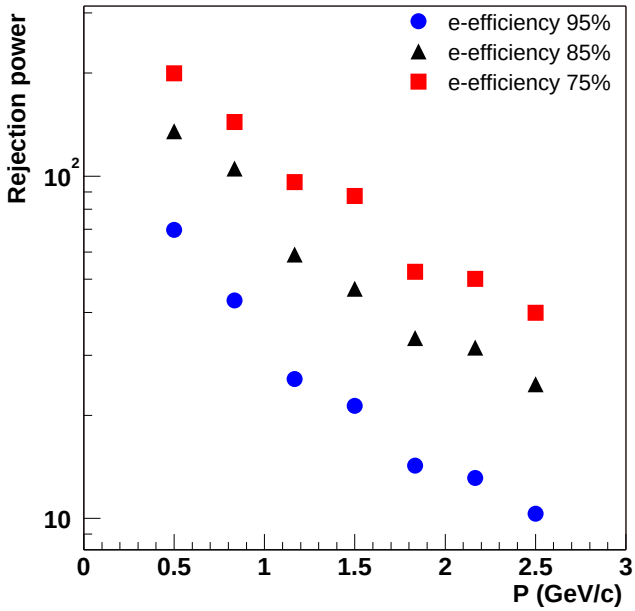

Figure 4.35: Rejection power as a function of momentum for different electron track efficiencies.

The first step is to simulate the experimental distributions for pions and electrons with Monte Carlo programs. To achieve the most realistic resultant distributions the simulated detector responses were put on top of the real data. The simulated energy loss by electrons and pions was then carefully compared to the experimental dE/dx distributions. After adjusting the mean values the data distributions were well described to high order. The rejection power then can be calculated from the simulated energy loss distributions for pions which is identical to a real data. For the given momentum interval the rejection power is represented by the integral of a cut part of distribution to the full integral:

$$\epsilon_{rej} = \int_{cut} \frac{\delta N}{\delta(dE/dx)}\,\delta(dE/dx) \Bigg/ \int \frac{\delta N}{\delta(dE/dx)}\,\delta(dE/dx). \tag{4.16}$$

The electron efficiency can be estimated in a similar way by integrating the simulated dE/dx distribution of electrons. Fig. 4.35 shows the rejection power of TPC as a function of the track momentum for three different electron track efficiencies. Due to the logarithmic rise of the mean energy loss for the relativistic pions the rejection power of the constant cut decreases with momentum at any level of electron efficiency shown. To efficiently suppresses pions at high momenta an inclined cut on dE/dx versus momentum is used in the electron analysis.

However, the higher the rejection of pions, the lower the single electron track efficiency. The dependence of the electron efficiency on the pion rejection is presented in

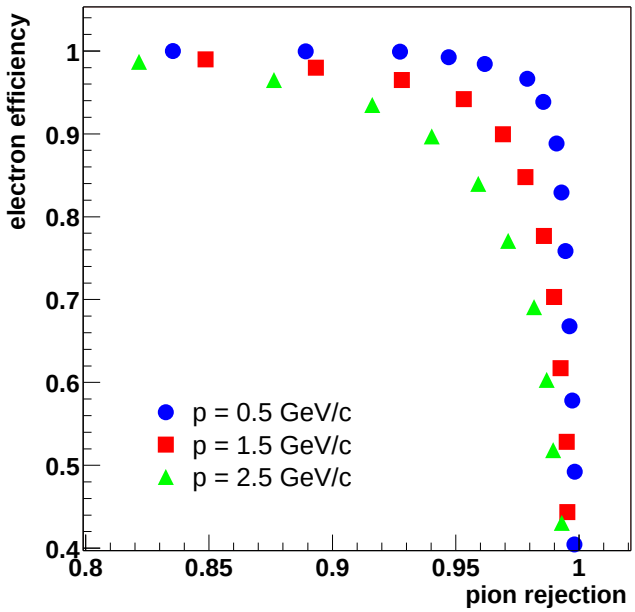

Figure 4.36: Rejection of electrons versus rejection of pions for different momenta.

Fig. 4.36 for three different momenta. For the 95% efficiency of the electron tracks with 0.5 GeV/c momentum the pion rejection reaches 99%. At this soft momentum the separation between pion and electron peaks is much better than at p = 2.5 GeV/c where, consequently, the pion rejection is only 90% for the same electron efficiency. Combined rejection power of the RICH-TPC is 9×10^4 at electron efficiency of 64% for the 1 GeV/c momentum.

4.6.6 Rejection of Close Pairs in TPC

Since the rejection of the photon conversions is of extreme importance it is worth to study the $\gamma \rightarrow e^+e^-$ process with the TPC. The selection of the conversion sample is done as follows. The electrons are identified in the TPC with $\mathrm{d}E/\mathrm{d}x > 260{+}25\,log(p)$. The distance between oppositely charged electrons must be below 2 mrad. Fig. 4.37 shows θ-distribution of the selected e^+e^- pairs. The enhanced amount of conversions at 13 mard corresponds to the inner ring of the TPC support. The tracks are well identified with 15 hits in average which is illustrated in the two-dimensional plot showing the number of hits on track as a function of theta (Fig. 4.37). The 8 spokes can be clearly seen in the correlation between θ- and ϕ-coordinated of the e^+e^- pairs represented in Fig. 4.38. The θ-acceptance cut of $>$ 14 mrad takes care of the γ's converting in the inner ring.

In most of the cases within the θ-acceptance the photon conversions can be divided into two classes: target conversions and conversions in the RICH2 mirror (R2M conversions) with a fake match to SDD. The target conversions are usually rejected to a high order by the correlated cut on $\mathrm{d}E/\mathrm{d}x$ in the silicon drift detectors. Thus the TPC re-

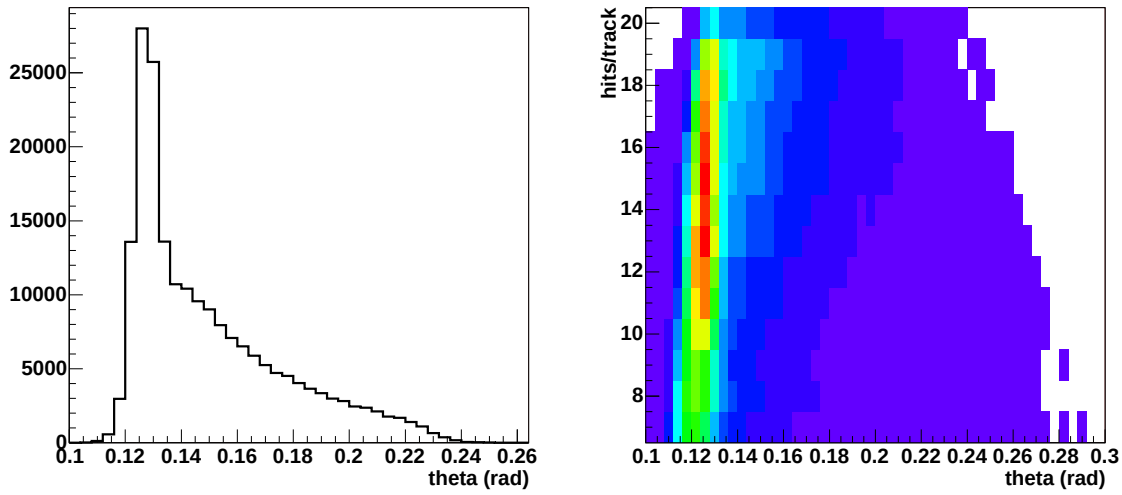

Figure 4.37: The θ-distribution of the conversions identified in the TPC (left panel) and number of hits on track as a function of the theta of track for identified conversions (right panel). The conversions in the inner ring of the TPC support form a peak at 13 mard.

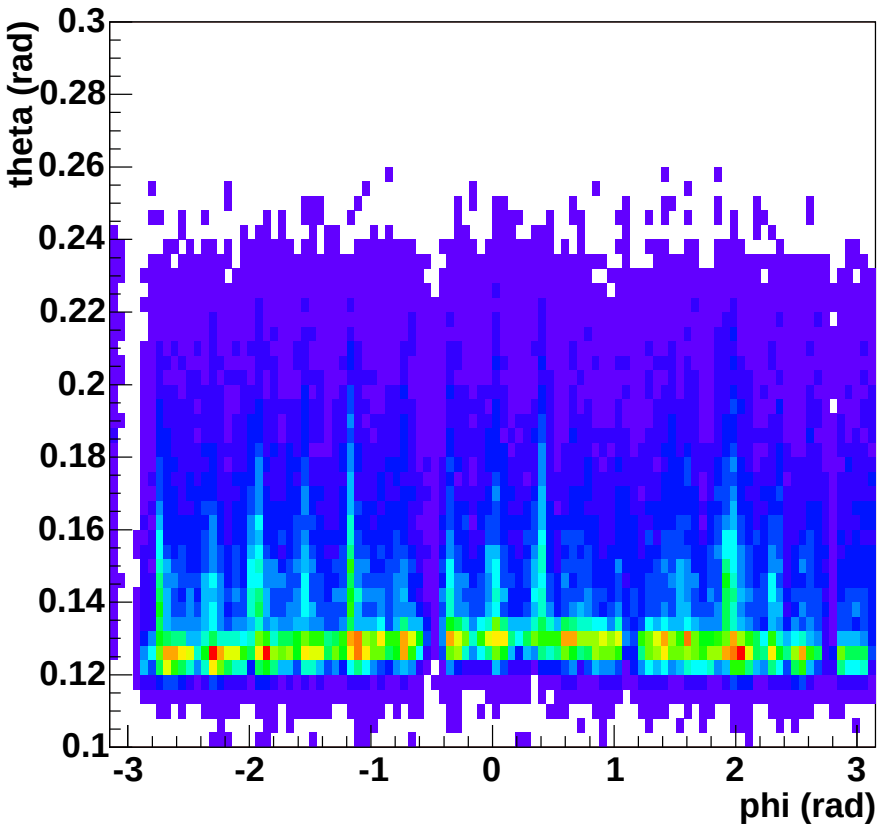

Figure 4.38: Angular distribution of the identified conversions in TPC. The inner ring and 8 spokes are clearly visible.

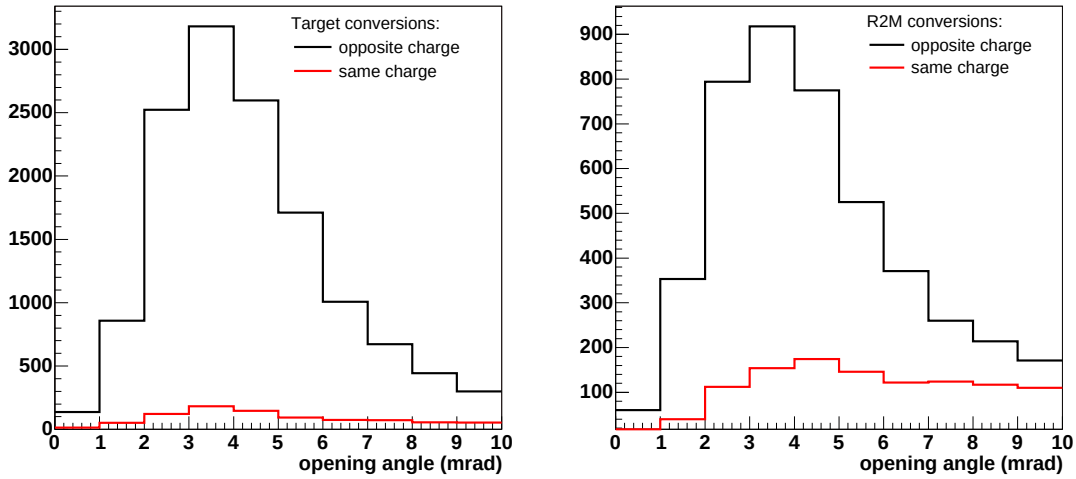

Figure 4.39: Opening angle of the e^+e^- pair identified as target conversion (left panel) and as conversion in the RICH2 mirror (right panel). The background level was estimated by the requirement of the identical charge for both tracks which enter a pair.

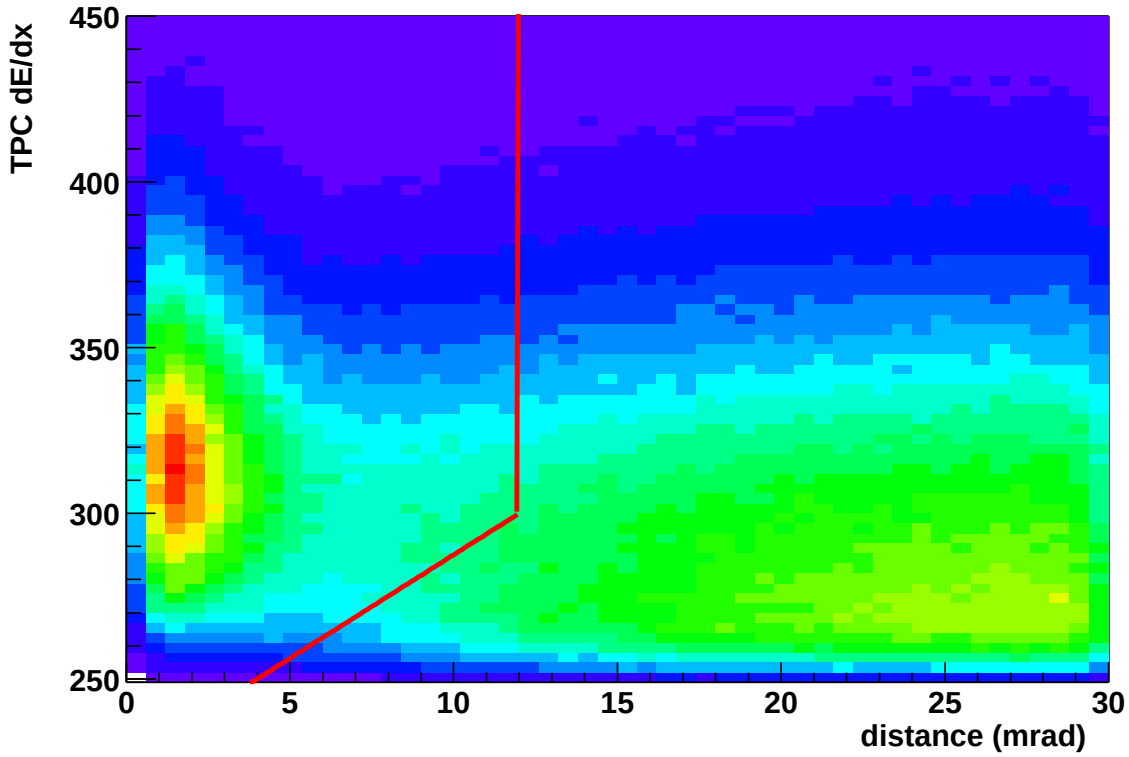

Figure 4.40: $\mathrm{d}E/\mathrm{d}x$ of the closest segment in the TPC as a function of the distance between global track and segment. The red line shows a cut applied to remove conversions.

moves only remaining conversions which were not previously rejected. Fig. 4.39 shows the distribution on the opening angle of the target conversions identified in the TPC as two oppositely charged electron tracks with dE/dx $>$ 260+25 $log(p)$ and with a number of hits on tracks above 15. One of TPC tracks must be matched to RICH ring and SDD track with dE/dx $>$ 1000 in both silicon drift detectors. A background was estimated by requiring the same charge for the two TPC tracks. Then the signal to background ratio for the target conversions is 15/1.

R2M conversions are of danger in case one electron leg is fakely matched to the hadron SDD track and ghost RICH ring. Such a sample was selected with the similar cuts as for the case of target conversions except dE/dx in SDD detectors. The energy loss of the SDD track must be below 1000 in SDD1 and SDD2 and there should be no match between second TPC track and another SDD track. The opening angle distribution of those TPC pairs is represented in Fig. 4.39. The background level is again calculated by the requirement of the same charge for the TPC tracks. Once the distance of 10 mrad is approached the signal to background ratio reaches ≈1/3. In the electron analysis the signal over background gets even worse since the dE/dx cut applied for TPC tracks is softer. Thus the cut on the closest TPC segment should be done in a safest way to keep single electron track efficiency high.

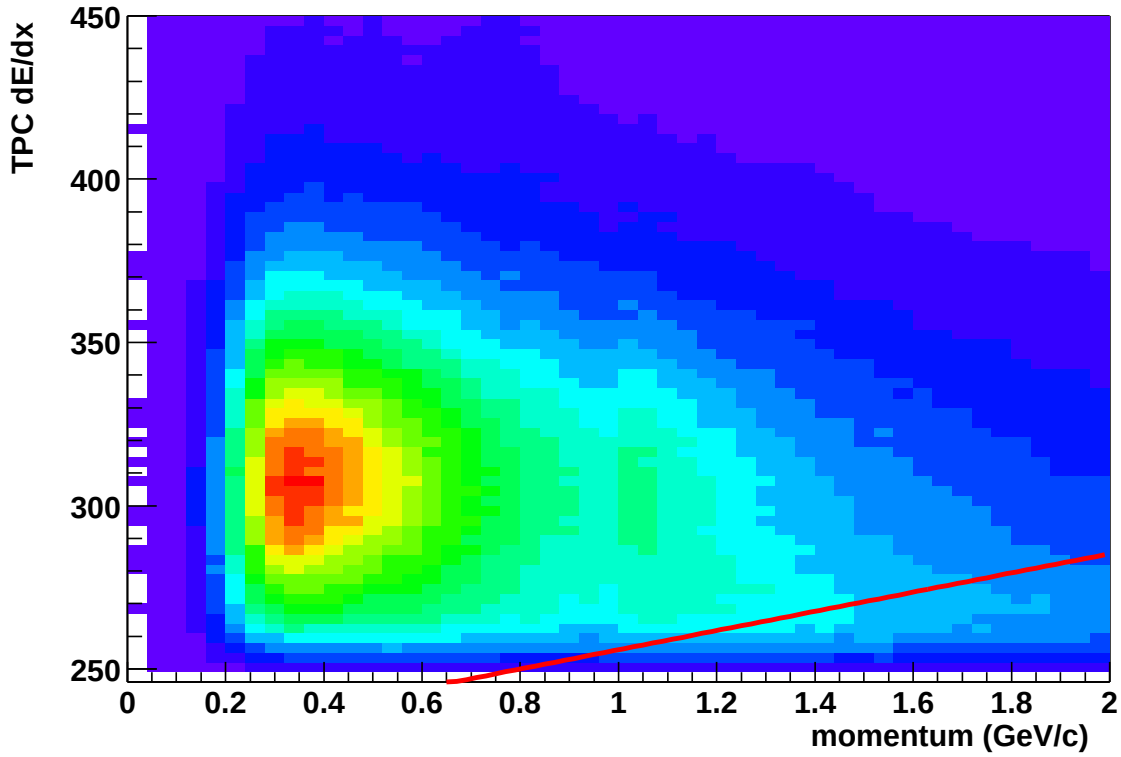

Figure 4.41: dE/dx of the closest segment in the TPC as a function of its momentum. The cut separating electrons and pions is indicated by the red line.

The close e^+e^- pairs show up best in the correlated track quantities. Fig. 4.40 shows a dependence of the dE/dx of the closest segment with opposite charge in the TPC on the distance between a global track and the segment. The electron pairs originated from conversions occupy the low opening angle values around 2 mrad and have an average dE/dx of ≈310 which corresponds to the specific energy loss of electrons. The pion tracks with lower dE/dx occur at much larger distances. However the first indication of pions is seen already at opening angles of about 8 mrad. The red line represents the cut which, being applied in combination with another two-dimensional cut discussed below, removes the conversions and suppresses the pion contamination. Fig. 4.41 illustrates the correlation between the dE/dx of the closest segment and its momentum. The conversion legs sit at low momenta with a mean electron dE/dx of 310 while pions form a structure with low energy loss towards high momenta. The red line shows the second correlated cut removing the pion contamination. In addition all global tracks, which have nearby a close oppositely charged electron segment within 2 mrad distance, are removed.

4.7 Subtraction of Combinatorial Background

4.7.1 Same-event Combinatorial Background

The like-sign event background can be defined as the arithmetic or the geometric mean of positron-positron and electron-electron uncorrelated pairs. It is known that the arithmetic mean is always larger (or equal in case of identical numbers) than the geometric mean. Thus the arithmetic mean is more strongly affected by outliers (i.e., extreme values) with respect to the geometric mean.

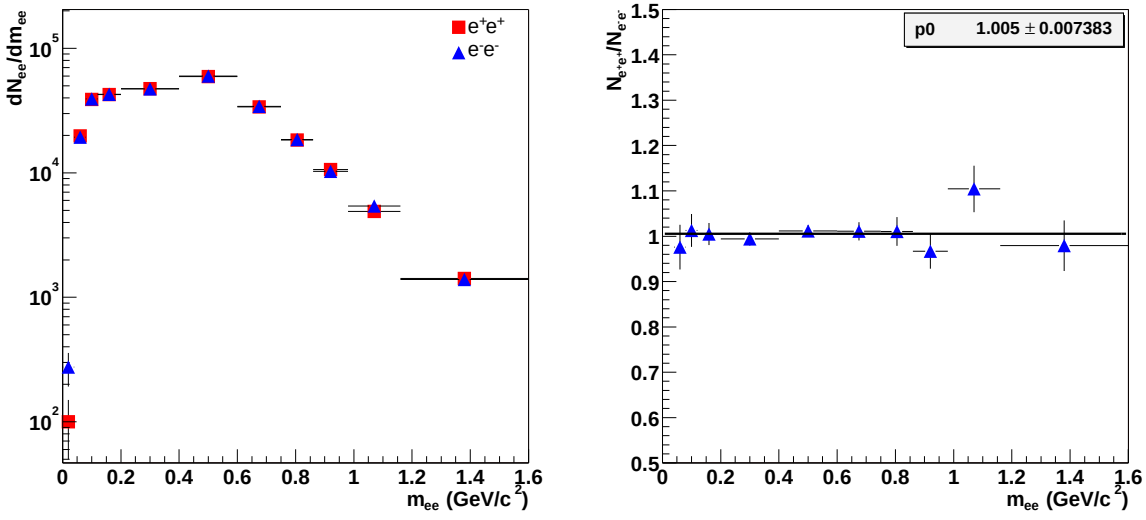

Figure 4.42: The like-sign background distributions (left panel) and the ratio of $N_{e^+e^+}$ to $N_{e^-e^-}$ (right panel). No charge asymmetry is observed.

Fig. 4.42 shows the ratio of $N_{e^+e^+}$ to $N_{e^-e^-}$. The ratio of the like-sign backgrounds of different charges is 1.005±0.007. According to the dependence of the relative difference

δ between the arithmetic and geometric means on the charge asymmetry Δ

$$\delta \approx \frac{1}{8}\Delta^2, \tag{4.17}$$

the discrepancy becomes significant on the level of $\Delta > 10\%$.

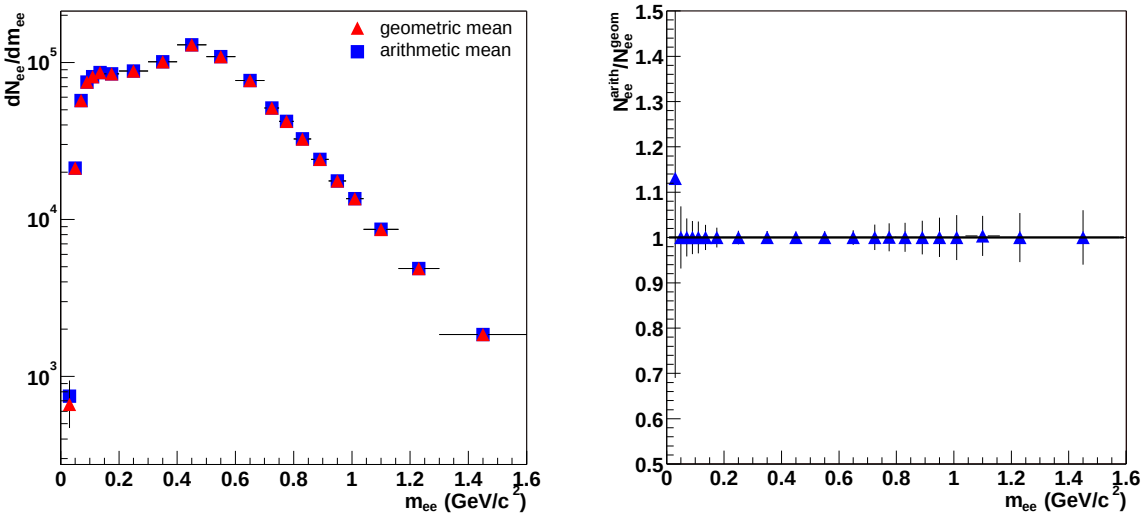

Figure 4.43: The geometric and arithmetic like-sign backgrounds (left panel) and the ratio of the two (right panel). Due to the absence of the charge asymmetry both distributions are identical.

Fig. 4.43 shows two backgrounds obtained using the arithmetic and geometric means. The difference between backgrounds is hardly seen. In the present analysis the geometric mean is used since it is generally more universal. Statistical error of the signal is defined as

$$\delta S_{+-} = \sqrt{N_{+-} + N_{++} + N_{--}}. \tag{4.18}$$

To improve the statistical error different approaches have been applied in previous analyses. The high statistical background can be generated by a random combination of single tracks assuming that p_t, θ and ϕ distributions are taken from the data. Alternatively the suitable fit function can be used to smooth the background in order to decrease statistical fluctuations. Another attempt was done in the 1999 analysis. The high statistical like-sign combinatorial background after few rejection steps was rescaled to fit the background after full rejection. The rescaled background was then used to reduce the statistical bin-to-bin errors in the final mass spectrum.

4.7.2 Mixed-event Technique

The event-mixing technique is an alternative to the like-sign method for the background construction. The mixing with different events allows to destroy the correlations between the tracks, to collect large statistics and to accurately determine the shape of the combinatorial background.

In the event-mixing technique all electrons and positrons of an event are paired with all electrons and positrons of 20 other events within the same centrality class. Every next event is chosen in random order. The charged particle multiplicities of the events are required to coincide within 5%. In contrast to the like-sign background accumulated over the events with at least two electron tracks, the event-mixing method contains also events with only one electron track. The validity of the event-mixing technique is confirmed with like-sign background distributions. Fig. 4.44 shows the comparison of the two invariant mass distributions: the unlike-sign background obtained with the event-mixing and the like-sign combinatorial background constructed by a geometric mean of N_{++} and N_{--}. The shapes of the two distributions are almost identical which is also confirmed by the ratio of the spectra presented in Fig. 4.45. The unlike-sign mixed event mass distribution is then normalized to the measured. The normalization factor is extracted from the fit to the ratio. The observed drop of the ratio at masses below 200 MeV/c^2 is due to pair effects discussed in section 6.5. Therefore, in the mass region $m_{ee} < 200$ MeV/c^2, the same event like-sign background is used.

One of the advantages of the event-mixing technique is a possibility to improve the statistical error of the mixed-event background by increasing the number of events for mixing.

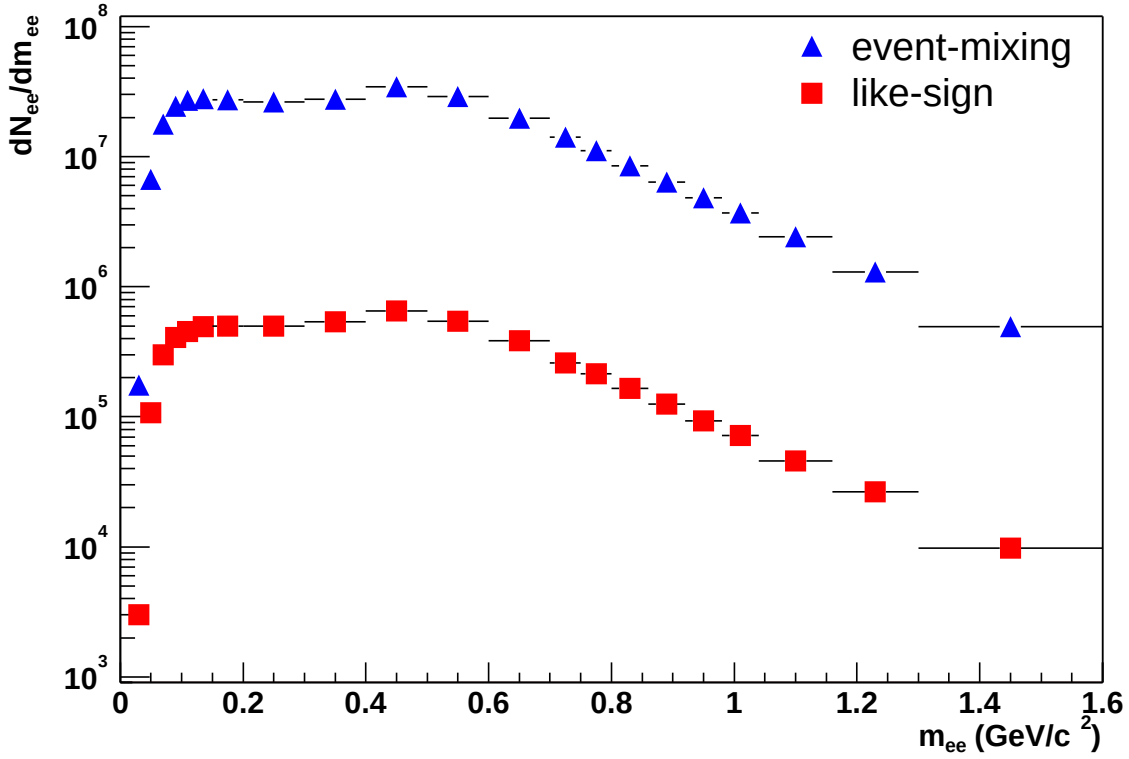

Figure 4.44: Comparison of the unlike-sign mass distribution obtained with event-mixing technique and the like-sign mass distribution.

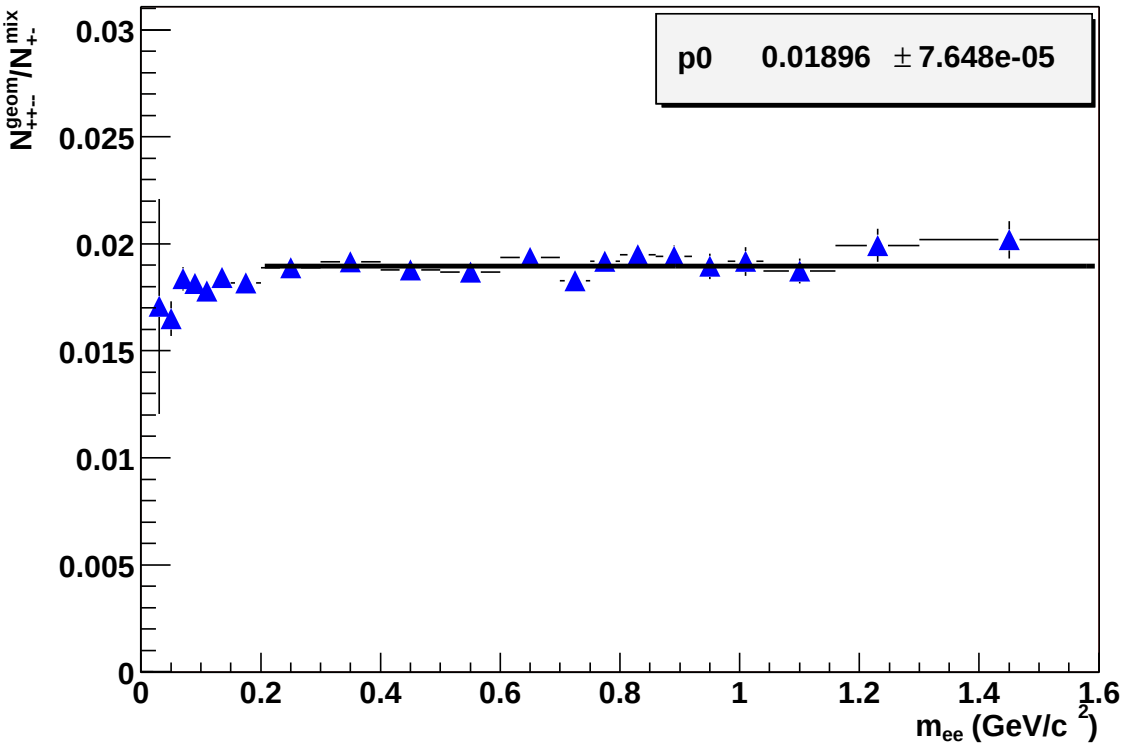

Figure 4.45: The ratio of the unlike-sign mixed event mass distribution and the like-sign mass distribution.

5

The GENESIS Generator

In order to distinguish a signal of interest from the conventional sources of e^+e^- pairs the invariant mass spectrum is compared to the superposition of known electromagnetic decays. The GENESIS generator [93] was developed to simulate the so-called "hadronic cocktail" which consists of the known hadron decays in proton-proton, proton-nucleus and nucleus-nucleus collisions. The cocktail serves as a baseline to compare with the experimental data. For instance, a good agreement was found between e^+e^- mass spectrum in proton-induced collisions and the hadronic cocktail, while in case of the heavy-ion beams an enhancement in the mass region $0.2 < \mathrm{m}_{ee} < 0.6$ GeV/c2 was observed.

The code has been rewritten in C++ to utilize COOL library and to easily extend the algorithms. The decays are simulated by JETSET routines [94].

The di-electron pair sources contributing to the low mass region are: π^0, η(547), ρ^0(770), ω(782), η'(958), ϕ(1020). The pseudo-scalars π^0, η and η' decay to $e^+e^-\gamma$, while the vector mesons ρ^0, ω and ϕ decay directly to e^+e^-. The ω and ϕ have an additional Dalitz decay channel: $\omega \to e^+e^-\pi^0$ and $\phi \to e^+e^-\eta$.

Each particle in the collision decays according to Poisson distribution with a mean given by the following formula:

$$\mu = \bar{N_{\pi^0}} \cdot \sigma/\sigma_{\pi^0} \cdot BR \cdot S, \tag{5.1}$$

where $\bar{N_{\pi^0}}$ is a mean π^0 multiplicity which is an input parameter, σ/σ_{π^0} is a particle production cross section over that of π^0, BR is the branching ratio of the decay, and S is a scale factor which is adjustable for each decay mode to obtain enough statistics for the decay mode.

In order to compare the hadronic cocktail and the data the event generator should be normalized in the same way to represent the pair production probability per event and per charged particle multiplicity measured in the CERES acceptance. All generated decays can be normalized with respect to π^0's and then multiplied by the ratio of the number of pions to the number of charged particles averaged over the CERES acceptance:

$$\langle N_{\pi^0} \rangle / \langle N_{ch} \rangle = 0.44. \tag{5.2}$$

Finally, the kinematic cuts are applied as for the data. Thus, the inclusive mass spectrum (hadronic cocktail) is generated including all processes with their proper strength.

In order to properly generate the hadronic cocktail the knowledge of the production cross sections, branching ratios, rapidity and transverse momentum distributions of the parent particles is required. Due to the fact that differential cross sections for many light mesons are not known, an appropriate model should be used to provide the missing information. Fairly good agreement was obtained between predictions of a thermal

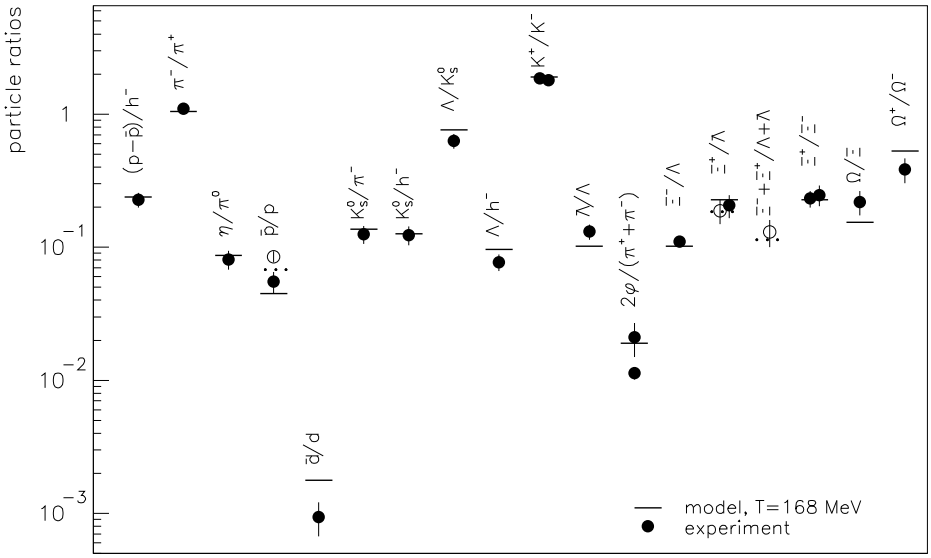

Figure 5.1: Comparison between the observed particle ratios and the predictions of the thermal model [2].

model [13, 95] and ratios of integrated hadron yields measured by several experiments for Pb-Pb central collisions at SPS energy (Fig. 5.1). The model describes particle ratios at chemical freeze-out with only two fit parameters, the temperature (T = 170 MeV) and the baryon chemical potential (μ_b = 68 MeV). For the cases when the measurements do not exist the cross sections of the hadrons relative to those of π^0 were taken from the thermal model. NA44 [7, 96], NA49 [97] and WA98 [98] experiments measured rapidity and transverse momentum distributions of hadrons. Rapidity distributions of negative charged hadrons measured by NA49 [99] was used for all hadrons, since the width of the distribution in lead-induced collisions seems to not change with particle mass [100].

The π^0 transverse momentum distributions measured by NA49, NA44 and WA98 as well as by CERES [1, 101, 102] can not be fitted with single exponential. Thus, the pion p_t spectrum was parameterized by

$$E\frac{d^3\sigma}{d^3dp} \propto a_1 \cdot e^{-\frac{m_t}{T_1}} + a_2 \cdot e^{-\frac{m_t}{T_2}} + a_3 \cdot e^{-\frac{m_t}{T_3}}, \tag{5.3}$$

where a_1 = 1, a_2 = 0.139, a_3 = 0.107 and three inverse slope parameters: T_1 = 0.1, T_2 = 0.23, T_3 = 0.102 GeV/c^2. The charged pion distributions measured by NA44 were used to extrapolate the inclusive transverse mass distributions obtained by WA98 to small m_t.

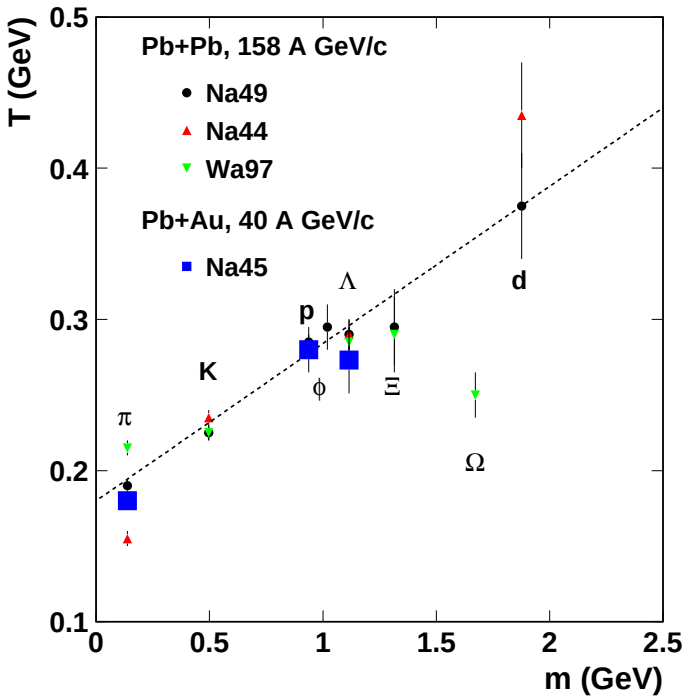

Figure 5.2: Inverse slope parameter as a function of mass [3–9].

For other hadrons an increase of inverse slope with mass was observed [2] due to the collective transverse expansion as shown in Fig. 5.2. This mass dependence of the inverse slope parameter can be parameterized as follows:

$$T = 0.175 + 0.115 \cdot m. \tag{5.4}$$

To generate the e^+e^- invariant mass spectrum for the Dalitz decays the electro-magnetic form factors were fitted to the Lepton-G experimental data [103, 104]. In case of the π^0- and the η-Dalitz decay the pole approximation

$$F(M^2) = (1 - b\,M^2)^{-1} \tag{5.5}$$

is used. While for the ω- and η'-Dalitz decays a Breit-Wigner function

$$|F(M^2)|^2 = \frac{m_\rho^4}{(M^2 - m_\rho^2)^2 + m_\rho^2\Gamma_\rho^2} \tag{5.6}$$

determines the form factors. For two-body decays of the ω and ϕ mesons the relativistic Breit-Wigner function is used:

$$\frac{dR}{dM^2} = \frac{(1-(3m_\pi/M)^2)^{3/2}}{(M^2-m_V^2)^2+m_V^2\Gamma_0^2}, \tag{5.7}$$

where M is the e^+e^- invariant mass, m_V is mass of the ω or the ϕ mesons, Γ_0 is the width of the ω or the ϕ. For a special case of the ρ meson, which has a width of about 150 MeV/c^2, a different evaluation was performed [93, 105]. Additional exponential term $\exp^{-M/T}$ slightly affects the ρ mass spectrum. The low mass region is increased, while the high masses become lower.

The branching ratios and relative cross sections are given in Table 5.1 for different decays. The decay branching ratios were taken from [106].

Particle	Decay	$\sigma_{tot}/\sigma_{\pi^0,tot}$	BR
π^0	$e^+e^-\gamma$	1.	$(1.198\pm0.032)\times10^{-2}$
η	$e^+e^-\gamma$	0.085	$(6.0\pm0.8)\times10^{-3}$
ρ	e^+e^-	0.094	$(4.67\pm0.09)\times10^{-5}$
ω	e^+e^-	0.069	$(7.14\pm0.13)\times10^{-5}$
ω	$e^+e^-\pi^0$		$(5.9\pm1.9)\times10^{-4}$
ϕ	e^+e^-	0.018	$(2.98\pm0.04)\times10^{-4}$
η'	$e^+e^-\gamma$	0.0078	$\approx5.6\times10^{-4}$

Table 5.1: The decays simulated in the generator, relative cross sections and branching ratios.

Emission angles of the electron and positron in the rest frame of decaying meson are generated according to a (1+$\cos^2\theta$) distribution for the $e^+e^-\gamma$ decays, where θ is measured with respect to the virtual photon direction. In case of the $\omega \to \pi^0 e^+e^-$ and the two-body decays the uniform distribution ($\cos\theta$) is used.

In order to compare the superposition of the generated decays to the experimental data the hadronic cocktail should be folded with the mass resolution. One of contributions to the mass resolution is given by the momentum resolution of the spectrometer which was parameterized as follows:

$$\frac{\Delta p}{p} = \sqrt{(2\%)^2 + (1\% \cdot p(GeV/c))^2}. \tag{5.8}$$

The pair opening angle resolution which although negligibly enters the mass resolution is given by

$$\sigma^2_{\theta_{ee}} \approx (\sqrt{2}\sigma_\theta)^2 + \sin^2\theta(\sqrt{2}\sigma_\phi)^2, \tag{5.9}$$

where the angular track resolution $\sigma_\theta \approx 0.6$ and $\sigma_\phi \approx 3.0$.

All kinematic cuts applied in the data are also applied for the cocktail (transverse momentum cut of > 0.2 GeV/c, pair opening angle cut of > 35 mrad and pseudorapidity acceptance $2.1 < \eta < 2.65$). Fig. 5.3 shows the folded with mass resolution hadronic cocktail after kinematic cuts and bremsstrahlung effects for the lead beam data.

The uncertainties in the branching ratios and in the form factors were discussed in detail in [24]. On systematic errors see also section 7.5.

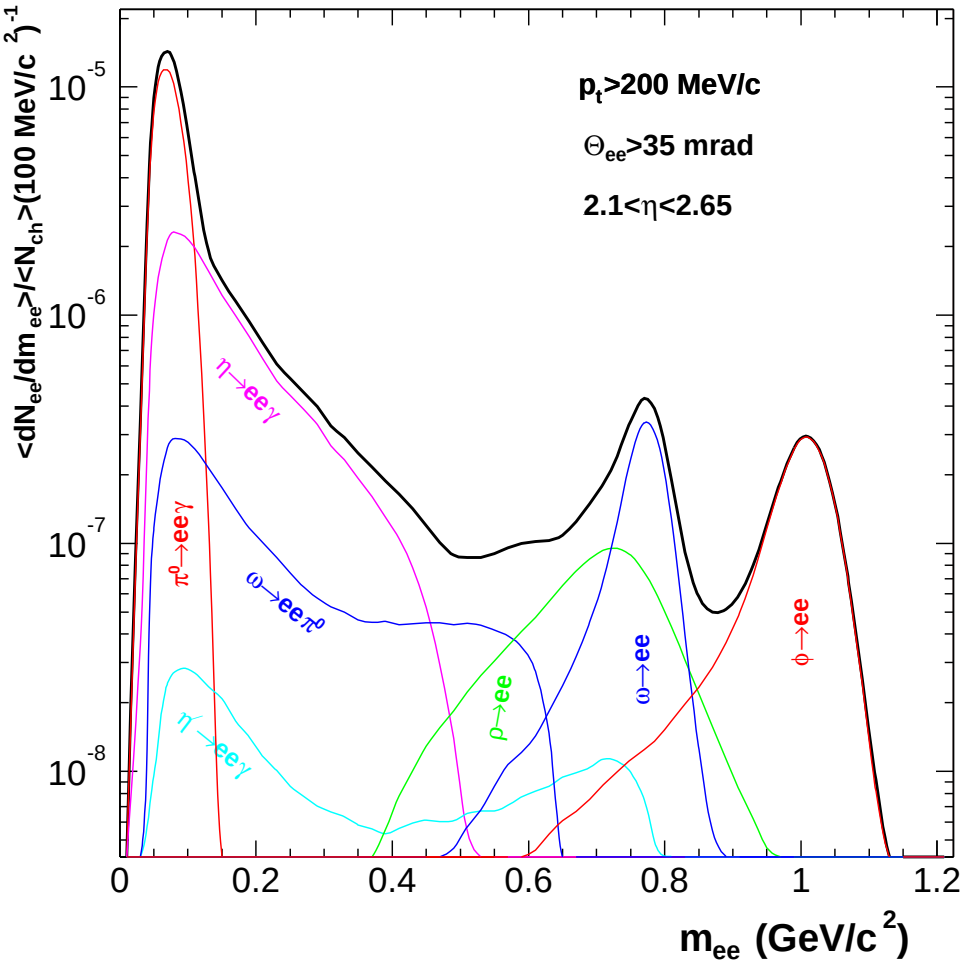

Figure 5.3: The hadronic cocktail folded with mass resolution after applying the kinematic cuts and bremsstrahlung effects. The black line shows the superposition of all contributions from the generated hadron decays.

6

Monte-Carlo Simulation

A purpose of the Monte-Carlo simulation is to estimate the pair reconstruction efficiency which is a measure of the analysis software ability to reconstruct e^+e^- pairs provided that both tracks are in the spectrometer acceptance. In order to produce Monte Carlo events on which to perform analysis a full chain of steps needs to be taken from generation of meson decays to production of the simulated data. The complete simulation procedure consists of the following steps:

- Required final-state particles are generated with CERES event generator GENESIS described in chapter 5. The Monte-Carlo study described in this chapter is based on four generated sources π^0-Dalitz, η-Dalitz, ρ and ϕ.

- The generated particles are then transported in the material of the experimental setup, simulating their interaction with it and the energy deposition which generates the detector response. This step is actually performed by passing generated events through a GEANT3 [107] Simulation of the CERES spectrometer. GEANT package provides full detector simulation including complete geometry of the experimental setup together with material description. The output of GEANT simulation is a set of digi-hits which include a record of were each particle traversed the detector and how much energy was deposited.

- GEANT simulation is followed by signal digitization and detector response simulation. During this phase the energy deposition of the particles is converted into the detector response such as times and voltages, formatted according to the output of the front-end electronics and the data acquisition system for every detector system. The digitization is tuned to closely reproduce the detector responses in the real data.

- The simulated detector signals are then overlayed on top of the real data in order to properly reproduce the event multiplicity. In this case the data play the role of background. The obtained event is then passed through the reconstruction algorithms producing hits, tracks and rings from the raw data. Note, that information about digi-hits is kept through all steps allowing to identify generated tracks at any level of the simulation procedure.

- Since the format of the output of the previous step is identical with the output of the real data analysis (step2), the next step (step3) is almost directly applied as in data with identical cuts.

- The final analysis (step4) includes a majority of rejection cuts. All efficiency estimates and MC studies are performed at this level.

6.1 Silicon Drift Detectors

The digitization procedure simulates different effects such as electronic noise, pickup and ballistic deficit. The electron cloud is distributed over the anodes in step of two anodes at the same time to simulate the scanner. The preamplifier chip amplifies the deposited charge into the voltage signal. The ballistic deficit and the anode dependent gain change the signal in both radial and azimuthal directions. Therefore the hit amplitude is not homogenous over the wafer. The signal is spread over 13 time-bins given by broadening due to the shaping time of the preamplifier chip and over 5 anodes influenced by diffusion and geometry. A Gaussian-like electronic noise is added on top of each cell. Tuning of the MC parameters allowed to achieve a good agreement between the data and the simulated distributions.

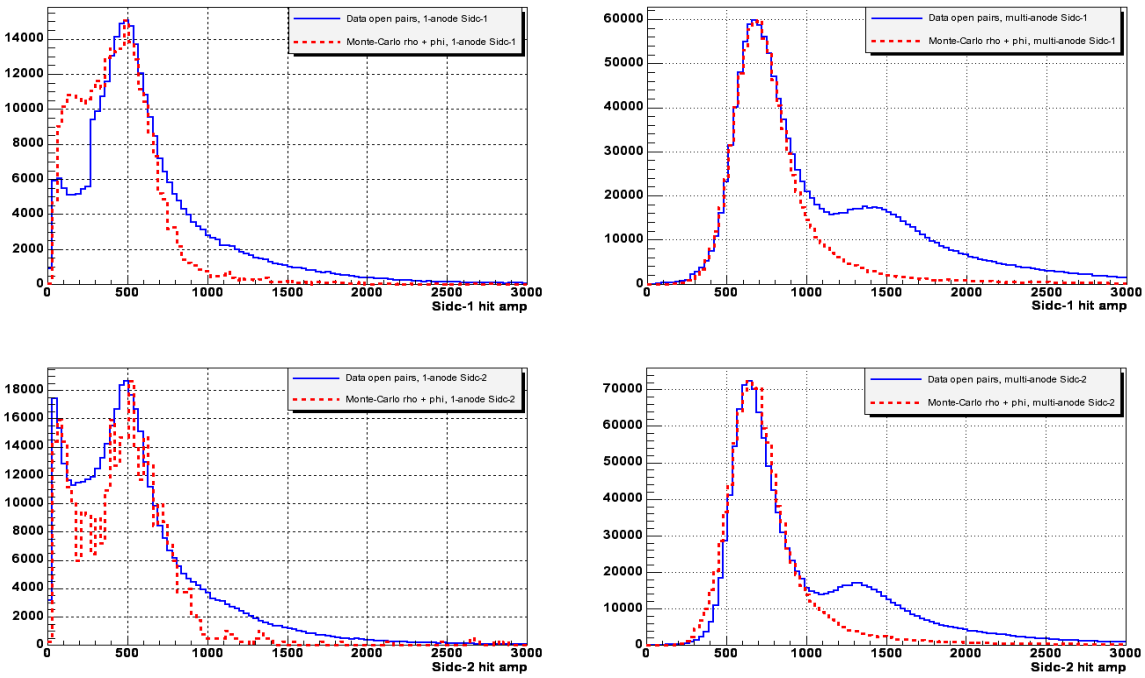

Figure 6.1: Energy loss in SDD1 (top) and SDD2 (bottom) plotted separately for single-anode hits (left) and multi-anode hits (right). MC simulations (red dotted curve) including $\rho \rightarrow e^+e^-$ and $\phi \rightarrow e^+e^-$ are shown on top of the data (blue solid curve).

A study of the energy loss in silicon drift detectors indicated a dependence of dE/dx on hit topology. Thus MC simulations were performed separately for single-anode hits and multi-anode hits. Fig. 6.1 illustrates a comparison of the energy loss distributions in both silicon drift detectors between data and MC simulation for different hit topologies. A second Landau peak in the data dE/dx distribution at approximately 1400 corresponds to the signal of closed unresolved tracks coming mostly from conversions. It is extremely difficult to clean up all target γ-conversions with a help of only RICH and TPC in the data, while in the simulation energy loss distribution was accumulated only for the reconstructed MC electron tracks from ρ and ϕ generated with opening angle much above two-hit resolution in SDD which results in the absence of double dE/dx peak. Thus, ignoring second peak, simulated energy loss distribution perfectly describes the data for a case of multi-anode hits in both silicon detectors. In case of single-anode hits a reasonable agreement was also observed for SDD1 and SDD2.

6.2 RICH Detectors

The signal of every digit is distributed over the array of 7×7 pads size using the inverse cosh-function. The pads under spoked and outside acceptance are ignored. Finally all generated pads pass the data cut on minimum amplitude. Digitized pads are then overlayed on top of the real data.

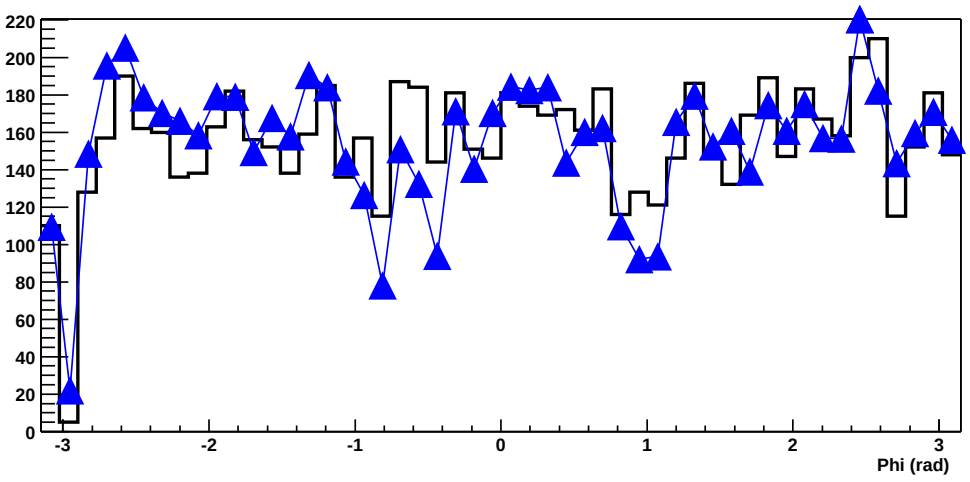

Figure 6.2: Comparison of the ϕ-distributions of the single electron tracks in the data (blue triangles) and simulation (black histogram) with ϕ-θ map of dead regions applied.

The known dead regions were switched off since all attempts to accurately describe the ϕ-distributions of the reconstructed rings by removing simulated pads falling into known dead areas failed. Instead the effect of dead areas was determined using the real data. The electron tracks selected in the TPC were matched to RICH rings. In case of

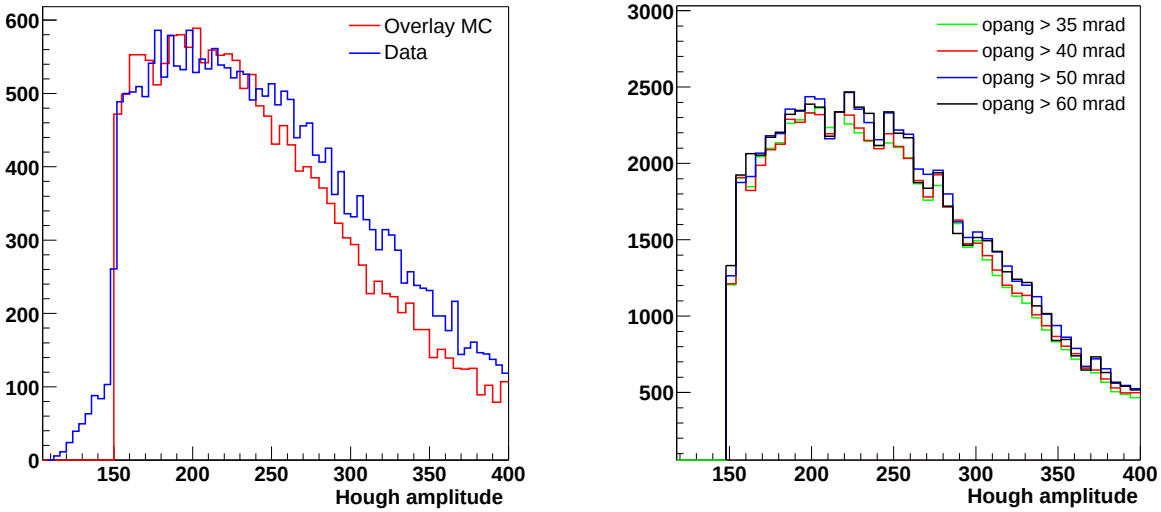

Figure 6.3: Hough amplitude distributions for the data Dalitz sample and the reconstructed π^0-Dalitz decays in the Monte-Carlo simulation (left panel) and simulated hough amplitude distributions for different opening angles of π^0-Dalitz decays (left panel).

the dead region no match was found. The resulting θ-ϕ map of the matched tracks was applied on the level of global tracks. A proper scaling of the map was done to account for the efficiency losses due to a cut on Hough amplitude of the rings. Fig. 6.2 shows the comparison of the ϕ-distributions of single tracks in the data and in the simulations. The two large areas with low efficiency at $\approx$ -1 mrad and 1 mrad can be seen. The dead regions are reasonably described by the MC using the constructed θ-ϕ map.

In order to study the performance of the RICH MC the Dalitz decay sample was selected in the real data. Two identified electron tracks via energy loss in the TPC with opening angle between 10 and 35 mrad were matched with SDD segments. The correlated cut on dE/dx in silicon drift detectors was applied to remove γ-conversions. Obtained SDD-TPC tracks were finally matched to RICH rings. No cuts on ring quantities were applied.

The Dalitz decays were also generated with GENESIS, passed through GEANT and finally reconstructed with the analysis software applying identical opening angle cut.

RICH rings are characterized by Hough amplitude, number of hits and sum analog amplitude. The comparison of the distributions on Hough amplitude obtained for the data and MC is shown in Fig. 6.3. Although a tail of the MC distribution deviates from the data , the overall shape is reproduced. Possible effect of the touching ring problem was clarified by varying a cut on the opening angle of the π^0-Dalitz decays (Fig. 6.3). For four different opening angle cuts from 35 mrad until 60 mrad the Hough amplitude distributions stay almost identical.

Fig. 6.4 illustrates the MC distributions on hits per ring and sum analog amplitude for both RICH1 and RICH2 plotted on top of the data distributions. A shift of 1 hit is observed

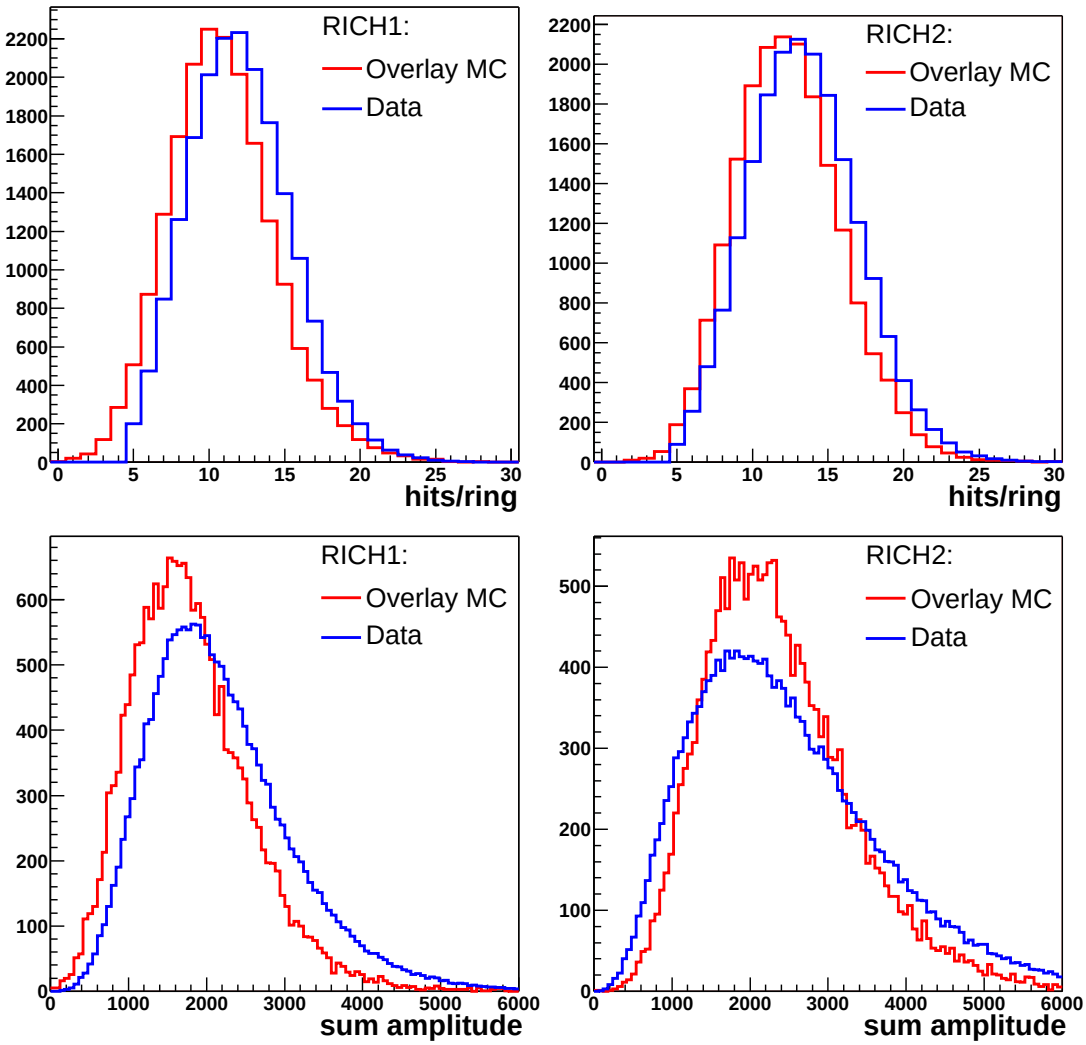

Figure 6.4: Comparison between the hits per ring (top) and sum amplitude (bottom) distributions in the data and in the Monte-Carlo simulation for RICH1 (left side) and RICH2 (right side).

for the hits on ring in the two RICH detectors. The observed disagreement might be an effect of the remaining gain fluctuations. An admixture of the γ-conversions to the π^0-Dalitz decay sample may also distort the resultant distributions, particularly increase a number of hits on rings. The sum analog amplitude distributions do not well coincide also. However in the data analysis the cuts on sum amplitude were discarded as a possible source of the systematic uncertainties. A cut on hits per ring in the data analysis is very soft and, thus, does not almost affect the efficiency.

6.3 The TPC

Simulation of the CERES TPC consists of the following steps:

- Generation of ionization along the track
- Electron propagation in the electric field
- Generation of the pad signal
- Creation of the ”raw” Monte-Carlo pixels

Generation of ionization is based on GEANT hits used to construct a straight track segment along which the primary ionization is randomly distributed. Primary specific ionization for each track is calculated according to [108]. Fluctuations of the number of primary collisions are well described by Poisson statistics [109]. The number of primary ion pairs is scaled with the segment length. For each primary ion pair, secondary ionization is calculated by generating a spectrum of δ-electrons.

Propagation in the electric field is then performed for each ionization electron. The drift velocity at a given position in the TPC is calculated using electric field table. To find a new position of the electron after a certain drift time a set of ordinary differential equations is solved numerically. After each iteration the transverse and longitudinal coefficients are used to smear the electron position. Th last increment of the drift time is calculated according to the knowledge of the exact position of the readout chamber.

The pad signal generation is based on the induced charge distribution. The ionization electrons arrive at a certain position on the pad plane. If z-position of the electron is outside of the anode wires region, the electron is assumed to be lost. The signal on the wire at which the primary ionization electron creates an avalanche, is generated. The induced charge distribution on the pad plane is calculated according to the Gatti single parameter empirical formula [110]. The pad response function is then computed by integrating the induced charge distribution over the pad area.

The raw MC pixels are defined as pad signals in a certain time-bin. The arrival time of the primary ionization electrons has been determined during the propagation of the electrons in the electric field of the TPC. The signal induced on the pads has long tails due to the long drift time of the ions produced by the avalanche. The start of the induced signal depends on the position of the primary electron with respect to the anode wire. The charge induced on the pad is spread out in time according to the time distributions of the induced signal for different positions of the primary electron with respect to the anode. The total time range is divided into 8×256 bins and the width of each time-bin corresponds to the transfer function of the TPC electronics. All the signals which fall into a given time-bin are summed up for each pad. The final list of pixels consist of the pad and plane numbers, time-bin, and amplitude.

The quantities of the TPC track are a number of hits on track, momentum, ϕ and θ coordinates and energy loss. In order to check whether the TPC MC is realistic the simulated distributions were compared to the data. Based on the electron tracks identified with strong cuts in the RICH the comparison between the data and the MC Dalitz decays is

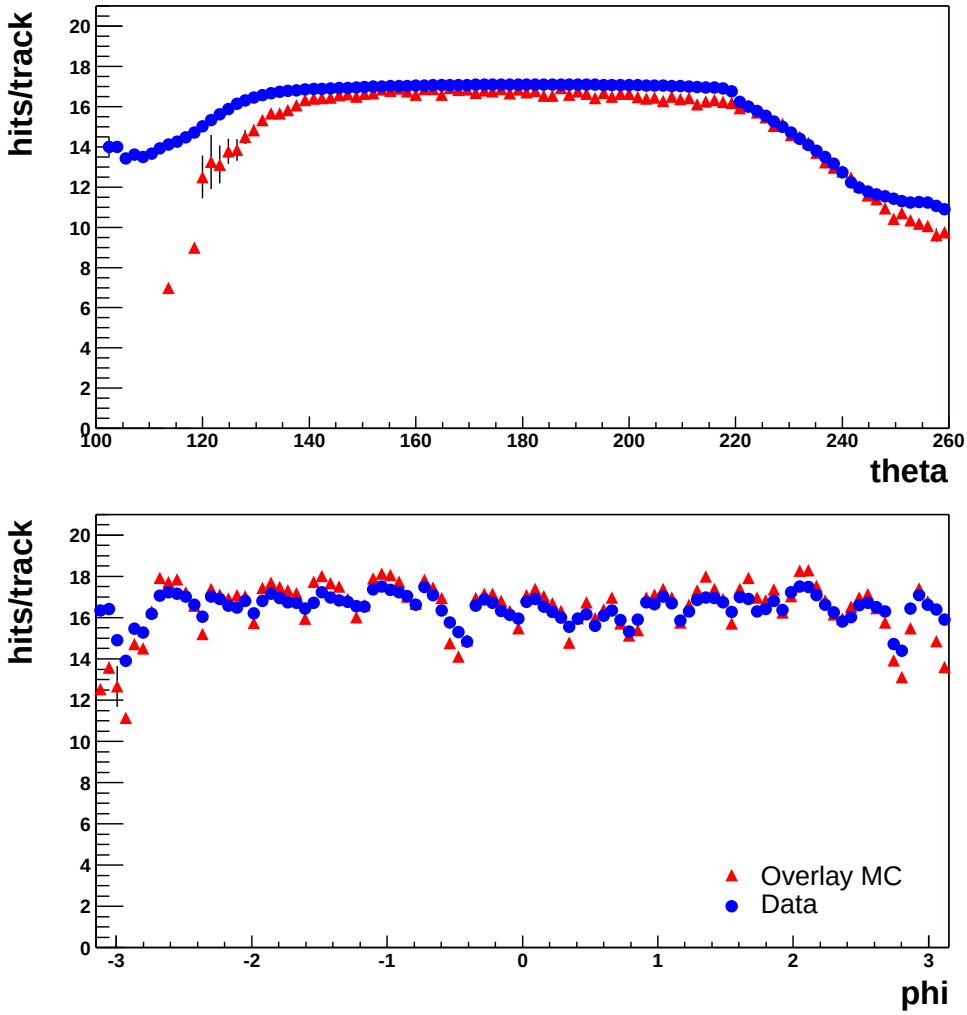

Figure 6.5: Number of hits on track as a function of theta (top) and phi (bottom) in the data and in the Monte-Carlo simulation.

performed. Fig. 6.5 shows the MC distribution of a number of hits on track as a function of θ and ϕ on top of the data. All 16 holes between chambers in the ϕ dependence as well as inefficient region at ϕ of approximately -3 mrad are well described. Thus rather good agreement within the TPC acceptance $0.141 < \theta < 0.244$ rad. is observed. A comparison of the energy loss by electrons between the simulation and the data is illustrated in Fig. 6.6. Again the MC distribution agrees with the data quite well. More comprehensive comparison of energy loss by both pions and electrons between data and overlay MC was performed for different momentum bins. Electron and pion tracks were generated with realistic momentum distributions, then put on top of the real events and reconstructed applying track quality cuts similar to the data. The overlay Monte Carlo exhibits good description of the data over the two orders of magnitude (limited by accumulated statistics) as illustrated in Fig. 6.7 for two momentum bins.

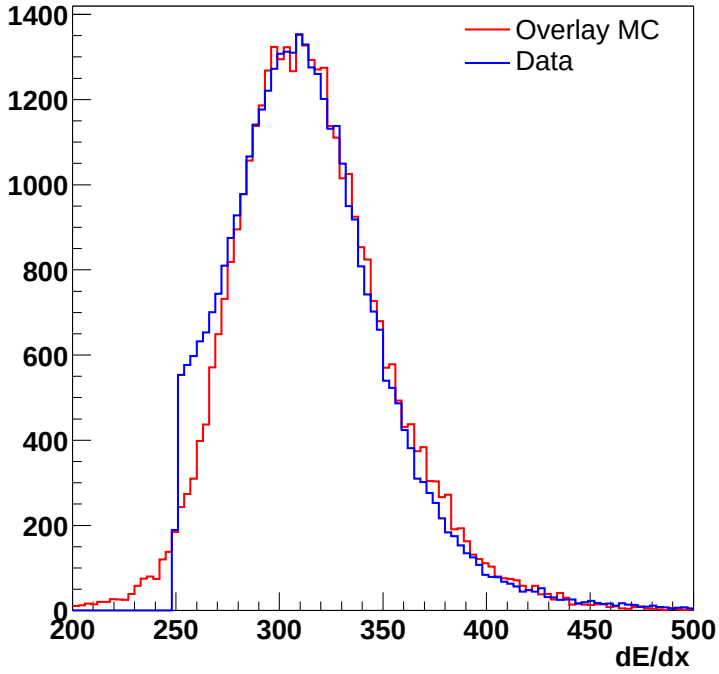

Figure 6.6: Comparison between energy loss distributions in the data and in the simulation.

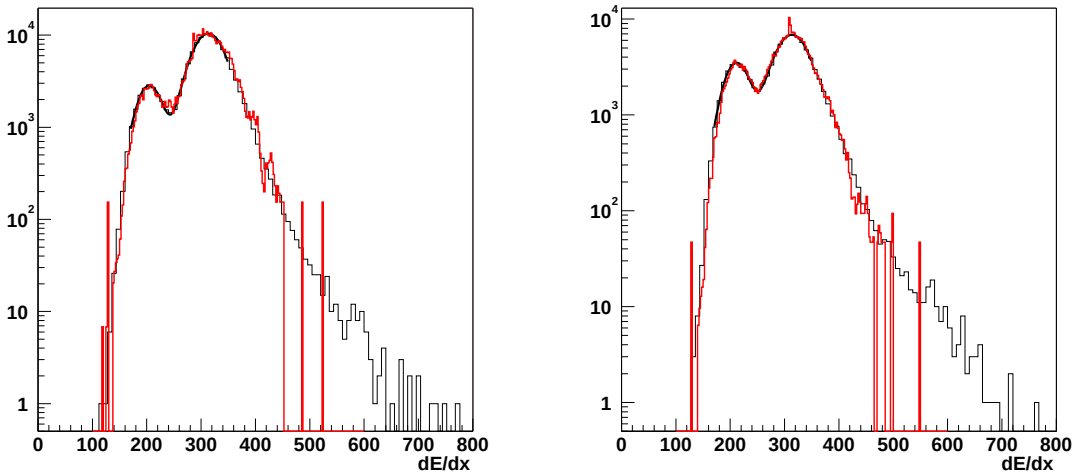

Figure 6.7: Comparison of the energy loss by electrons and pions between data (black histogram) and overlay MC (red histogram) for two different momenta p = 0.83 MeV/c (left panel) and p = 1.17 MeV/c (right panel).

6.4 Matching between Detectors

Once all segments in separate detectors are reconstructed, they are matched in order to create global tracks. Since in the data analysis the cuts are applied on the matching

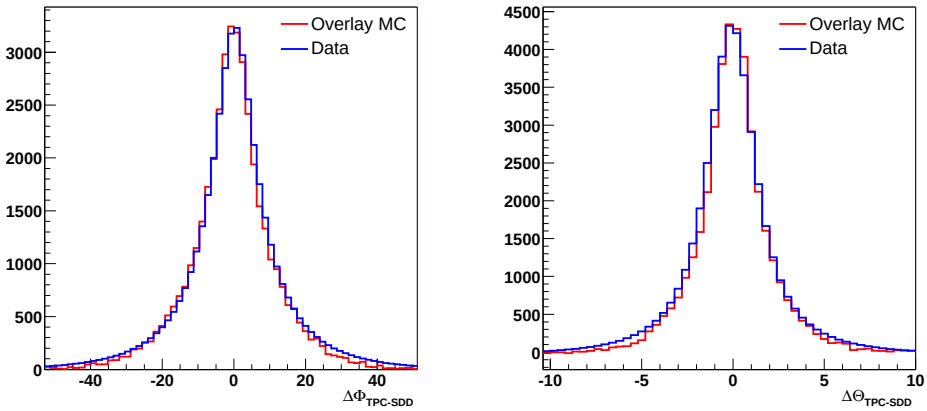

Figure 6.8: Comparison of the ϕ- (left) and θ- (right) matching distributions in the data and in the Monte-Carlo simulation for SDD and TPC combination.

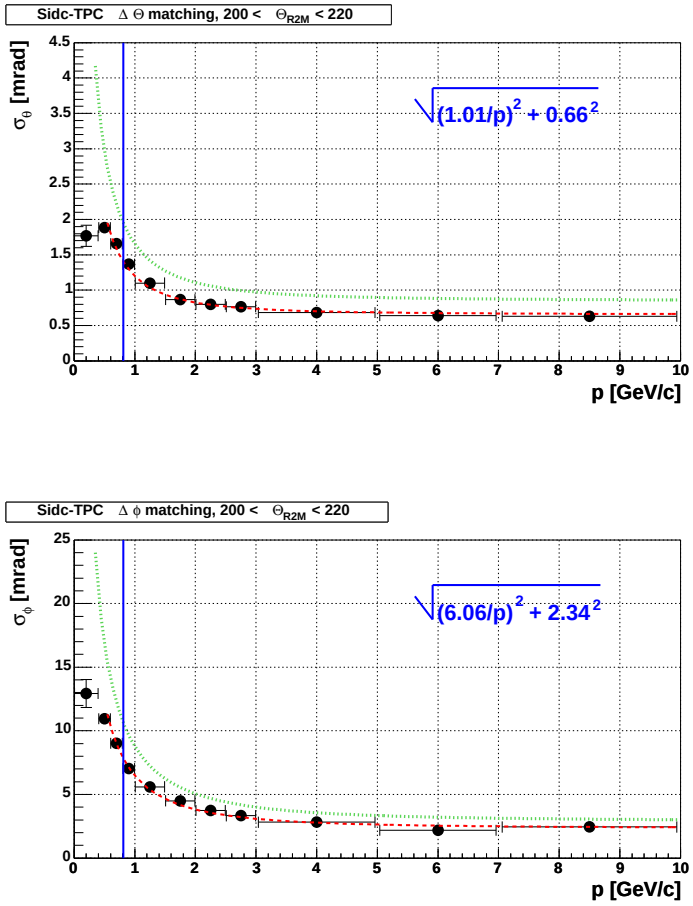

Figure 6.9: Width of the matching distributions between SDD and TPC in θ (top) and ϕ (bottom) as a function of momentum for a case of multi-anode hits on SDD tracks. The black points represent the simulation. Parameterization of the simulated width is indicated by red curve. The data parameterization is shown by green curve.

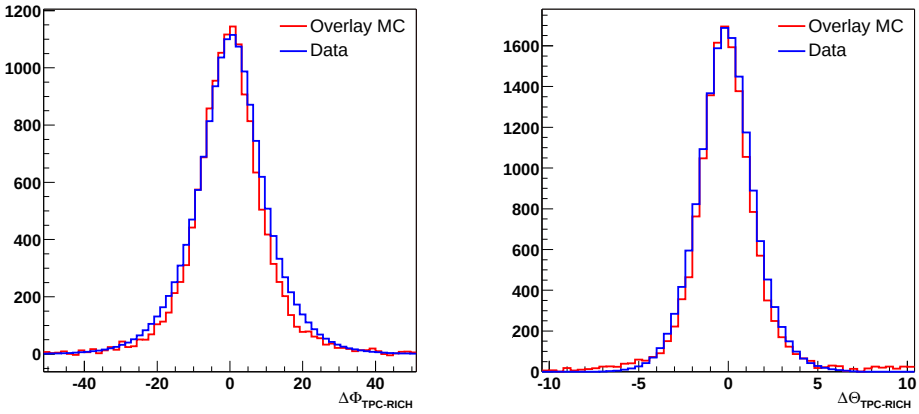

Figure 6.10: Comparison of the ϕ- (left) and θ- (right) matching distributions in the data and in the Monte-Carlo simulation for RICH and TPC combination.

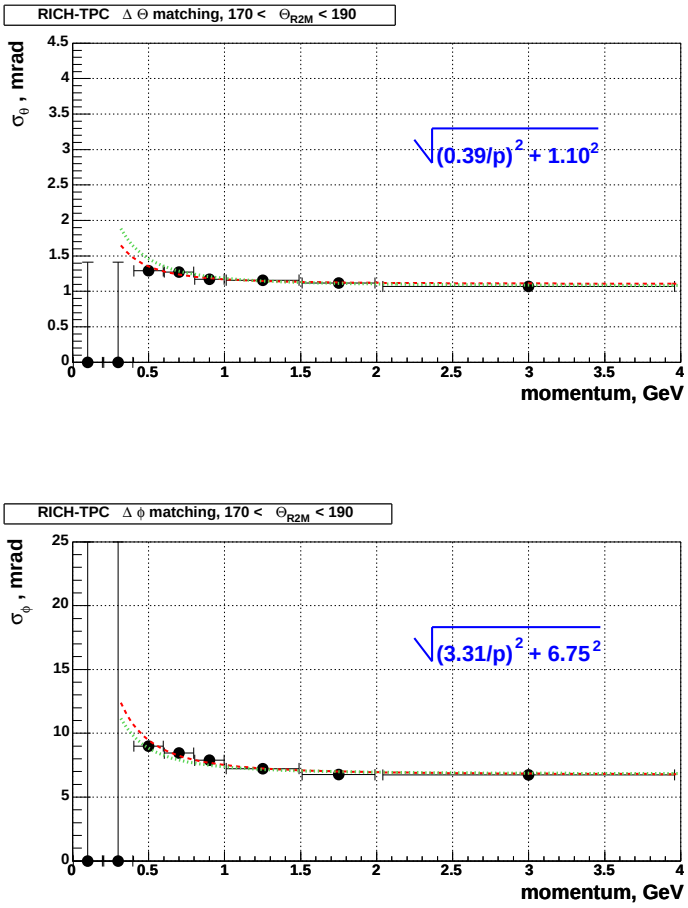

Figure 6.11: Width of the matching distributions between RICH and TPC in θ (top) and ϕ (bottom) as a function of momentum. The MC points are parameterized by the momentum dependent function (red curve). The parameterization of the data with identical type of function is shown by green curve.

distributions, the width and the mean of the matching between different detectors must be similar in the data and in the simulation. The overall matching distributions in ϕ and in θ for the data and the Monte-Carlo are shown in Fig. 6.8 for SDD and TPC combination and in Fig. 6.10 for RICH and TPC combination. Simulated with overlay MC technique distributions seam to accurately describe the data for both detector combinations SDD-TPC and RICH-TPC. However the width of the matching distributions depends on momentum of the track due to multiple scattering effects and therefore this dependence was taken into account. The observed dependence of the width on θ and SDD hit topology was also simulated in Monte-Carlo. The width of the simulated matching distribution in ϕ and in θ as a function of momentum for the θ-bin $170 < \theta < 190$ mrad. is displayed in Fig. 6.11 for the RICH-TPC. The parameterization of the data is well described by the MC dependence of the width of both $\Delta\phi$ and $\Delta\theta$ matching distributions. In case of match to SDD detector system, simulated distributions were checked for different combinations of SDD hit topologies similarly to the data. The SDD tracks were divided into three groups: tracks with two single-anode hits, tracks with single-anode and multi-anode hits, and tracks with two multi-anode hits. Fig. 6.9 shows the momentum dependent width of the MC matching distribution in ϕ and in θ within the θ-bin $200 < \theta < 220$ mrad for a case of two multi-anode hits on SDD tracks. Both the MC and the data parameterizations are reasonably close.

6.5 Pair Reconstruction Efficiency

To be able to compare the data with the hadronic cocktail and/or the theoretical calculations, the reconstructed e^+e^- pairs must be absolutely normalized. One part of the normalization procedure is the correction of the reconstructed electron pairs according to the pair reconstruction efficiency. The efficiency correction is done on the event-by-event basis multiplying every e^+e^- pair with the inverse efficiency for that event.

After the responses of all the detector systems are simulated properly the generated distributions can be used to compute the track reconstruction efficiencies. In order to cover low and high mass ranges detected by the CERES experiment, the four decays - $\pi^0 \rightarrow \gamma e^+e^-$, $\eta \rightarrow \gamma e^+e^-$, $\rho \rightarrow e^+e^-$ and $\phi \rightarrow e^+e^-$ were generated with GENESIS generator applying standard analysis cuts as theta acceptance of $0.141 < \theta < 0.244$ rad., transverse momentum cut of $p_t > 0.2$ GeV/c and opening angle cut of 35 mrad. Thus there are always only two MC electron tracks per event originated from the primary decay within the acceptance of the spectrometer. The total number of generated events is $2{\cdot}10^5$ for each decay mode. Then the full simulation of detectors was performed by GEANT3 including simulation of interactions in the material and the energy deposition as already discussed. The output of GEANT3 was digitized and overlayed on the real data in order to reproduce real occupancy in the detectors. The obtained event was then analyzed by the CERES reconstruction software following all steps of the data analysis: step2, step3 and step4. Identical cuts were applied for the MC tracks as for the data. The momentum and theta distributions of the generated decays before and after analysis cuts are illustrated in Fig. 6.12 and Fig. 6.13[1], respectively.

[1]Theta acceptance, transverse momentum cut and opening angle cut are applied for both cases before

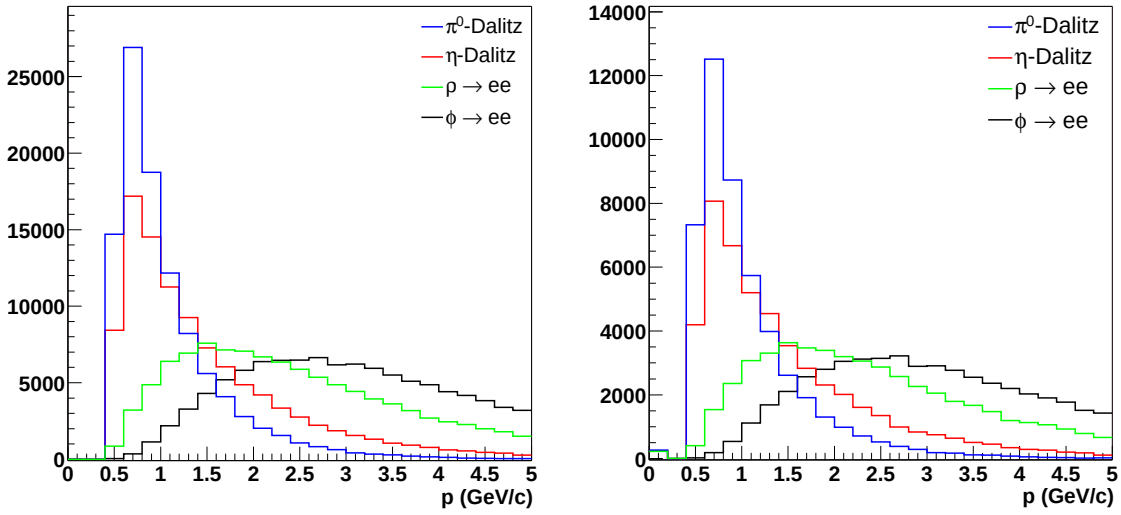

Figure 6.12: Momentum distributions of four generated decays before analysis cuts (left panel) and after analysis cuts (right panel).

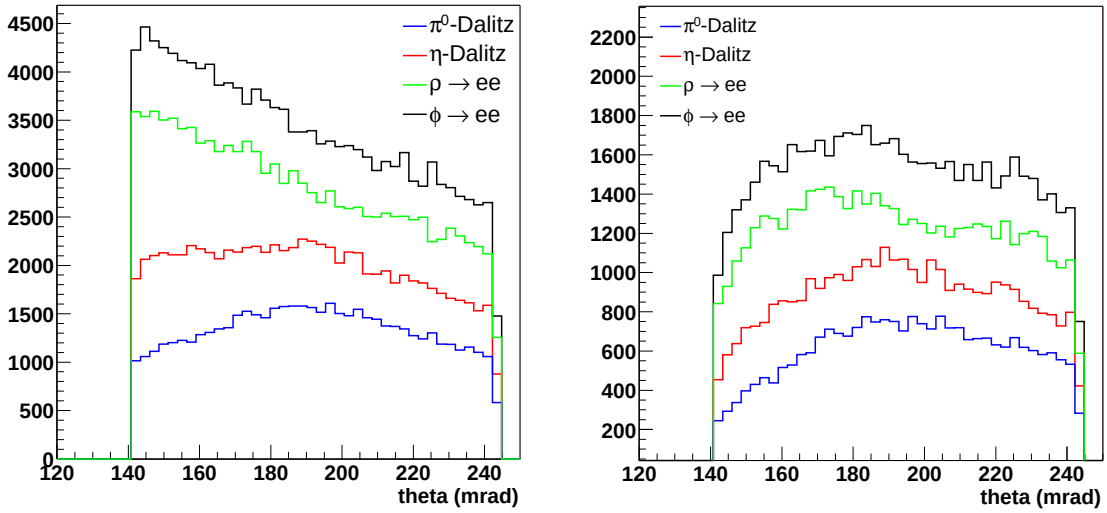

Figure 6.13: Theta distributions of four generated decays (π^0, η, ρ, ϕ) before analysis cuts (left panel) and after analysis cuts (right panel).

The single track efficiency is determined as a ratio of reconstructed tracks surviving all analysis cuts and initial generated tracks. The pair efficiency is similarly defined requiring two tracks being reconstructed. In order to accurately evaluate the pair efficiency, the various dependencies of the single track efficiency on θ, track momentum and event multiplicity were studied. The track reconstruction efficiency in the TPC starts to decrease far below 1 GeV/c momentum which approximately corresponds to transverse momentum cut of 0.2 GeV/c. Therefore in the low momentum region close to applied p_t cut

and after analysis cuts.

the efficiency is not expected to depend on momentum. On the other hand, the momentum dependent cut on specific energy loss in TPC may influence the track efficiency at high momenta which can mostly affect the ϕ meson. This has been investigated for four generated sources as a function of momentum. The results are shown in Fig. 6.14. In

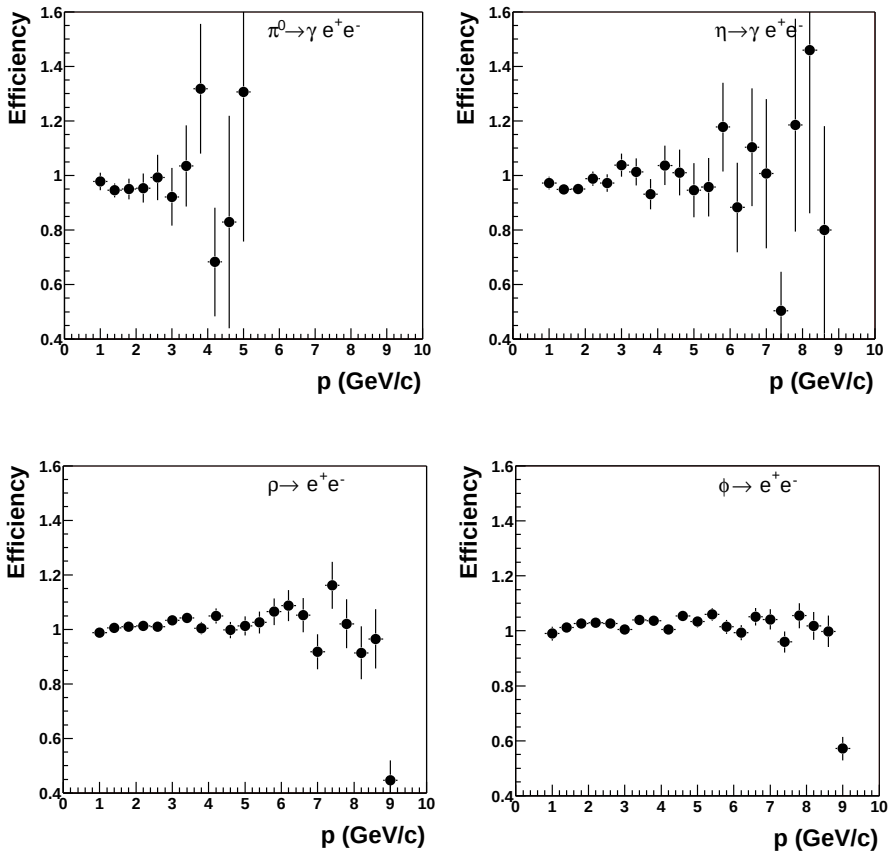

Figure 6.14: Single track efficiency as a function of momentum for four simulated decays (π^0, η, ρ, ϕ).

fact, the momentum dependence of the efficiency was observed neither for low momenta nor for the high momentum region proving that the gliding cut on the TPC dE/dx versus momentum with low slope is a safe one.

Another study of the efficiency as a function of θ was also performed for four simulated decays as shown in Fig. 6.15. A strong dependence of the track efficiency on θ was found. Moreover all four sources exhibit very similar dependencies in terms of shape and absolute values. To study the multiplicity dependence of the reconstruction efficiency the multiplicity was divided into five bins. Fig. 6.16 displays the single track efficiency dependence on θ for lowest and highest multiplicity bins.

A reasonable parameterization of the efficiency as a function of θ is performed by a fit with polynomial. Although the observed dependence of the efficiency on the event multiplicity is weak, it was absorbed in the efficiency correction procedure described below.

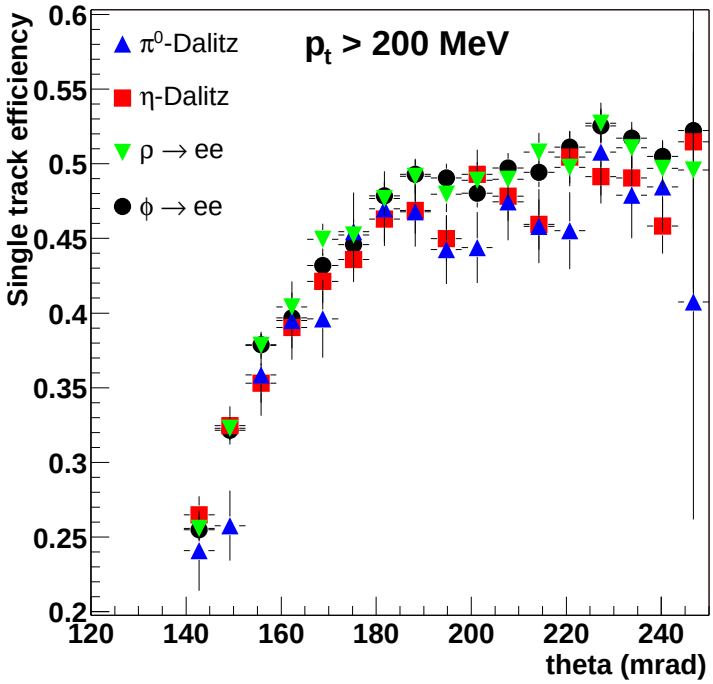

Figure 6.15: Single track efficiency as a function of theta for four simulated with GENESIS sources (π^0, η, ρ, ϕ).

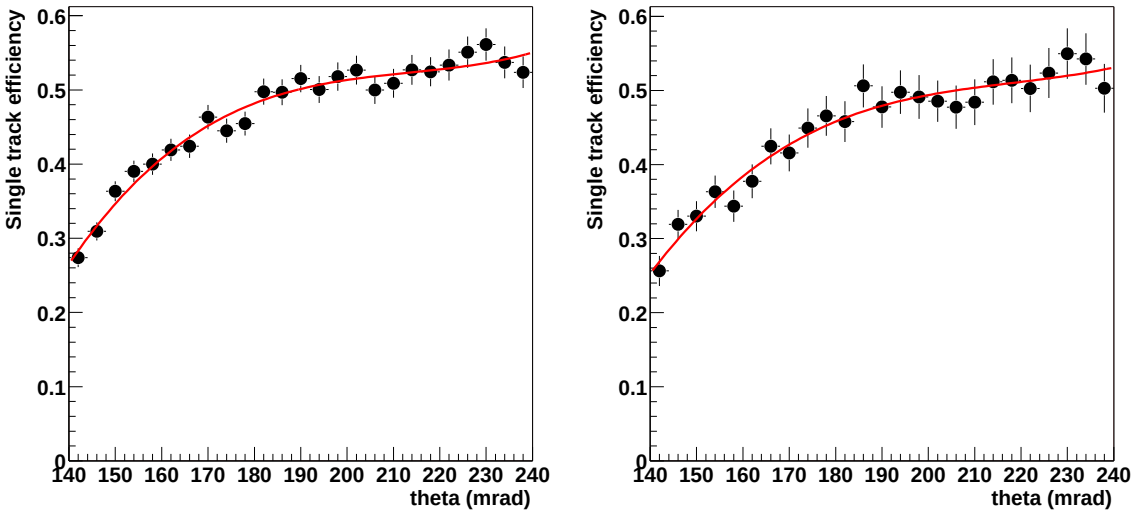

Figure 6.16: Single track efficiency as a function of theta for first multiplicity bin (left panel) and last multiplicity bin (right panel).

For a track with θ-coordinate from a given event with multiplicity m the reconstruction efficiencies ϵ_1 and ϵ_2 are derived from the parameterization for the same θ for lowest m_1 and highest m_2 multiplicity bins. A line is then constructed based on the two points (ϵ_1,

m_1) and (ϵ_2, m_2). This line describes a dependence of the efficiency on the multiplicity for a given θ. Finally the track efficiency is extracted from the line equation for a given event multiplicity m:

$$\epsilon = \frac{\epsilon_2 \cdot m_1 - \epsilon_1 \cdot m_2}{m_1 - m_2} + \frac{\epsilon_1 - \epsilon_2}{m_1 - m_2} \cdot m. \tag{6.1}$$

Fig. 6.17 shows a dependence of the reconstruction efficiency on the event multiplicity for four different θ bins. The parameterizations of efficiency dependences calculated according to the described procedure show good description of the separate efficiency values for each θ-bin within statistical errors as illustrated in Fig. 6.17.

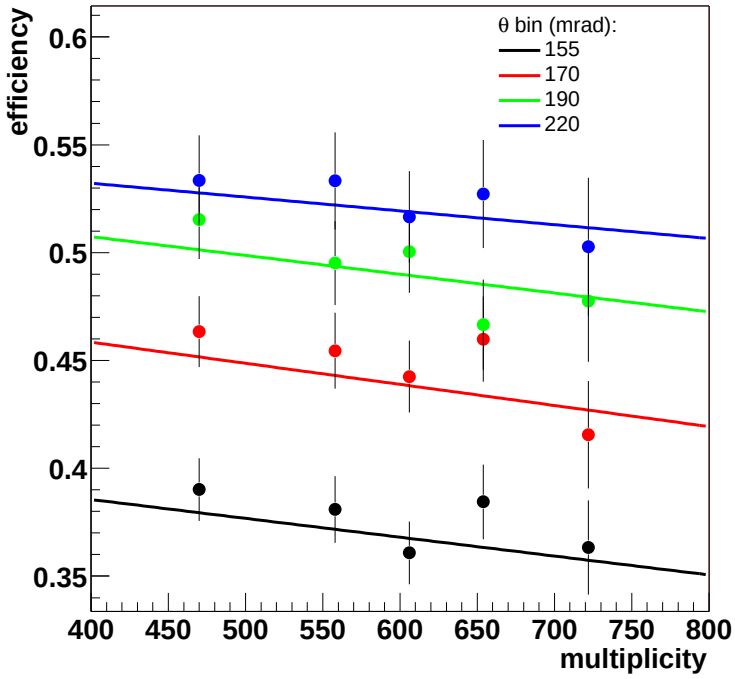

Figure 6.17: Single track efficiency as a function of multiplicity for different theta values. The parameterizations of the efficiency dependence are shown by lines. A reasonable agreement between the parameterization and the actual values of the efficiencies is observed.

In the absence of pair effects the pair reconstruction efficiency ϵ_{ee} can be decomposed into the products of the track efficiencies:

$$\frac{1}{\epsilon_{ee}} = \frac{1}{\epsilon_{track1}(\theta_1, N_{ch}) \cdot \epsilon_{track2}(\theta_2, N_{ch})}, \tag{6.2}$$

where $\epsilon_{track1}(\theta_1, N_{ch})$ and $\epsilon_{track2}(\theta_2, N_{ch})$ are the derived single track efficiencies as a function of θ and event multiplicity. To investigate the possible pair effects the pair reconstruction efficiency corrected for the single track efficiency as a function of θ and event multiplicity was plotted against an opening angle (Fig. 6.18).

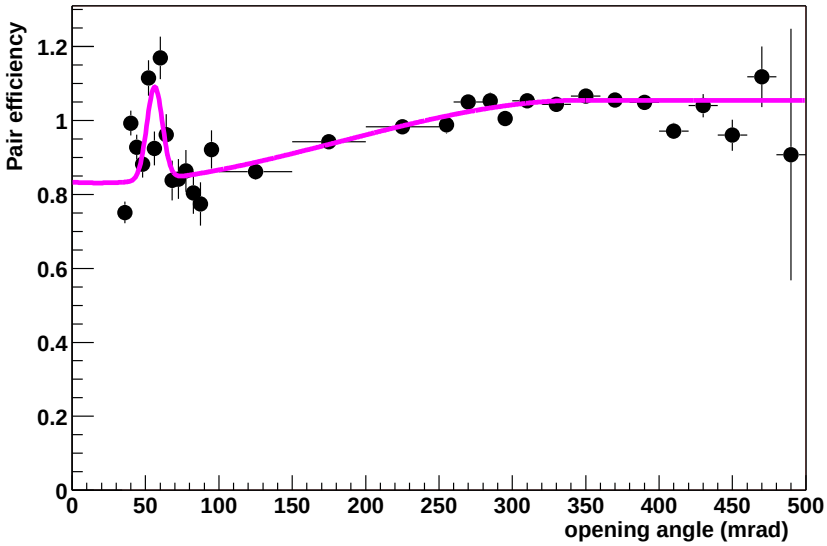

Figure 6.18: Pair efficiency as a function of opening angle between two tracks belonging to th same event. Parameterization of the efficiency dependence absorbs an effect of touching ring leading to a peak at 60 mrad (approximately twice the radius of electron ring).

To cover wide opening angle range the four simulated sources were summed up. The two pair effects were observed. The first one is the peak at 60 mard corresponding to two touching rings. In fact, one electron ring helps with its hits to another ring located two ring radiuses apart resulting in increasing reconstruction efficiency of such a pair. The second pair effect is the underlying drop of efficiency which starts at opening angles of approximately 250 mrad. and continues down to very small opening angles. Actually, due to the analysis opening angle cut of 35 mrad, a behavior of the pair efficiency in the region between 0 and 35 mrad is not known (assumed to be flat matching a decrease of efficiency in the region $65 < \theta_{ee} < 250$ mrad). This surprising drop of the pair efficiency can be accounted for by the specific construction of the experimental setup. The geometrical effect may arise from a location of the radial spokes in both RICH detectors (10 spokes in RICH1 and 16 spokes in RICH2) with a distance between spokes comparable to the diameter of the electron ring. Moreover the pair efficiency drop was found to be a consequence of the dependence of efficiency on $\Delta\phi$ between two electron tracks while a dependence of pair efficiency on $\Delta\theta$ was not observed. This speaks in favor of the geometrical effects responsible for the decrease of pair efficiency. An attempt to additionally correct single tracks by track efficiency as a function of ϕ did not resolve a problem and the specific behavior of pair efficiency blow 250 mrad remained. The dependence of the pair efficiency on the opening angle θ_{ee} was then parameterized by

$$p(\theta_{ee}) = p_0 + p_1 \cdot \theta_{ee} + p_2 \cdot \theta_{ee}^2 + p_3 \cdot \theta_{ee}^3 + C \cdot \exp(-0.5(\theta_{ee} - M)/w)^2), \qquad (6.3)$$

where M corresponds to a mean of the peak at 60 mrad., w is a peak width, C is the

normalization of the Gaussian and p_0, p_1, p_2, p_3 are the parameters of the polynomial. For the mixed event background the parameterization was based only on a polynomial of third order as shown in Fig. 6.19. Since the peak at 60 mrad is a result of the touching rings, this structure must not present in the event mixing when two tracks combined in a pair come from different events.

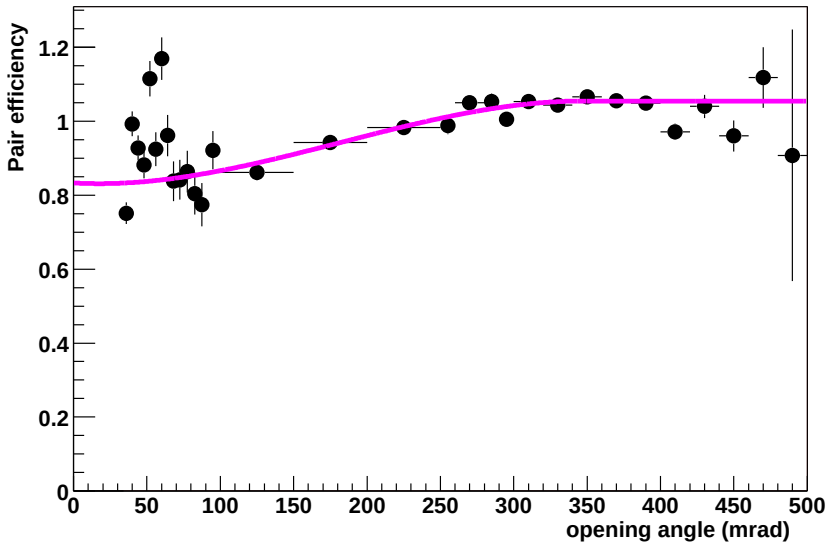

Figure 6.19: Pair efficiency as a function of opening angle between two tracks from the same event. Parameterization of the efficiency dependence is done for the pair efficiency correction of the mixed event background. The peak at 60 mrad is ignored as a feature of the pairs with both tracks coming from the same event.

According to all studied effects the pair efficiency factorizes into track efficiencies depending on N_{ch} and θ and additional corrections for pair effects:

$$\frac{1}{\epsilon_{ee}} = \frac{1}{\epsilon_{track1}(\theta_1, N_{ch}) \cdot \epsilon_{track2}(\theta_2, N_{ch}) \cdot \epsilon_{ee}(\theta_{ee})}, \tag{6.4}$$

where $\epsilon_{ee}(\theta_{ee})$ is the parameterization of the par efficiency dependence on the pair opening angle which is done differently for the pairs with both tracks from the same event and for the mixed event pairs as discussed above.

7

Results

In this chapter the final results of the experimental analysis of dilepton production in Pb-Au collisions at 158 A GeV from the 2000 run are discussed. The data are compared to the expectations based on free decay processes of the various hadrons in the final state and to the calculations based on the free $\pi\pi$ annihilation which is expected to be a dominant source of e^+e^- pairs at SPS energies. In order to learn about the type of medium modifications needed, in fact, to account for the experimental results, the data are compared to different theoretical models invoking in-medium modifications.

7.1 Data Normalization

In the absence of a new physics an ion-induced reactions can be considered as a mere superposition of the nucleon-nucleon collisions. Therefore the dilepton production probability per event scales with the event multiplicity. Thus the data are normalized to represent the pair production probability per charged particle within the CERES rapidity acceptance:

$$\frac{\langle dN_{ee}/dm_{ee}\rangle}{\langle N_{ch}\rangle} = \frac{(dN_{ee}/m_{ee})_{corr}}{N_{ev}\cdot\langle dN_{ch}/d\eta\rangle\cdot\Delta\eta}, \tag{7.1}$$

where $(dN_{ee}/m_{ee})_{corr}$ is the number of measured e^+e^- pairs per mass interval corrected for efficiency as described in the chapter 6.5, N_{ev} is the total number of analyzed events, $\langle dN_{ch}/d\eta\rangle$ is the charged particle rapidity distribution per unit of rapidity at the CERES acceptance, $\Delta\eta$ is the CERES fiducial acceptance (0.55).

7.2 Mass Spectrum

The absolutely normalized e^+e^- invariant mass spectrum after mixed-event background subtraction is shown in Fig 7.1. The procedure of the normalization was described in previous section. For the efficiency correction see section 6.5. The numbers of electron

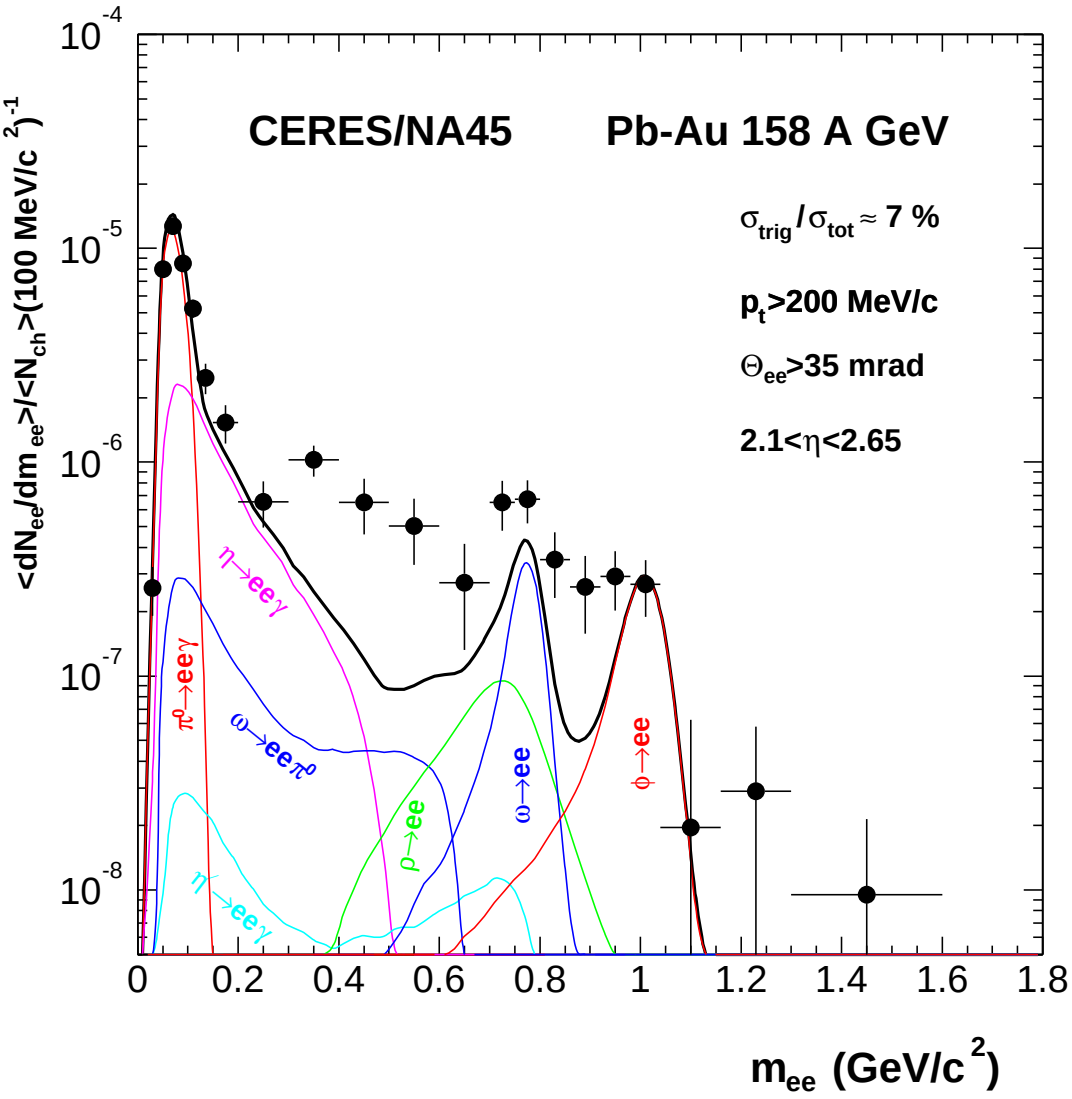

Figure 7.1: Inclusive e^+e^- invariant mass spectrum for Pb-Au collisions at 158 GeV/c per nucleon. The spectrum is corrected for pair efficiency and normalized to $\langle N_{ch} \rangle$. The solid black curve represent the expected yield of all hadronic sources.

pairs together with the signal to background ratios in the final sample for low- and high-mass regions are given in Table 7.1. The statistical errors of the data are shown as vertical bars.

Comparison of the e^+e^- invariant mass spectrum and hadronic decays (see Fig 7.1) shows a good agreement within the errors for the masses below 200 MeV/c^2 where the expected yield is dominated by π^0-Dalitz decays. However, for the high-mass region above 200 MeV/c^2 the data significantly overshoot the hadronic decay cocktail in contrast to the proton-induced reactions where the excellent agreement with the expectations from hadronic decays was found. In the mass region $0.2 < m_{ee} < 1.1$ GeV/c^2 the en-

Mass range (MeV/c^2)	Signal	S/B
m $<$ 200	5470 $\pm$ 168	1/2
m $>$ 200	2818 $\pm$ 258	1/21

Table 7.1: Yields of e^+e^- pairs and signal-to-background ratio for different mass regions.

hancement factor (the ratio of the integrated measured yield to the yield obtained from the hadronic decays) is 2.45 $\pm$ 0.22[stat] $\pm$ 0.38[syst] $\pm$ 0.74[decays]. The normalized yield of e^+e^- pairs integrated for the masses 0.0 $< m_{ee} <$ 0.2 GeV/c^2 is (8.44 $\pm$ 0.28[stat] $\pm$ 1.33[syst])$\times 10^{-7}$. Integrating the normalized yield in the mass region 0.2 $< m_{ee} <$ 1.1 GeV/c^2 gives (4.49 $\pm$ 0.41[stat] $\pm$ 0.70[syst])$\times 10^{-7}$. Systematic errors are described in section 7.5.

A continuum exceeding the hadronic cocktail occupies the mass region between 200 MeV/c^2 and 600 MeV/c^2. Different to all previous CERES results, the resonance structure triggered by vector mesons is seen for the masses above 600 MeV/c^2. Due to improved mass resolution with radial-drift TPC the ω and ϕ vector mesons are measured. The yield of the ϕ meson in the electromagnetic decay has been studied in detail [111]. A yield of $dN/dy(\phi \rightarrow e^+e^-)$ = 2.04 $\pm$ 0.49[stat] $\pm$ 0.32[syst] is obtained. After correction for acceptance and efficiency this value agree with the yield on K^+K^- measured also by CERES. The difference larger than 1.6 between two channels is expected at 95% confidence level.

In addition it is also interesting to look at transverse pair momentum dependence of the electron pair yield. The mass spectra with different pair-p_t^{ee} cuts $p_t^{ee} <$ 500 MeV/c and $p_t^{ee} >$ 500 MeV/c are shown in Fig 7.2. Two spectra (left panel and right panel) are very different both in shape of the continuum and in the absolute number of pairs for the mass region 200 $< m_{ee} <$ 700 MeV/c^2. The enhancement in the high-mass region is larger for $p_t^{ee} <$ 500 MeV/c whereas for the masses below 200 MeV/c^2 the data are perfectly described by the hadronic cocktail. The ratio of the integrated normalized yield of e^+e^- pairs to the yield derived from the sum of the hadronic sources in the mass region 0.2 $< m_{ee} <$ 0.6 GeV/c^2 is 2.26 $\pm$ 0.27[stat] $\pm$ 0.35[syst] $\pm$ 0.68[decays] for $p_t^{ee} >$ 500 MeV/c and 4.29 $\pm$ 1.15[stat] $\pm$ 0.67[syst] $\pm$ 1.29[decays] for $p_t^{ee} <$ 500 MeV/c.

7.3 Pair-pt Spectra

In order to discriminate different mechanisms leading to a strong dilepton enhancement in the invariant mass spectra, the dilepton transverse momenta (the total momentum of the dilepton pair perpendicular to the beam axis of the colliding nuclei) have been measured. Fig. 7.3 shows the transverse pair momentum distributions for the three mass regions $m_{ee} <$ 200 MeV/c^2, 200 $< m_{ee} <$ 700 MeV/c^2 and $m_{ee} >$ 700 MeV/c^2 compared with expectations from hadronic decays. The single particle transverse momentum cut $p_t >$ 200 MeV/c^2 strongly effects the pair transverse momentum distribution for masses below 400 MeV/c^2 at low pair-p_t^{ee}.

For masses below 200 MeV/c^2 the data agree with the predictions from the cock-

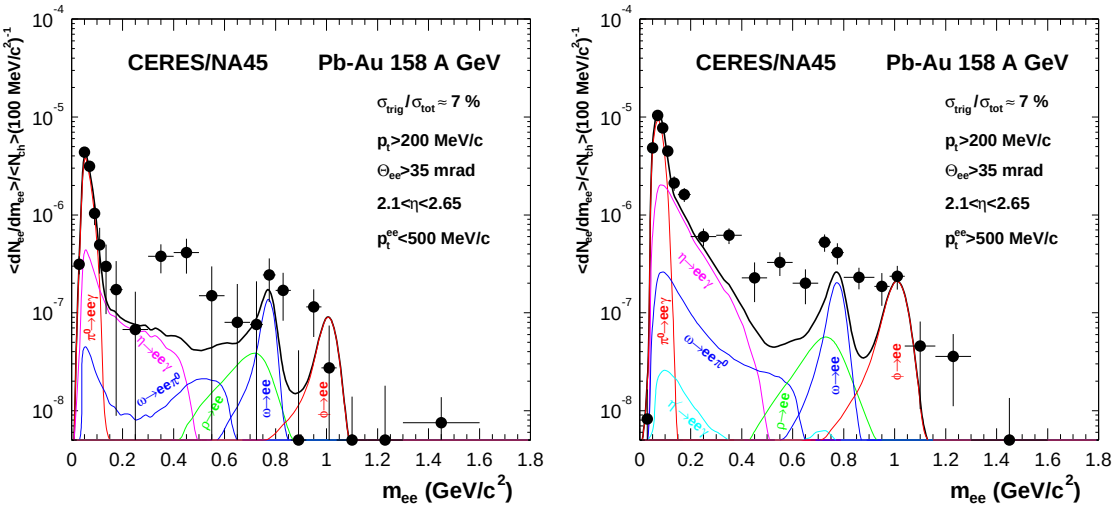

Figure 7.2: Inclusive mass spectra for the two transverse pair momentum bins. Left panel: $p_t^{ee} <$ 500 MeV/c. Right panel: $p_t^{ee} >$ 500 MeV/c. The solid line shows the hadronic decay cocktail.

tail dominated in this mass region by π^0-Dalitz and η-Dalitz decays (top panel). In the mass region 200 $< m_{ee} <$ 700 MeV/c^2 the experimental points lie significantly above the hadronic decay contributions (middle panel). The enhancement previously seen in the invariant mass spectrum shows up also in the transverse pair momentum distributions. The effect is strongest for pair-$p_t^{ee} <$ 600 MeV/c. In the third mass bin above 700 MeV/c^2 enhancement of the data over the cocktail still remains although somewhat lower in magnitude than in the middle mass region. The excess of the experimental points for $m_{ee} >$ 700 MeV/c^2 corresponds to the excess observed in the e^+e^- mass spectrum between the ω and the ϕ vector mesons.

7.4 Multiplicity Dependence of Enhancement

One of the main evidences for a 'non-trivial' source of the dilepton pairs in heavy ion collisions is the dependence of the dilepton signal on the charge particle density. Fig. 7.4 displays the enhancement factors as a function of $dN_{ch}/d\eta$ for three e^+e^- invariant mass regions: $m_{ee} <$ 200 MeV/c^2, 200 $< m_{ee} <$ 600 MeV/c^2 and $m_{ee} >$ 600 MeV/c^2.

If hadron decays are the only sources of dielectron pairs, as is the case in p-p and p-A collisions, the data should scale linearly with charged multiplicity, as indicated by the horizontal line in Fig 7.4. This behavior is observed in the lowest mass region which is occupied by the Dalitz decays representing a trivial hadronic sources of the e^+e^- pairs. However, taking into account that the cocktail yield per number of charged particles does not depend on N_{ch}, the data clearly exhibit a stronger than linear dependence as a function of charged multiplicity within higher mass windows. The largest effect is observed for the masses between 200 and 700 MeV/c^2, whereas in the resonance region for masses above 600 MeV/c^2 the enhancement is somewhat reduced.

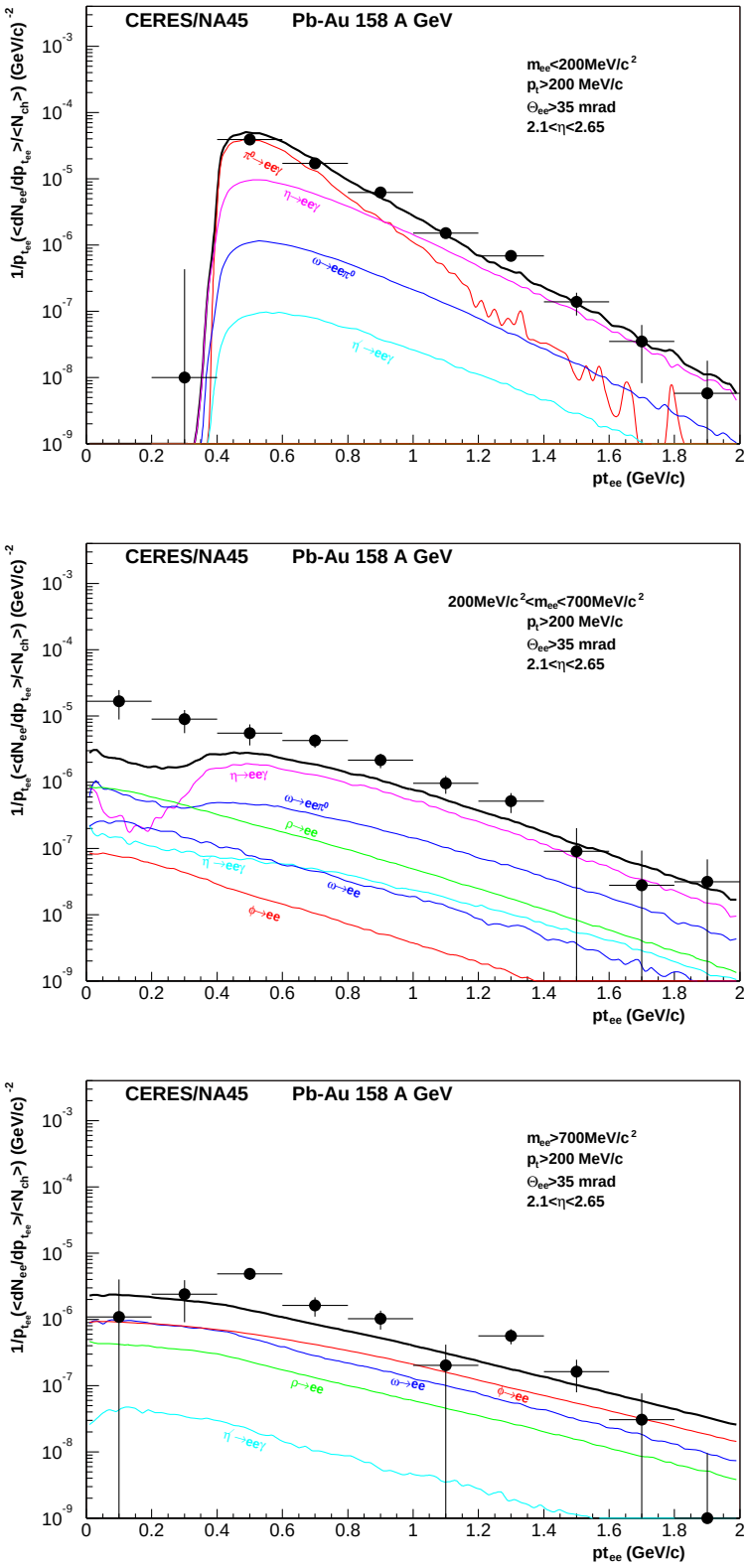

Figure 7.3: Transverse pair momentum distributions for the three mass regions $m_{ee} < 200$ MeV/c^2, $200 < m_{ee} < 700$ MeV/c^2 and $m_{ee} > 700$ MeV/c^2 compared to hadronic cocktail.

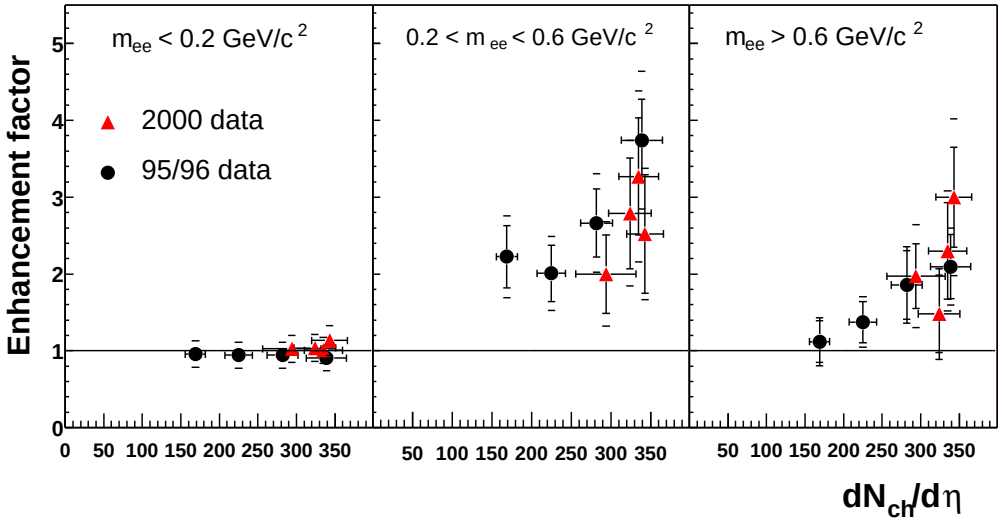

Figure 7.4: Enhancement factor as a function of charged particle density as found in Pb-Au collision systems for three mass regions. The expectation from the final-state hadron decays is shown by solid horizontal line indicating the enhancement factor 1. 2000 analysis is represented by the red triangles while the back points represent the result of the 95/96 combined data.

In fact, there are different expectations on the dependence of dilepton yield on the charged particle density

$$\frac{dN_{ee}}{d\eta} \sim (\frac{dN_{ch}}{d\eta})^{\alpha}. \tag{7.2}$$

In [112] the quadratic dependence (α = 2) is predicted while other proposals predict weaker dependence of e^+e^- pairs on charged particle multiplicity (α = 1.1 [113] and α = 1.3 [114]).

The observed stronger-than-linear scaling of the dilepton yield on N_{ch} provides a support for the two-body annihilation reactions as a dominant source of the electron pair enhancement. Unfortunately, still large statistical errors do not allow to distinguish between possible different scenarios of the scaling behavior, like a threshold effect or a saturation behavior.

7.5 Systematic Errors

The sources of the systematic errors include errors in the event generator and errors in the event analysis. The three main contributions to the systematics in the data analysis are the uncertainties in the efficiency correction, in the normalization of the mixed-event

background and in the normalization of the dilepton yield on the charged particle density.

The systematic uncertainties in the event generator are different for the low-mass and high-mass regions. The main contributions to the systematics for the masses $m_{ee} < 200$ MeV/c^2 dominated by π^0-Dalitz are the uncertainties in the relative production cross section of the π^0 and the parameterization of the transverse momentum and the input rapidity distributions. For m_{ee} above 200 MeV/c^2 the sources of the systematic errors are the detailed properties of the electro-magnetic decays as well as the relative production cross sections of the high mass mesons. A detail description of the uncertainties in the event generator can be found in [24, 30]. The systematic errors of the hadronic cocktail were estimated to be 8% for the low-mass and 30% for the high mass regions.

In the data analysis the errors in the efficiency correction arise from the fact that simulated detector responses do not exactly match the experimental data distributions. Thus the cuts applied might affect the simulated and the real tracks in a slightly different way leading to increase or decrease of the estimated efficiency. The dominant contribution to the error in the efficiency correction is given by a cut on the non-linear Hough amplitude of the ring (see section 6.2). A detailed study of the Hough amplitude distributions was performed in the data on the Dalitz sample. The simulated Hough amplitudes are shifted relative to the data by up to 10% depending on the selection criteria of the data Dalitz sample. To account for the observed relative difference between the data and the MC, the cut on the Hough amplitude that is lower by 10% than in the data was applied. This leads to a change in the pair reconstruction efficiency of 8%. Thus the shift in the distribution of Hough amplitudes is assumed to introduce a 4% systematic error. All other distributions are well reproduced by the MC (chapter 6) with exception of the sum analog amplitudes and number of hits per ring in both RICH detectors. The cuts on sum analog amplitude have been completely discarded as potentially dangerous ones leading large systematic uncertainties. The number of hits per ring in the simulation was observed to be shifted by approximately 1 hit relative to the data. This required consequently lowering of the corresponding cuts on MC information. In order to estimate a total sum effect of all cuts on systematics, the relative changes in the open Dalitz decay yields between pre-rejection stage and post-rejection stage have been studied separately for the data and MC. In order to suppress the γ-conversion admixture to the Dalitz sample in the data for a case of the pre-rejection stage, cuts on SDD $\mathrm{d}E/\mathrm{d}x$ and on Hough amplitude were applied. They correspond to cuts number 1 and 2 in Fig. 4.24. Thus the pre-rejection stage corresponds to cut number 2, while the post-rejection stage corresponds to cut number 11. The identical first two cuts were applied for the MC Dalitz sample in a case of the pre-rejection stage. It is also worth to note that the first SDD $\mathrm{d}E/\mathrm{d}x$ cut performed on multi-anode hits is perfectly reproduced by the MC simulations (see section 6.1) and therefore gives a negligible contribution to systematics. The ratio of the Dalitz yield at the post-rejection stage to the Dalitz yield at the pre-rejection stage gives a relative rejection. The estimated relative rejection of Dalitz decays is 0.71 in the data and 0.69 in the MC. Therefore the relative difference between these two ratios is 2.8%. The contribution of the Hough amplitude cut, not accounted for by the study of the Dalitz decay yields, has already been estimated as 4%. Matching cuts of $3{\cdot}\sigma$ lead to 2.8% error for a pair. Therefore the total systematic uncertainty of the pair efficiency correction can be considered as 5.6%.

The next contribution to the systematic error is the normalization of the mixed event

background. The error of the fit of the ratio of the geometric mean of the like-sign e^+e^+ and e^-e^- mass spectra to the mixed event background contributes to the systematic uncertainty with 8.5% given the signal-to-background ratio of 1/21.

The systematic error of N_{ch} was estimated by checking the sensitivity of the results to small modifications of the analysis procedure [81] as varying the positions and the width of the ϕ regions, varying the range of normalization during fake subtraction, choice of $\Delta\phi$ in the two-track extrapolation, *etc*. The quadratic sum of all effects on N_{ch} was estimated to be 12%.

Therefore the overall systematic error is 15.7% (uncertainties in the cocktail are not included).

7.6 Theoretical Interpretations

This section briefly reviews main theoretical efforts in studying the experimental data on the low mass dilepton production.

7.6.1 Free $\pi^+\pi^-$ Annihilation in the Hadronic Fireball

At full CERN SPS energies the ratio of pions to baryons is approximately 5:1. Therefore, as already mentioned, the dominant in-medium source is expected to stem from $\pi^+\pi^-$ annihilation

$$\pi^+\pi^- \rightleftharpoons \rho \rightarrow e^+e^-. \tag{7.3}$$

All calculations based on the free $\pi^+\pi^-$ annihilation have the common feature. Although an increased total yield approximately agrees with the experimental data, the shape of the spectra strongly deviates from the data. All theoretical calculations produce too much yield around the free ρ mass and too little below, which is a consequence of the free pion electromagnetic form factor peaking at the ρ resonance.

Incompatibility of free $\pi^+\pi^-$ annihilation shows up in the all CERES results obtained in the ion-induced reactions. Although the strong excess of the data over the hadronic cocktail observed in the early sulfur runs is somewhat reduced in the 1995/96 combined data analysis as well as in the 2000 data analysis displayed in Fig. 7.5, the inclusion of the free $\pi^+\pi^-$ annihilation can still not resolve the discrepancy with the data.

While in the ion-induced systems the cocktail is somewhat close to saturating the data in the ρ/ω region, the free $\pi^+\pi^- \rightarrow \rho^0 \rightarrow e^+e^-$ process has its maximum contribution. However, for the SPS conditions the excited nuclear system is expected to spend a significant part of its space-time history in a hadronic phase with a large pion component. Therefore $\pi^+\pi^-$ annihilation can not be neglected in favor of other different processes with flat characteristics as a function of invariant mass ($q\bar{q}$ annihilation). Considering $\pi^+\pi^-$ annihilation as a dominant process, essential medium modifications are expected to give additional strength to the low mass dilepton yield resulting in filling the 0.3-0.6 GeV/c^2 mass region without giving too much yield around the free ρ meson mass.

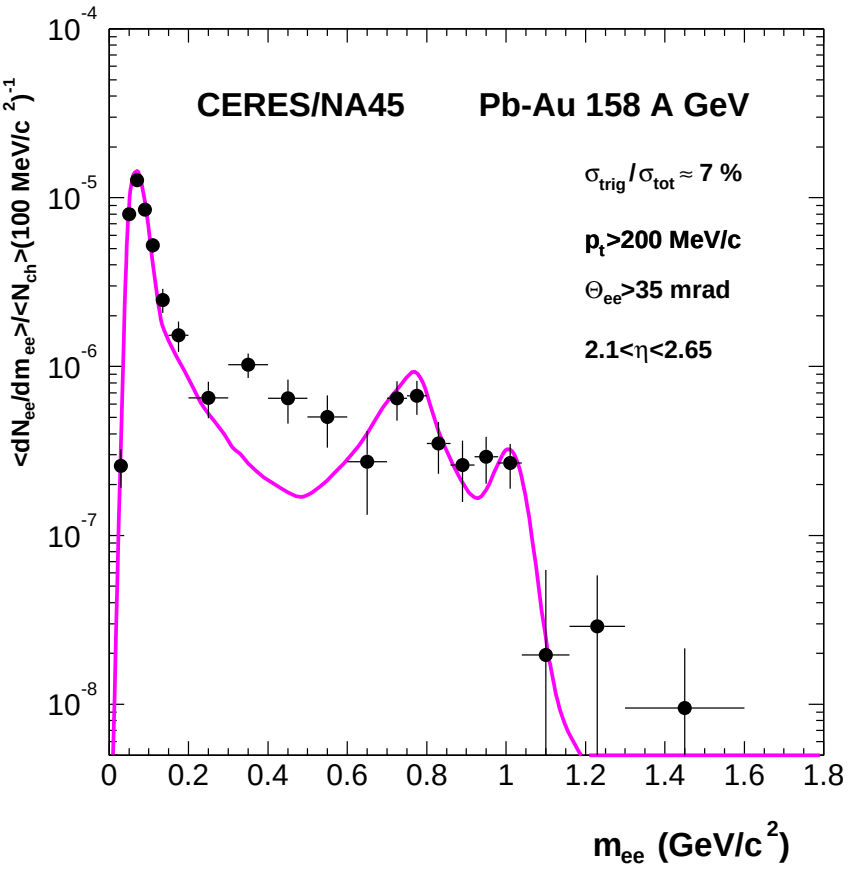

Figure 7.5: Comparison of e^+e^- mass spectrum with the calculation based on $\pi^+\pi^-$ annihilation using the free ρ spectral function.

7.6.2 In-medium Modifications of the Vector Mesons

Large efforts have been undertaken to investigate the in-medium ρ meson properties due to its prominent role in heavy ion dilepton measurements. As discussed in the introduction, among the light vector mesons the short-lived ρ decays inside the fireball which makes it most sensitive to the in-medium modifications.

There are two main approaches which include medium-induced changes of the vector meson properties:

- The approach developed by Brown and Rho, in which the masses of vector mesons reduce as a function of the density and essentially in proportion to the disappearance of the quark condensate. In this intuitive picture the observed dilepton yield provides a direct link to the chiral symmetry restoration.

- A different approach was developed by Rapp and Wambach, implying a dynamical modifications of the ρ spectral function due to coupling to the dense hadronic medium. Calculations based on this technique fit the experimental data in the region of dilepton continuum equally well but deviate from the Brown-Rho scaling

results in the mass range between ω and ϕ resonances. This difference allows a discrimination of the two theoretical approaches which will be discussed later in this section.

Brown-Rho scaling.

One of most prominent approaches that has been successfully applied to explain the low-mass dilepton enhancement in the CERES data in connection with chiral restoration transition is based on the Brown-Rho (BR) scaling. In the dilepton context, the most relevant feature is the decrease of the ρ-meson mass at finite temperature and density which leads to a strong excess of e^+e^- pairs below the free ρ mass through the $\pi\pi$ annihilation channel. As long as no collisional broadening in the ρ width is included, the e^+e^- yield is sharply centered around the corresponding in-medium mass m^*_ρ.

The first step in the derivation of Brown-Rho scaling is the construction of the effective Lagrangian by introducing an effective "glueball" field χ. Proportional to the gluon condensate the trace anomaly of QCD breaks the symmetry of the Lagrangian. Thus, when the gluon condensate is melted, the scale invariance is restored and the chiral transition with light quarks occurs. The χ field can be understood as consisting of a soft χ^* and hard χ' components

$$\chi = \chi^* + \chi'. \tag{7.4}$$

The soft part governs the in-medium modifications in the chiral effective Lagrangian and scales with the quark condensate. Assuming the symmetries of the Lagrangian remain untouched the variations in the quark condensate are postulated to scale with a density dependent change in masses. Thus the approximate Brown-Rho scaling relation reads

$$\Phi = \frac{f^*_\pi}{f_\pi} \approx \frac{m^*_\rho}{m_\rho} \approx \frac{m^*_\omega}{m_\omega} \approx \frac{\langle q\bar{q}\rangle^*}{\langle q\bar{q}\rangle}, \tag{7.5}$$

where f^*_π is in-medium pion decay constant defined as $f^*_\pi = f_\pi \cdot \chi^*/\chi_0$. The in-medium quantities are referred as "*" while "0" refers to vacuum values. Consequently, according to the BR scaling, the masses of non-strange vector mesons vanish in the dance matter together with the quark condensate, the order parameter of the chiral transition.

The Brown-Rho "dropping mass" hypothesis received an independent support by QCD sum rules calculations of Hatsuda and Lee [115], who estimated the density and temperature dependence of m^*_ρ,

$$m^*_\rho = m_\rho(1 - C\frac{\varrho_B}{\varrho_0})(1 - (\frac{T}{T^\chi_c})^2)^\alpha \tag{7.6}$$

with C = 0.15, T^χ_c = 200 MeV and α = 0.3.

The calculation based on Brown-Rho scaling is in good agreement with low-mass e^+e^- enhancement observed in the experimental data (Fig 7.6). The added QGP contribution is small and insensitive to initial temperature and details of the phase transition construction. Indeed, the fireball spends relatively small fraction of its space-time evolution in the QGP phase at the SPS energies. Thus, in fact, the effect of the quark-untiquark annihilation from the QGP phase in the low mass region is negligible.

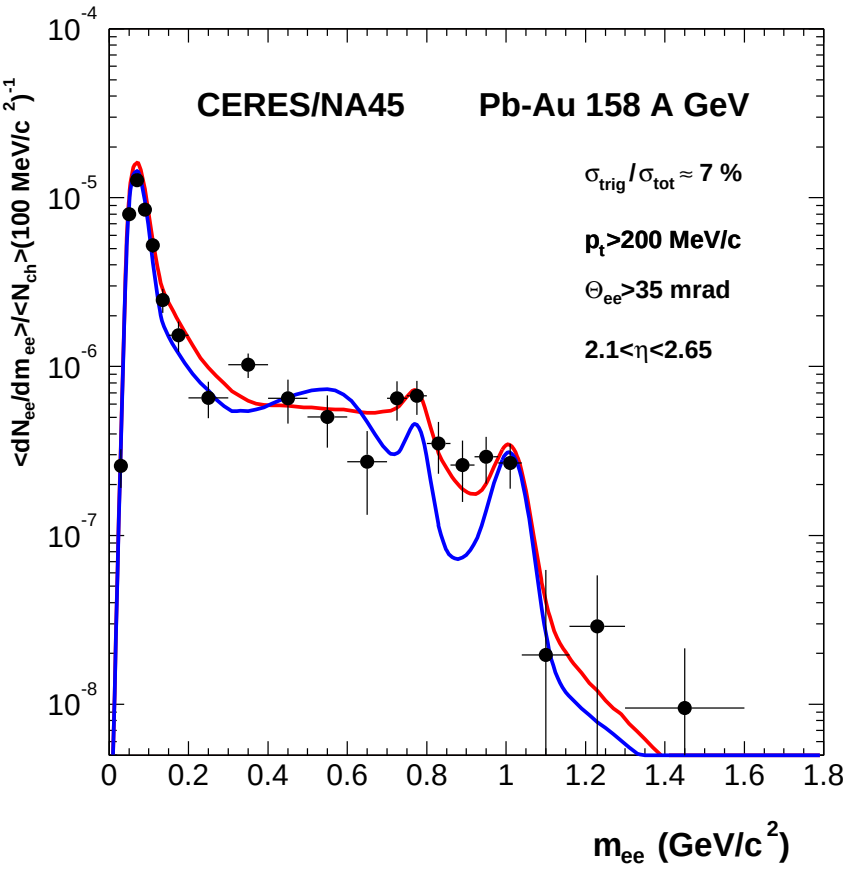

Figure 7.6: Comparison of e^+e^- mass spectrum with fireball calculations using thermal production rates from in-medium $\pi^+\pi^-$ annihilation in two scenarios. Red line: hadronic cocktail plus $\pi^+\pi^-$ annihilation employing the in-medium ρ spectral function plus QGP, blue line: hadronic cocktail plus $\pi^+\pi^-$ annihilation using a dropping ρ mass plus QGP.

The early phase is characterized by hadronic initial conditions of T $\approx$ 170 MeV and $\varrho_B \approx 2.5\varrho_0$. In this phase the in-medium mass m^*_ρ is close to the two-pion threshold. While the expanding hot fireball dilutes and cools, m^*_ρ starts to rise and sweeps across the low-mass region thus filling the dilepton continuum between 0.3 and 0.6 GeV/c^2. At the same time, the ρ contribution to the free ρ peak is strongly reduced, which is also in agreement with the data. For the ω-meson the situation is different. Although in BR scaling the ω mass is subjected to the same reduction as the ρ mass, the medium modifications of the ω meson have a very little impact on the dilepton spectrum due to the fact, that the $\omega \rightarrow e^+e^-$ decays mostly occur after the hadronic freeze-out where medium effects are absent. Therefore the final number of ω mesons is roughly equal to the case where no dropping masses are assumed.

Rapp-Wambach approach.

An approach developed by Rapp and Wambach assumes a modification of both π and ρ properties due to phenomenologically inferred interactions with the surrounding hadrons in the hot and dense gas which are encoded in the ρ-meson spectral function. The approach is based on nuclear and finite-temperature many body techniques including constraints from nuclear photoabsorption [116] and $\pi N \rightarrow \rho N$ data [117], Rhosobar excitations on thermally excited baryon resonances as well as a more complicated assessment of the mesonic contributions [118].

In the hot and dense matter the ρ meson couples directly to the surrounding nucleons and thermal mesons. A vector-meson selfenergy is given by

$$\Sigma_\rho = \Sigma_{\rho\pi\pi} + \Sigma_{\rho M} + \Sigma\rho B. \tag{7.7}$$

$\Sigma_{\rho M}$ describes the interactions with surrounding hot mesons ($M = \pi, K, \rho$, ...) and $\Sigma_{\rho B}$ arises from the interactions with dense baryons ($B = N, \Lambda, \Delta$, ...). $\Sigma_{\rho\pi\pi}$ incorporates medium modifications of the free $\rho \rightarrow \pi\pi$ decay. The outcome of the calculations is a strong increase of the imaginary part of the ρ-meson selfenergy. This consequently broadens the ρ-meson spectral function beyond recognition of any resonance structure. It was shown that the temperature effects lead to a small mass shift and a negligible broadening of the ρ spectra function. Thus, am important point to note is that the baryons, rather than pions which govern the finite temperature effects, in the hadronic fireball are at the origin of the dilepton enhancement.

In contrast to "dropping mass" scenario, the many-body approach provides a sufficient yield in the vector meson region (Fig 7.6). Thus the in-medium spectral function seems to describe the data better (normalized χ^2 = 0.6) in the region between the ω and ϕ than BR scaling (normalized χ^2 = 3.9). As already mentioned, the dileptons originated from $q\bar{q}$ annihilation in the QGP phase, added to in-medium broadening ρ, contribute mostly to the e^+e^- yield above 1 GeV/c^2, while the contribution of the QGP phase for the masses below 1 GeV/c^2 relative to that of the hadronic phase is very small.

Independent confirmation of this result was obtained by NA60 experiment in $\mu^+\mu^-$ channel [119]. They conclude, independent of any comparison to theoretical modeling, that the ρ primarily broadens in In-In collisions, but does not show any noticeable shift in mass.

7.6.3 Transverse Pair Momentum Dependencies

The dependency of the dilepton tranverse momentum observed in the data can be related to a break of the Lorenz invariance of space-time in the thermal frame, in which the matter as a whole is at rest. This implies that the vector meson spectral functions separately depend on invariant mass $M = \sqrt{q_0^2 - \vec{q}^2}$ and three-momentum. Moreover, their polarization states are no longer isotropic, but split up into two completely independent modes, described in terms of longitudinal and transverse components.

Both the BR scaling and the in-medium spectral function approaches which successfully reproduced the e^+e^- invariant mass spectra, are also applied to calculate the transverse momentum spectra [117, 120] The reduction of the ρ mass is also reflected in the transverse pair momentum dependence due to the thermal occupation factor, which de-

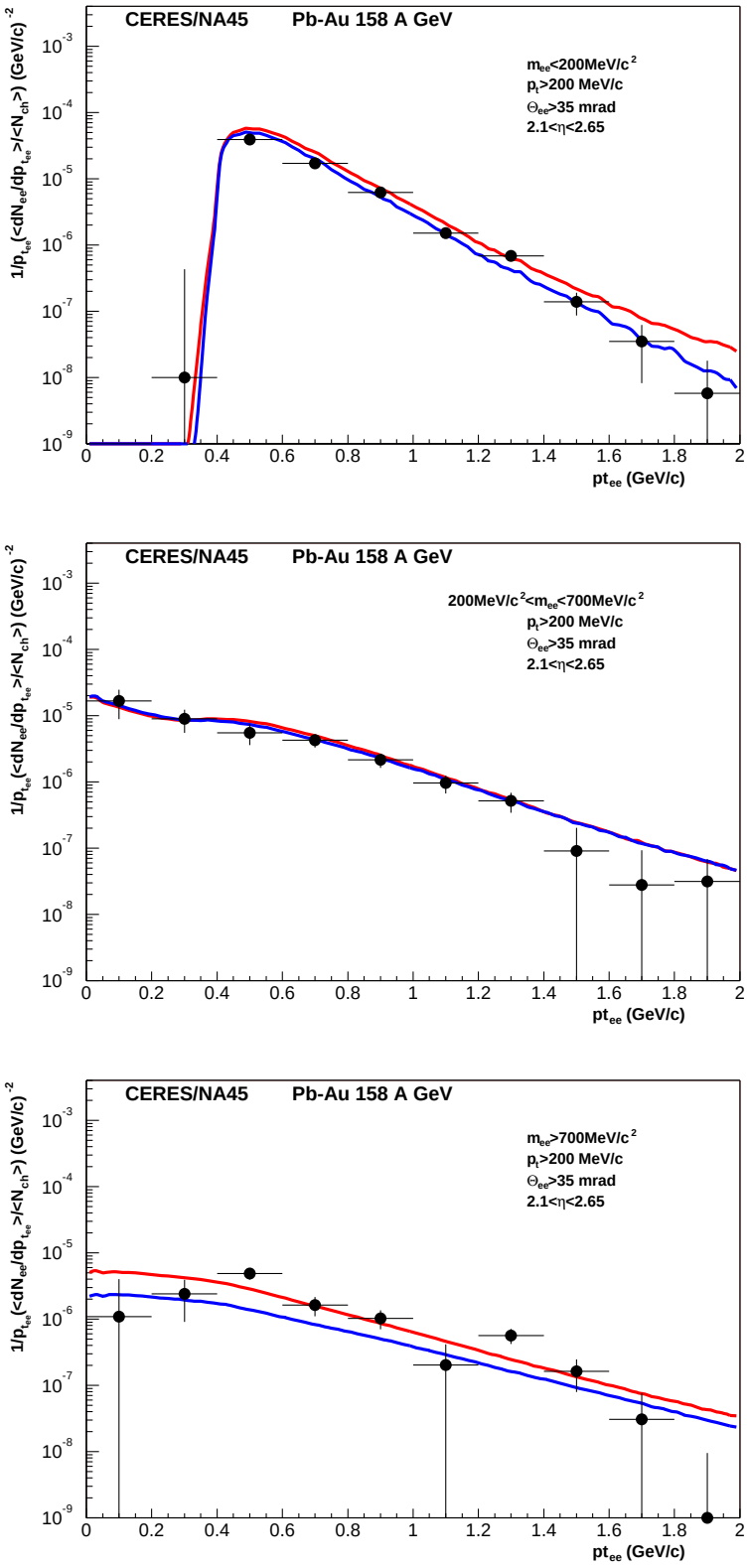

Figure 7.7: Comparison of transverse pair momentum distributions for the three mass regions $m_{ee} < 200$ MeV/c^2, $200 < m_{ee} < 700$ MeV/c^2 and $m_{ee} > 700$ MeV/c^2 with theoretical calculations using a thermal fireball model including $\pi^+\pi^-$ annihilation with a dropping ρ mass plus hadronic cocktail (blue curve) and $\pi^+\pi^-$ annihilation with the in-medium ρ spectral function plus hadronic cocktail (red curve).

pends on energy. Therefore the three-momentum dependence of $q_0 = \sqrt{(m_\rho^*)^2 + \vec{q}^2}$ is more pronounced for small ρ mass m_ρ^*. The calculation based on BR scaling scenario is illustrated in Fig. 7.7. A theoretical curve is in good agreement with the data. In the mass region 200 $< m_{ee} <$ 700 MeV/c^2 the dropping ρ mass curve is enhanced mostly at transverse pair momenta below 700 MeV/c, which is a consequence of the relative enhancement of the ρ mesons of small three-momentum.

The many-body approach includes more complicated three-momentum dependencies predicted on the basis of photoabsorption analysis [116]. A spectral function calculations [121] results in a similar to the dropping ρ mass behavior. As shown in Fig. 7.7, the theoretical curve for the many-body approach agrees with the data as well.

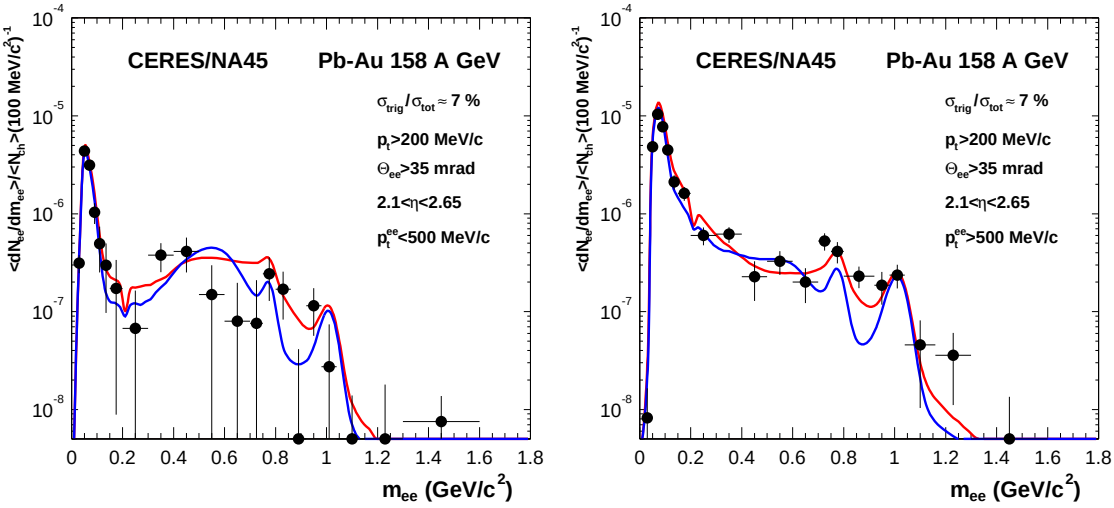

Figure 7.8: Inclusive mass spectra for the two transverse pair momentum bins. Left panel: $p_t^{ee} <$ 500 MeV/c. Right panel: $p_t^{ee} >$ 500 MeV/c. The data are compared to three theoretical calculations: dropping in-medium ρ mass (blue curve) and a medium-modified ρ spectral function (red curve).

Another projection of the data is the invariant mass spectra for two different regions of transverse pair momentum, $p_t^{ee} <$ 500 MeV/c and $p_t^{ee} >$ 500 MeV/c illustrated in Fig. 7.8. Again, the major part of the low mass enhancement is concentrated in the low momentum bin. The data are nicely reproduced by both a dropping ρ mass and the in-medium broadened spectral function, which confirms the predictions based on photoabsorption data.

7.7 Summary

The thesis reports on a new CERES measurement of electron-pair production in 158 A GeV Pb-Au collisions which was performed in the year 2000 with the upgraded experimental setup. The newly installed TPC improved mass resolution in the vector meson region as

well as rejection capabilities. The analysis of the 18.2×10^6 events confirmed the previous findings of a strong enhancement of the e^+e^- pairs over the expectations from the hadronic decays for the masses $0.2 < m_{ee} < 0.6$ GeV/c^2. While, as expected, the low mass region below 0.2 GeV/c^2 dominated by π^0-Dalitz decays is described by the expectations from the hadronic decays. The normalized yield of e^+e^- pairs integrated for the masses $0.0 < m_{ee} < 0.2$ GeV/c^2 is $(8.44 \pm 0.28[\text{stat}] \pm 1.33[\text{syst}])\times10^{-7}$. Integrating the normalized yield in the mass region $0.2 < m_{ee} < 1.1$ GeV/c^2 gives $(4.49 \pm 0.41[\text{stat}] \pm 0.70[\text{syst}])\times10^{-7}$. The ratio of the normalized yield of e^+e^- pairs to the sum of the contributions from hadronic decays integrated in the mass region $0.2 < m_{ee} < 1.1$ GeV/c^2 is $2.45 \pm 0.22[\text{stat}] \pm 0.38[\text{syst}] \pm 0.74[\text{decays}]$. The measured transverse pair momentum spectra indicate that dilepton enhancement is located mostly at low p_t^{ee}. This is also confirmed by the difference in the enhancement factors in the e^+e^- invariant mass spectra for $p_t^{ee} < 500$ MeV/c and $p_t^{ee} > 500$ MeV/c. The observed stronger-than-linear scaling of the dilepton signal on the charge particle density supports the two-body annihilation reactions as a dominant source of the electron pair enhancement. The results are in agreement with two other analysis of the 2000 data [67, 92].

The major result reported in this thesis is the discrimination between two competing theoretical approaches accounting for the strong low-mass dilepton pair excess. The two models, both including in-medium modifications of the vector meson properties, describe the data below the 0.7 GeV/c^2 reasonably well but exhibit different behavior between the ω and the ϕ mesons. Due to a careful calibration of the TPC and the improved mass resolution of 3.8% (at ϕ) it could be established that the characteristic feature of the dropping ρ mass scenario showing a deep gap in the mass spectrum between ω and ϕ is not met by the data. Rather the data is better supported by the in-medium spectral function approach, yielding a goodness of fit normalized $\chi^2 = 0.6$ in the mass region $0.8 < m_{ee} < 0.98$ GeV^2, compared to $\chi^2 = 3.9$ for the dropping ρ mass calculation, where the gap in yield is filled in by the broadened ρ.

Bibliography

[1] J. Slivova, *Azimuthal Correlations of High-pt Pions in 158 AGeV/c Pb-Au Collisions measured by the CERES/NA45 Experiment*, PhD thesis, Charles University in Prague, Czech Republic, 2003.

[2] J. Stachel, Nucl. Phys. **A 654**, 119 (1999), nucl-ex/9903007.

[3] WA98 Collaboration, M. Aggarwal *et al.*, Nucl. Phys. **A 638**, 147 (1998).

[4] WA97 Collaboration, R. Lietava, J. Phys. G: Nucl. Part. Phys. **25** (1999).

[5] WA97 Collaboration, E. Andersen *et al.*, Phys. Lett. **B 433**, 209 (1998).

[6] NA49 Collaboration, H. Appelshäuser *et al.*, Phys. Lett. **B 444**, 523 (1998).

[7] NA44 Collaboration, M. Kaneta *et al.*, Nucl. Phys. **A 638**, 419 (1998).

[8] NA49 Collaboration, I. Bearden *et al.*, Phys. Rev. Lett. **78**, 2080 (1997).

[9] NA49 Collaboration, G. Roland, Nucl. Phys. **A 638**, 91 (1998).

[10] P. Braun-Munzinger and J. Stachel, Nucl. Phys. **A606**, 320 (1996), nucl-th/9606017.

[11] P. Braun-Munzinger, Nucl. Phys. **A663**, 183 (2000), nucl-ex/9909014.

[12] U. Heinz and M. Jacob, p. 7 (2000), nucl-th/0002042.

[13] P. Braun-Munzinger and J. Stachel, Nucl. Phys. **A 638** (1998), nuclex/9803015.

[14] F. Karsch, Lect. Notes Phys. **583**, 209 (2002).

[15] F. Karsch, Phys. Lett. **B478**, 447 (2000), hep-lat/0002003.

[16] F. Karsch, Nucl. Phys. Proc. Suppl. **83**, 884 (2000), hep-lat/9909014.

[17] E. Shuryak, Phys. Lett. **B78**, 150 (1978).

[18] NA38 Collaboration, M. Abreu *et al.*, Phys. Lett. **B 368**, 230 (1996).

[19] NA50 Collaboration, M. Gonin *et al.*, Nucl. Phys. **A 610**, 404 (1996).

[20] NA50 Collaboration, E. Scomparin *et al.*, Nucl. Phys. **A 610**, 331 (1996).

[21] HELIOS-3 Collaboration, M. Masera, Nucl. Phys. **A590** (1995), 93.

[22] A. Angelis *et al.*, Eur. Phys. J. **C5** (1998), 63.

[23] CERES Collaboration, G. Agakichiev *et al.*, Eur. Phys. J. **C4** (1998).

[24] CERES Collaboration, G. Agakichiev *et al.*, Eur. Phys. J. **C4**, 231 (1998).

[25] C. P. d. l. Heros, *Low-mass e^+e^- production in S-Au collisions at 200 GeV/c*, PhD thesis, Weizmann Institute of Science Rehovot, Izrael, 1996.

[26] CERES Collaboration, G. Agakichiev *et al.*, Phys. Rev. Lett. **75** (1995).

[27] T. Ullrich, *Production von e^+e^--Paar Emission in S-Au-Kollisionen bei 200 GeV/u* (Doctoral thesis, University of Heidelberg, Germany, 1994).

[28] CERES Collaboration, G. Agakichiev *et al.*, Phys. Lett. B **422**, 405 (1998), nucl-ex/9712008.

[29] CERES Collaboration, G. Agakichiev *et al.*, Nucl. Phys. A **638**, 159 (1998).

[30] CERES Collaboration, G. Agakichiev *et al.*, Eur. Phys. J. C **41**, 475 (2005).

[31] B. Lenkeit, *Electron-Positron-Paar Emission in Pb-Au-Kollisionen bei 158 A GeV* (Doctoral thesis, University of Heidelberg, Germany, 1998).

[32] B. Lenkeit *et al.*, Nucl. Phys. **A661**, 23 (1999), nucl-ex/9910015.

[33] C. Voigt, *Production von e^+e^--Paaren in ultrarelativisischen Pb-Au Kollisionen bei 160 A GeV* (Doctoral thesis, University of Heidelberg, Germany, 1998).

[34] G. Hering, *Dielectron production in heavy-ion collisions at 158 GeV/c per nucleon* (Doctoral thesis, Technical University Darmstadt, Germany, 2002).

[35] E. Socol, *Dilepton production in Pb-Au collisions at 158 GeV per nucleon using the CERES detector*, PhD thesis, Weizmann Institute of Science Rehovot, Izrael, 1999.

[36] CERES Collaboration, I. Ravinovich *et al.*, Nucl. Phys. **A 638**, 159 (1998).

[37] CERES Collaboration, D. Adamova *et al.*, Phys. Rev. Lett. **91**, 042301 (2003), nucl-ex/0209024.

[38] S. Damjanovic, *Electron-pair production in Pb-Au collisions at 40 AGeV* (Doctoral thesis, University of Heidelberg, Germany, 2002).

[39] CERES Collaboration, H. Appelshäuser, Nucl. Phys. **A 698**, 253 (2002).

[40] CERES Collaboration, J. Wessels, Nucl. Phys. **A 715**, 262 (2003).

[41] W. Cassing, W. Ehehalt, and C. Ko, Phys. Lett. **B 363**, 35 (1995).

[42] G. Li, C. Ko, G. Brown, and H. Sorge, Nucl. Phys. **A 611**, 539 (1996).

[43] G. Brown and M. Rho, Phys. Rept. **269**, 333 (1996), hep-ph/9504250.

[44] R. Rapp and J. Wambach, Adv. Nucl. Phys. **25**, 1 (2000), hep-ph/9909229.

[45] R. Rapp, G. Chanfray, and J. Wambach, Nucl. Phys **A 617**, 472 (1997), hep-ph/9702210.

[46] R. Baur *et al.*, Nucl. Instr. Meth. **A 343**, 87 (1994).

[47] CERES Collaboration, T. Ullrich *et al.*, Nucl. Phys. **A 610**, 317 (1996).

[48] R. Baur *et al.*, Nucl. Instr. Meth. **A 371**, 16 (1996).

[49] P. Holl *et al.*, Nucl. Instr. Meth. **A 337**, 367 (1996).

[50] E. Gatti and P. Rehak, Nucl. Instrum. Meth. **A225**, 608 (1984).

[51] P. Holl, Nucl. Instrum. Meth. **A377**, 367 (1996).

[52] R. Baur *et al.*, Nucl. Instr. Meth. **A 355**, 329 (1994).

[53] A. Marin, Nucl. Phys. **A661**, 673 (1999).

[54] B. Yu *et al.*, IEEE Trans. Nucl. Sci. **NS-38**, 454 (1991).

[55] CERES Collaboration, W. Schmitz, CERES-Note **01-98** (1998).

[56] W. Schmitz, *Lambda-Production in Pb-Au-Kollisionen bei 40 AGeV* (Doctoral thesis, University of Heidelberg, Germany, 2001).

[57] CERES Collaboration, R. Baur, P. Ernst, G. Gramegna, and M. Richter, Nucl. Instr. and Meth. **A 409**, 278 (1998).

[58] H. Tilsner, *Two-particle correlations at 40, 80, and 158 AGeV Pb-Au collisions* (Doctoral thesis, University of Heidelberg, Germany, 2002).

[59] P. Holl *et al.*, CERN/SPSLC 96-50 SPSLC/R110 .

[60] S. Esumi, private communications (2002).

[61] V. Yurevich, private communication (2005).

[62] http://castor.web.cern.ch/castor/ .

[63] http://root.cern.ch .

[64] D. Dougherty and T. O'Reilly, *Unix text processing* (Howard W.Sams, 1987).

[65] http://consult.cern.ch/service/afs/ .

[66] http://batch.web.cern.ch/batch/ .

[67] A. Cherlin, *Low-mass dielectron production in Pb-Au collisions at 158 A GeV using the upgraded CERES spectrometer*, PhD thesis, Weizmann Institute of Science Rehovot, Izrael, 2005.

[68] H. Sako, private communications (2003).

[69] J. Milošević, *Investigation of Azimuthal Asymmetries in Charged and Strange Particle Distributions from CERES* (Doctoral thesis, University of Heidelberg, Germany, 2006).

[70] A. Cherlin, private communications (2003).

[71] A. Marin, Private communications (2005).

[72] CERES Collaboration, A. Marin, J. Phys. **G 30**, 1007 (2004).

[73] Garfield version 7.02. CERN package. Magboltz interface. .

[74] L. Dietrich, *Optimierung der Elektron-Pion-Separation in der CERES-TPC* (Diploma thesis, University of Heidelberg, Germany, 2001).

[75] M. Huk, P. Igo-Kemenes, and A. Wagner, Nucl. Instrum. Meth. **A267**, 107 (1988).

[76] A. Manafov, GSI, private communication (2001).

[77] R. Wright Jr. and M. Sweet, *OpenGL SuperBible, Second Edition* (Pearson Education, 1999).

[78] S. Meyers, *Effective STL: 50 Specific Ways to Improve Your Use of the Standard Template Library* (Addison-Wesley Professional, 2001).

[79] J. Wernecke, *Inventor Mentor, The: Programming Object-Oriented 3D Graphics with Open Inventor* (Addison Wesley Professional, 1994).

[80] CERES Collaboration, G. Agakichiev *et al.*, Nucl. Instr. Meth. **A 394**, 225 (1997).

[81] D. Miskowiec, Internal Note, CERES collaboration (2005).

[82] D. Miskowiec, GSI, private communication (2005).

[83] http://www.gsi.de/ misko/overlap .

[84] A. Andronic, private communication (2005).

[85] U. Müller *et al.*, Nucl. Instr. and Meth. **A343**, 279 (1994).

[86] J. Bächer *et al.*, ibidem , 273.

[87] P. Hough, U.S. Patent No. 3069654 (1962).

[88] CERES Collaboration, G. Agakichiev *et al.*, Nucl. Instr. Meth. **A 371**, 243 (1996).

[89] W. Ludolphs, *Measurement of Open Charm in 158 AGeV/c Pb-Au Collisions* (Doctoral thesis, University of Heidelberg, Germany, 2006).

[90] CERES Collaboration, W. Schmitz, Jour. Phys. G **28**, 1861 (2002).

[91] W. Allison and J. Cobb, Ann. Rev. Nucl. Part. Sci. **30**, 253 (1980).

[92] O. Busch, (Doctoral thesis in preparation, Technical University Darmstadt, Germany).

[93] H. Sako, GSI Techn. Report 03-24 (2000).

[94] T. Sjoestrand, Manual **CERN-TH.7112/93** (1993).

[95] P. Braun-Munzinger, I. Heppe, and J. Stachel, Phys. Lett. **B 465**, 15 (1999), nucl-th/9903010.

[96] NA44 Collaboration, M. Kaneta *et al.*, J. Phys. **G 23**, 1865 (1997).

[97] NA49 Collaboration, H. Appelshäuser *et al.*, Nucl. Phys. **A 638**, 91 (1998).

[98] WA98 Collaboration, M. Aggarwal *et al.*, Phys. Rev. Lett. **81**, 4087 (1998).

[99] NA49 Collaboration, F. Sikler *et al.*, Nucl. Phys. **A 661**, 341 (1999).

[100] NA49 Collaboration, F. Höhne *et al.*, Nucl. Phys. **A 661**, 485 (1999).

[101] CERES Collaboration, G. Agakichiev *et al.*, Phys. Rev. Lett. **92**, 032301 (2004), nucl-ex/0303014.

[102] CERES Collaboration, F. Ceretto *et al.*, Nucl. Phys. **A 638**, 467 (1998).

[103] R. Dzhelyadin *et al.*, Phys. Lett. **102B**, 239 (1981).

[104] L. Landsberg *et al.*, Phys. Rep. **128**, 301 (1985).

[105] B. Friman and J. Knoll, private communications (2004).

[106] S. Eidelman *et al.*, Phys. Lett. **B 592**, 1 (2004).

[107] R. Brun *et al.*, CERN DD/EE/84-1 .

[108] V. Ermilova *et al.*, Sov. Phys. JETP **29**, 861 (1969).

[109] F. Sauli, CERN Preprint **77-09** (1977).

[110] E. Mathieson, NIM **A270**, 602 (1988).

[111] CERES Collaboration, D. Adamova *et al.*, (2005), nucl-ex/0512007.

[112] V. Cerny, P. Lichard, and J. Pisut, Z.Phys **C31**, 163 (1986).

[113] J. Cleymans, K. Redlich, and D. Srivastava, Phys. Lett. **B 420**, 261 (1998).

[114] E. Feinberg, Nuovo Cim. **A34**, 391 (1976).

[115] T. Hatsuda, Nucl. Phys. **A 544**, 27 (1992).

[116] R. Rapp, M. Urban, M. Buballa, and J. Wambach, Phys. Lett. **B 417**, 1 (1998).

[117] R. Rapp, Edition Frontiers (1998), nucl-th/9804065.

[118] R. Rapp and C. Gale, Phys. Rev. **C60**, 024903 (1999), hep-ph/9902268.

[119] NA60 Collaboration, S. Damjanovic, To appear in the proceedings of 18th International Conference on Ultrarelativistic Nucleus-Nucleus Collisions (2005), nucl-ex/0510044.

[120] G. Brown, G. Li, R. Rapp, M. Rho, and J. Wambach, Acta Phys. Polon. **B 29**, 2309 (1998).

[121] R. Rapp and J. Wambach, hep-ph/9907502.

Acknowledgments

Since I joined the CERES collaboration, I have enjoyed a pleasant working atmosphere and many useful discussions with colleagues. I wish to thank Prof. Johanna Stachel for inviting me to participate in CERES experiment and guiding my work on the dilepton data analysis with excellent advises and assistance.

I am also very thankful to Ana Marin for her help, numerous discussions, careful reading of the preliminary draft of this thesis and many helpful comments.

Next, I wish to thank Hejdar Agakichiev for his advises and help with some projects. I am also thankful to Alex Cherlin for a joined effort to complete the analysis of the data and to Oliver Busch for sharing his results on the RICH performance.

I wish also to thank various members of the CERES collaboration for their contribution in different parts of this work: Dariusz Antończyk, Harald Appelshäuser, Peter Glässel, Kirill Filimonov, Anar Manafov, Dariusz Miśkowiec, Hirouki Sako, Thomas Wienold, Peter Wurm and others.

I am thankful to Jovan Milošević, Jana Bielčíková and Wilrid Ludolphs for many interesting discussions on non-physics topics and just for a nice time spent together.

Finally, I wish to thank my wife Oksana and my family for their love, patience and support during all these years.

CERES/NA45 Collaboration

D. Adamová [a], G. Agakichiev[b], D. Antończyk[b], A. Andronic[b], H. Appelshäuser[c], V. Belaga[d], J. Bielčíková[e k], P. Braun-Munzinger[b], O. Busch[b], R. Campagnolo[e], A. Cherlin[f], S. Damjanovic[e], T. Dietel[e], L. Dietrich[e], A. Drees[g], S. I. Esumi[e], K. Filimonov[e], K. Fomenko[d], Z. Fraenkel[f], C. Garabatos[b], P. Glässel[e], G. Hering[b], J. Holeczek[b], M. Kaliski[b], S. Kniege[c], V. Kushpil[a], W. Ludolphs[e], A. Maas[b], A. Manafov[b], A. Marín[b], J. Milošević[e], D. Miśkowiec[b], L. Musa[i], R. Ortega[e], Y. Panebrattsev[d], O. Petchenova[d], V. Petráček[e], M. Ploskon[c], S. Radomski[b], J. Rak[b], I. Ravinovich[f], P. Rehak[h], H. Sako[b], W. Schmitz[e], J. Schukraft[i], S. Sedykh[b], W. Seipp[e], S. Shimansky[d], R.Soualah[e], J. Stachel[e], M. Šumbera[a], H. Tilsner[e], I. Tserruya[f], G. Tsiledakis[b], J. P. Wessels[j], T. Wienold[e], B. Windelband[e], J. P. Wurm[k], S. Yurevich[e], V. Yurevich[d]

[a] NPI/ASCR, Řež, Czech Republic
[b] GSI, Darmstadt, Germany
[c] Universität Frankfurt, Germany
[d] JINR, Dubna, Russia
[e] Universität Heidelberg, Germany
[f] Weizmann Institute, Rehovot, Israel
[g] Department for Physics and Astronomy, SUNY Stony Brook, USA
[h] Brookhaven National Laboratory, Upton, USA
[i] CERN, Geneva, Switzerland
[j] Universität Münster, Germany
[k] Max-Planck-Institut für Kernphysik, Heidelberg, Germany